Pseudo-ductility in CFRP laminates through the ply weakening method

by

Jingjing Sun

A Thesis submitted in fulfilment of the requirements for the degree of Doctor of Philosophy and the Diploma of Imperial College London

Department of Aeronautics

Imperial College London

Declaration of Originality

The work presented hereafter is based on research carried out by the author at the Department of Aeronautics of Imperial College London and it is all the author's own work except where otherwise acknowledged. No part of the present work has been submitted elsewhere for another degree or qualification.

Signature 

Date 30/05/2019.

Copyright Declaration

The copyright of this thesis rests with the author and is made available under a Creative Commons Attribution Non-Commercial No Derivatives licence. Researchers are free to copy, distribute or transmit the thesis on the condition that they attribute it, that they do not use it for commercial purposes and that they do not alter, transform or build upon it. For any reuse or redistribution, researchers must make clear to others the licence terms of this work.

Acknowledgements

I would like to thank my supervisor Prof. Paul Robinson for offering me this opportunity to be involved in the High Performance Ductile Composite Technology (HiPerDuCT) programme, the patient guidance and consistent weekly discussion and advices during the past four years. I would also like to express my gratitude to Dr. Omar Bacarreza Nogales. Their selfless help and guidance expanded the scope and deepened my understanding of the composite research.

I am grateful to all the members involved in the HiPerDuCT programme, a collaborative project between Imperial College London and the University of Bristol, for sharing their knowledge of composite research.

I would like to express my gratitude to the staffs in the Aeronautics Department. I would like to thank Dr Frank Gommer for the encouragement and valuable suggestions, Gary Senior and Jonathan Cole for their help on sample preparation and training for the Ultrasonic C-scan, SEM and X-ray scanning machines, Joseph Meggyesi and Keith Wolstenholme for their patient tutorial and consistent support on mechanical testing and the training for optical strain gauges, Dr Gianmaria Bullegas and Mark Grant for the kind help and training on the laser machine, Dr Carla Gispert and Dr David Anthony for their tutorial on the Acoustic Emission equipment, Dr Francesca Pernice for her discussion, advices on my research topic and the joy provided me outside the research. I would also like to thank Dr Jonathan Fuller (from the University of Bristol) for the arrangement of X-ray CT scanning of my samples and tutorial on the X-ray CT post-processing software.

Last, but not the least, I would like to thank my parents, for their love, encouragement and support for me to pursuit my dream to study abroad and throughout the PhD.

Abstract

High-performance continuous Fibred Reinforced Polymer (FRP) composites have high specific stiffness and strength but lack ductility. This work presents a strategy to promote progressive failure and 'pseudo-ductility' in CFRP laminates by introducing periodic ply weakening (continuous cuts or perforations normal to the fibre direction) into selected plies.

An analytical model based on Linear Elastic Fracture Mechanics (LEFM) was devised for unidirectional (UD) laminates. The model considers the evolution of interlaminar stress transfer zones (initiated from the ply weakenings) in a rigid-perfectly-plastic matrix system. The predicted pseudo-ductile stress-strain response consists of an initial approximately-linear stage with stiffness close to that of the continuous composite, an intermediate metal-like plateau stage and a final strain-hardening stage. The tensile response is tailorable by adjusting the geometry and distribution of the ply weakenings and the ratio of the continuous and the weakened plies.

The analytical predictions were validated by tensile tests of weakened UD laminates and the results confirmed that the pseudo-ductility was controlled by delamination or debonding initiated from the ply cuts or perforations, respectively.

A preliminary study showed that pseudo-ductility can be achieved in multi-directional laminates, by embedding weakened 0° plies between Quasi-Isotropic (QI) sub-laminates. For the perforation weakening method, it was found that the fibre orientation in the plies adjacent to the weakened plies has a significant influence on the pseudo-ductility.

Table of Content

LIST OF PUBLICATIONS **10**

LIST OF FIGURES **11**

LIST OF TABLES **23**

ABBREVIATIONS **24**

NOMENCLATURE **25**

1. Introduction **28**

1.1 Motivation 28

1.2 Pseudo-ductility 28

1.3 Aim and approach 29

1.4 Structure of the thesis 30

2. Literature Review **31**

2.1 Ductility mechanisms in natural materials 31

2.2 Pseudo-ductility mechanisms in composite materials 32

2.2.1 Classification of pseudo-ductility mechanisms 32

2.2.2 Fibre hybridization 33

2.2.3 Fibre reorientation/hidden length mechanisms 55

2.2.4 Interphase, interface and interlock techniques 62

2.3 Conclusions 65

3. Analytical modelling of UD laminates containing weakened plies and interfaces **67**

3.1 Introduction 67

3.2 Simplified analytical models for UD laminates containing continuous cuts and combined cuts and weakened interface 68

3.2.1 Simplified analytical model for UD laminates containing continuous cuts 68

3.2.2 Simplified analytical model for UD laminates containing continuous ply cuts and interface weakening 74

3.3 Simplified analytical model for UD laminates containing ply perforations 76

3.3.1 Simplified analytical model for UD perforated laminates that fractured by debonding of the perforated fibre bundles 79

3.4 Comparison of the tensile performance of UD laminates containing cuts, cuts and interface weakening and perforations, predicted by the simplified analytical models 81

3.5 Refined analytical model for the UD laminates containing continuous cuts 82

3.5.1 Initial almost (or approximately)-linear stage 82

3.5.2 Intermediate plateau stage 85

3.5.3 Final strain-hardening stage 86

3.6 Refined analytical model for the UD laminates containing periodic perforations 89

3.6.1 Initial approximately-linear stage 90

3.6.2 Intermediate plateau stage 93

3.6.3 Final strain-hardening stage 94

3.7 Parametric study of the tensile performance of UD laminates containing cut or perforated plies (predicted by the refined analytical models) 96

3.7.1 Material 97

3.7.2 Parametric study of the tensile response of UD laminates containing continuous cuts ... 97

3.7.3 Parametric study of the tensile response of UD laminates containing periodic perforations 99

3.8 Conclusions 101

4. Experimental investigation of pseudo-ductility in UD laminates containing continuous cuts 102

4.1 Introduction 102

4.2 Experimental details 102

4.2.1 Specimen types 102

4.2.2 Specimen fabrication 104

4.2.3 Mechanical testing 106

4.3 Results and discussion 107

4.3.1 Tensile performance of 4-ply configurations 107

4.3.2 Tensile performance of 6-ply configurations 112

4.3.3 Tensile performance of 12-ply configurations 116

4.4 Conclusions 118

5. Experimental investigation of pseudo-ductility in UD laminates containing ply perforations 122

5.1 Introduction 122

5.2 Experimental details 122

5.2.1 Specimen types 122

5.2.2 Specimen fabrication 126

5.2.3 Mechanical testing 128

5.3 Results and discussion 128

5.3.1 Laminates with a single line of perforations 128

5.3.2 Laminates with multiple lines of perforations 151

5.3.3 Comparison of the configurations containing a single and multiple lines of cuts or perforations 170

5.4 Conclusions 172

6. Experimental investigation of pseudo-ductility in multi-directional laminates containing ply cuts or perforations 173

6.1 Introduction 173

6.2 Experimental details 173

6.2.1 Specimen design details 174

6.2.2 Specimen fabrication 178

6.2.3 Mechanical testing 180

6.3 Results and Discussion 180

6.3.1 Tensile response of multi-directional configurations (1) to (4) 180

6.3.2 Failure mechanisms 184

6.4 Conclusions 207

7. Conclusions and future work 208

7.1 Conclusions 208

7.2 Recommendations for future work 210

References 211

Appendix 1: Comparison of analytical tensile response of the specimen free and gauge lengths 221

Appendix 2: Laser milling machine 224

Appendix 3: Pseudo-yield stress identification technique for the pseudo-ductile multi-directional configurations 225

List of Publications

Conference Papers & Oral Presentation

J. Sun, O. Bacarreza, P. Robinson. Pseudo-ductility in UD CFRP through interlaminar and ply weakening. 17th European Conference on Composite Materials (ECCM 17), Munich, 26-30 June 2016.

J. Sun, O. Bacarreza, P. Robinson. Pseudo-ductility in quasi-isotropic CFRP through ply weakening. 21th International Conference on Composite Materials (ICCM 21), Xi'an, 20-25 August 2017.

J. Sun, M. F. Pernice, O. Bacarreza, P. Robinson. Pseudo-ductility in 0-degree fibre dominated CFRP through ply weakening. 18th European Conference on Composite Materials (ECCM 18), Athens, 24-28 June 2018.

List of Figures

Figure 1.1 Schematic tensile stress-strain curve of conventional CFRP composites. 28

Figure 1.2 Schematic pseudo-ductile tensile stress-strain response. 29

Figure 2.1 Synergistic toughening mechanisms in multiple length scales of healthy human cortical bone. Copied from [19]. 31

Figure 2.2 Damage diffusion, crack deflection and shearing deformation mechanisms in nacre-inspired structure, under tension. Copied from [24]. 32

Figure 2.3 Classification of pseudo-ductility induction strategies. 33

Figure 2.4 Schematics of (a) interply, (b) inter-yarn or intraply and (c) intermingled continuous fibre hybrids (green and black relate to two types of fibres). Copied from [28]. 34

Figure 2.5 Damage mode map of potential failure processes of carbon-glass/epoxy interlayer hybrids with various absolute and relative thicknesses of the carbon and glass plies. Copied from [33]. 35

Figure 2.6 Schematic tensile responses of a conventional hybrid composite (showing an unstable load drop) and a pseudo-ductile thin-ply carbon-glass hybrid accompanied with progressive fragmentation and localized delamination. Copied from [48]..... 36

Figure 2.7 Pseudo-ductile tensile stress-strain responses of UD (a) S glass-TR30 carbon and (b) T1000 carbon (intermediate modulus) - XN80 carbon (ultra-high modulus) continuous interlayer hybrids. Adapted from [48] [49]. 36

Figure 2.8 Tensile response of QI hybrid with the layup of $[45h/90h/-45h/0h]_s$ (h represents a carbon/carbon hybrid sub-laminate with the layup of $[T1000_2/XN\text{-}80_1/T1000_2]$). Adapted from [50]. 37

Figure 2.9 Schematics of the distribution of ply orientation and material in the (a) 'orientation blocked' and (b) 'orientation dispersed' carbon/glass interlayer hybrid QI laminates. Adapated from [54]. 38

Figure 2.10 The integration of interlaminar stresses, Int (σ_{zz}), Int (σ_{xz}) and Int (σ_{yz}) (along the transverse direction from the free edge to the mid-line of the laminate (i.e. b_0)) at the critical interfaces of the 'orientation dispersed' and 'orientation blocked' layups. Copied from [55]..... 39

Figure 2.11 Tensile response of pseudo-ductile QI hybrids with the'orientation dispersed' layups of (a) $[45°_h/90°_h/-45°_h/0°_h]_s$ (the subscript 'h' refers to a hybrid sub-laminate with one LFS carbon layer, embeded in two HFS carbon layers), i.e. a $\pi/4$ sub-laminate angle interval, (b) $[60°G/-60°G/0°G/0°C/60°C/-60°C]_s$ (G for S-glass, C for thin-ply carbon), i.e. $\pi/3$ sub-laminate angle interval. Copied from [50] [54]. 40

Figure 2.12 (a) An example of non-crimp 3D orthogonal fibre architecture and (b) the side views of the hybrid carbon/S2 glass/Dyneema (z-yarn) preform. Adapted from [56]. 41

Figure 2.13 (a) Schematic warp direction relative to the z-yarn Dyneema binders and (b) tensile stress-strain response in the warp direction of the hybrid 3D woven composite. Adapted from [56].. 41

Figure 2.14 (a) Cross-sectional micrograph of a cured intermingled glass-carbon fibre tows reinforced epoxy lamina and (b)Tensile stress-strain curves of UD non-hybrid carbon fibre/epoxy, non-hybrid glass fibre/epoxy and intermingled carbon-glass fibre/epoxy specimens. Adapted from [57]. 42

Figure 2.15 Schematic layup of the interlayer carbon fibre mat and woven polypropylene fibre reinforced polypropylene hybrid laminate. Copied from [69]. 43

Figure 2.16 Tensile stress-strain curve of a pseudo-ductile CFRPP and SRPP woven hybrid with successive dispersed delamination with increasing load. Adapted from [68]. 44

Figure 2.17 (a) Schematic edge view of a continuous glass fibre-discontinuous carbon fibre hybrid laminate with the top view of a periodically cut carbon ply with cuts spans across the specimen width, (b) tailorable pseudo-ductile tensile stress-strain respons of S-glass/TR30 carbon epoxy hybrids with 25mm-long carbon platelets and the specimen images at increased stress levels. Adapted from [70]. 44

Figure 2.18 (a) Schematic geometry of periodically perforated CFRPP plies, sandwiched in continuous woven SRPP plies and selected representative (b) tensile stress-strain curves of UD perforated CFRPP/continuous woven SRPP interlayer hybrids with different CFRPP perforation patterns (the legends F, C and S represent cut fraction, step length and cut length, respectively). Copied from [71]. 45

Figure 2.19 Tensile stress-strain curves of random-oriented short carbon fibre mat reinforced PP/woven SRPP interlayer hybrids with various (a) layups and (b) (c) volume fractions of CFRPP and matrix systems. (PP and MAPP refer to polypropylene and maleic-anhydride modified polypropylene matrix, respectively.) Adapted from [73]..... 47

Figure 2.20 Schematics of HiPerDiF (a) lab-scale alignment and pre-impregnating rig and (b) method to manufacture highly aligned (a) single type and (a) intermingled short fibre hybrids. Copied from [78] [81]. 47

Figure 2.21 Schematics of (a) modified HiPerDiF method to manufacture controlled volume of different types of short fibres and (b) an instance of short carbon and glass bundles, in distinct regions of intralayer hybrids. Copied from [81]. 48

Figure 2.22 Typical damage modes in pseudo-ductile interlayer hybrids made of continuous S-glass prepregs with HiPerDiF technique manufactured highly aligned short fibre reinforced prepregs containing (a) intermingled high modulus /high strength short carbon fibres, (b) reclaimed carbon fibres and (c) virgin carbon fibres. Copied from [78], [82], [80], respectively. 49

Figure 2.23 (a) Schematics of the interlayer hybrid laminates containing intermingled aligned short fibres in the middle discontinuous plies, (b) typical failure mechanisms of hierarchical hybrid pseudo-ductile laminates and (c) pseudo-ductile tensile stress-strain curve of hierarchical interlayer hybrids with highly aligned high modulus carbon (HMC) and high strength carbon (HSC) short fibre prepregs sandwiched in continuous S-glass prepregs. Adapted from [78]. ... 50

Figure 2.24 (a) Experimental tensile stress-strain curves of HiPerDiF method manufactured intermingled carbon and glass short fibre hybrids with carbon fibre volume fractions ranged from 0.1 to 0.5 and (b) the corresponding micrographs of the cross-sections ((a) to (b)) of the hybrids shown in (a). Copied from [76]. 51

Figure 2.25 (a) Cross-sections of intralayer hybrids with strategically arranged high modulus LFS carbon (shown in light grey) and HFS E-glass (shown in dark grey) fibre bundles at different locations with 33% volume fraction of carbon and (b) experimental stress-strain curves of different commingled carbon (shown in grey) and glass (shown in green) fibre arrangement. Copied from [81] and [86]. 52

Figure 2.26 (a) Tensile stress-strain curves and (b) the edge views of the 'brick-and-mortar' specimens before and after tests. Copied from [89]. 53

Figure 2.27 (a) Schematics of the hierarchical 'brick-and-mortar' laminates and the (b) tensile response for laminates with various geometric parameters (at hierarchy level 1) and SEM edge view images of fractured specimens. Copied from [87]. 54

Figure 2.28 Statistical distribution of fibres with different misalignment angles (on the left) and the corresponding tensile stress-strain curves (on the right) of the (a) control (i.e. as received), (b) gas-textured and (c) non-constrained annealed carbon fibre/PA-12 tapes. Copied from [5]. 56

Figure 2.29 (a) SEM images of dry microbraids made of Dyneema (left) and Kevlar (right) fibres with approximate 15° braiding angles and (b) tensile responses of cross-ply [0°/90°]3 laminate with Dyneema briaided in a regular brading architecture (legends UD, A, B,C represent braiding bias angles,where UD refers to unidirectional and UD<A<B<C in terms of magnitude). Copied from [91]. 57

Figure 2.30 (a) 2D schematic of 2×2 [±θ] biaxial braided yarns and (b) comparison of FE modelled tensile performance of 2×2 [±θ] braids with different braiding angles and the equivalent angle-ply laminates manufactured with carbon fibre/EPON 9504 resin prepregs. Copied from [65] [93]. 58

Figure 2.31 (a) 3D schematic of laminate made of triaxial-braided yarns (shown in red, blue and green) and the top views of the (b) [0°/±30°], (c) [0°/±45°] and (d) [0°/±60°] angle arrangements. Copied from [95] [94]..... 58

Figure 2.32 1F directional tensile response of straight-sided specimens made of [0°/±30°], [0°/±45°] and [0°/±60°] triaxially braided yarns reinforced prepregs and DIC strain maps at selected points. Copied from [94]. 59

Figure 2.33 Tensile stress-strain curves of thin-ply angle-ply (a) $[\pm 25°_5]_s$ laminate and (b) pseudo-ductile $[\pm 26°_5/0°]_s$ laminates with X-ray CT scanning diagrams at increasing strain levels showing progressively accumulated 0° fragmentation. Adapted from [8][11]. 61

Figure 2.34 Schematics of out-of-plane wavy sandwiched structure composed of three unit cells. Copied from [6]. 61

Figure 2.35 Failure process of successful (without premature delamination) wavy-ply sandwich structure. Copied from [6]..... 62

Figure 2.36 Schematics of (a) cross-sectional of layers of nanostructured 'brick-and-mortar' coating on the circumference of a fibre with crack deflection among nanoplatelets and (b) shear effect between interlocked nanoplatelets. Copied from [98]. 63

Figure 2.37 Fragmentation of the un-treated baseline (control) fibre (left) and more dispersed fragments in a nacre-inspired nanoplatelets coated fibre (right) in single fibre fragmentation test (white arrows represent the lengths of fragments). Copied from [98]. 63

Figure 2.38 (a) Schematic edge views of the 'brick-and-mortar' laminates constructed with long overlap length, with (or without) interleaving films of different material and thicknesses and (b) the corresponding tensile stress-strain response and the images of the baseline and lamiantes with 50μm thick interleaving films. Copied from [101] [102]. 64

Figure 2.39 (a) Example 3D printed polymer interlocked bow-tie prototype with clamping devices designed for tensile testing and (b) tensile stress-strain curves of bow-tie shaped interlocking configurations made of CFRP under tension with and without preloading. Copied from [103]. 65

Figure 3.1 Schematic diagrams of a ply containing (a) continuous cuts, (b) lines of periodic perforations and (c) interface weakening in the region of the continuous cuts that are transverse to the fibre direction. 67

Figure 3.2 Schematic side views of a UD laminate with an enlarged sub-laminate showing the RVE of length, *L*. 68

Figure 3.3 Schematic top view of a UD ply with periodic transverse continuous cuts. 69

Figure 3.4 Schematic pseudo-ductile tensile stress-strain response and the failure process shown on the side view of a UD laminate containing cuts in the central block of plies. 69

Figure 3.5 Schematics of the evolution of the axail tensile stress distribution in the continuous plies, σ_U, and the platelet, σ_c, at (a) the beginning, (b) the intermediate phase and (c) the end of the initial linear elastic stage, predicted by the simplified analytical model. (Note the interface area between the continuous block and the platelet is exaggerated to clearly show the different interlaminar zones). 70

Figure 3.6 Schematic evolution of tensile stress distribution in the block of continuous plies and the platelet at (a) the beginning, (b) the intermediate phase and (c) the end of the plateau stage, where the remote average tesnile stress, σ_∞, is constant during the entire plateau stage and is equivalent to the pseudo-yield stress, σ_{yc}, predicted by the simplified analytical model**.** 72

Figure 3.7 Evolution of axial stress distribution in the block of continuous plies and the platelet in the RVE, at (a) the beginning and (b) ultimate failure point of the final linear-elastic stage, predicted by the simplified analytical model. 73

Figure 3.8 Tensile stress-strain response of a UD laminate containing continuous cuts in selected plies predicted by the simplified analytical model 73

Figure 3.9 Schematic top view of a UD ply with weakened interface along the periodic cuts. 74

Figure 3.10 Schematic tensile stress-strain curve of a UD laminate containing partially weakened interface between the block of continuous plies and the platelet. 75

Figure 3.11 Schematic (a) side view of a n_T-ply UD laminate containing perforations in the central (n_T - n_U) plies and (b) the top view of a perforated ply containing three lines of periodic perforations. 76

Figure 3.12 Schematic cross-sectional views of a perforated laminate (fibres pointing out of the paper) with the failure processes of (a) perforations grow transversely to form a continuous cut, before the onset of delamination between the blocks of the continuous and the perforated plies and (b) perforations induced debonding at the perimeters of the perforated fibre bundles and propagates in the fibre direction. 77

Figure 3.13 Schematic tensile stress-strain curves (plotted on the same length scale) of the two potential types of failure processes for UD laminates containing perforations 78

Figure 3.14 Schematic cross-section of a UD laminate containing periodic perforations in the central (n_T - n_U) perforated plies (fibre direction points out of the paper). 79

Figure 3.15 Schematc tensile stress-strain response and the coordinates of key points for a UD perforated pseudo-ductile laminate that failed by debonding of the perforated fibre bundles. .. 80

Figure 3.16 Schematic pseudo-ductile tensile stress-strain responses predicted by (a) the simplified and (b) the refined 'shear-lag' effect models. 82

Figure 3.17 Schematic variation of tensile stress distribution in the block of continuous plies and the platelet in the RVE: (a) subjects no external stress, (b) formation and elongation of two stress transfer zones with length of $l_k/2$, initiated from the two ends of the platelet, under increasing average tensile stress, and (c) the stress transfer zones reaching the critical length, $l_{kC}/2$, once the average tensile stress, σ_∞, reaches the critical delamination stress, σ_{yc} 83

Figure 3.18 Schematic shear stress-shear displacement relation for rigid perfectly-plastic interlaminar matrix. 83

Figure 3.19 Schematic stress distribution in the continuous plies and the platelet next to the interlaminar stress transfer zone (highlighted in the RVE), at an average stress σ_∞, during the initial approximately-linear stage. 84

Figure 3.20 Schematics of the process of the translating of the delaminated, stress transfer and intact interlaminar zones and the associated variation of the axial stress in the continuous plies and the platelet at (a) the beginning, (b) the intermediate phase and (c) the end of the plateau stage in the tensile stress-strain response. 86

Figure 3.21 Schematic evolution of the tensile stress distribution in the continuous plies and the platelet when (a) the stress transfer zones of critical length, $l_{kC}/2$, just meet at the mid-point of the platelet, when the remote tensile stress is equal to the pseudo-yield stress, σ_{yc}, (b) the combined stress transfer zone contracts as the average stress, σ_∞, is further increased above σ_{yc} and (c) ultimate failure of the continuous plies when the peak axial stress in the continuous plies, $\sigma_{yc}n_T/n_U$, becomes equivalent to the tensile strength of the material, σ_0. 87

Figure 3.22 3D schematics of (a) the architecture of a UD laminate containing four lines of periodic perforations in the central perforated plies and (b) a zoom-in diagram of a RVE with a central perforated fibre bundle of length, L, with a highlighted cross-section plane and (c) the corresponding cross-sectional view of the highlighted plane. 90

Figure 3.23 Schematic (a) RVE with labelled debonding planes surrounding the central perforated fibre bundle and the stress distribution in the (b) central perforated fibre bundle and (c) the surroudning continuous part in $x \in [0, L/2]$. 91

Figure 3.24 Schematic axial stress distribution in the continuous plies and the perforated fibre bundle in the RVE at (a) the beginning, (b) an intermediate phase and (c) the end of the initial approximately-linear stage of the stress-strain response of a UD laminate containing perforations. 92

Figure 3.25 Evolution of axial stress distribution in the continuous part, the perforated fibre bundle and the interface beween the two parts in the RVE, at (a) the beginning, (b) the intermediate phase and (c) the end of the plateau stage in the tensil stress-strain response. 93

Figure 3.26 Evolution of the stress distribution in the continuous part and the central perforated fibre bundle in the RVE at (a) the beginning, (b) the intermediate phase and (c) the end of the final strain-hardening stage of the tensile stress-train response. 94

Figure 3.27 Tensile response of pseudo-ductile laminates containing ply cuts and various geometric parameters of L, n_T, n_U and $\sigma_{yc}n_T/n_U$. 98

Figure 3.28 Analytical tensile stress-strain response of pseudo-ductile 'perforated ply' laminates with the same total number of plies and the number of weakened plies and different perforation geometries or continuous cuts. 100

Figure 4.1 Schematic side views of seven UD configurations containing cuts: (1) 4-ply specimen with cuts in the middle of free length of the 2 middle plies; (2) 4-ply specimen with cuts in the 2 middle plies at 10 mm intervals throughout the free length; (3) 6-ply specimen with cuts in the centre of the free length of the 2 middle plies; (4) 6-ply specimen with three sets of cuts at 10 mm intervals in the middle 2 plies (at the centre of the free length); (5) 6-ply specimen with cuts in the 2 middle plies at10 mm spacing throughout the free length; (6) 12-ply specimen containing 2 sub-laminates each with the same ply cut pattern as the configuration (3) and (7) 12-ply specimen containing 2 sub-laminates each with the same ply cut pattern as the configuration (5). 103

Figure 4.2 Schematic top and side views of a UD specimen with the location of speckle pattern and video extensometer target points and a schematic top view of an example cut ply containing continuous cuts at 10 mm intervals throughout the free length. 104

Figure 4.3 Schematic diagrams of the (a) cutting profile of a prepreg to manufacture configuration (2) UD specimens containing thirteen 10 mm apart continuous cuts and (b) the alignment tool. . 105

Figure 4.4 Good alignment of cuts in adjacent plies in cured panel showing no delamination. 106

Figure 4.5 Experimental and analytical (predicted by the simplified and refined analytical models) tensile stress-strain responses of 4-ply configurations (a) (1) and (b) (2). 108

Figure 4.6 DIC strain contour plots and the corresponding axial strain distribution along a common reference line at selected stress levels of the tensile response of a configuration (2) specimen. 110

Figure 4.7 Analytical (predicted by the simplifed and refined analyticsal models) and experimental (measured by Imetrum video extensometer) tensile stress-strain responses of 6-ply (a) configuration (3), (b) configuration (4) and (c) configuration (5). 113

Figure 4.8 Tensile stress-strain curves (measured from 120 mm gauge length) and the corresponding ultrasonic C-scan images (showing the back-wall signal attenuation) for a series of interrupted tests on a 6-ply specimen containing thirteen cuts. 115

Figure 4.9 Analytical (predicted by the simplified and refined analytical models) and experimental (measured by Imetrum video extensometer) tensile responses of the 12-ply configurations (a) (6) and (b) (7). 117

Figure 5.1 Schematic (a) top and (b) side view of a UD tensile specimen containing lines of perforations at 10 mm intervals, (c) the top views of a middle perforated ply in this specimen and (d) top view of a perforated ply containing a single line of perforations in the middle of the gauge length. 123

Figure 5.2 Schematic of the geometry of a line of perforations relative to a 15 mm wide specimen. 124

Figure 5.3 Schematic of an example perforation pattern (shown in blue) in a prepreg used to manufacture ten specimens of M-5000 configuration and the outlines of specimens (shown in black) used to separate specimens from the panel. 127

Figure 5.4 X-ray CT images of three sectional planes (A), (B) and (C) of a partially tested 4-ply UD specimen containing S-800 perforation pattern, showing the quality of periodic 800 μm long perforations and well-aligned perforations in the two middle plies. 127

Figure 5.5 Analytical and experimental tensile stress-strain curves of UD 4-ply configurations containing a single line of (a) S-Continuous cut and (b) S-50, (c) S-250, (d) S-500, (e) S-800 and (f) S-5000 perforation patterns, respectively. 130

Figure 5.6 Experimental tensile stress-strain curves of UD 4-ply configurations containing a single line of (a) S-Continuous cut and (b) S-50, (c) S-250, (d) S-500, (e) S-800 and (f) S-5000 perforation patterns, respectively. 131

Figure 5.7 (a) Optical microscopic image of the top view and SEM topographs of (b) the cross-section of the two middle perforated plies with well-aligned 50 μm perforated fibre bundles and (c) the top view of a perforated ply, showing the typical matrix 'cusps' formed by interlaminar shearing, in a tested 'S-50' specimen. 135

Figure 5.8 Tensile load-time diagram of specimen (4) of configuration (3) and the DIC contour plots of the 50 mm long middle part of the gauge length at seven load levels and the axial strain distribution along two section lines for $P3$, $P4$ and $P5$ (different strain colour scale is used for $P5$ to $P7$)..... 139

Figure 5.9 DIC images and strain distribution along two sectional lines at selected load levels for a specimen of configuration (4), i.e. 'S-500'. 142

Figure 5.10 DIC images and strain distribution along two sectional lines at selected load levels for specimen (3) of configuration (5), i.e. 'S-800'..... 145

Figure 5.11 DIC images and strain distribution along three sectional lines at selected load levels ((a) $P1$ to $P6$ and (b) $P7$ to $P10$ for specimen (3) of configuration (6), i.e. 'S-5000'. 149

Figure 5.12 Experimental and analytical stress-strain curves of three UD 4-ply configurations, i.e. (a) M- Continuous cuts, (b) M-5000 and (c) M-800, containing multiple continuous cuts or lines of perforations in the two middle plies. 152

Figure 5.13 Experimental stress-strain curves of three UD 4-ply configurations , i.e. M- Continuous cuts, M-5000 and M-800, containing multiple continuous cuts or lines of perforations in the two middle plies (without the response predicted by the refined analytial model). 153

Figure 5.14 DIC images and strain distribution along three sectional lines at selected load levels for specimen (5) of configuration (8). 158

Figure 5.15 Experimental (along section lines 1, 2 and 3) and analytical axial strain distribution (predicted by the refined analytical model presented in Chapter 3) for load levels $P5$ and $P6$, shown in Figure 5.14. 159

Figure 5.16 (a) X-ray CT images at selected sections of a specimen containing multiple lines of 5000 μm perforations, i.e. configuration 'M-5000', tested to a stress, where debonding around the perforated fibre bundles has occurred and (b) the plan view at section e2-e2. 162

Figure 5.17 DIC images and strain distribution along three sectional lines at selected load levels for specimen (3) of configuration (9). 164

Figure 5.18 (a) X-ray CT images of the top and side views, (b) and (c) the cross-sectional optical micrographs, of a 'M-800' specimen tested close to failure. 167

Figure 6.1 Schematic layups of the UD 4-ply laminate and the multi-directional laminate. 174

Figure 6.2 Schematic cross-section of a multidirectional perforated-ply configuration showing the RVE. 175

Figure 6.3 Schematic of the multi-directional specimen containing cuts or perforations. 179

Figure 6.4 Schematic showing the position of the '5P-5S' perforation pattern within a specimen. .. 179

Figure 6.5 Tensile stress-strain responses of the multi-directional configurations. 181

Figure 6.6 Tensile stress-strain curve and DIC strain contour plots (under different colour scales) at selected load levels. 185

Figure 6.7 Transverse cracks in the surface 90° ply of a partially tested pristine baseline specimen. 185

Figure 6.8 Axial strain distribution plots at selected stress levels for the pristine baseline configuration (DIC facet size:19 pixel and facet distance: 11 pixel). 186

Figure 6.9 Axial strain distribution plots at selected stress levels for the pristine baseline configuration (DIC facet size:19 pixel and facet distance: 15 pixel). 187

Figure 6.10 Tensile response of a cut-ply multidirectional spcimen and the DIC strain contour plots at six stress levels. 189

Figure 6.11 Axial strain distribution along the longitudinal section line shown in the DIC strain contour plots for the cut-ply multidirectional spcimen shown in Figure 6.10. 190

Figure 6.12 The tensile stress-strain curve of a multi-directional cut-ply specimen tested to 654 MPa and the DIC strain contour plot at 654 MPa..... 191

Figure 6.13 Microscopic images of the polished cross-section of the specimen shown in Figure 6.12. 192

Figure 6.14 Tensile response of a perforated specimen with the $[90°/0°/\pm45°/0p°]_s$ layup and DIC strain contour plots (measured with 19 pixel facet size and 15 pixel facet point distance) at four selected stress levels. 193

Figure 6.15 Axial strain distribution along the longitudinal section line shown in the DIC strain contour plots of the spcimen ('5P-5S'- $[90°/0°/\pm45°/0°p]_s$) shown in Figure 6.14. 194

Figure 6.16 Aixal strain distirbution normalized by the tensile strain of a pristine specimen at the four stress levels for the specimen ('5P-5S'- $[90°/0°/\pm45°/0°p]_s$) shown in Figure 6.14. 195

Figure 6.17 Tensile stress-strain response of a '5P-5S' pattern perforated specimen with the layup of $[90°/0°/\pm45°/0°p]_s$ tested to a stress close to failure and the DIC strain contour plot at the maximum stress. 197

Figure 6.18 Microscopic images of a polished cross-section of the '5P-5S' pattern perforated specimen (with the layup of $[90°/0°/\pm45°/0°p]_s$) specimen shown in Figure 6.17. 198

Figure 6.19 Tensile stress-strain response of a '5P-5S' pattern perforated specimen with the modified layup of $[90°/\pm45°/0°/0°p]_s$ and the DIC strain contour plots (measured with 19 pixel facet size and 15 pixel facet point distance) at six selected stress levels. 200

Figure 6.20 Axial strain distribution plots along the longitudinal section line shown in the DIC strain contour plots in Figure 6.19 (for the '5P-5S'- $[90°/\pm45°/0°/0°p]_s$ specimen)..... 201

Figure 6.21 Axial strain distribution (at stress levels 3 to 6, shown in Figure 6.20) normalized by the tensile strain of a pristine specimen, for the '5P-5S'- $[90°/\pm45°/0°/0°p]_s$ specimen..... 202

Figure 6.22 Tensile stress-strain response of a '5P-5S'-$[90°/\pm45°/0°/0°p]_s$ specimen, tested to 875 MPa and the DIC strain contour image and the axial strain distribution curve at 875 MPa. 204

Figure 6.23 Ultrasonic C-scan and X-ray scanning images of a specimen containing '5P-5S' perforation pattern and the layup of $[90°/\pm45°/0°/0°p]_s$ tested to 875 MPa. 205

List of Tables

Table 3.1 Mechanical properties of UD cured ply M21/T800S laminates. 97

Table 4.1 Summary of the key analytical and experimental (for a 120 mm gauge length) mechanical properites of the seven types of UD laminates containing ply cuts. (Coefficient of variation is given in the parentheses). 120

Table 5.1 Geometry of (I) UD configurations containing a single line of perforations and (II) UD configurations containing periodic lines of perforations. 125

Table 5.2 Key tensile properties of UD 4-ply laminates containing a single line of continuous cut and perforations of various lengths. (Coefficient of variation, in %, is given in the parentheses.) 132

Table 5.3 Summary of the failure processes of configurations (1) to (6), containing a single continuous cut or a line of perforations. 150

Table 5.4 Key tensile properties of UD 4-ply laminates containing mulitple lines of continuous cuts or perforations of various lengths. (Coefficient of variation, in %, is given in the parentheses.) 154

Table 5.5 Summary of the failure process of configurations (7), i.e. 'M-cut', containing mulitple lines of continuous cuts, and configurations (8) and (9), i.e. 'M-5000' and 'M-800', containing multiple lines of 5000 μm and 800 μm perforations, respectively. 169

Table 5.6 Comparison of the failure process of configurations containing multiple continuous cuts or lines of 5000 μm or 800 μm perforations , i.e. configurations 'M-cut', 'M-5000' and 'M-800' 'M-cut', with the corresponding configurations containing a single continuous cut or line of perforations, i.e. configurations 'S-cut', 'S-5000' and 'S-800', respectively. 171

Table 6.1 Summary of the investigated multi-directional configurations. 177

Table 6.2 Mechanical properties of a UD M21/T800S lamina 178

Table 6.3 Key experimental mechanical properties of the multi-directional configurations (Coefficient of variation, in %, are given in the parentheses). 182

Table 6.4 Summary of the failure mechanisms of the multi-directional configurations. 206

Abbreviations

ASTM	American Society for Testing and Materials
CFRP	Carbon Fibre Reinforced Polymer
CLA	Classic Laminate Analysis
CoV	Coefficient of Variation
CRAG	Composite Research Advisory Group
CT	Computed Tomography
DIC	Digital Image Correlation
FRP	Fibre Reinforced Polymer
HiPerDuCT	High Performance Ductile Composite Technology
ILSS	Interlaminar Shear Strength
LEFM	Linear Elastic Fracture Mechanics
QI	Quasi-isotropic
RVE	Representative Volume Element
UD	Unidirectional
WD	Wide-band
RoM	Rule of Mixture

Nomenclature

A	Gross cross-sectional area of a UD laminate
A_0	Gross cross-sectional area of a multi-directional laminate
A_{del}	Cross-sectional area of the continuous part in a multi-directional laminate containing continuous cuts
A_{deb}	Cross-sectional area of the continuous part in a multi-directional laminate containing perforations
A_T	overall cross-sectional area of the unit width RVE
A_U	overall cross-sectional area of the continuous part in the RVE
D	Longitudinal length of interface weakening in a RVE
E_0	Longitudinal elastic modulus of a pristine UD laminate
E_{11}	Young's modulus of a pristine UD lamina
E_{21}	Transverse modulus of a pristine UD lamina
E_{0M}	Longitudinal elastic modulus of a pristine multi-directional laminate
E_{1M}	Longitudinal elastic modulus of the continuous part in a multi-directional laminate containing cuts or perforations
E_{fs}	Secant modulus of the final strain-hardening stage of a pseudo-ductile UD laminate containing either cut or perforated plies
E_{ft}	Tangent modulus of the final strain-hardening stage of a pseudo-ductile UD laminate containing either cut or perforated plies
E_{is}	Secant modulus of the initial approximate-linear stage of a UD laminate containing either cut or perforated plies
E_{it}	Tangent modulus of the initial approximate-linear stage of a pseudo-ductile UD laminate either cut or perforated plies
E_m	Secant modulus of intermediate linear-elastic stage in UD laminates containing both ply cuts and interface weakening
G_{12}	Shear modulus of a pristine UD lamina
G_{II}	Mode II strain energy release rate

G_{IIC}	Mode II fracture toughness
h	Ply thickness
l_k	Stress transfer zone length
l_{kC}	Critical stress transfer zone length
L	Length of a Representative Volume Element (RVE)
n	Number of perforations in each perforated line
n_T	Total number of plies in a ply weakened UD laminate
n_U	Number of continuous plies in a ply weakened UD laminate
P	Length of a perforation
q	Interface weakening factor
V_f	Fibre volume fraction
w	Width of a Representative Volume Element (RVE)
$\delta_{\frac{l_k}{2},c}$	Extension of the platelet referring to half of the stress transfer zone in the RVE
$\delta_{\frac{l_k}{2},p}$	Extension of the perforated fibre bundle referring to half of the stress transfer zone in the RVE
$\delta_{L,U}$	Extension of the continuous plies in the RVE
δ_{rC}	Critical relative interlaminar shear displacement
$\delta_{r,\frac{l_k}{2}}$	Relative shear displacement between the continuous plies and the platelet next to a stress transfer zone in the RVE of a UD laminate
$\sigma_{\boldsymbol{U}}$	Tensile stress distribution in the block of continuous plies
$\sigma_{\boldsymbol{c}}$	Tensile stress distribution in the block of cut plies
$\sigma_{\boldsymbol{p}}$	Tensile stress distribution in the block of perforated plies
σ_{yq}	Pseudo-yield stress for delamination initiation and propagation at the weakened interface of UD laminates containing weakened interface and ply cuts
σ_{ycM}	Pseudo-yield stress for a multi-directional laminate containing cuts
σ_{ypM}	Pseudo-yield stress for a multi-directional laminate containing perforations

ε	Average tensile strain
ε_{fc}	Tensile strain of final strain-hardening stage for UD laminates containing ply cuts
ε_{fp}	Tensile strain of final strain-hardening stage for UD laminates containing perforations
ε_{ult}	Ultimate tensile failure strain
ε_y	Pseudo-yield strain for UD laminates containing either ply or interface weakening
υ_{12}	Poisson's ratio
σ_0	Longitudinal tensile strength of a UD laminate
σ_∞	Average tensile stress
σ_{ult}	Ultimate failure stress of a laminate
σ_{yc} or $\sigma_{\infty c}$	Pseudo-yield stress for UD a laminate containing cuts
σ_{yp}	Pseudo-yield stress for UD a laminate containing perforations
τ_y	Interlaminar shear strength

Chapter 1

Introduction

1.1 Motivation

Continuous carbon fibre reinforced polymer (CFRP) composites have outstanding specific stiffness and strength, high resistance to fatigue damage and corrosion and are highly tailorable. These materials are therefore ideal for weight-sensitive structural applications, such as in aerospace and transportation.

However, CFRP composites are usually brittle and behave in a linear-elastic manner until failure, with little or no warning, as shown in Figure 1.1. Such brittleness results in the use of large safety factors in engineering design, which significantly reduces the benefit provided by the high specific stiffness and strength. Moreover, brittle composites often suffer from a 'size effect' problem, i.e. the mechanical properties measured in laboratory-sized coupons overestimate the actual properties of the full-size engineering structures, for example increasing the structure volume results in reduced strength [1]–[4].

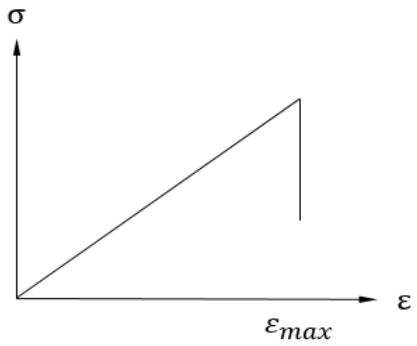


Figure 1.1 Schematic tensile stress-strain curve of conventional CFRP composites

1.2 Pseudo-ductility

This thesis reports an investigation of a strategy to overcome the brittleness of CFRP composites.

In metallic materials, ductility is induced by the relative sliding or dislocation of layers of metallic atoms. However, it is difficult to recreate this mechanism in carbon fibre composites. Strategies to achieve ductility in CFRP composites therefore commonly forms on modification to the architecture, so that damage develops gradually in a distributed fashion throughout the material or exploit a 'hidden length' mechanism [5]–[11]. The resulting ductile-like tensile behaviour is termed as 'pseudo-ductility'.

Figure 1.2 shows two types of pseudo-ductile tensile response, which consist of an initial approximately-linear stage, an intermediate plateau stage and a final strain-hardening stage [12] [13]. This figure also includes definitions of key parameters that characterize the pseudo-ductility, as shown below:

- The initial modulus is defined as the chord modulus measured from the strain range of [0.05%, 0.25%] in the initial stage;
- The pseudo-yield stress and strain are defined as the stress and strain at (a) the transition point to the plateau stage, for a tensile stress-strain response containing a sharp transition to the intermediate plateau stage (see stress-strain response 1 in Figure 1.2) and (b) the intersection point of the initial modulus line at a 0.2% offset strain and the tensile stress-strain response, for the case where there is a much more gradual transition, as shown in the stress-strain response 2 in Figure 1.2;
- Pseudo-ductile strain is defined as the difference between the ultimate failure strain and the elastic strain at the ultimate failure stress based on the initial modulus, for tensile response containing a stable intermediate plateau stage [13] [14].

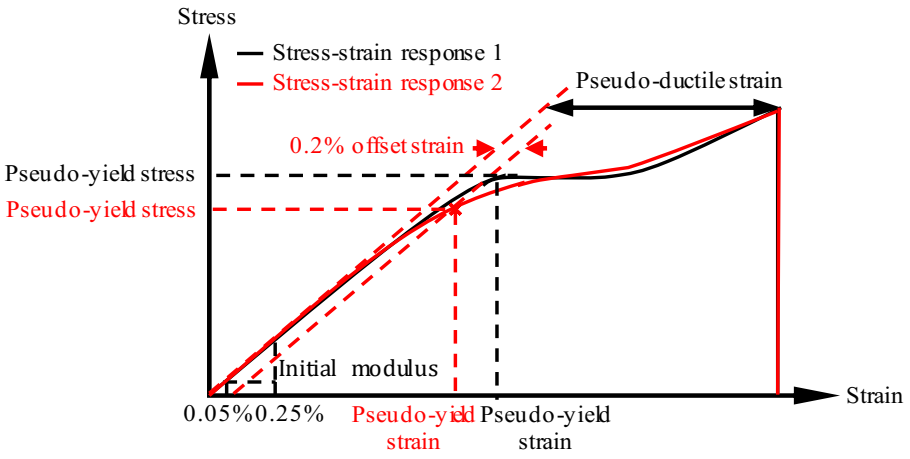


Figure 1.2 Schematic pseudo-ductile tensile stress-strain response.

1.3 Aim and approach

The aim of the research described in this thesis was to explore how ply weakening and interface weakening could be used to achieve pseudo-ductility in CFRP laminates. 'Ply weakening' was introduced by inserting continuous cuts or perforations into selected plies. 'Interface weakening' was implemented by reducing the interlaminar fracture toughness of selected interfaces in the composite

laminate. The ply and interface weakening approaches were initially investigated for unidirectional (UD) laminates, using analytical models based on Linear Elastic Fracture Mechanics (LEFM). The ply weakening patterns which were predicted to promote good pseudo-ductile tensile performance were then validated through experiments. Ply weakening patterns were also investigated in multi-directional laminates, that are relevant to practical engineering applications.

Quantitatively, the aim of the project was to achieve pseudo-ductile laminates with:

- a high initial stiffness of at least 80% of the Young's modulus of the pristine CFRP material;
- a high pseudo-yield stress of at least 70% of the ultimate failure strength of the pseudo-ductile laminate.

1.4 Structure of the thesis

The thesis consists of 7 chapters and are structured as below:

Chapter 2: This chapter presents a review of the techniques and methods reported in the published literature to improve the ductility of CFRP composites, the tensile performance of these composites and the mechanisms reported for the improved ductility.

Chapter 3: A simplified analytical model is proposed to predict the tensile behaviour of UD laminates, containing ply weakening with or without interface weakening. The models were then refined by considering the evolution of stress transfer zone induced by the weakenings.

Chapter 4 & 5: These chapters describe experiments investigating the tensile UD laminates containing various patterns of ply cuts and perforations, respectively. The experimental performance of each configuration is compared to the analytical predictions.

Chapter 6: This chapter presents a preliminary investigation of the effectiveness of cuts or perforations to pseudo-ductility in multi-directional laminates.

Chapter 7: This chapter summarizes the main achievements of this PhD project and recommendations for the future research.

Chapter 2

Literature review

2.1 Ductility mechanisms in natural materials

Many natural structures, such as bone, bamboo and nacre are composed of compliant and stiff components and are light but tough [15]–[20]. These tough natural materials always have much higher strain-to-failure than the stiff components, resulting from mechanisms of damage diffusion, crack deflection, pull out of the stiff components and plastic deformation of the compliant component. An example of the toughening mechanisms in multiple length scales, ranging from nano- to macro-levels, is shown in Figure 2.1. The strategic organization of the microscopic constituent architectures facilitates the control of damage modes at the various length scales.

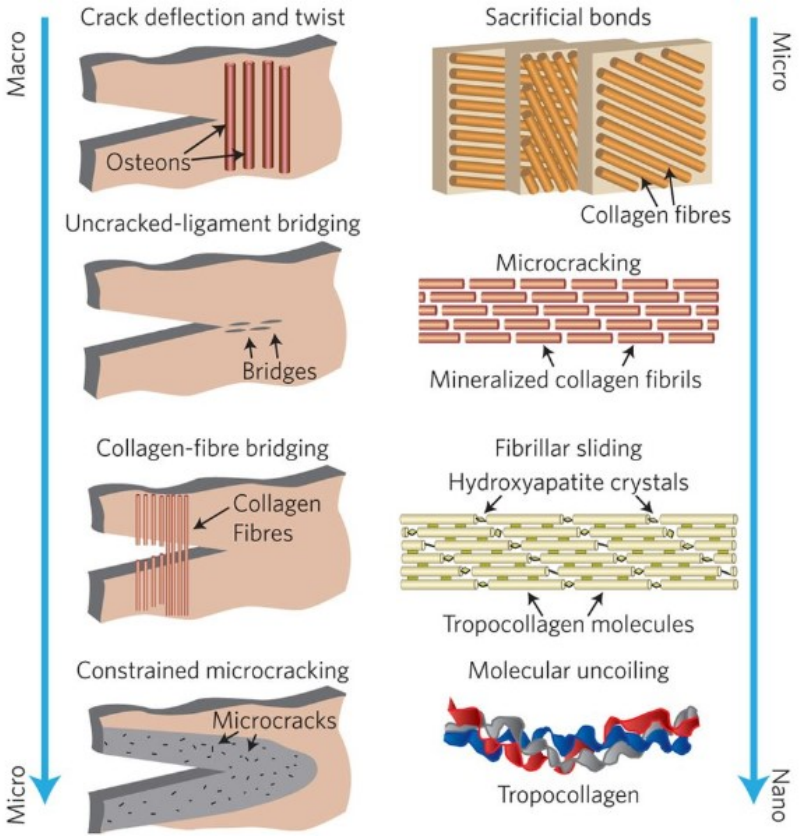


Figure 2.1 Synergistic toughening mechanisms in multiple length scales of healthy human cortical bone. Copied from [19].

Recently, these mechanisms have been transferred to fibre reinforced composites by replicating the architectures of the natural materials [21]–[23]. Composite laminates, mimicking the nacre-inspired

structure shown in Figure 2.2, were manufactured to generate the platelet pull out, shearing between interlayered platelets and diffused minor damage mechanisms that can enhance ductility [23]. A drawback of this configuration is that it is always accompanied with reduced strength, due to the discontinuities in the stiff components.

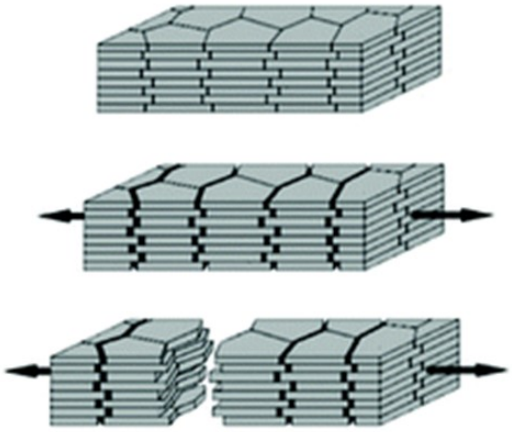


Figure 2.2 Damage diffusion, crack deflection and shearing deformation mechanisms in nacre-inspired structure, under tension. Copied from [24].

2.2 Pseudo-ductility mechanisms in composite materials

2.2.1 Classification of pseudo-ductility mechanisms

As shown in Figure 2.3, the pseudo-ductile configurations reviewed in this chapter are classified in three categories:

- Fibre hybridization
- Fibre rotation and 'hidden' length
- Interphase/ interface/components boundary engineering

Each category is further divided based on the geometric characteristics or architecture of constituent materials.

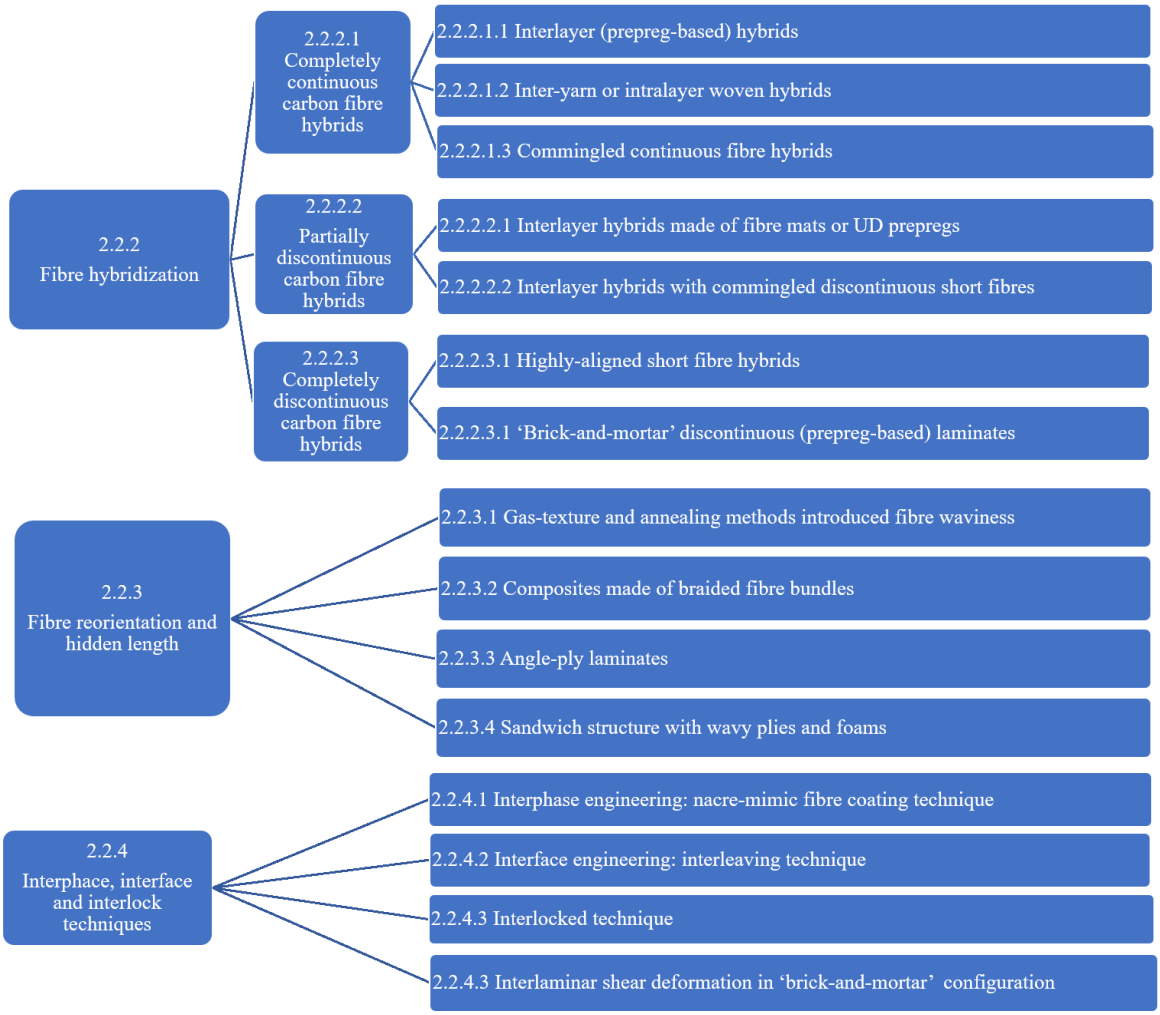


Figure 2.3 Classification of pseudo-ductility induction strategies

2.2.2 Fibre hybridization

Fibre hybrid composites are defined as composites with combined two or more types of fibre reinforcements, in which the synergistic effect enhances specific mechanical properties of the hybrid, making the hybrid superior to the constituent non-hybrid composites [25]–[29]. Fibre hybrids have been employed to fulfil various engineering requirements, such as design for lightweight, shape-memory and toughened structures [30]–[32]. Recently hybridization has been used to promote pseudo-ductility in fibre reinforced polymer composites. Specifically, this section focuses on pseudo-ductile hybrid composites that contain carbon fibres. Depending on the geometry of carbon fibres, the reviewed hybrids are classified as completely continuous carbon fibre hybrids (Section 2.2.2.1), partially

continuous carbon fibre hybrids (Section 2.2.2.2) and completely discontinuous carbon fibre hybrids (Section 2.2.2.3).

2.2.2.1 **Completely continuous carbon fibre hybrids**

Depending on the arrangement of fibres, the continuous fibre hybrids can be classified as interlayer, inter-yarn (or intraply) and intimately intermingled fibre hybrids, as shown in Figure 2.4. Pseudo-ductile tensile responses achieved in these three types of continuous fibre hybrids are presented in Sections 2.2.2.1.1, 2.2.2.1.2 and 2.2.2.1.3, respectively.

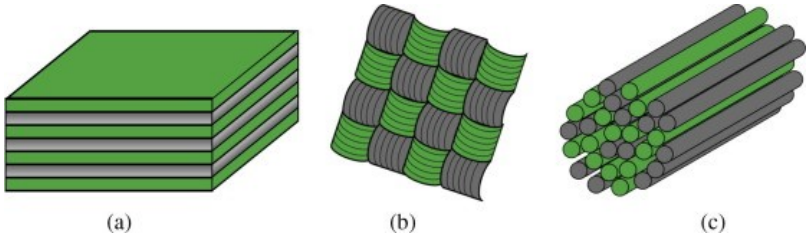


Figure 2.4 Schematics of (a) interply, (b) inter-yarn or intraply and (c) intermingled continuous fibre hybrids (green and black relate to two types of fibres). Copied from [28].

2.2.2.1.1 Interlayer (prepreg-based) hybrids

The ply level hybridization is implemented by stacking together UD prepregs, composed of continuous fibres with different strains to failure and a compatible matrix system, for instance, embedding the high stiffness but low failure strain (LFS) carbon fibre/epoxy prepregs within glass fibre/epoxy prepregs with low stiffness but high failure strain (HFS), or hybridizing different grades of carbon prepregs, with different strains-to-failure. Most of the interlayer hybridizing research has examined UD laminates, some work has been performed on QI or multi-directional laminates.

Analytical and Finite Element (FE) models [33]–[35] revealed four potential failure mechanisms of the continuous interlayer hybrids can occur and are dominated by the absolute thickness and relative thickness ratios between the HFS and LFS plies. The four failure mechanisms are demonstrated in a damage mode map, shown in Figure 2.5, including (1) a sudden brittle fracture developed throughout the entire laminate thickness, (2) single crack throughout the LFS plies, followed by an abrupt unstable delamination between the HFS and LFS plies [36]–[38], (3) progressively developed dispersed LFS fragmentation and (4) ideally, progressively developed dispersed LFS fragmentation with local delamination. It is also reported that only the failure mechanism (4) can provide a pseudo-ductile tensile response with a stable intermediate plateau stage (without load drop) and a final strain-hardening stage,

in the tensile stress-strain response. Trade-offs between the pseudo-ductile strain and pseudo-yield stress (see Figure 1.2) were observed for variable material combinations and geometric parameters.

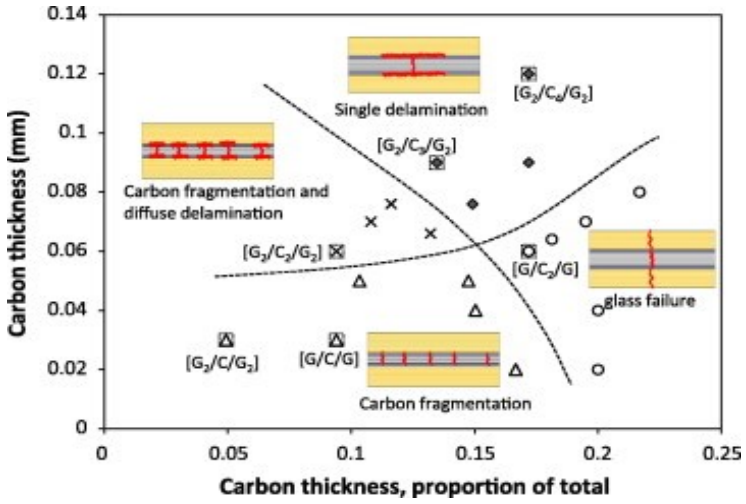


Figure 2.5 Damage mode map for potential failure processes of carbon-glass/epoxy interlayer hybrids with various absolute and relative thicknesses of the carbon and glass plies. Copied from [33].

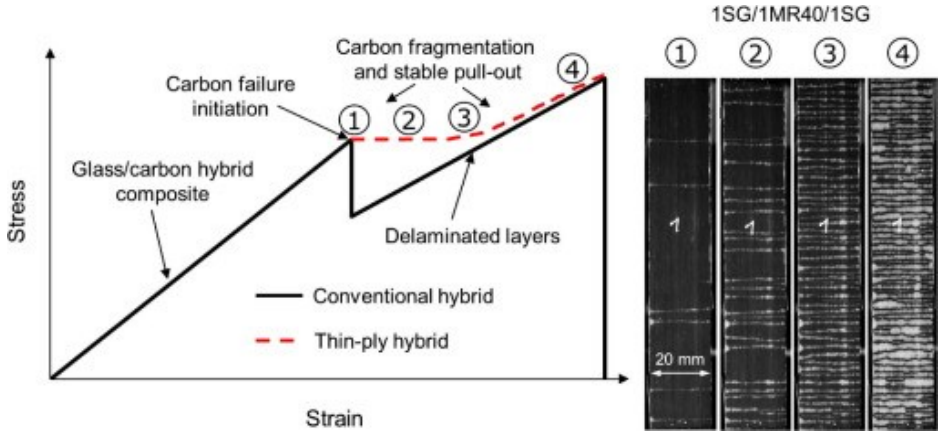
The load drops observed in the interlayer hybrids, made of conventional thickness prepregs (see Figure 2.6 (a)), were eliminated once the thin-ply carbon prepregs were used as the LFS plies [39]–[45]. (The thin-ply carbon fibre prepregs manufactured with the spread-tow technique, have a nominal cured ply thickness of about 0.03 mm, which is about 4 to 8 times thinner than the conventional prepregs.) In terms of mechanical performance, low prepreg thickness is associated with low strain energy release rate, therefore higher stress is required to achieve the critical strain energy release rate for the onset of delamination and matrix cracking [46][47].

A typical pseudo-ductile response and the damage development process, for an example thin-ply carbon-glass hybrid, is shown in Figure 2.6. The mechanisms associated with the initial linear-elastic, intermediate plateau and final stages of the response shown in Figure 2.6 (a), are summarized below:

- During the initial linear-elastic stage, strains in the two types of constituents are identical. The involvement of the low stiffness HFS constituent results in a significantly reduced overall stiffness compared to the relatively stiffer LFS constituent.

- The LFS plies gradually fragment at dispersed locations once reaching the failure strain of the LFS material. The fragmentation is accompanied with matrix cracking or minor localized delamination, as shown in Figure 2.6 (b). Further loading results in the gradual pull-out of the LFS fragments from the HFS plies. This progressive damage development process promotes the pseudo-yielding and the following plateau (highlighted red line) stages in the stress-strain curve.

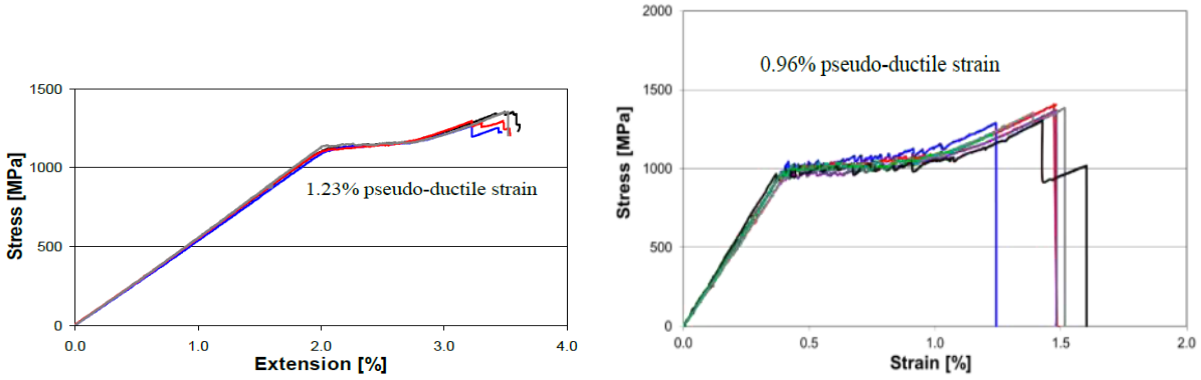
- The HFS plies must be sufficiently strong to tolerate the load transferred from the fragmented LFS plies. After the fragmentation saturation, the load is mainly carried by the HFS plies, until ultimate fractures at the strain-to-failure of the HFS plies. This process is displayed as the final strain-hardening stage.



(a) (b)

Figure 2.6 (a) Schematic tensile responses of a conventional hybrid composite (black line, showing an unstable load drop) and a pseudo-ductile thin-ply carbon-glass hybrid (red dash line) accompanied with (b) progressive fragmentation and localized delamination. Copied from [48].

Both UD glass-carbon [36][33][48] and carbon-carbon [49] hybrids have demonstrated pseudo-ductility and progressive failure processes. The average pseudo-ductile strains for these two hybrids are 1.23% and 0.96%, respectively, as shown in Figure 2.7.



(a) (b)

Figure 2.7 Pseudo-ductile tensile stress-strain responses of UD (a) S glass-TR30 carbon and (b) T1000 carbon (intermediate modulus) - XN80 carbon (ultra-high modulus) continuous interlayer hybrids. Adapted from [48] [49].

Hybridization was also examined as a means of introducing pseudo-ductility to QI and multi-directional laminates, which possess a wider engineering application scope. One way to achieve this was to utilize the original UD pseudo-ductile hybrid laminates as the sub-laminates and placing them in the π/4 orientation intervals to construct the final QI laminate. The failure mechanisms observed in a UD pseudo-ductile carbon/carbon (with different grades of carbon plies and distinct strain-to-failure) hybrid laminate were successfully transferred to a QI hybrid prototype. Undesirable premature free-edge delamination at the inter-sublaminate interfaces occurred at the early phase of the plateau stage in the tensile response, as shown in Figure 2.8 [50]. The inter-sublaminate delamination can trigger ultimate fracture under bending or fatigue loading conditions, thereby the authors defined this inter-sublaminate delamination strain as the failure strain.

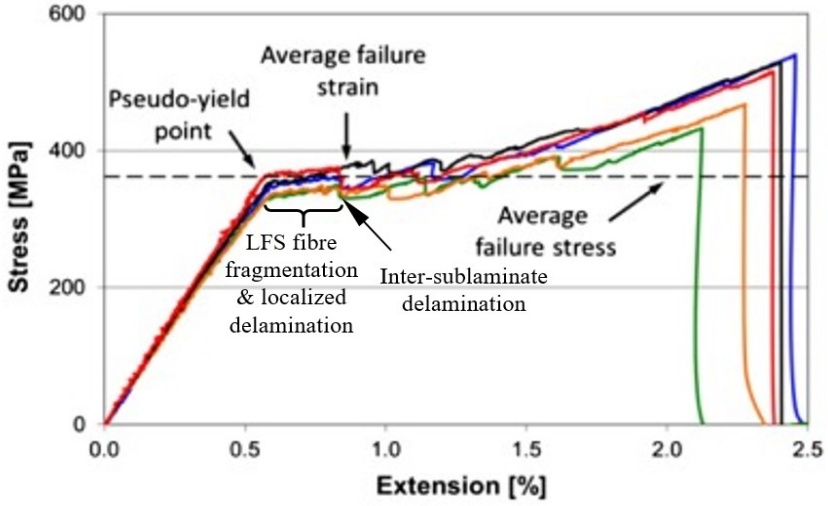


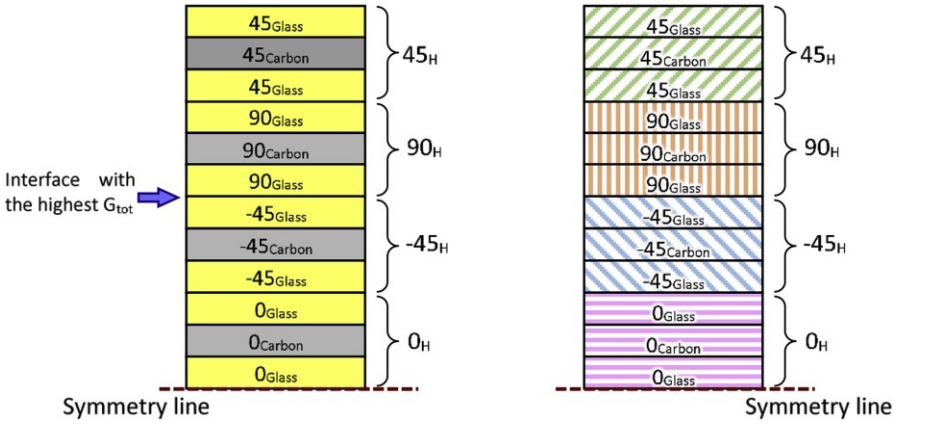
Figure 2.8 Tensile response of QI hybrid with the layup of [45h/90h/-45h/0h]s (h represents a carbon/carbon hybrid sub-laminate with the layup of [$T1000_2$/XN-80_1/$T1000_2$]). Adapted from [50].

The free-edge delamination issue was prohibited using strategically designed layups for the pseudo-ductile continuous QI and multi-directional carbon/carbon (with distinct failure strains) [50] and carbon/glass [51]–[55] hybrids. Two grades of unstable delamination, namely the 'mode II intra-sub-laminate delamination' and 'mixed-mode inter-sub-laminate delamination (mainly at the free edges)' should be prevented. To fulfil these requirements, the hybrid layup was designed with:

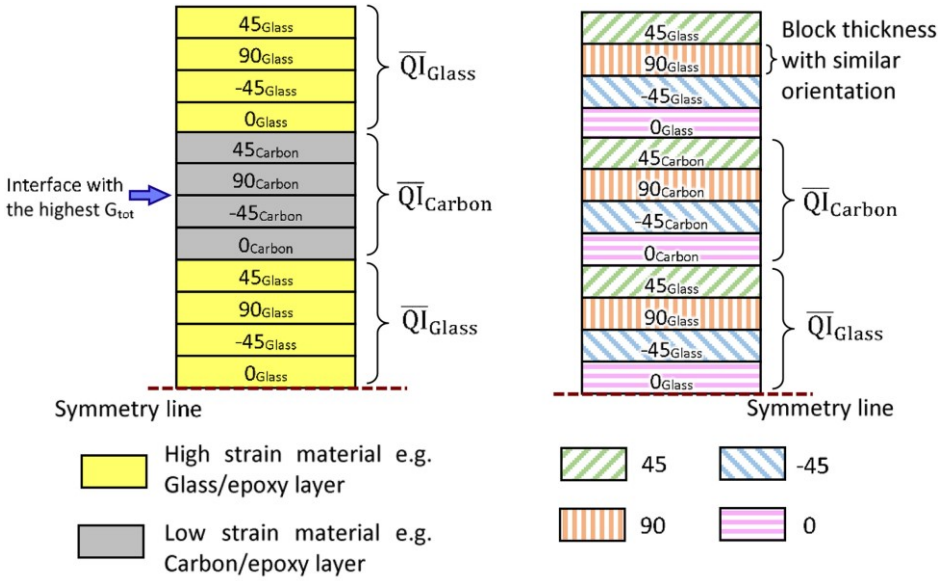
- Gradual LFS material fragmentation within the sub-laminate to avoid unstable intra-sub-laminate delamination;
- Low sub-laminate thickness to avoid free edge delamination.

Further study was performed to investigate the effects of ply orientation and constituent material distribution in the layup on the pseudo-ductility. Two layups, characterized as 'orientation blocked

while material dispersed' and 'orientation dispersed while material blocked' (shortened as 'orientation blocked' and 'orientation dispersed' in the following content), were proposed and compared [54]. The ply orientation and material distribution in the QI hybrids, with the sublaminates placed at π/4 angle interval, are schematically shown in Figure 2.9 (a) and (b), respectively.



(a)



(b)

Figure 2.9 Schematics of the distribution of ply orientation and material in the (a) 'orientation blocked' and (b) 'orientation dispersed' carbon/glass interlayer hybrid QI laminates. Adapated from [54].

The FE modelling results illustrate that the 'orientation dispersed' QI hybrid layup has significantly lower interlaminar normal and shear stresses in the vicinity of free edges, making the laminate less likely to delaminate at free edges [54] [55], as shown in Figure 2.10. Note that due to the singularity of interlaminar stresses at the free edge (y=0) (see Figure 2.10), the integrals of the interlaminar stresses

in a variable characteristic length of b_0 at the interface most prone to free edge delamination were compared.

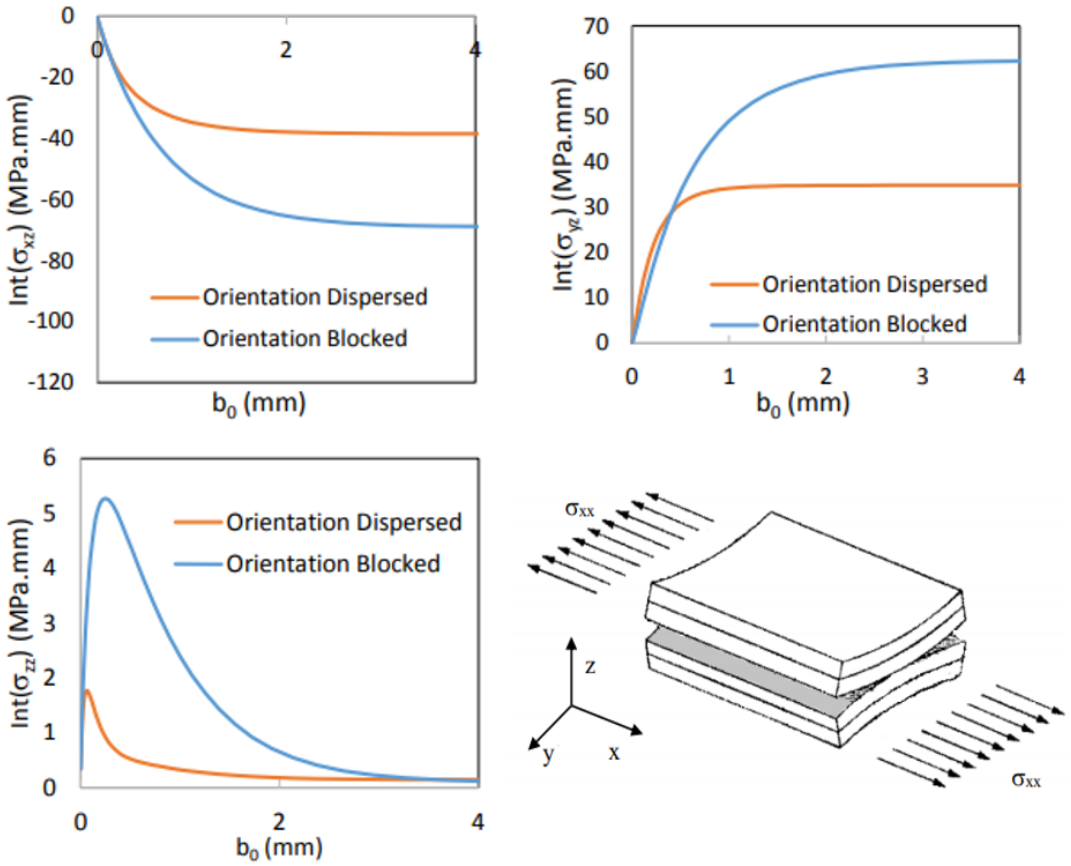


Figure 2.10 The integration of interlaminar stresses, Int (σ_{xz}) (i.e. $\int_0^y \sigma_{xz}(y,0)dy$), Int (σ_{yz}) (i.e. $\int_0^y \sigma_{yz}(y,0)dy$) and Int (σ_{zz}) (i.e. $\int_0^y \sigma_{zz}(y,0)dy$), along the transverse direction from the free edge to the mid-line of the laminate (i.e. b_0), at the critical interface in the 'orientation dispersed' and 'orientation blocked' layups. Copied from [55].

Pseudo-ductile tensile responses were successfully achieved in the QI hybrids with the 'orientation dispersed' layups, containing carbon/glass hybrid sub-laminates placed at both $\pi/3$ and $\pi/4$ ply orientation intervals (see Figure 2.11) [52] [54]. In both pseudo-ductile cases (see Figure 2.11), the progressive fragmentation and localized minor delamination, that mainly occurred in the LFS plies o the loading directional sub-laminates, promoted the pseudo-yielding and plateau in the tensile response. The less stiff HFS components provided the residual load-bearing capacity after the failure of the LFS plies, promoting the final strain-hardening tensile response. In addition, an analytical damage mode map for QI hybrids, like that for UD hybrids, was also proposed in [52].

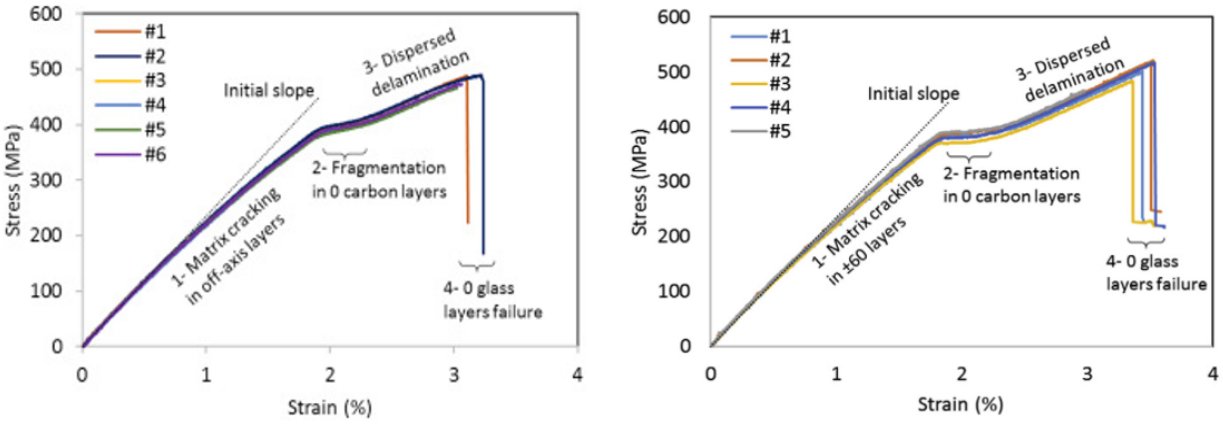
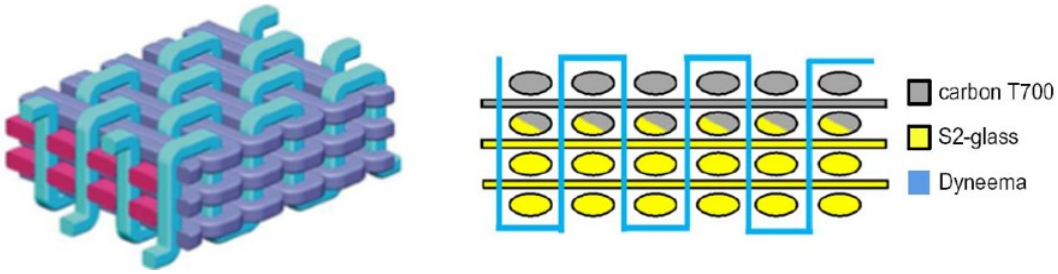


Figure 2.11 Tensile response of pseudo-ductile QI hybrids with the'orientation dispersed' layups of (a) a π/4 sub-laminate angle interval, [45°$_h$/90°$_h$/-45°$_h$/0°$_h$]s (the subscript 'h' refers to a hybrid sub-laminate with one LFS carbon layer, embeded in two HFS carbon layers), and (b) a π/3 sub-laminate angle interval, [60°G/-60°G/0°G/0°C/60°C/-60°C]s (G for S-glass, C for thin-ply carbon). Copied from [50] [54].

2.2.2.1.2 Inter-yarn or intralayer woven hybrids

The hybridization strategy was also implemented in an intralayer or inter-yarn hybrid composite. An example architecture of the preform used a hybrid non-crimp 3D woven composite is shown in Figure 2.12 (a) [56], where each colour relates to a specific type of material. The preforms were fabricated by stacking 2.5 consecutive warp and weft layers of carbon fibre yarns with 4.5 consecutive warp and weft layers of S2-glass yarns, and Dyneema z-yarn binder, as shown in Figure 2.12 (a). The distribution of carbon and glass is asymmetric in this layup, as shown in Figure 2.12 (b). The heterogeneity of the composites enables distinct stress-states along different loading directions. Progressive failure process with more ductile tensile response (see Figure 2.13 (b)) was observed in the in-plane tensile test, performed in the direction containing higher volume fraction of S2-glass fibres, along which the Dyneema z-yarn binders were oriented (see Figure 2.13 (a)). The X-ray CT tomograms of specimens loaded to different load levels revealed that matrix cracking and minor delamination resulted in the small stiffness reduction prior to the load drop, shown in Figure 2.13 (b). The gradually developed carbon and glass tow cracking, delamination around the fibre tows and extensive delamination of Dyneema z-yarns from the carbon and glass fibre tows, promoted the load drops in the tensile response. The Z-yarn Dyneema can arrest the delamination between carbon or glass fibres and matrix. The tensile strength is determined by the volume fractions of each type of yarns, while the strain-to-failure is dominated by the S2-glass yarns in this loading direction.



(a) (b)

Figure 2.12 (a) An example of non-crimp 3D orthogonal fibre architecture and (b) the side views of the hybrid carbon/S2 glass/Dyneema (z-yarn) preform. Adapted from [56].

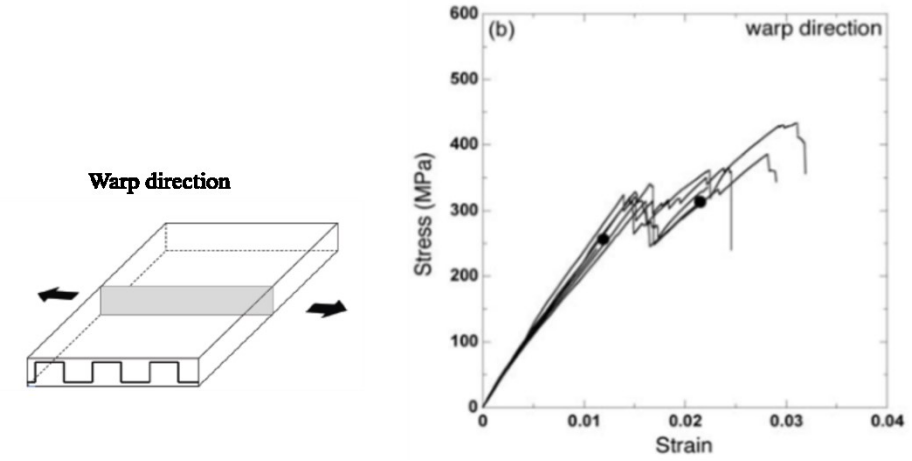
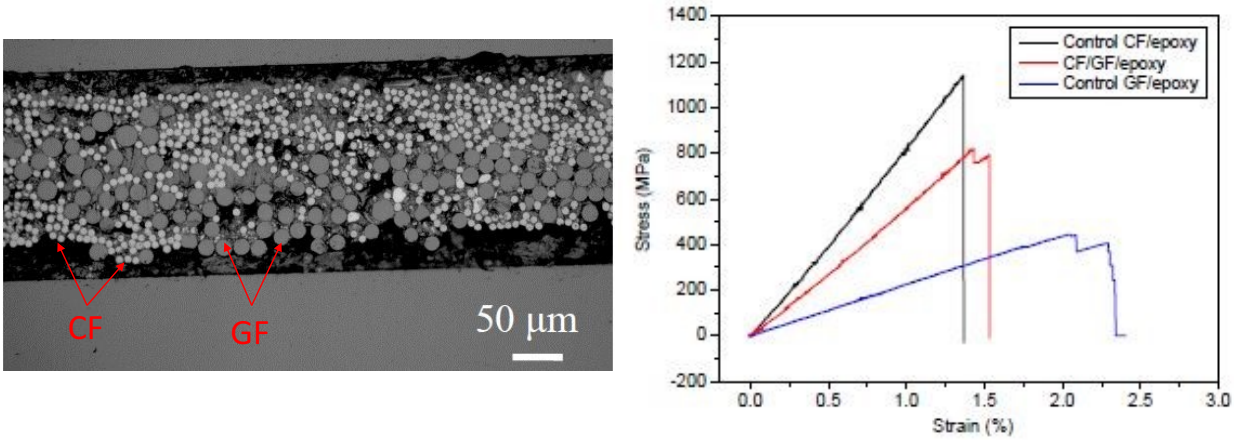


Figure 2.13 (a) Schematic warp direction relative to the z-yarn Dyneema binders and (b) tensile stress-strain response in the warp direction of the hybrid 3D woven composite. Adapted from [56].

2.2.2.1.3 Commingled continuous fibre hybrids

Scaling down to the fibre filament level, commingling of different types of fibre filaments was implemented using an air-flow-assisted spreading and commingling technique. The method allows the filaments to be inserted into another type of fairly spaced filaments (see Figure 2.14 (a)) [57]. Figure 2.14 (b) shows the tensile stress-strain behaviour of the epoxy matrix composite containing intermingled carbon and glass fibres. The overall fibre volume fraction is around 30% to 40% and the carbon to glass fibre volume ratio is 1.55:1. The strain-to-failure of the intimately commingled glass/carbon fibre epoxy composites is on average 14 percent higher than that of the LFS carbon fibres, without significantly compromised stiffness and strength. The first load drop is due to the carbon fibre breakage in the intermingled carbon-glass fibre/epoxy hybrids, and the strain is higher than the failure strain of non-hybrid control carbon fibre/epoxy baseline. This is due to the 'hybrid effect'.



(a) (b)

Figure 2.14 (a) Cross-sectional micrograph of a cured intermingled glass-carbon fibre tows reinforced epoxy lamina and (b)Tensile stress-strain curves of UD non-hybrid carbon fibre/epoxy, non-hybrid glass fibre/epoxy and intermingled carbon-glass fibre/epoxy specimens. Adapted from [57].

In hybrid composites, it is always observed that the strain at the onset of the LFS fibres failure is higher than the strain-to-failure of the non-hybrid composite made by the LFS fibres only [14], [43], [44], [58]–[63]. This phenomenon was named as 'hybrid effect'. Recent research suggested that the enhanced failure strain of the LFS fibes in the hybrids, is predominately because of the stress concentration in the vicinity of the incipient failed LFS fibres is effectively redistributed to the adjacent fibres or (further scaling up) to the adjacent plies. The diffused stress concentration can delay the formation of critical sized cluster of failed LFS fibres, i.e. ultimate fracture. It was widely accepted that relatively low LFS to HFS volume ratio or finely dispersed LFS fibres among the HFS fibres, tends to enhance the failure strain of the LFS material in the hybrids [61]–[67].

2.2.2.2 **Partially discontinuous carbon fibre hybrids**

2.2.2.2.1 Interlayer hybrids made of fibre mats or UD prepregs

One issue with the UD completely continuous interlayer hybrids, presented in Section 2.2.2.1.1, is the restriction in the relative and absolute thicknesses of the HFS and LFS plies. In the completely continuous architectures, 'yielding' is promoted by the LFS component fragmentation. The 'thickness limitation' was resolved whilst retaining the pseudo-ductile characteristics, once the continuous LFS material is completely or partially replaced with short fibres. Properly designed discontinuous component profiles can also mitigate or eliminate the unstable load-drops induced by the sudden release of strain energy at the onset of LFS material fragmentation, albeit the discontinuity induces slight

reduction in the initial stiffness. In addition, this partial discontinuity architecture indicates the potential to achieve pseudo-ductility in a single composite material system, without hybridization.

In the partially discontinuous composites, the previous 'fibre-property-determined' damage modes are transferred to be dominated by matrix properties. 'Yielding' is determined by the interlaminar matrix shearing deformation and the evolution of the plastic zone initiated from the discontinuities during the loading process, for given fibre-matrix interphase properties [64]. These characteristics have been demonstrated in different material combinations. Gradual and dispersed fibre fragmentation, delamination and fibre pull out are the typical damage modes in the pseudo-ductile partially discontinuous laminates. The geometry, such as length and aspect ratio, of the discontinuous constituents plays a significant role in the tensile failure mechanisms and consequently the tensile behaviour.

Progressive failure process was also observed in the interlayer hybrids made of carbon fibre mats or UD carbon fibres reinforced polypropylene (CFRPP) with self-reinforced polypropylene (SRPP) made of woven polypropylene (PP) fibre tows (see Figure 2.15) [65]–[67]. The four typical damage development processes after the initial carbon fracture, resemble those for the UD carbon-glass hybrids (see Figure 2.5), were also identified in the CFRPP- SRPP hybrids. The failure process is determined by the arrangement of hybridized materials (for example, UD or randomly distributed fibre mat), relative volume fraction and the relative layer thickness of the CFRPP and SRPP [68]. An example of progressive damage process with multiple load-drops in the stress-strain curve, caused by multiple dispersed fragmentation and unstable delamination, is shown in Figure 2.16. These intermediate load drops arose from the unstable delamination, are appeared at the instant of fragmentation.

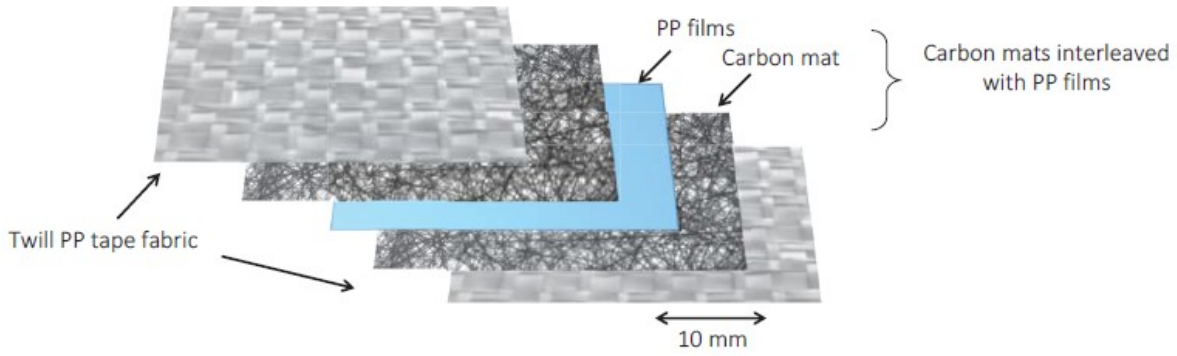


Figure 2.15 Schematic layup of the interlayer carbon fibre mat and woven polypropylene fibre reinforced polypropylene hybrid laminate. Copied from [69].

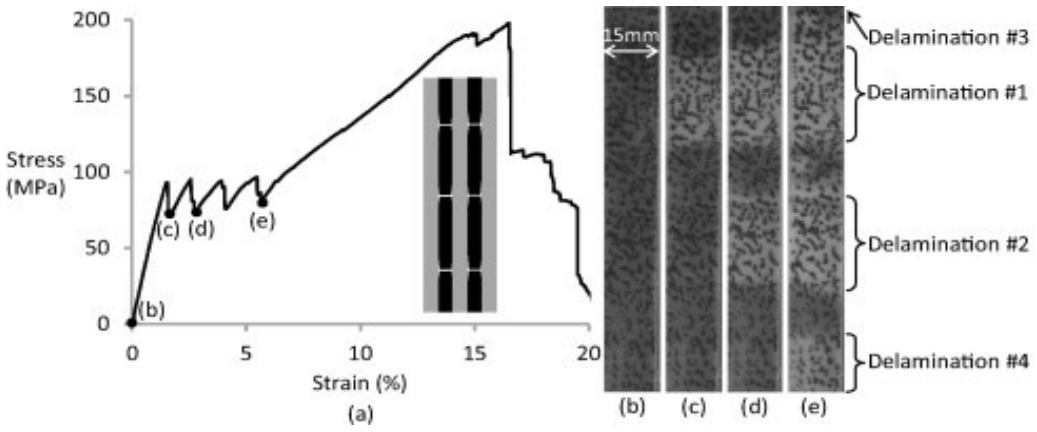
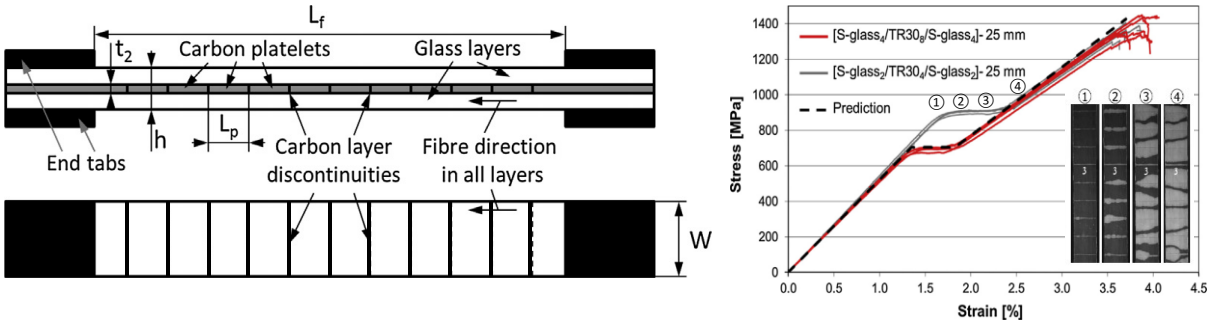


Figure 2.16 Tensile stress-strain curve of a pseudo-ductile CFRPP and SRPP woven hybrid with successive dispersed delamination with increasing load. Adapted from [68].

Introducing discontinuities into selected continuous UD prepregs is the most direct way to fabricate partially discontinuous laminates. Pseudo-ductility was achieved in prepreg-based glass/carbon interlayer hybrids containing periodic continuous cuts in the middle LFS carbon plies, as shown in Figure 2.17 (a) [70]. Yielding in the tensile response occurs once delamination is initiated from the cuts, as shown in Figure 2.17 (b). Delamination occurs when the strain energy release rate reaches the mode II fracture toughness under increasing tensile load. The progressive delamination propagation along the interface between the continuous and discontinuous plies generates a plateau stage in the tensile response.

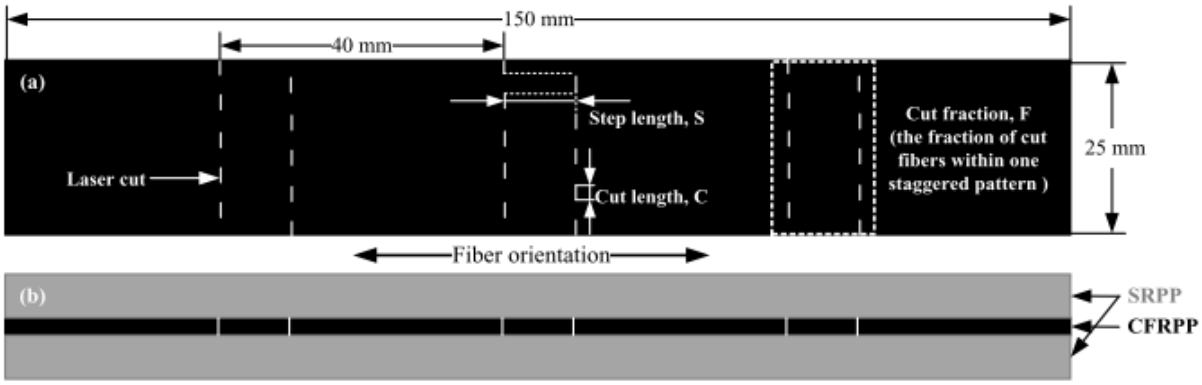


(a) (b)

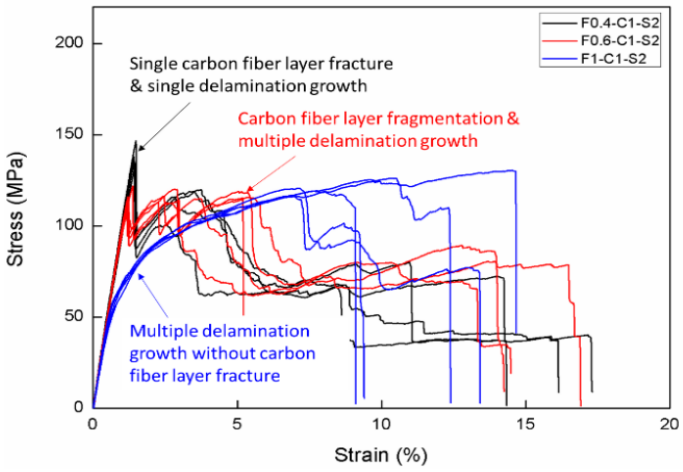
Figure 2.17 (a) Schematic edge view of a continuous glass fibre-discontinuous carbon fibre hybrid laminate with the top view of a periodically cut carbon ply with cuts spans across the specimen width, (b) tailorable pseudo-ductile tensile response of S-glass/TR30 carbon epoxy hybrids containing 25 mm carbon platelets and the images of a specimen at increased stress levels. Adapted from [70].

Pseudo-ductile response with a yielding behaviour followed by a long plastic stage was later achieved by replacing the across-width continuous cuts with periodic discontinuous perforations [71] [72]. This

approach provides higher volume fractions of load-bearing continuous fibres in the laminate and therefore a higher initial stiffness, compared with that of the counterparts containing continuous cuts. Damage modes of dispersed fragmentation of unperforated fibre bundles, progressive debonding and pull out of the perforated fibre bundles in the LFS plies, were depicted in laminates with different perforation profiles and fractions of perforated fibres. For instance, periodic perforations were introduced in UD carbon fibre reinforced polypropylene (CFRPP) prepregs, sandwiched between woven self-reinforced polypropylene (SRPP) plies (see Figure 2.18 (a)). Properly designed perforation geometries promote progressively developed sub-critical damages, such as fibre breakage or delamination at dispersed locations, which prevent the release of excessive strain energy at the onset of these damages. Such perforation geometries can produce a more stable and gradual failure process, as shown in Figure 2.18 (b), and effectively mitigate or even eliminate the potential load-drops.



(a)



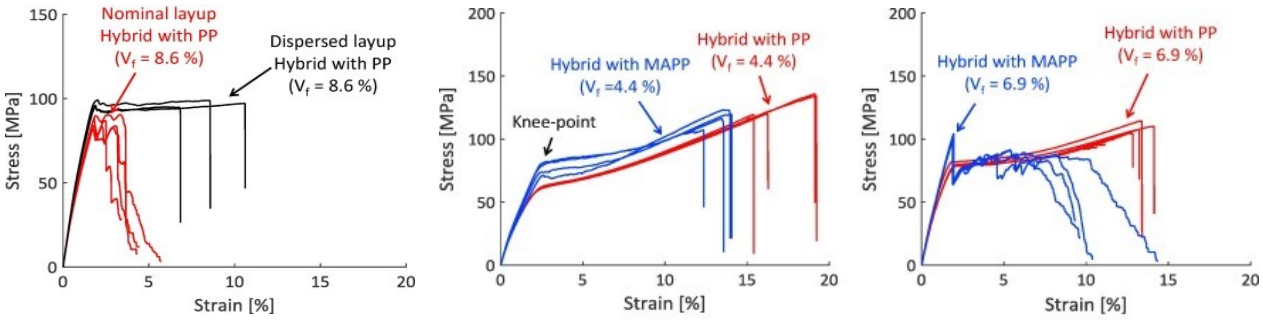
(b)

Figure 2.18 (a) Schematics of periodically perforated CFRPP plies, sandwiched in continuous woven SRPP plies and (b) the tensile responses of such hybrid laminates containing variable perforation patterns in the CFRPP plies (the legends F, C and S represent cut fraction, step length and cut length, respectively). Copied from [71].

2.2.2.2.2 Interlayer hybrids with commingled discontinuous short fibres

The ‘partially discontinuous pseudo-ductile interlayer hybrids’ can also be manufactured by replacing the cut or perforated prepreg-based plies with pre-impregnated randomly oriented or aligned short-fibre-based plies. In these short fibre-based interlayer hybrids, the properties of the interfaces between adjacent continuous and discontinuous plies can be regarded as higher scaled properties, the fibre-matrix interphase properties, such as the interfacial shear strength (IFSS) and fracture toughness of the fibres/matrix interphase can be regarded as lower scaled properties (in nanometres). The properties in both scales determine the eventual damage development process. Unlike the ply fragmentation, delamination and fibre bundle pull out that were observed in the prepreg-based interlayer hybrids (see section 2.2.2.1), damages in these short fibre hybrids are scaled down to the fragmentation of short fibres (normally designed longer than the critical length), short fibre debonding and pull-out of short fibres from the matrix. The interaction and synergistic effects among these multi-scaled geometric and mechanical properties play a significant role in the overall hybrid tensile response.

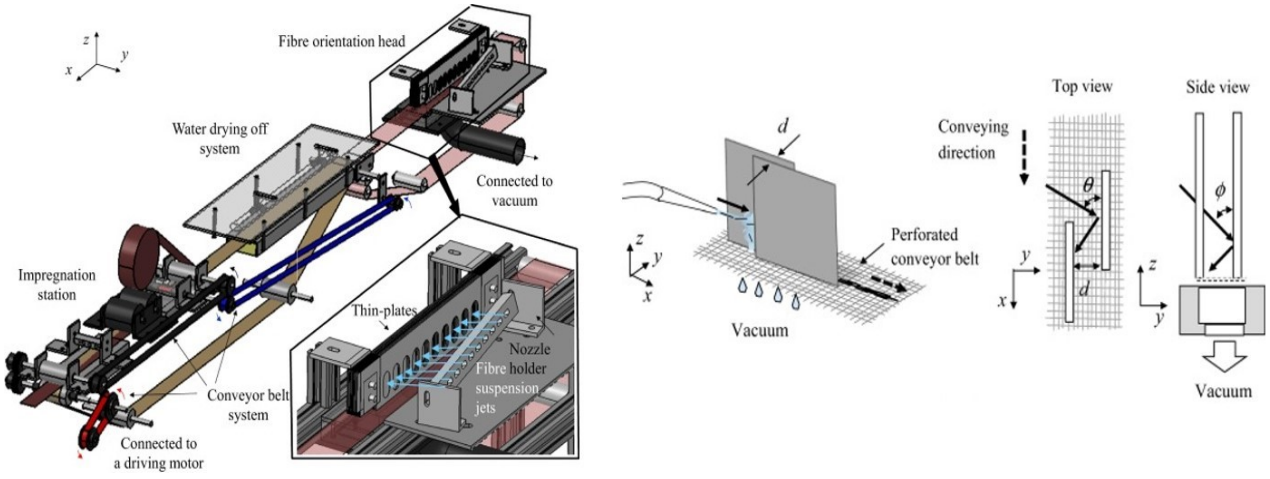
For instance, pseudo-ductility with a strain-hardening stage was demonstrated in the partially discontinuous CFRPP/woven SRPP hybrid laminates, which has not been achieved in the previously reviewed CFRPP/SRPP material systems (presented in 2.2.2.2.1). The superior performance was obtained by replacing the prepreg-based perforated UD CFRPP plies (see Figure 2.18) with pre-impregnated randomly-oriented short-carbon-fibres mats [73]. The authors found that the highly dispersed CFRPP and SRPP layup (see Figure 2.19 (a)) and a relatively low volume fraction of carbon fibres (see Figure 2.19 (b) and (c)) in the hybrids, tend to promote a more stable and progressive tensile failure process. This material arrangement provides improved redistribution of stress concentration induced by the initial matrix cracks, fibre-matrix debonding and carbon ply fragmentation. In addition, the weaker carbon fibre/matrix interphase, provided by using the polypropylene (PP) matrix, triggers earlier onset of fibre-matrix shear failure and the following pull-out, which can effectively suppress the load drops, that appeared in the counterpart cases associated with stronger and tougher interphase, produced by using the maleic-anhydride modified polypropylene (MAPP) matrix, see Figure 2.19 (c).



(a) (b) (c)

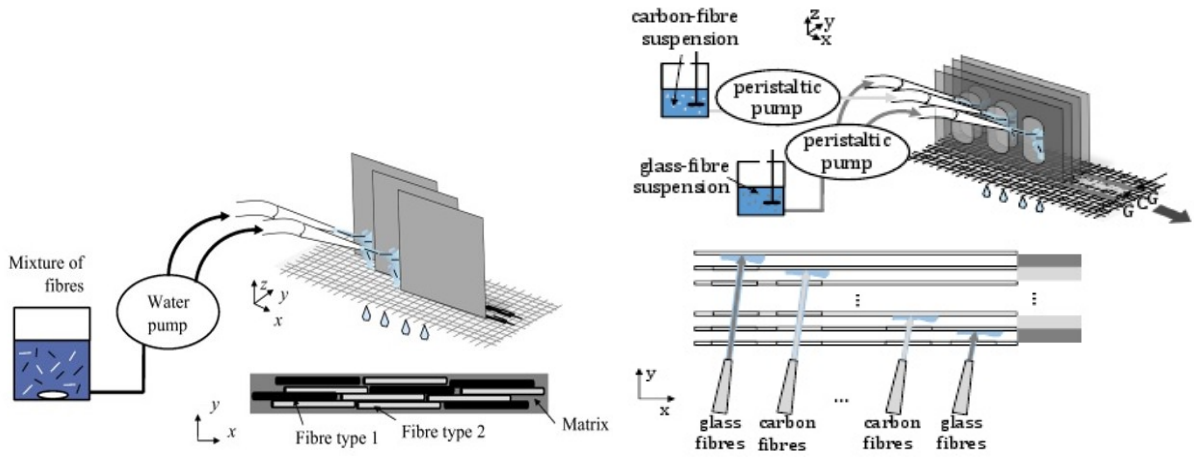
Figure 2.19 Tensile stress-strain curves of random-oriented short carbon fibre mats reinforced PP/woven SRPP interlayer hybrids with various (a) layups and (b) (c) volume fractions of CFRPP and matrix systems. (PP and MAPP refer to polypropylene and maleic-anhydride modified polypropylene matrix, respectively.) Adapted from [73].

The discontinuous plies can also be presented in other formats, such as pre-impregnated highly aligned single type or hybrid short fibres. The recently developed HiPerDiF method, as shown in Figure 2.20, was invented to fabricate prepregs with high volume of highly aligned short fibres of different length scales [74]–[77], materials [78], and even reclaimed fibres used to generate green composites [77][79][80]. A further modified assembly line (see Figure 2.21) can also maximize the intermingling, control the distribution of different bundles and bundle sizes [81]. This technique was used to manufacture intraply hybrids.



(a) (b)

Figure 2.20 Schematic of HiPerDiF (a) lab-scale alignment and pre-impregnating rig and (b) method to manufacture highly aligned (a) single type and (a) intermingled short fibre hybrids. Copied from [78] [81].



(a) (b)

Figure 2.21 Schematics of (a) modified HiPerDiF method to manufacture controlled volume of different types of short fibres and (b) an instance of short carbon and glass bundles, in distinct regions of intralayer hybrids. Copied from [81].

Pseudo-ductile hybrids can also be manufactured by sandwiching highly aligned short fibre prepregs, fabricated using the HiPerDiF method, between prepregs reinforced by HFS continuous fibres. Transparent continuous S- or E-glass prepregs were used as the HFS material to provide the residual load-bearing ability and assist the direct visual detection of 'stress whitening' caused by fragmentation and delamination of the internal plies.

Damage mode maps [77][80][82] indicate that fibre length [77], relative fibre volume fraction and constituent fibre selection [78][76], as well as the associated fibre-matrix interphase properties of the hybrids, can trigger different damage mechanisms and combinations of damage mechanisms. Just as for the continuous hybrids discussed in Section 2.2.2.1, absolute thickness and thickness-ratio of the continuous and discontinuous plies must also be considered in the design process to avoid catastrophic failure [77].

The damages commonly seen in short-fibre composites are fibre-matrix debonding (mainly in composites with relatively short discontinuous fibres) and fibre fragmentation (mainly in composites with longer discontinuous fibres). These damages are mainly influenced by the fibre strength and the overlap length between adjacent fibres, respectively [83][84]. Most pseudo-ductile interlayer hybrids using highly aligned discontinuous fibres were designed with relatively long fibres to promote progressive fibre fragmentation.

The damages observed in these continuous and short fibre reinforced interlayer hybrids include progressively developed dispersed fibre fragmentation across specimen width, fibre pull-out and fragmentation-induced delamination between the continuous and short-fibre plies, as shown in Figure

2.22. These damages were observed in the plateau and final strain-hardening stages in the tensile responses.

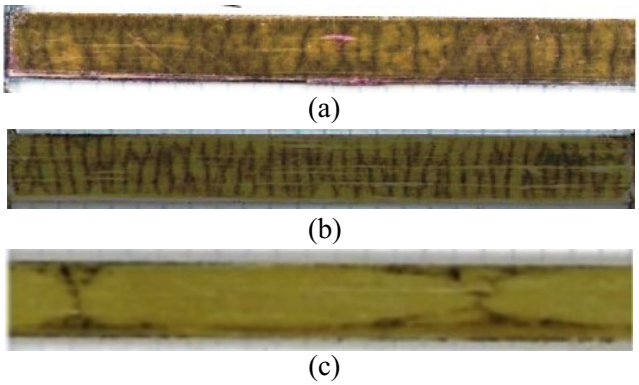


Figure 2.22 Typical damage modes in pseudo-ductile interlayer hybrids made of continuous S-glass prepregs with HiPerDiF technique manufactured highly aligned short fibre reinforced prepregs containing (a) intermingled high modulus /high strength short carbon fibres, (b) reclaimed and (c) virgin carbon fibres. Copied from [78], [82] and [80], respectively.

Interestingly, in hierarchical hybrid composites consisting both intralayer and interlayer hybridization (see Figure 2.23(a)), the synergistic effects of the intralayer and the interlayer hybridization can be used to optimize the progressive damage development (see Figure 2.23 (b)). On the aspect of intralayer hybridization, the lengths (related to either fibre-matrix debonding or fibre fragmentation of individual fibres), relative failure strains, relative volume fractions of different types of short fibres (associated with the cluster sizes of fragmented fibre bundles and the stress transition between adjacent short fibres) determine the damage development within the discontinuous short-fibre prepregs [83][84]. Scaling-up, the relative mechanical and geometric properties of the continuous and the discontinuous plies control the resulting damage development. As an example, initially damage appears as dispersed fragmentation of the LFS short fibres, the fragmentation gradually expands and leads to the fragmentation of the intermediate failure strain (IFS) short fibres and finally the dispersed fragmentation of the overall intermingled layer. This process refers to the stages from P2 to P5 in Figure 2.23 (b) and the tensile response prior to point P5 in Figure 2.23 (c). The fragmentation saturates before reaching the mode II fracture toughness, i.e. the onset of dispersed macro-scale delamination between the high failure strain (HFS) continuous plies and the discontinuous plies. This delamination process relates to the stage from P5 to P6 in Figure 2.23 (b) and (c)). The HFS plies sustains the following loading process. The laminate fractures at the strain close to the strain-to-failure of the HFS plies.

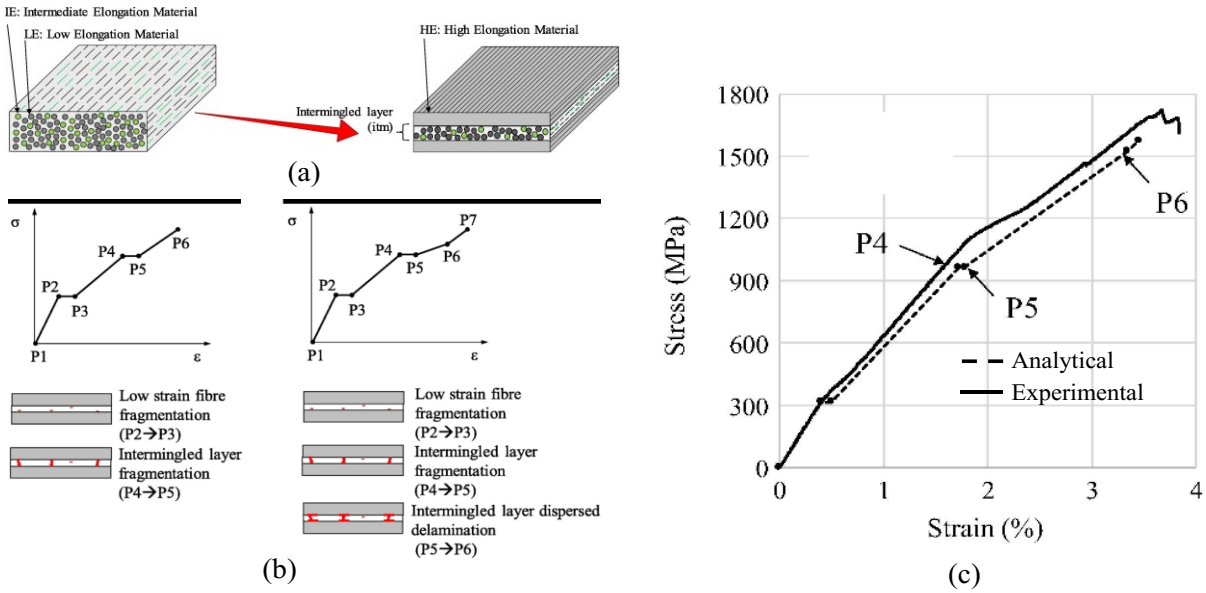


Figure 2.23 (a) Schematic of the interlayer hybrid laminates containing intermingled aligned short fibres in the middle discontinuous plies, (b) typical failure mechanisms of hierarchical hybrid pseudo-ductile laminates and (c) pseudo-ductile tensile stress-strain curve of hierarchical interlayer hybrids with highly aligned high modulus carbon (HMC) and high strength carbon (HSC) short fibre prepregs sandwiched in continuous S-glass prepregs. Adapted from [78].

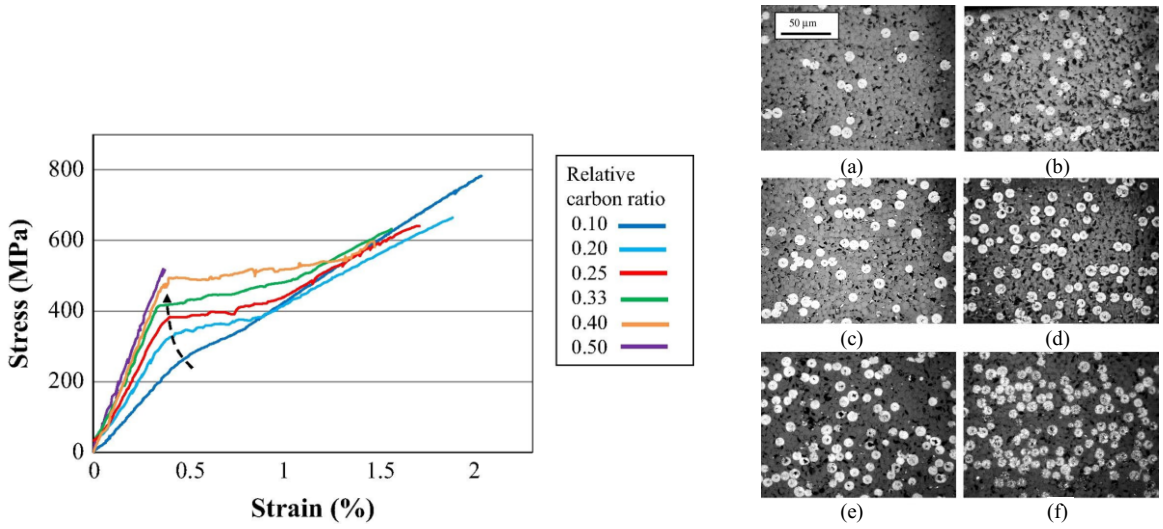
2.2.2.3 **Completely discontinuous carbon fibre hybrids**

Pseudo-ductility can also be achieved in completely discontinuous fibre hybrids (containing no continuous fibres). Section 2.2.2.3.1 presents the pseudo-ductility in hybrids made of highly-aligned intermingled short fibres. The performance of laminates made of staggered discontinuous carbon prepregs is also shown in Section 2.2.2.3.2, for comparison.

2.2.2.3.1 Highly-aligned short fibre hybrids

Figure 2.24 (a) demonstrates how the initial stiffness and pseudo-yield stress of highly-aligned intermingled carbon and glass short fibre hybrids (see Figure 2.24 (b)), manufactured by the HiPerDiF technique, increase with the carbon fibre volume fraction of up to 50% [76][85]. 3 mm discontinuous fibres that are much longer than the short fibres used in conventional short fibre composites (of about 0.5 mm), were employed to promote progressive fibre fragmentation. The progressive and dispersed LFS carbon fibre fragmentation induces a pseudo-yield and the following plateau in the tensile response. The fragmentation saturates at the end of the plateau. The residual surviving short fibres (predominately the HFS glass fibres) contribute to the final strain-hardening response. In the case with 50% of carbon

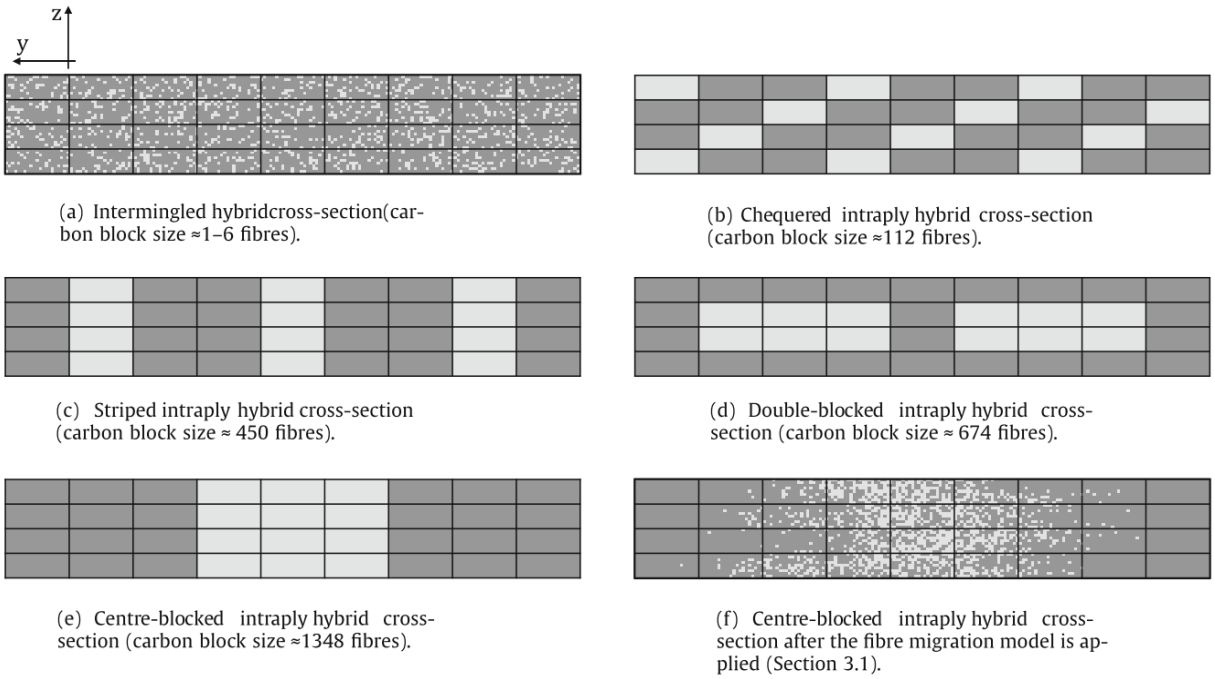
fibres, no yielding or strain-hardening is shown, at the breakage of critical sized carbon fibre bundles, where the HFS glass fibres can not tolerate the extra stress redistributed from the fragmented carbon.



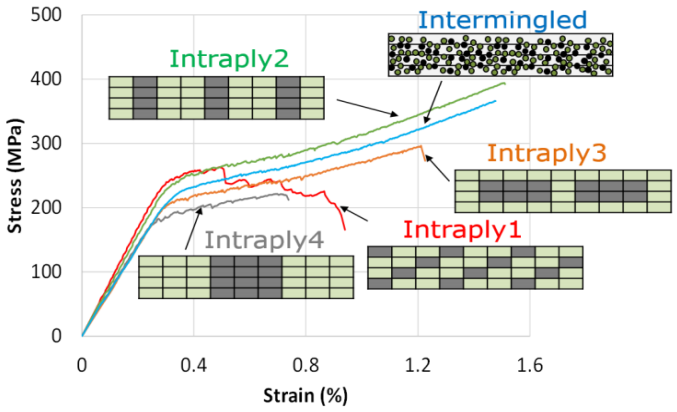
(a) (b)

Figure 2.24 (a) Tensile response of HiPerDiF method manufactured intermingled carbon and glass short fibre hybrids containing 0.1 to 0.5 volume fractions of carbon fibre and (b) the corresponding cross-sectional micrographs of the hybrids shown in (a). Copied from [76].

The HiPerDiF technique permits different types of fibre bundles with specific sizes to be accurately placed in an intralayer hybrid, as schematically shown in Figure 2.25 (a) [86]. Yielding, with or without a rising plateau and strain-hardening, were achieved both analytically and experimentally in all carbon/E-glass short fibre intralayer hybrids displayed in Figure 2.25 (a) [81] [86]. The pseudo-ductile stress-strain responses of these hybrids are shown in Figure 2.25 (b). Previous pseudo-ductile cases have presented the impact of stress redistribution capacity of the less stiff HFS short fibres after the appearance of initial clusters of broken stiffer LFS fibres on the tensile performance [61]. The tensile response shown in Figure 2.25 (b) indicates the 'effectiveness of stress redistribution in laminates with properly arranged clusters of constituent fibres' is also applicable in this case. The authors concluded that the higher degree of isolation between adjacent LFS carbon fibres and the surrounding HFS glass fibres, the higher the potential for higher pseudo-yield stress, ultimate failure strain and stress (see Figure 2.25 (b)).



(a)



(b)

Figure 2.25 (a) Cross-sections of intralayer hybrids with strategically arranged high modulus LFS carbon (shown in light grey) and HFS E-glass (shown in dark grey) fibre bundles at different locations with 33% volume fraction of carbon and (b) experimental stress-strain curves of different commingled carbon (shown in grey) and glass (shown in green) fibre arrangement. Copied from [81] and [86].

2.2.2.3.2 'Brick-and-mortar' discontinuous (prepreg-based) laminates

The 'brick-and-mortar' architecture that enables large quantity of plastic deformation of the compliant 'mortar' among staggered stiff 'bricks' has been widely studied and replicated in different materials, for example composites [18][87]. Significant non-linearity was observed in tensile tests (see Figure

2.26 (a)). This is attributed to the progressive matrix shearing between adjacent long platelets and the pull out of delaminated platelets in between the ply discontinuities (see Figure 2.26 (b). In this larger scaled completely discontinuous configuration, the matrix decohesion occurs at a strain lower than the strain-to-failure of the platelets, so fibre fragmentation does not happen. Thereby the ultimate failure is 'matrix-dominated'. Geometric parameters, such as the aspect ratio, the overlap length of stiff 'bricks' [88] and the matrix constitutive law, which can be rigid perfectly-plastic, perfectly-plastic, strain-hardening, softening, etc, were confirmed to play key roles in determining the shear/plastic deformation under tension [89].

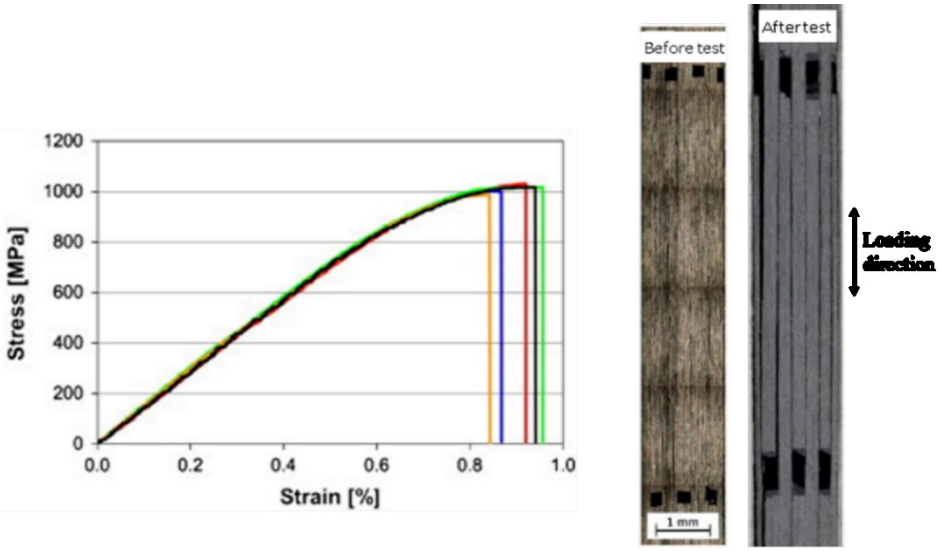
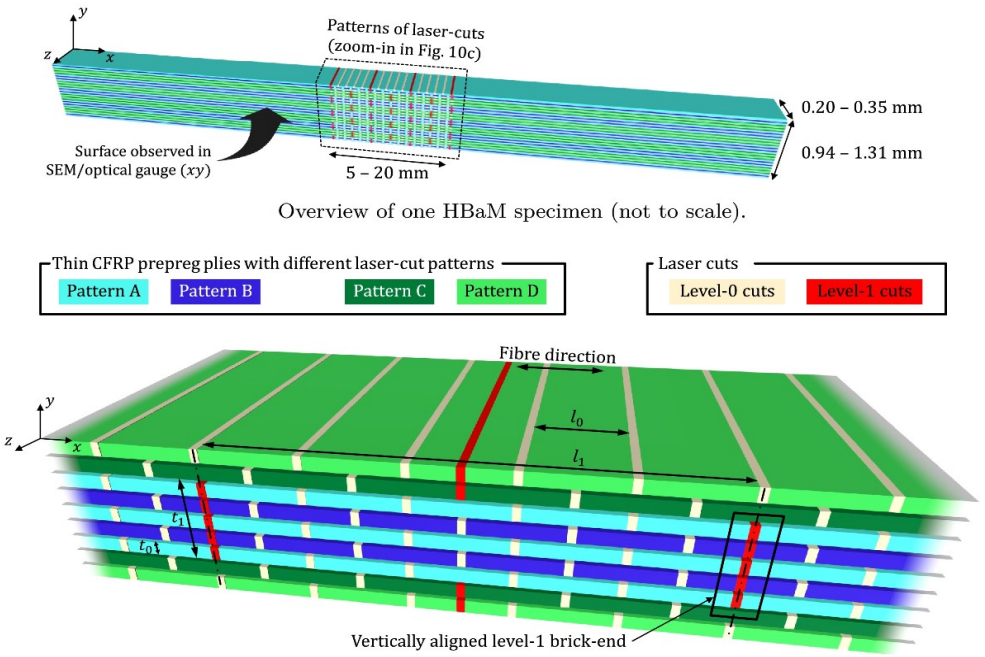
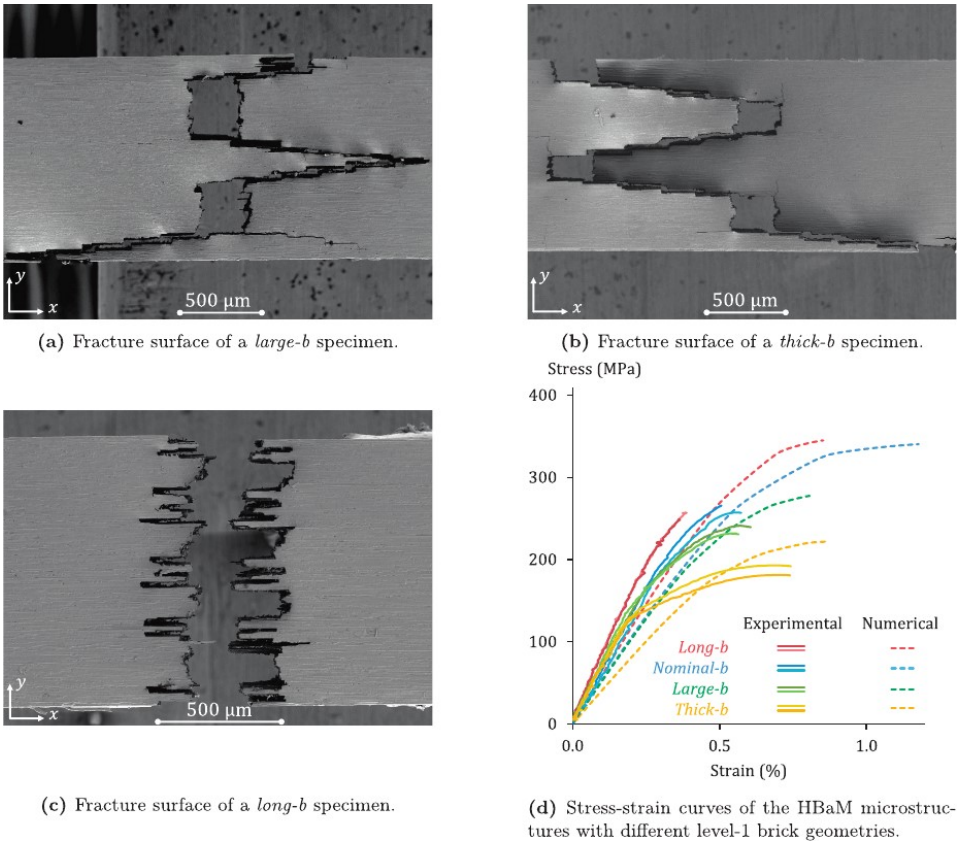


Figure 2.26 (a) Tensile stress-strain curves and (b) the edge views of the 'brick-and-mortar' specimens before and after tests. Copied from [89].

An hierarchical 'brick-and-mortar' architecture was also studied in laser perforated thin-ply ($\sim 30\mu m$ thick) carbon/epoxy laminates [87]. Laser milled, staggered perforations were carefully laid out in the through-thickness direction of small coupons, as shown in Figure 2.27 (a). The experimental non-linear tensile responses shown in Figure 2.27 (b), indicate trade-offs between the tensile strength and failure strain. The SEM edge views shown in Figure 2.27 (b) indicate that cracks can migrate perfectly along the hierarchical through-thickness discontinuous profiles for properly spaced perforations. Crack deflection, fibre/matrix debonding and platelets pull-out were identified at a higher geometric hierarchy level. The strain-to-failure is determined by the overall longitudinal pull-out length along the hierarchical fractals, the strength is closely related to the hierarchy levels. The results also demonstrate the importance of improving the plastic deformation from the synergistic effect of the damage mechanisms in meso (i.e. multiple length) scales.



(a)



(b)

Figure 2.27 (a) Schematics of the 'brick-and-mortar' laminates containing two hierarchy levels (level-0 and level-1) of cuts and the (b) tensile responses for various geometric parameters (i.e. 'b') defined by the 'level-1 cuts' and SEM edge view images of fractured specimens. Copied from [87].

These ‘brick-and-mortar’ configurations suggest that the plasticity following an initial almost-linear stage in the tensile response can be improved by enhancing the matrix shear deformation and fibre/platelet pull-out effects, i.e. to increase the energy dissipation, in these discontinuous architectures. The limitations for these completely discontinuous architectures are the significantly compromised strength (due to the discontinuity) and relatively low strain-to-failure (due to damage localization and lack of strain-hardening) compared to the continuous counterparts. Recent research indicated the potential to improve the strain of these ‘brick-and-mortar’ architectures, with well-retained high initial stiffness and tensile strength, by partially increasing the interlaminar fracture toughness. The technique used is the ‘interleaving technique’, as shown in Section 2.2.4.2.

2.2.3 Fibre reorientation/hidden length mechanisms

Most of the previously reviewed pseudo-ductile hybrids presented in Section 2.2.2.1 were achieved by promoting progressively developed non-critical sized damages at dispersed locations. In most cases, the overall tensile failure strain was confined by that of the HFS constituents. However, a preferable pseudo-ductile composite should possess the enhancement of the ultimate failure strain, which can be achieved by strategically introducing ‘hidden length’, as an example. Several approaches exploiting the ‘fibre waviness’ or ‘rotation of off-axis fibres’ have been proposed to accomplish this goal [90].

Introducing waviness to continuous fibres before consolidation is an effective way to enhance ultimate failure strain. The matrix plasticity permits gradual re-orientation or straightening of the wavy fibres towards the loading direction and exposes the length hidden in the wavy profiles. The geometric characteristics and materials must be designed properly so that the structure can deform gradually and be tolerant to the onset of initial damages, prior to the onset of fibre reorientation. The following content presents the ‘fibre waviness’ approach implemented in fibre filaments (Section 2.2.3.1), in 3D microbraid yarns (Section 2.2.3.2) and in an out-of-plane wavy sandwich structure (Section 2.2.3.4). The in-plane fibre reorientation was investigated in angle-ply laminates and is presented in Section 2.2.3.3.

2.2.3.1 **Gas-texture and annealing methods introduced fibre waviness**

PA-12 matrix composites with large variation in carbon fibre waviness have been fabricated using gas texturing and non-constrained annealing techniques [5]. Results show the non-constrained annealing method can improve the failure strain by 34%, as shown in Figure 2.28.

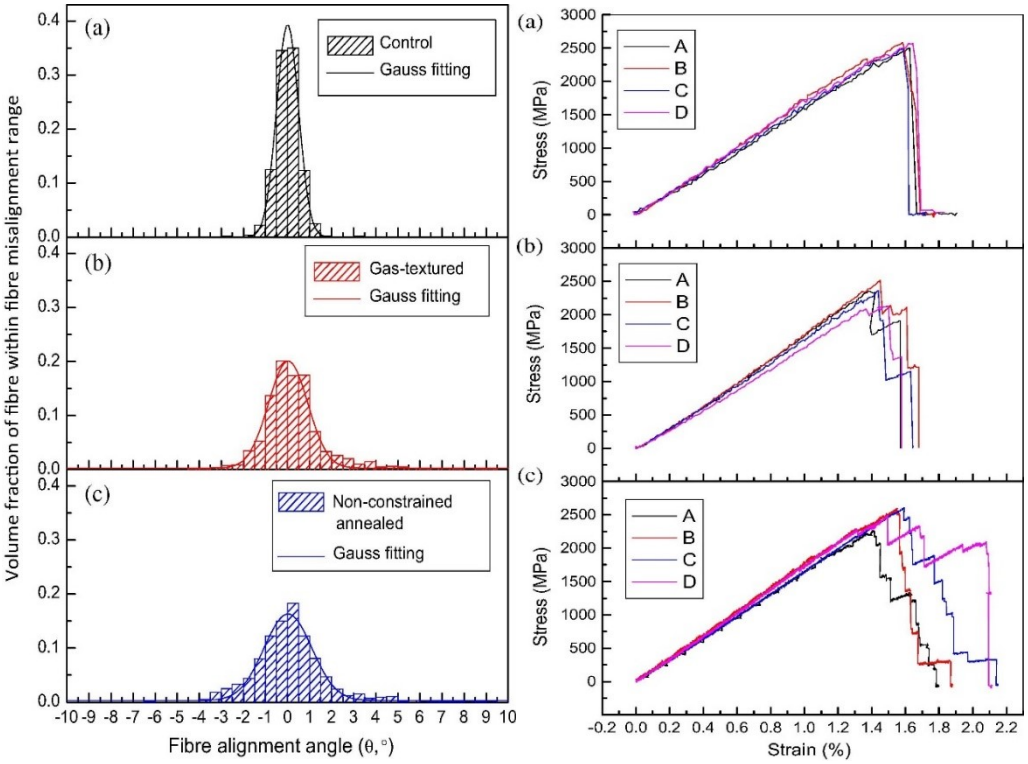


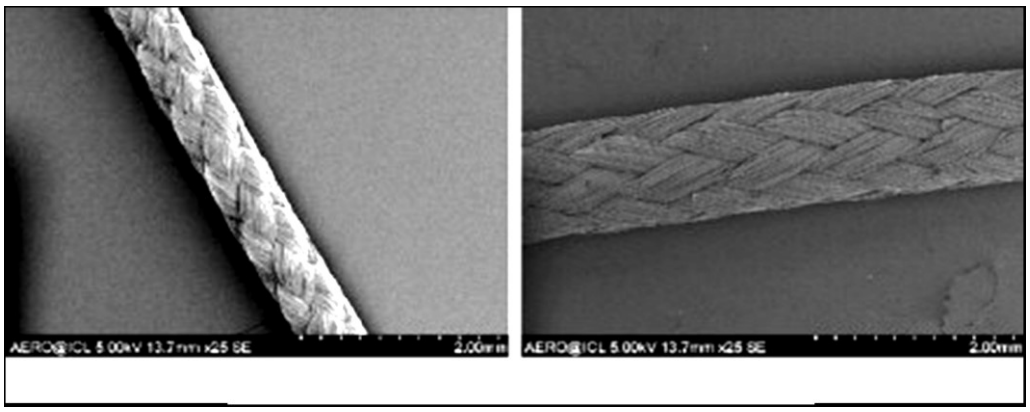
Figure 2.28 Statistical distribution of fibres with different misalignment angles (on the left) and the corresponding tensile stress-strain curves (on the right) of the (a) control (i.e. as received), (b) gas-textured and (c) non-constrained annealed carbon fibre/PA-12 tapes. Copied from [5].

The fibre damages that occurred during the 'gas-texture' method (see Figure 2.28 (b)) results in the premature failure and lower failure strain compared to that of the baseline materials, shown in Figure 2.28 (a). The 'non-constrained annealing' technique was able to introduce variable fibre waviness. The variation in the extent of fibre waviness means the fibres with least waviness break before those with higher waviness and so promote a gradual failure process. The wavy fibres gradually rotate to the loading direction during the loading process. The extra elongation hidden in these rotating fibres contributes to the improvement of ultimate failure strain.

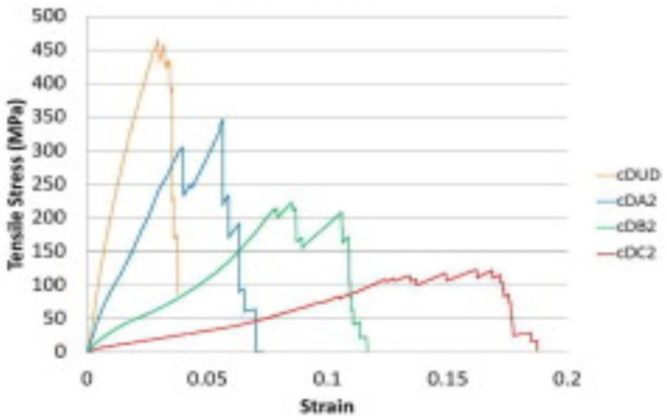
2.2.3.2 **Composites made of braided fibre bundles**

Fibre waviness was also introduced using the microbraiding method. Cross-ply laminates made of microbraid Dyneema or Kevlar fibres (see Figure 2.29 (a)) in a thermoplastic matrix were tested under tension [91]. Both types of composites failed in a stepwise manner frequently with a significant load drop before the ultimate failure (see Figure 2.29 (b)). The load drops are initially induced by the outer layer fibre breakage and abrupt unstable interlayer delamination in the neighbourhood of the fibre break, at stresses close to the ultimate fracture. Higher braiding angles tend to provide lower initial stiffness, higher failure strain and more severe delamination. An obvious trade-off between initial stiffness and

strength is shown in Figure 2.29 (b). For higher braiding angles, the more dispersed premature outer layer fibre breakage results in less severe stress concentration in the remaining fibres. As a consequence, the failure process is more progressive with higher failure strain than the tensile strain of the baselines containing non-braided constituent.



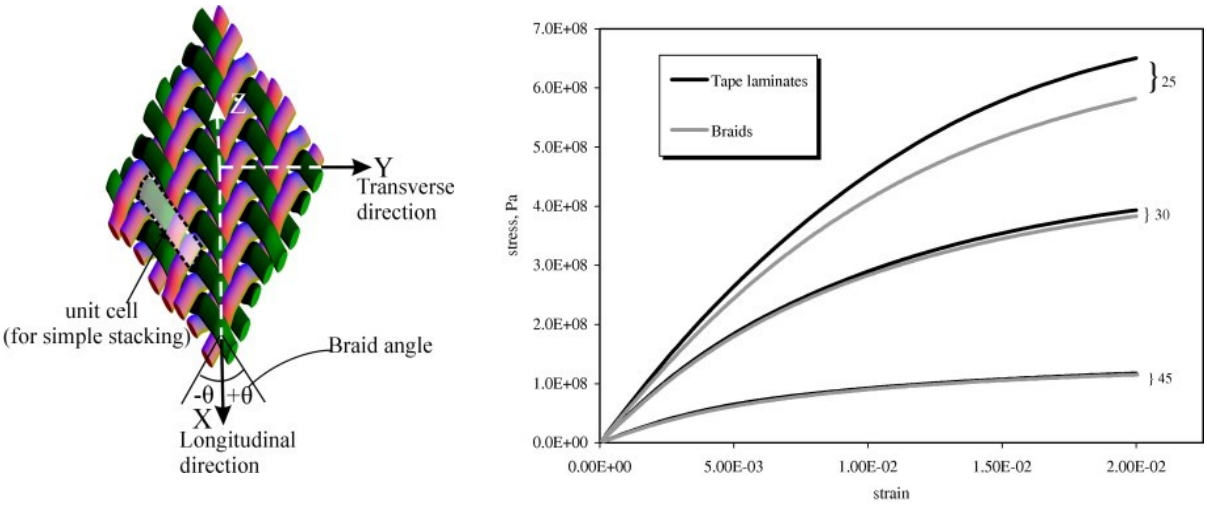
(a)



(b)

Figure 2.29 (a) SEM images of dry microbraids made of Dyneema (left) and Kevlar (right) fibres with approximate 15° braiding angles and (b) tensile responses of cross-ply $[0°/90°]_3$ laminates with Dyneema briaided in a regular brading architecture (UD, A, B and C in the legends represent braiding bias angles,where UD refers to 0° and UD<A<B<C in terms of magnitude). Copied from [91].

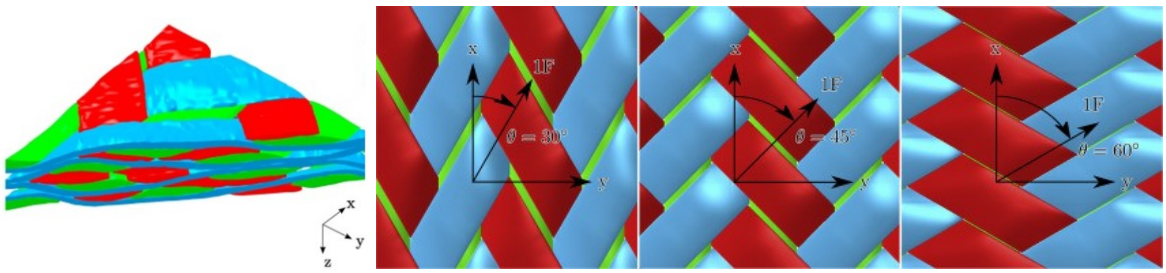
Another special laminate architecture was constructed by stacking layers of 2×2 biaxial braided yarns reinforced prepregs (see Figure 2.30 (a)) [92][93]. The non-linearity (see Figure 2.30 (b))) observed in the tensile response of tensile tests on the longitudinal loading direction (labelled in Figure 2.30 (a)), was induced by the tow undulation and matrix plasticity.



(a) (b)

Figure 2.30 (a) 2D schematic of 2×2 [±θ] biaxial braided yarns and (b) comparison of FE modelled tensile performance of 2×2 [±θ] braids with different braiding angles and the equivalent angle-ply laminates manufactured with carbon fibre/EPON 9504 resin prepregs. Copied from [65] [93].

Pseudo-ductile tensile response consisting an intermediate unstable plateau and a strain-hardening stages was achieved in a 4-ply interlayer laminate, made of non-hybrid triaxial-braided yarns/epoxy prepregs, as shown in Figure 2.31 (a) [94] [95]. The layup of the triaxial braids in a layer is represented as [0°/±θ], with 0° parallel to the x direction, as shown in Figure 2.31 (b) to (d), where the red and blue yarns are in the x and 1F directions, respectively. The variation in different directional tensile response is driven by different damage mechanisms. Non-linearity without plateau or strain-hardening was observed in the x and y loading directions. The tensile responses of laminates with triaxial braiding angles of [0°/±30°], [0°/±45°] and [0°/±60°], loaded in the 1F direction, are shown in Figure 2.32.



(a) (b) (c) (d)

Figure 2.31 (a) 3D schematic of laminate made of triaxial-braided yarns (shown in red, blue and green) and the top views of the (b) [0°/±30°], (c) [0°/±45°] and (d) [0°/±60°] angle arrangements. Copied from [95] [94].

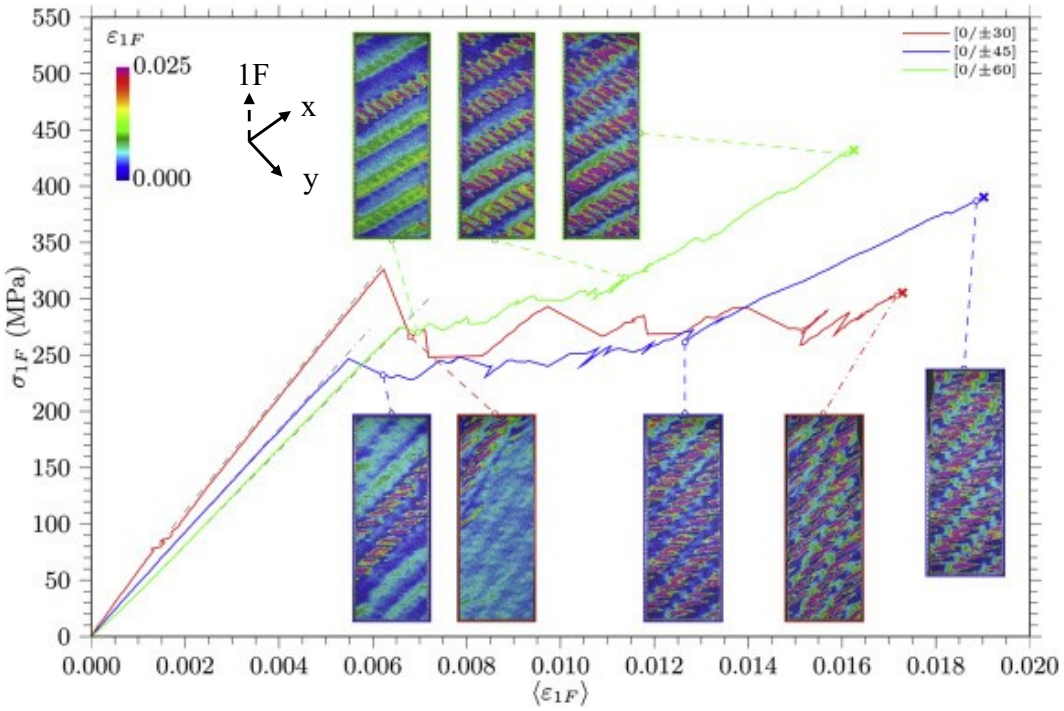


Figure 2.32 1F directional tensile response of straight-sided specimens made of [0°/±30°], [0°/±45°] and [0°/±60°] triaxially braided yarns reinforced prepregs and DIC strain maps at selected points. Copied from [94].

Mechanisms driving pseudo-ductility in the '1F' loading direction are summarized below:

- Initial almost-linear-elastic stage: the straightening of highly undulated loading directional (1F) braided yarns induces out-of-plane stress to the adjacent off-axis yarns, while the overlaying yarns is tolerant to the through-thickness stress and the intersecting yarn textile architecture arrests the extensive through-thickness matrix cracks (mostly at resin pockets). A lower off-axis yarn angle gives higher initial stiffness.

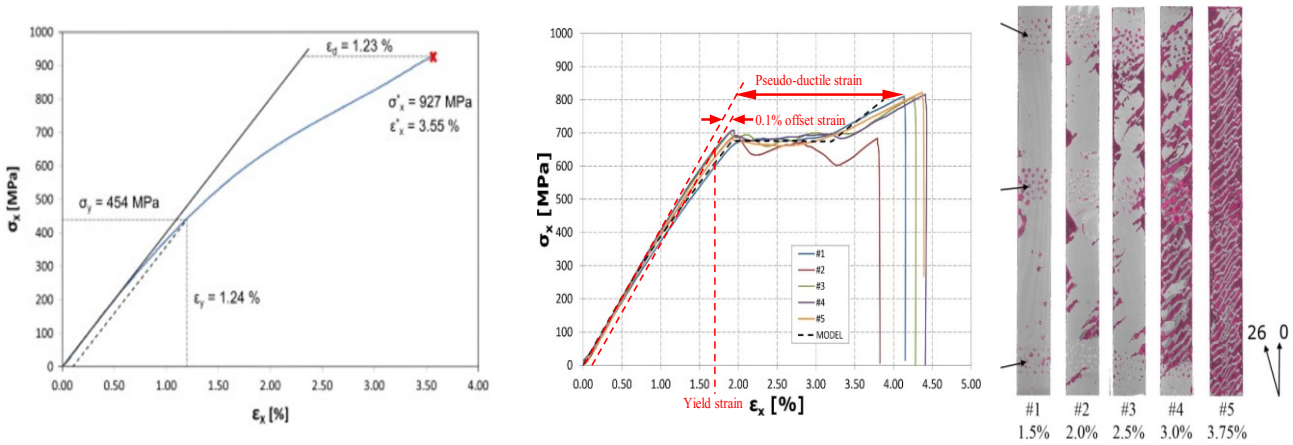
- Load-drops appeared after the onset of non-linearity: Once the adjacent overlying yarns are not strong enough to support the out-of-plane stress (i.e. matrix cracking saturation), sudden delamination in the adjacent interface along a subsurface x directional yarn appears and extends across specimen width. The lack of support from the adjacent yarns results in progressive off-axis yarn pull-out and matrix cracking in adjacent yarns, and eventually multiple load drops. The progressive crack deflection granted by this braiding architecture, makes the interlayer braided laminates more energy-absorbing.

- Strain-hardening stage: The gradual rotation of the residual off-axis yarns toward the loading direction, as well as the residual straightened 1F directional continuous fibres provide the residual load-bearing ability, i.e. the strain-hardening behaviour in the tensile response.

Delamination developed throughout the loading direction at the failure point. Ultimate failure occurs when the tensile strain is close to the strain-to-failure of the yarns in the loading (i.e. 1F) direction.

2.2.3.3 **Angle-ply laminates**

Considerable non-linearity before failure (see Figure 2.33 (a)) was observed in the studies of $[\pm\theta^{\circ}\text{n}]$s laminates [7], [8]. The reorientation of the angled plies (with carefully selected angles) towards the 0° loading direction, permitted by matrix plasticity, promotes necking in the specimens and non-linearity in the tensile stress-strain response. The constituent thin-ply carbon material effectively delayed the advent of premature damages, such as matrix cracking and delamination, before the ultimate failure. The rotation and straightening of the angled plies in the loading direction extracts the hidden length embedded in the angled pies and provides a considerable stiffening in the tensile stress-strain response. $[\pm 26^{\circ}{}_{5}]$s layup achieved 1.2% pseudo-ductile strain. A laminate with modified layup of thin-ply $[\pm 26^{\circ}{}_{5}/0^{\circ}]$s [9][10] consisting high modulus 0° plies placed among the standard modulus $\pm 26^{\circ}$ plies, achieved a pseudo-ductile response with a superior strain-hardening (see Figure 2.33). Dispersed fragmentation in the 0° plies and local delamination between the $-26^{\circ}/0^{\circ}$ interfaces were identified before rotation of the $\pm 26^{\circ}$ fibres towards the loading direction. The synergistic gradual fragmentation and fibre rotation effects contribute to higher initial stiffness and overall failure and pseudo-ductile strains than each individual 'angle-ply' or 'gradual fragmentation' strategy. In this case, the blocked $[\pm 26^{\circ}{}_{5}]$ plies and the middle 0° plies can be regarded as the UD HFS and LFS materials in the continuous UD interlayer hybrids, presented in Section 2.2.2.1.1. Layup combining angle-plies with 0° plies were later investigated in other loading conditions, and confirmed these layups are notch insensitive as the fragmentation and local delamination can effectively redistribute the stress-concentration near an open-hole [11]. In addition, the $[\pm\theta^{\circ}\text{n}]$s and $[\pm 26^{\circ}{}_{5}/0^{\circ}]$s layups were confirmed to be 'ductile', rather than 'pseudo-ductile' as excellent stiffness was retained, despite a small amount of 0°fragmentation in the $[\pm 26^{\circ}{}_{5}/0^{\circ}]$s layup, under quasi-static cyclic loading [96]**.** In addition, both FE and experimental results confirmed that thin ply angle-ply $[\pm\theta^{\circ}{}_{m}/0^{\circ}{}_{n}]$s laminates with larger pseudo-ductile strain to 'yield' strain ratios, as defined in Figure 2.33 (b), tend to be less sensitive to notches under tension [11].



(a) (b)

Figure 2.33 Tensile stress-strain curves of thin-ply angle-ply (a) [±25°5]s laminate and (b) pseudo-ductile [±26°5/0°]s laminates with X-ray CT scanning diagrams at increasing strain levels showing progressively accumulated 0° fragmentation. Adapted from [8][11].

2.2.3.4 **Sandwiched structure with wavy-plies and foams**

An out-of-plane wavy skin sandwiched structure composed of wavy UD carbon/epoxy plies enclosing crushable foam cores (see Figure 2.34) is another promising approach to significantly improve the failure strain [6]. The failure process and the associated mechanisms are illustrated in Figure 2.35. Extra extension is provided via crushing the foam cores, which then permit the out-of-plane reorientation/straightening of skin composite under tensile loading. The deformation of the foam core absorbs energy during crushing. A trade-off between the tensile strength and strain-to-failure was reported for various geometric parameters and constituent material properties, particularly those of the foam core material. Balanced strength and failure strain can be achieved by using intermediate wave aspect-ratios (i.e. axial length/amplitude of the sinusoidal wavy unit), thin skins and short bridging regions.

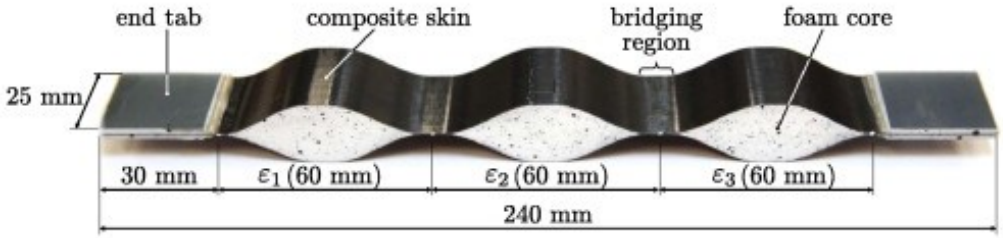


Figure 2.34 Schematics of out-of-plane wavy sandwiched structure composed of three unit cells. Copied from [6].

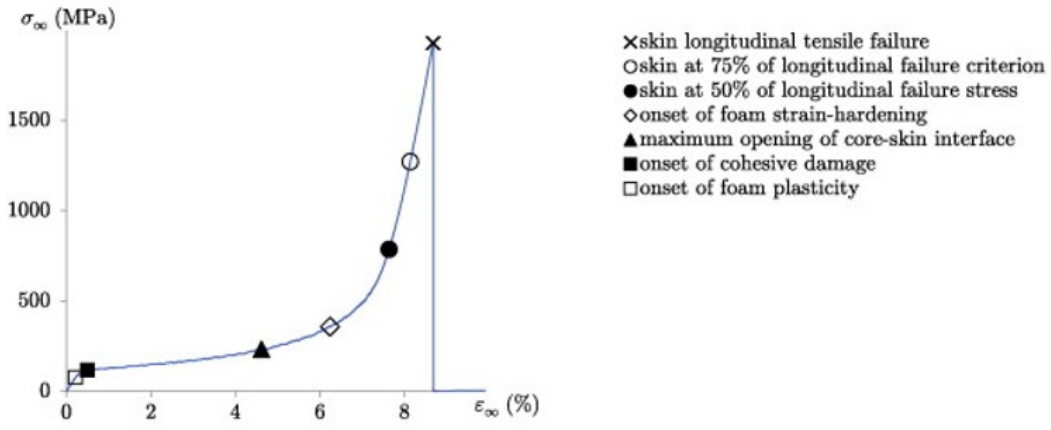


Figure 2.35 Failure process of successful (without premature delamination) wavy-ply sandwich structure. Copied from [6].

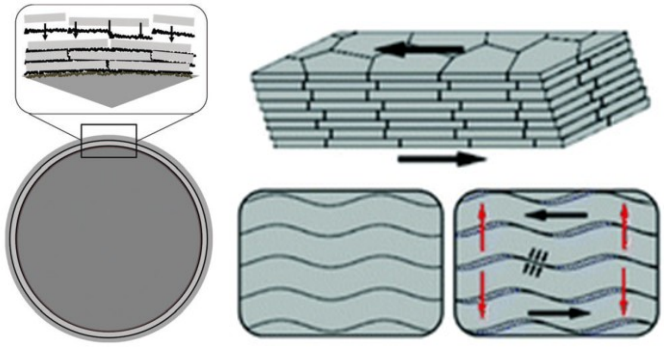
2.2.4 Interphase, interface and interlock techniques

The other category of strategies to generate overall strain enhancement is to engineer the nano-scaled fibre-matrix interphase (Section 2.2.4.1), or the micro-scaled interface between adjacent layers in interlayer laminates (Section 2.2.4.2), or further scaling up to the macro-level, relatively 'slidable' boundaries between interlocked composite components (Section 2.2.4.3). The fundamental theory behind these strategies is to generate the mechanisms, such as damage diffusion, crack deflection, and most importantly amplifies plastic deformation of the compliant matrix or fibre pull-out or mechanical friction.

2.2.4.1 **Interphase engineering: nacre-mimic fibre coating technique**

One fibre-matrix interphase modification consists of a coherent 'brick-and-mortar', nacre-mimic nanometre-scale coating, which was deposited around carbon fibre filaments (see Figure 2.36) [97]–[99] The synergistic crack deflection among staggered nanoplatelets and nanoplatelet sliding spread the stress concentration induced by propagating cracks to a larger region. In addition, the curved nanoplatelets surface profile gradually arrest the crack propagation, so as to delay the formation of a critical size damage cluster [99]. Compared with higher length scaled 'brick-and-mortar' architectures, the nanostructured platelets lead to denser process zone, therefore improves the fibre-matrix interphase stress transfer ability. These mechanisms promote progressively developed diffuse carbon fibre fragmentation (as shown in Figure 2.37) and sliding of the fragmented fibre segments in the matrix, i.e.

substantial plastic deformation of the interphase, leading to 30% and 15% improvement in the tensile strain-to-failure and tensile strength of the impregnated composites containing coated fibre tows, compared with those containing uncoated sized fibres [99]. The coated nacre-inspired interphase makes the interface neither too strong (to avoid brittle single fibre fracture) nor too weak (to inhibit unstable fibre-matrix debonding). The intermediate strength (or IFSS) nanostructured interphase promotes crack deflection in the nanostructured coatings, progressive slippage of fibres, which effectively redistribute the stress concentration promoted by the initial fragments along the fibres, so as to delay the formation of critical cluster of fibre breaks [99].



(a) (b)

Figure 2.36 Schematics of (a) cross-sectional of layers of nanostructured 'brick-and-mortar' coating on the circumference of a fibre with crack deflection among nanoplatelets and (b) shear effect between interlocked nanoplatelets. Copied from [98].

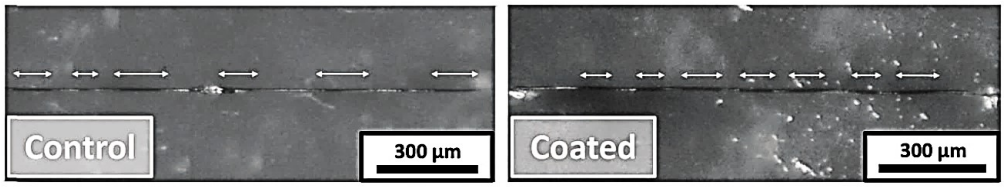


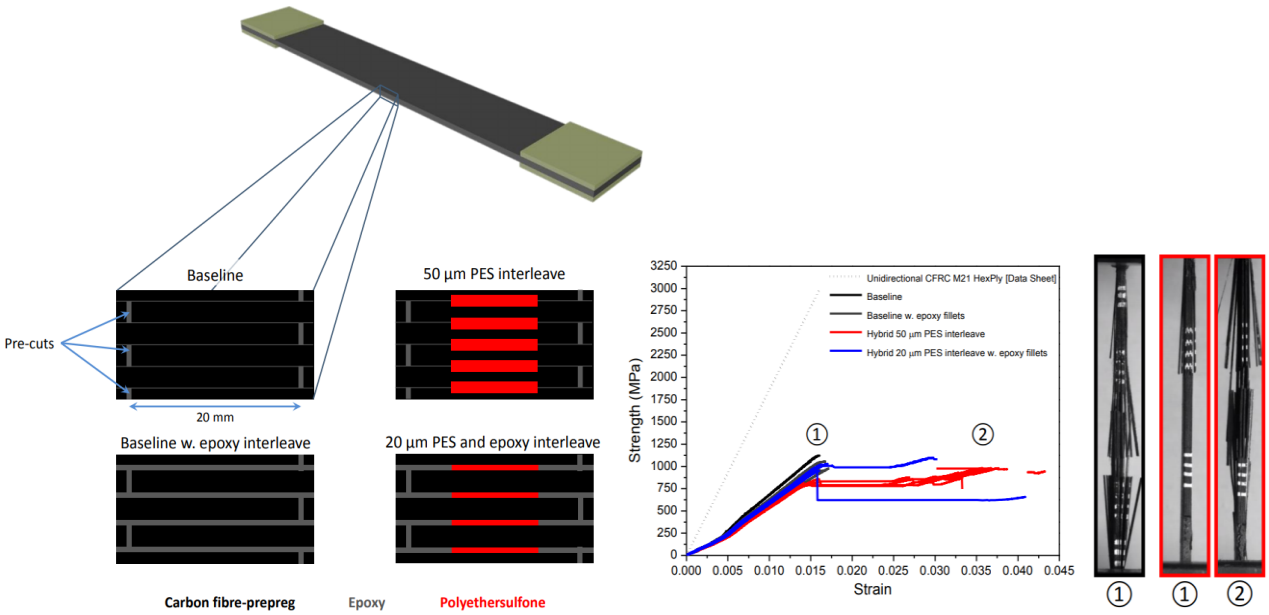
Figure 2.37 Fragmentation of the un-treated baseline (control) fibre (left) and more dispersed fragments in a nacre-inspired nanoplatelets coated fibre (right) in single fibre fragmentation test (white arrows represent the lengths of fragments). Copied from [98].

2.2.4.2 **Interface engineering: interleaving technique**

The 'interleaving' technique has demonstrated the ability to delay the catastrophic formation of a critical size cluster of broken fibres in continuous fibre composite laminates [100]. Interleaving is implemented by inserting tougher polymeric films, for example thermoplastic films with various geometries and properties, between adjacent prepregs during layup. The associated high plastic deformation ability of the interleaving films enables larger stress transfer zones to be formed at the crack tips (i.e. enhances

the redistribution of stress concentrated at the cracks), thereby isolating the sub-critical sized clusters of broken fibres, which suppress the spread of cracking to adjacent plies and delays ultimate failure.

Interleaving has also been used to improve the tensile strain of the prepreg-based 'brick-and-mortar' laminates, presented in Section 2.2.2.3.2. CFRP 'brick and mortar' specimens were produced with epoxy, thermoplastic PES and combined epoxy and PES interleaves in the middle of the platelet-overlap region between adjacent platelets [101], [102] (see Figure 2.38 (a)). The images captured at the stress peaks of the non-interleaved baseline and the specimens containing 50µm interleaving PES films, marked by '①' in Figure 2.38 (b) demonstrated that the thicker and tougher PES films in the middle of the platelet-overlapping region (see Figure 2.38 (a)) can prevent the interlaminar cracks from catastrophically propagating throughout the entire interface at the failure strength. Instead the PES film specimens have improved the strain-to-failure by creating gradual delamination and pull-out, as shown in Figure 2.38 (b). According to the experimental results shown in Figure 2.38 (b), the strain-to-failure of the interleaving laminates is at least twice that of the baseline laminates without PES and this is achieved without significantly compromising the initial stiffness and strength. In addition, the tensile response of the interleaved laminates containing thicker 50µm PES films (red lines) tend to be more repeatable compared to the laminates with the thinner 20µm combined epoxy and PES interleaves (blue lines), as shown in Figure 2.38 (b).

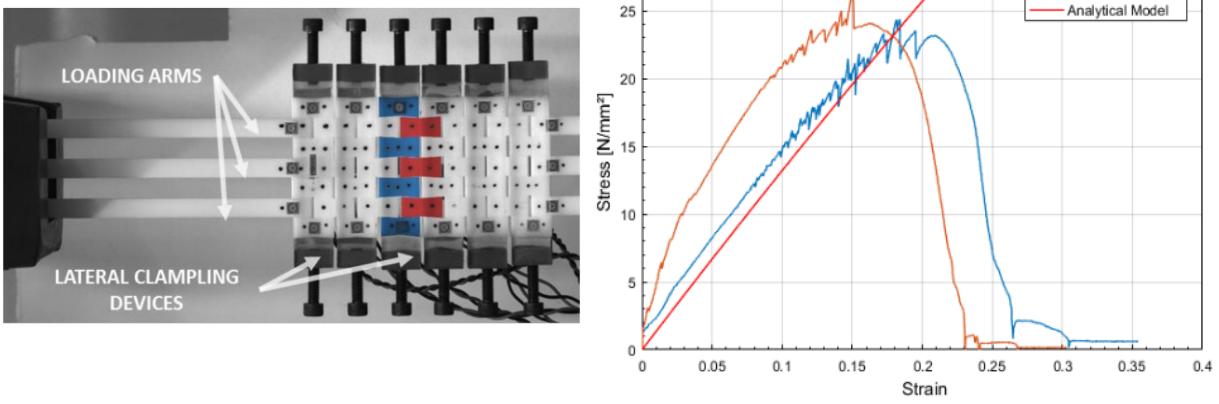


(a) (b)

Figure 2.38 (a) Schematic edge views of the 'brick-and-mortar' laminates constructed with long overlap length, with (or without) interleaving films of different material and thicknesses and (b) the corresponding tensile stress-strain response and the images of the baseline and lamiantes with 50µm thick interleaving films. Copied from [101] [102].

2.2.4.3 **Interlocked technique**

A significantly enhanced strain-to-failure can be achieved by harnessing the friction at the sliding boundaries between adjacent interlocked bow-tie and dog-bone shaped blocks (see Figure 2.39 (a)) [103]. The amount of sliding that can be achieved between the surfaces of adjacent CFRP blocks is dependent on the geometry and layup of the blocks. Tensile tests on the CFRP specimens have shown an ultimate strain which is more than 10 times higher than that of the UD composite (of approximate 1.9%) (see Figure 2.39 (b)).



(a) (b)

Figure 2.39 (a) Example 3D printed polymer interlocked bow-tie prototype with clamping devices designed for tensile testing and (b) tensile stress-strain curves of bow-tie shaped interlocking configurations made of CFRP under tension with and without preloading. Copied from [103].

2.3 Conclusions

This chapter has described the strategies that can achieve and tailor pseudo-ductility in composite materials. The strategies include composite hybridization and the employment of innovative composite architectures (ranging from nano- to macro-scales). The findings from these strategies are summarized below:

- Avoiding the formation of localized critical cluster size of broken fibres, which have relatively higher stiffness and lower strain-to-failure or sudden fibre-matrix debonding and delamination, accompanied with excessive energy dissipation, is key to prohibit brittle failure.

- To facilitate progressive initiation and development of non-critical sized damage at dispersed locations, it is essential that the stress process zones ahead of crack tips can effectively diffuse the stress concentration. The stress transfer capacity of the process zone can be influenced by the relative spacing and distribution of fibres (or plies) and the plastic deformation of the fibre-matrix interphase and the interface between adjacent plies. Less stress concentration in the neighbouring survived fibres (or plies), after the onset of initial damage, provides a more progressive failure process and potentially higher residual load-bearing capacity.

- For the reviewed pseudo-ductile cases containing continuous fibres, the continuous fibres in the loading direction commonly sustain high strength and determine the overall failure stress and strain. The stress concentration in continuous fibres, arose from the incipient internal damages, always results in a lower structural failure strain, compared to the critical strain-to-failure of the continuous fibres. On the contrary, for pseudo-ductile cases made of short fibre composites, higher strain-to-failure than that of the constituent fibres, promoted by matrix plastic deformation and fibre pull-out. However, this was always accompanied with low tensile strength.

- All the results show that to achieve pseudo-ductility, there is always a trade-off in other properties, such as initial stiffness, ultimate strength and density or additional complexity in the manufacture process.

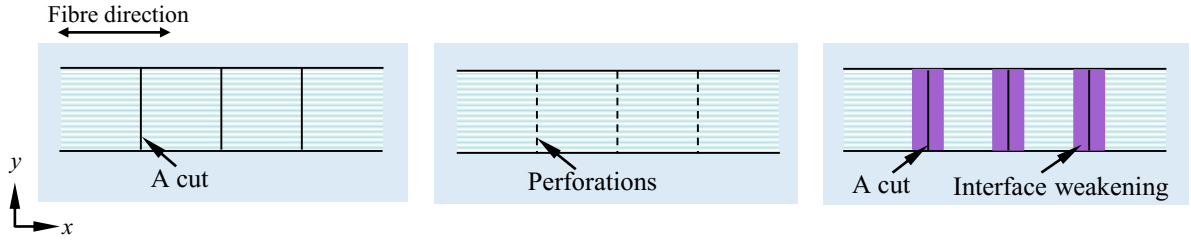
This thesis describes an exploitation of an alternative simple method of achieving pseudo-ductility which can be used in a single CFRP material (and therefore has no impact on the density) and which holds the potential of insignificant loss in the initial stiffness.

Chapter 3

Analytical modelling of UD laminates containing weakened plies and interfaces

3.1 Introduction

This chapter presents the analytical models developed to design the 'ply-weakened' and 'ply- and interface-weakened' UD laminates made of a single type of CFRP material. The 'ply weakening' is achieved by introducing 'continuous cuts' or 'periodic perforations' into selected plies of a laminate. Schematic diagrams of a 'cut' and a 'perforated' UD plies are shown in Figure 3.1 (a) and (b). The interface weakening is achieved by reducing the toughness of the interlaminar interface symmetrically located in the neighbourhood of each cut, as shown in Figure 3.1 (c).



(a) (b) (c)

Figure 3.1 Schematic diagrams of a ply containing (a) continuous cuts, (b) lines of periodic perforations and (c) interface weakening in the region of the continuous cuts that are transverse to the fibre direction.

This chapter is structured as follows: Section 3.2 presents the simplified fracture mechanics based analytical models, for the tensile performance of UD laminates containing 'ply cuts' and the combined 'ply cuts and interface weakening'. Section 3.3 presents the tensile performance of UD laminates containing ply perforations. The effect of ply cuts and perforations on the pseudo-ductile tensile performance, predicted using the simplified models is compared in Section 3.4. Refined analytical models for the cut and perforated ply laminates, considering the 'shear-lag effect' and a rigid-perfectly plastic matrix constitutive law, are presented in Section 3.5 and Section 3.6. The properties of the UD carbon fibre/epoxy prepregs used in this PhD project, and the effects of geometric factors, such as perforation length, distance between adjacent cuts, etc, on the tensile behaviour of cut- and perforated-ply laminates, evaluated using the refined models are presented in Section 3.7. The conclusions of the

potential to achieve pseudo-ductility in UD laminates, using the ply and interface weakening strategies, are drawn in Section 3.8.

3.2 Simplified analytical models for UD laminates containing continuous cuts and combined cuts and weakened interface

3.2.1 Simplified analytical model for UD laminates containing continuous cuts

This section presents a simple analytical model to predict the tensile response of a UD laminate containing continuous cuts in selected plies. Consider a laminate consisting a single or several repetitive sets of sub-laminates. Each sub-laminate consists a total number of n_T plies, with an even number of n_U continuous (i.e. pristine) plies evenly positioned above and below a block of $(n_T - n_U)$ plies, which contain cuts (see Figure 3.2). The cuts are designed to initiate stable delamination at the interfaces between the cut and the adjacent uncut plies. The cut plies contain periodic continuous cuts, that are transverse to the fibre direction and equally spaced in the fibre direction. The distance between adjacent transverse ply cuts, i.e. the length of the discontinuous platelets formed after introducing the cuts in the $(n_T - n_U)$ plies, is L, as displayed in Figure 3.3. The ply cuts in adjacent cut plies of the sub-laminate are aligned in the through-thickness direction. Note that the cuts in adjacent sub-laminates could be offset relative to each other but this has no impact on the prediction of the modelling described here. The longitudinal stress transfer between adjacent platelets is neglected. The model can be simplified by analysing the Representative Volume Element (RVE) of length, L, and unit width, highlighted in red in Figure 3.2. The RVE consists $\frac{n_U}{2}$ continuous plies, a platelet consisting $\frac{(n_T - n_U)}{2}$ discontinuous plies and the interlaminar matrix between the continuous block and the platelet.

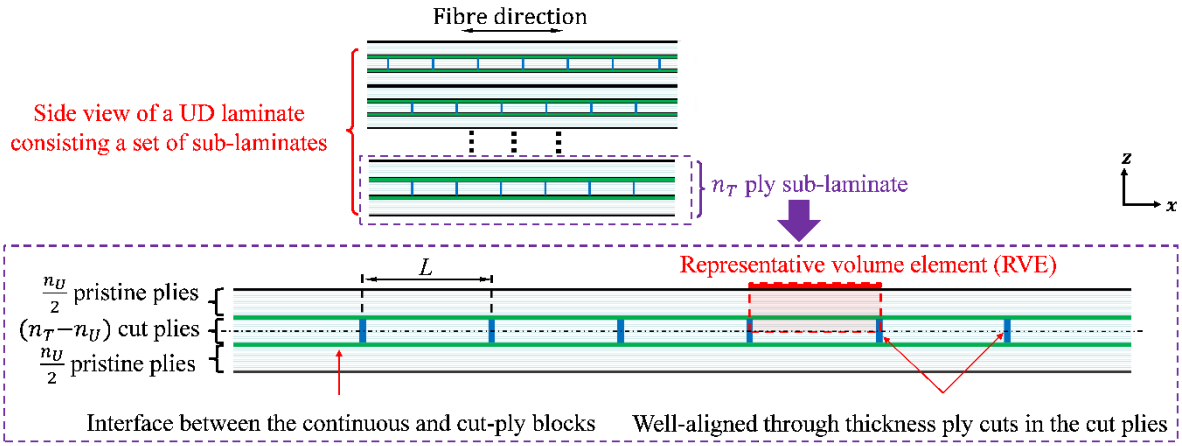


Figure 3.2 Schematic side views of a UD laminate with an enlarged sub-laminate showing the RVE of length, L.

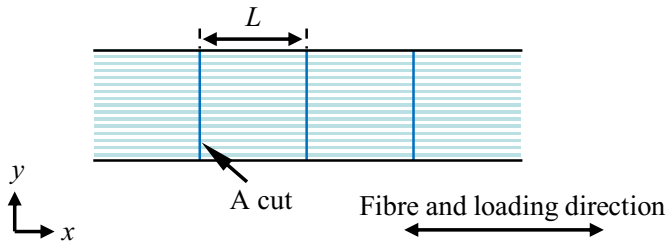


Figure 3.3 Schematic top view of a UD ply with periodic transverse continuous cuts.

Note that in the simplified models, the axial stress is assumed as uniform throughout the thickness of the RVE. The longitudinal evolution of the stress transfer zones, formed in the vicinity of cuts between the block of the pristine plies and the platelet formed by cuts, is neglected. It is assumed that there is no significant loss of stiffness due to the presence of cuts until the onset of delamination has occurred. Therefore, the stress-strain response is linear-elastic in the initial stage, as shown in Figure 3.4. It is shown later that for a uniform interlaminar fracture toughness, the stress required for the initiation and propagation of the delamination is constant and this results in the intermediate plateau in the schematic stress-strain response (see Figure 3.4). At the end of the plateau stage predicted by this simplified model, the cut plies are assumed to completely delaminate (i.e. separate) from the pristine plies, which continue to carry the load in the final linear-elastic stage.

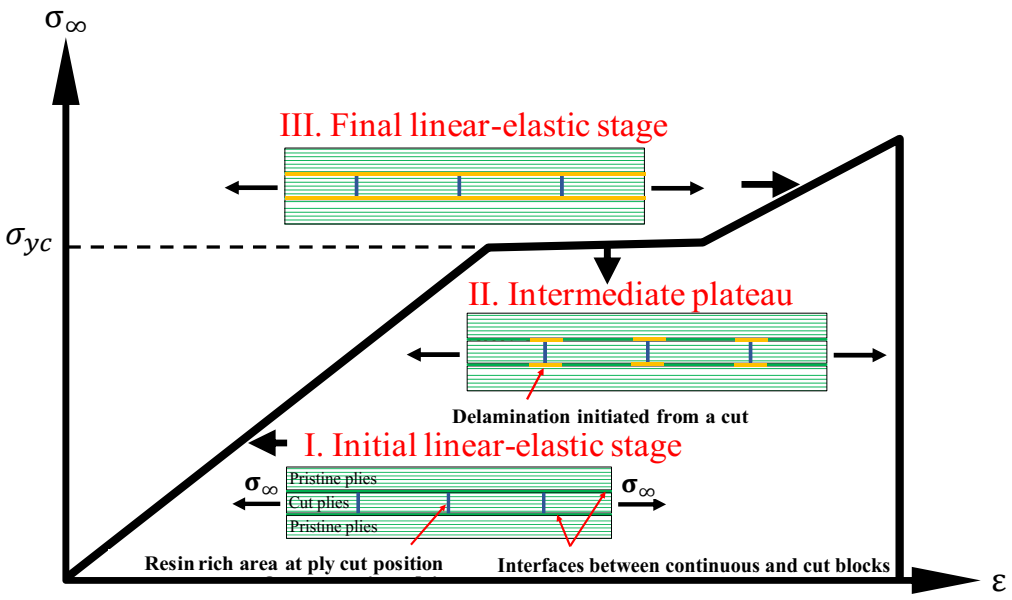


Figure 3.4 Schematic pseudo-ductile tensile stress-strain response and the damage evolution process shown on the side view of a UD laminate containing cuts in the central block of plies.

3.2.1.1 **Initial linear elastic stage**

It is assumed that the RVE is subjected to an average tensile stress, σ_∞. The evolution of tensile stress distribution in the block of continuous plies and the platelet (especially at the cut positions), with gradually increased σ_∞, in the simplified model, is shown in Figure 3.5 (a) to (c). As mentioned before, the model assumes that the axial stress is uniform through-the-thickness of the block of continuous plies and the platelet.

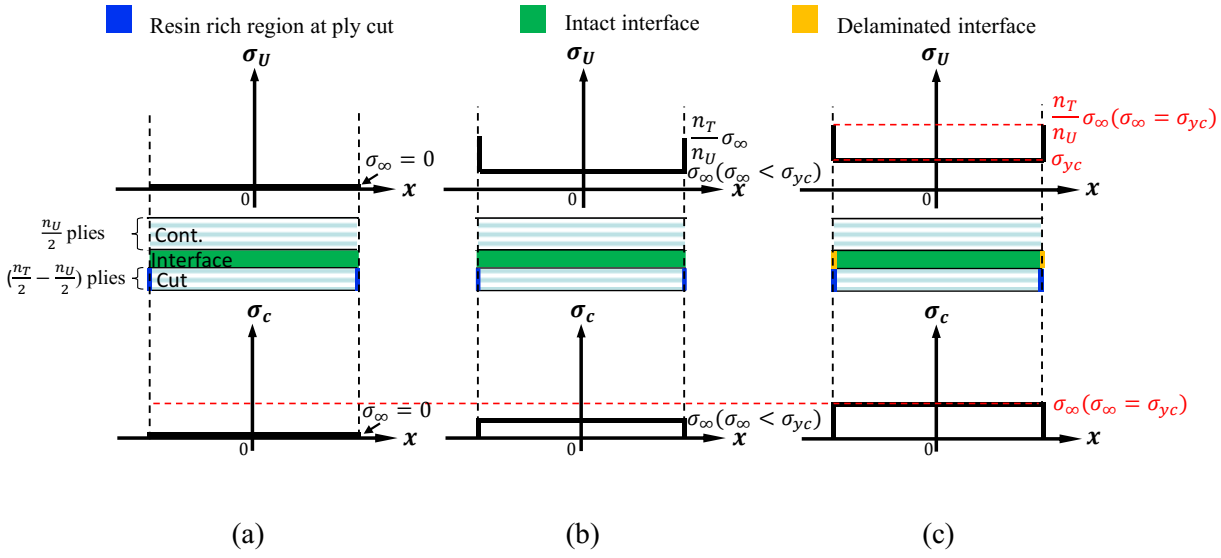


Figure 3.5 Schematics of the evolution of the axial tensile stress distribution in the continuous plies, σ_U, and the platelet, σ_c, at (a) the beginning, (b) the intermediate phase and (c) the end of the initial linear elastic stage, predicted by the simplified analytical model. (Note the interface area between the continuous block and the platelet is exaggerated to clearly show the different interlaminar zones).

In the simplified model, tensile stress is transferred from the platelet to the outer block of continuous plies at the cut positions or ends of a platelet by shearing of the interlaminar matrix, as the average tensile stress, σ_∞, gradually increases (see Figure 3.5 (b)). Delamination, shown as the yellow area in Figure 3.5 (c), is initiated at the cut positions once the average tensile stress, σ_∞, reaching the critical tensile stress, $\sigma_{\infty c}$ (or σ_{yc}), which is formulated in the subsequent Section 3.2.1.2. As mentioned before, in the simplified model, the loss of stiffness due to the fibre discontinuities and the consequent stress transfer between the blocks of continuous plies and the platelet at the cut positions, is neglected. Therefore the initial stage is assumed to be linear-elastic. The longitudinal strain, ε, corresponding to the increasing stress, σ_∞, prior to the intermediate plateau stage is given by Eq.3.1.

$$\varepsilon = \frac{\sigma_\infty}{E_0} \qquad 3.1$$

where, E_0 is the longitudinal Young's modulus of the pristine UD composite.

3.2.1.2 **Intermediate plateau stage**

According to Linear Elastic Fracture Mechanics (LEFM), once the strain energy release rate, G_{II}, reaches the mode II interlaminar fracture toughness, G_{IIc}, the interface between the platelet and the block of continuous plies simultaneously fracture at the two cut positions in the RVE. The delamination initiated from both ends of the interface is assumed to simultaneously propagate axially towards the mid-point of the RVE. The mode II strain energy release rate, G_{II}, is calculated basing on the LEFM-based methodology, proposed in [104] and is given by Eq. 3.2.

$$G_{II} = -\frac{1}{2}\left[\frac{{\sigma_\infty}^2 A_T}{2E_0} - \frac{\sigma_\infty^2 A_T^2}{2A_U E_0}\right] \tag{3.2}$$

where A_T and A_U are the overall cross-sectional area of the unit width RVE and the cross-sectional area of the continuous plies in the RVE. A_T and A_U are expressed as $n_T h$ and $n_U h$, respectively, where h is the ply thickness. Equating G_{II} and G_{IIc} and substituting the expressions for A_T and A_U into Eq. 3.2 gives the equation for the critical average stress, $\sigma_{\infty C}$, causing delamination initiation and growth.

$$\sigma_{\infty \mathrm{C}} = 2\sqrt{\frac{G_{IIC} E_0 n_U}{n_T h(n_T - n_U)}} \tag{3.3}$$

Eq. 3.3 does not consider the length of the propagating delamination and therefore provided G_{IIC} constant, $\sigma_{\infty C}$ is also constant for both initiation and propagation of the delamination. Eq. 3.4 must be satisfied to ensure the continuous plies to not fail in tension prior to delamination initiation.

$$\frac{n_T}{n_U}\sigma_{\infty \mathrm{C}} < \sigma_0 \tag{3.4}$$

Eq. 3.4 indicates that the delamination growth is neutrally stable in load control and therefore stable under displacement control. The predicted stress-strain response exhibits a plateau during the delamination growth stage and $\sigma_{\infty C}$ can be considered as the pseudo-yield stress, σ_{yc}, of this UD laminate containing ply cuts. Therefore, the condition for no tensile failure prior to delamination given by Eq. 3.4 can also be expressed as $\frac{n_T}{n_U}\sigma_{\mathrm{yc}} < \sigma_0$. Strain at the onset of delamination, referring to the first point of the intermediate plateau in the tensile stress-strain curve is calculated as $\frac{\sigma_{yc}}{E_0}$. The variation of tensile stress distributed in the block of continuous plies and the platelet, during the plateau stage, is displayed in Figure 3.6. Delamination initiated from the two ends of the RVE propagate into the pristine interlaminar region, when the average tensile stress reaches σ_{yc} and continues to grow, until encountering in the middle of the RVE. The peak stresses in the continuous plies and the platelet are $\frac{n_T}{n_U}\sigma_\infty$ and σ_∞, where the average tensile stress, σ_∞, is equivalent to σ_{yc}, as shown in Figure 3.6. The

average tensile strain increases gradually with a constant average tensile stress, during the plateau stage (see Figure 3.4).

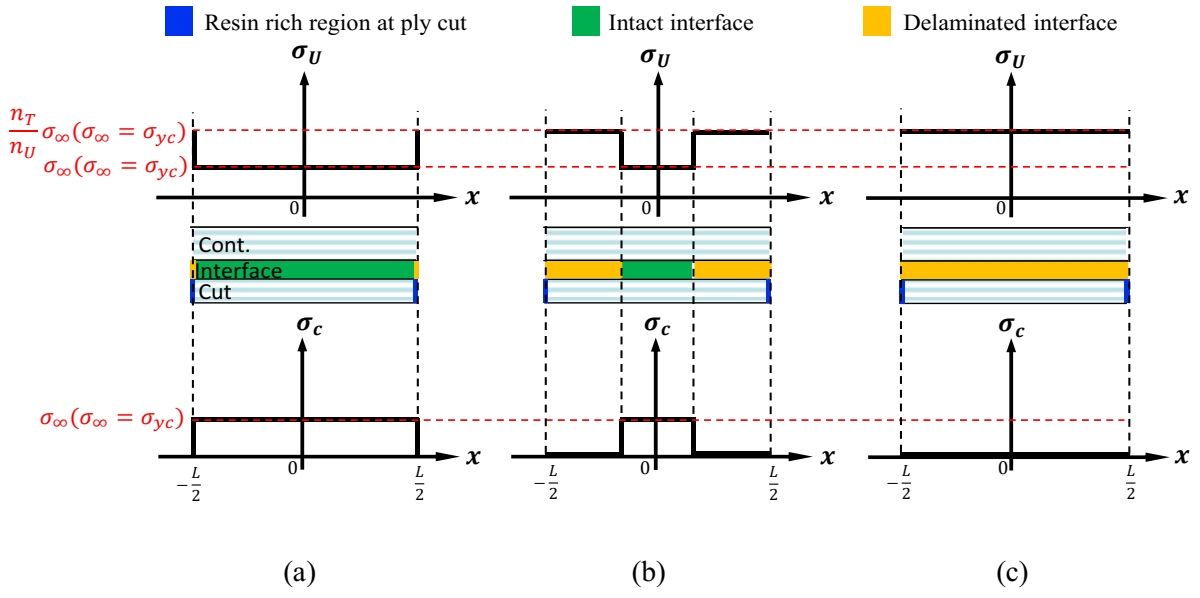


Figure 3.6 Schematic evolution of tensile stress distribution in the block of continuous plies and the platelet at (a) the beginning, (b) the intermediate phase and (c) the end of the plateau stage, where the remote average tensile stress, σ_∞, is constant during the entire plateau stage and is equivalent to the pseudo-yield stress, σ_{yc}, predicted by the simplified analytical model.

3.2.1.3 **Final linear-elastic stage**

Assuming the platelet completely delaminates from the continuous plies by the end of the plateau, and only the remaining continuous plies will continue to carry the load and therefore the stress-strain response will be linear elastic in this final stage. The effective Young's modulus of the RVE after the complete delamination, E_{fc}, is given as $\frac{n_U}{n_T}E_0$. The strain at the onset of the final linear-elastic stage, ε_{fc}, is therefore given by Eq. 3.5.

$$\varepsilon_{fc} = \frac{n_T \sigma_{yc}}{n_U E_0} \tag{3.5}$$

Ultimate failure occurs when $\sigma_\infty = \frac{n_U}{n_T}\sigma_0$, where σ_0 is the tensile strength of a pristine UD laminate. Given the effective Young's modulus as $\frac{n_U}{n_T}E_0$, the strain at failure is $\frac{\sigma_0}{E_0}$, i.e. the strain-to-failure of a pristine laminate.

The variation of tensile stress distributed in the platelet and the outer block of continuous plies with further increased average tensile stress, σ_∞, in the final strain-hardening stage is schematically shown in Figure 3.7.

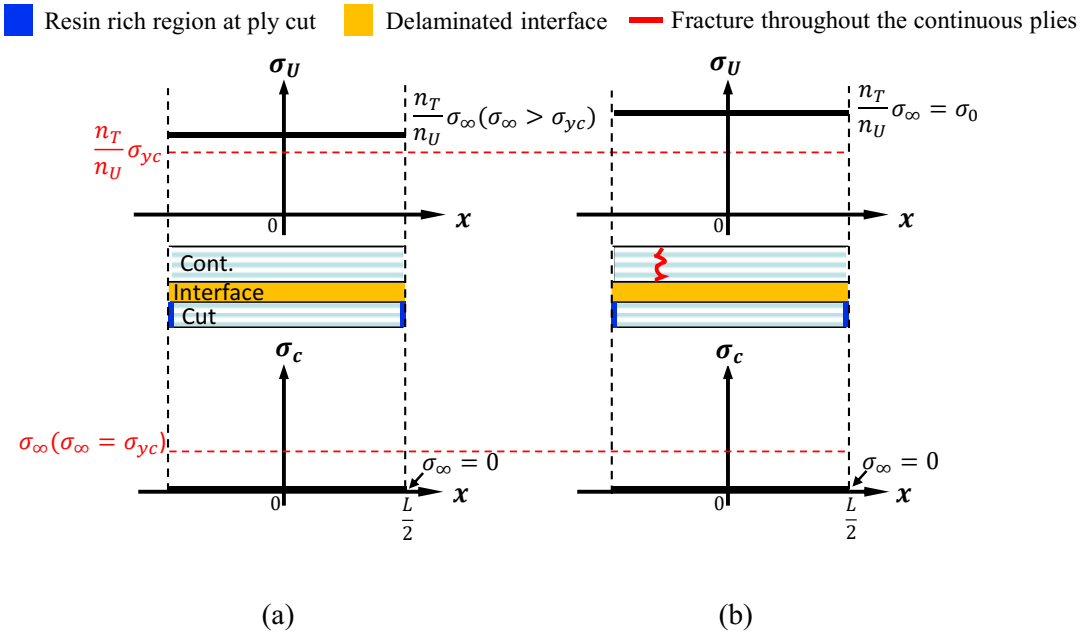


Figure 3.7 Evolution of axial stress distribution in the block of continuous plies and the platelet in the RVE, at (a) the beginning and (b) ultimate failure point of the final linear-elastic stage, predicted by the simplified analytical model.

The coordinates of the transition points and the moduli of the two linear-elastic stages are shown on the schematic stress-strain curve in Figure 3.8.

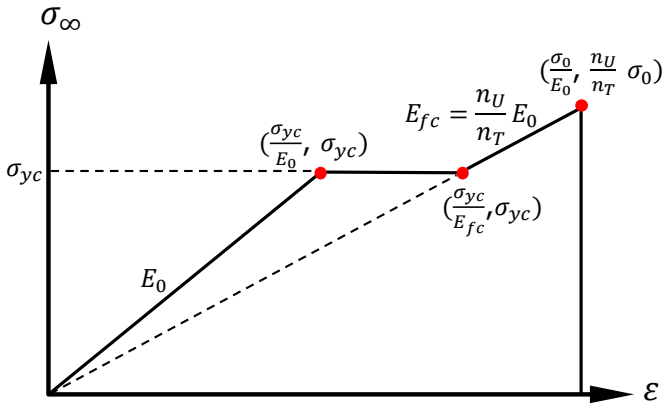


Figure 3.8 Tensile stress-strain response of a UD laminate containing continuous cuts in selected plies, predicted by the simplified analytical model.

3.2.2 Simplified analytical model for UD laminates containing continuous ply cuts and interface weakening

This section extends the simplified model for UD laminates with ply cuts to include partially weakened interfaces in the region of cuts, as shown in Figure 3.9. Other than this weakening of the interfaces, all the previous assumptions apply here. It should be noted that the interface weakening pattern is only introduced at the interfaces between the blocks of cut plies and the adjacent pristine or continuous plies. The interface weakened zone of length D is symmetrically placed along each cut to reduce the interlaminar fracture toughness. The fracture toughness of the weakened region is qG_{IIC}, where q is the interface weakening factor ($q \in [0,1]$). The lower toughness in the weakened zone means that delamination initiation and growth will occur at a lower value of remote stress σ_∞ than in the non-weakened interfaces.

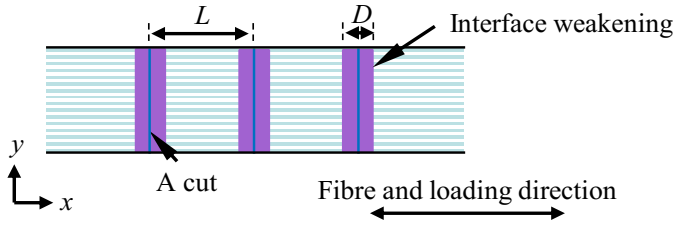


Figure 3.9 Schematic top view of a UD ply with weakened interface along the periodic cuts.

A schematic diagram of the expected tensile stress-strain response is shown in Figure 3.10. There are two plateaux, related to the weakened and pristine interlaminar regions. The two plateaux are connected by an intermediate linear-elastic stage. The stresses of the two plateaux are related to the specific interlaminar fracture toughness of the weakened and the pristine interlaminar regions, i.e. qG_{IIC} and G_{IIC}, respectively. At a critical average tensile stress, σ_{yq}, related to the reduced toughness of the weakened interface, which is equivalent to $\sqrt{q}\sigma_{yc}$ (see Figure 3.10), delamination is initiated from the cuts and propagates along the weakened interface. At the end of the first plateau stage, the weakened region is completely delaminated. The load now needs to be increased further to cause delamination in the pristine interlaminar region and during this loading phase the RVE behaves in a linear-elastic manner with a reduced elastic modulus of E_m. Delamination continue to grow along the pristine interlaminar region, when the average tensile stress, σ_∞, reaches σ_{yc} (given by Eq. 3.3) and continues to grow along the pristine interface, until the entire platelet is completely delaminated from the pristine plies at the end of the second plateau. The second plateau is followed by a final linear-elastic stage, where the pristine uncut plies continue to carry the load until ultimate failure.

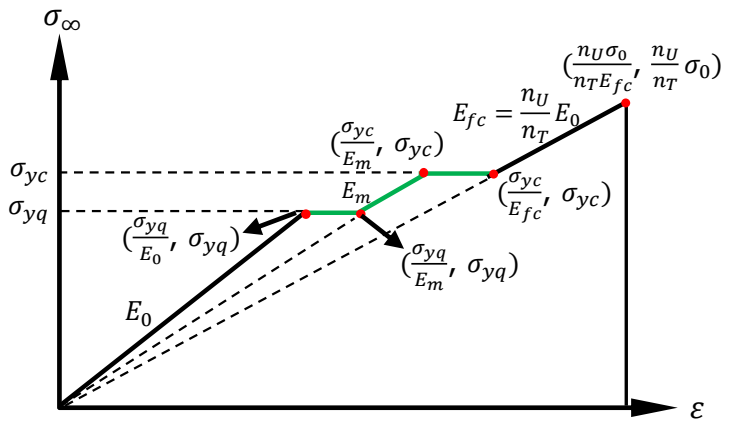


Figure 3.10 Schematic tensile stress-strain curve of a UD laminate containing partially weakened interface between the block of continuous plies and the platelet.

The coordinates of the highlighted points and moduli of the three linear-elastic stages, shown in the schematic stress-strain response (see Figure 3.10), are deduced using the same methodology presented in Section 3.2.1.

As before, the modulus of the initial linear-elastic stage is taken as E_0. The expression of stress σ_{yq}, related to the onset and propagation of delamination along the weakened interlaminar regions in the RVE, can be determined from Eq. 3.3 by replacing G_{IIC} with qG_{IIC}. It can be seen that the σ_{yq} (see Eq. 3.6) is $\sqrt{q}$ times the stress for the second plateau, σ_{yc} (see Eq.3.3).

$$\sigma_{yq} = 2\sqrt{\frac{qG_{IIC}E_0 n_U}{n_T h(n_T - n_U)}} = \sqrt{q}\sigma_{yc} \qquad 3.6$$

The strain at the onset of the first plateau stage is $\frac{\sigma_{yq}}{E_0}$. To calculate the strain at the end of the first plateau, where the weakened interlaminar regions are completely separated from the pristine plies, the effective Young's modulus of the intermediate linear-elastic stage (see Figure 3.10), E_m, is required. E_m is related to the overall volume fraction of the outer continuous plies and the residual un-delaminated part of the platelet, as shown in Eq. 3.7.

$$E_m = \frac{n_U L + (L - D)(n_T - n_U)}{n_T L} E_0 \qquad 3.7$$

Thus, the strains at the beginning and end points of the intermediate linear-elastic stage are $\frac{\sigma_{yq}}{E_m}$ and $\frac{\sigma_{yc}}{E_m}$, respectively. Assuming the platelet is completely delaminated from the pristine plies at the end of the second plateau stage, the modulus of the final linear-elastic stage, E_{fc}, is given as $\frac{n_U}{n_T} E_0$, as before. Thus,

strain of the beginning point of the final linear-elastic stage is calculated as $\frac{\sigma_{yc}}{E_{fc}}$. The pristine plies fracture once the average tensile stress, σ_∞, reaches $\frac{n_U}{n_T}\sigma_0$, the corresponding overall strain-to-failure is equivalent to $\frac{\sigma_0}{E_0}$.

3.3 Simplified analytical model for UD laminates containing ply perforations

As described at the beginning of this chapter, the other way to implement 'ply weakening' is to introduce 'perforations'. Ply cuts can be regarded as a special 'perforation' profile, where there is no gap between adjacent transverse perforations. In this section, the simplified analytical modelling method is used to predict the tensile performance of UD laminates containing periodic perforations in selected plies.

A schematic side view of a UD n_T-ply laminate is shown in Figure 3.11 (a). The perforations are introduced in the central $(n_T - n_U)$ plies. Perforations in adjacent perforated plies are perfectly aligned in the through-thickness direction. The perforations are perpendicular to the fibres as shown in the schematic top view of a perforated ply (see Figure 3.11 (b)). The length of the perforation is *P*, as shown in the top view. The longitudinal distance between adjacent lines of perforations is *L*. This arrangement makes the perforations periodically spaced in both axial and transverse directions and leaves bundles of completely continuous fibres in the axial direction of the perforated plies, as shown in Figure 3.11 (b). This extra proportion of continuous fibres in the central $(n_T - n_U)$ perforated plies means practically higher initial stiffness than that of the laminates containing continuous cuts.

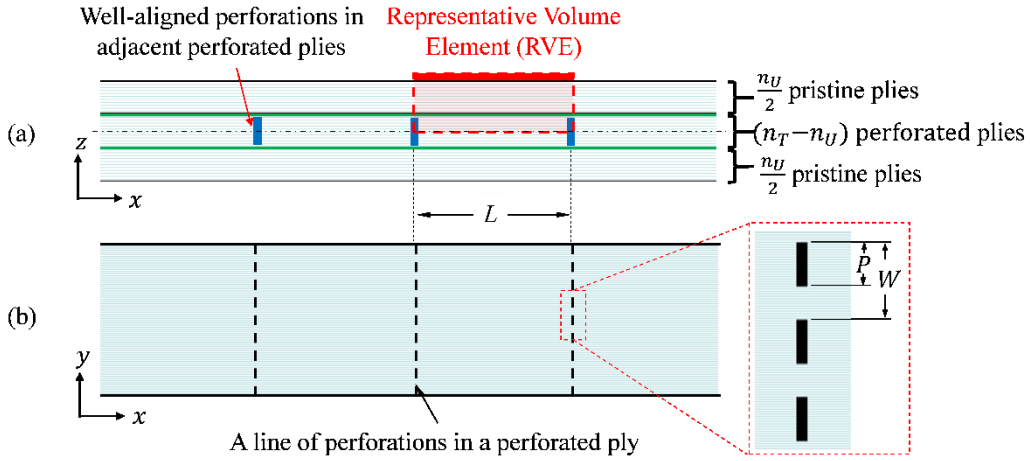


Figure 3.11 Schematic (a) side view of a n_T-ply UD laminate containing perforations in the central $(n_T - n_U)$ plies and (b) the top view of a perforated ply containing three lines of periodic perforations.

It is important to notice that localized stress concentration is induced at the ends of each perforation, which may influence the failure process. Two types of failure processes may occur, which are briefly described and schematically demonstrated on the cross-sectional view of a UD perforated laminate, as shown in Figure 3.12.

- Perforations grow transversely to form a continuous cut:

High stress concentration at the ends of each perforation could potentially trigger transversely propagating cracks, which eventually join up to form a continuous cut across the entire ply, as shown in the case (a) in Figure 3.12. The following behaviour is like the 'cut-ply' case described in Section 3.2.1.2, where delamination occurs at the interfaces between the blocks of continuous and cut plies, once the average tensile stress reaching the critical value.

- Debonding around the perimeters of the perforated fibre bundles propagates longitudinally:

Transverse propagation of cracks at the ends of perforations does not occur and instead debonding of the perforated fibre bundles occurs and propagates in the fibre direction, as shown in the case (b) in Figure 3.12.

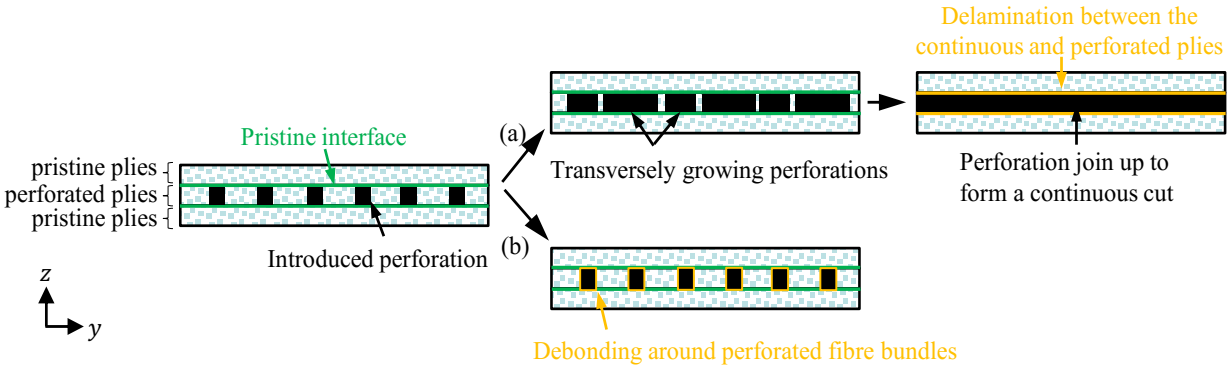
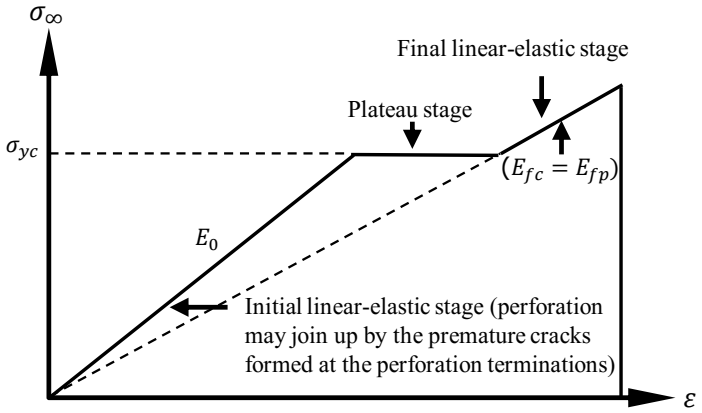
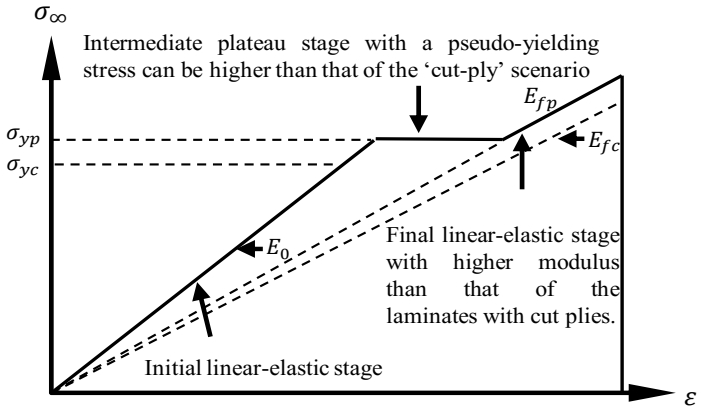


Figure 3.12 Schematic cross-sectional views of a perforated laminate (fibres pointing out of the paper) with the failure processes of (a) perforations grow transversely to form a continuous cut, before the onset of delamination between the blocks of the continuous and the perforated plies and (b) perforations induced debonding at the perimeters of the perforated fibre bundles and propagates in the fibre direction.

The schematic tensile stress-strain responses for the two types of failure processes are presented in Figure 3.13. Similar to the 'cut-ply' case, shown in Section 3.2.1, the effect of ply weakening, i.e. perforations in this case, on the initial modulus of the UD laminate, is neglected and the Young's modulus of initial linear-elastic stage is E_0, as shown in Figure 3.13 (a) and (b).



(a)



(b)

Figure 3.13 Schematic tensile stress-strain curves (plotted on the same length scale) of the two potential types of failure processes for UD laminates containing perforations

For failure process case (a), in which the perforations grow transversely to form a continuous cut, as shown in Figure 3.12 (a), the joined-up perforations result in the formation of platelets in the perforated plies. The following predicted tensile behaviour is identical to that of the 'cut-ply' laminate, shown in Section 3.2.1.2. Delamination is initiated from the continuous cracks and propagates along the interfaces between the blocks of the perforated and the continuous plies, towards the mid-point of the platelet. The stress for the onset and propagation of delamination, i.e. the pseudo-yield stress, can be calculated using Eq. 3.3, used for the 'cut-ply' laminates (see Figure 3.13 (a)). As before, the perforated plies are assumed to be completely delaminated from the outer continuous plies at the end of the intermediate plateau stage. In the final linear-elastic stage, the outer continuous plies continue to carry

the load until ultimate fracture. This means the modulus of the final linear-elastic stage, E_{fp}, is equivalent to that of the 'cut-ply' laminates, E_{fc} (see Figure 3.13 (a)).

A higher pseudo-yield stress than that of the 'cut-ply' case can be achieved (see Figure 3.13 (b)), when the transverse propagation of cracks induced by the perforations does not occur, instead, debonding of the perforated bundles propagating axially along the interfaces above and below the perforated bundles and between the adjacent perforated and unperforated bundles occurs. The debonding results in a significant loss of stiffness and a plateau in the stress-strain response. At the end of the plateau, the perforated bundles are completely debonded from the continuous fibres and the load is only carried by the continuous part in the final linear-elastic stage. A lower proportion of perforated fibres results in a stiffer final linear-elastic stage and a higher ultimate tensile strength.

3.3.1 Simplified analytical model for UD perforated laminates that fractured by debonding of the perforated fibre bundles

A schematic diagram of the cross-section of a UD perforated laminate containing periodic perforations is shown in Figure 3.14. The fibre bundle debonding stress, σ_{yp}, is closely related to the geometry of the perforation profile.

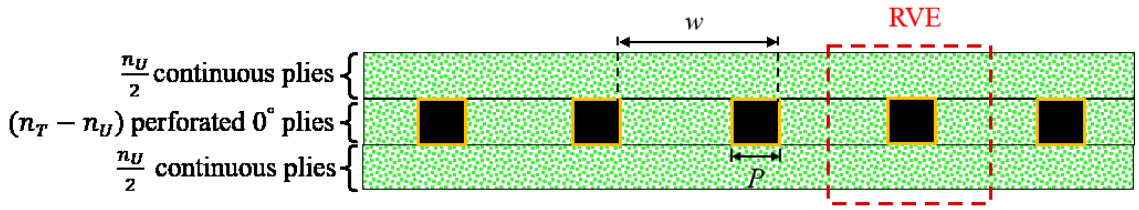


Figure 3.14 Schematic cross-section of a UD laminate containing periodic perforations in the central (n_T-n_U) perforated plies (fibre direction points out of the paper).

As shown in Figure 3.14, debonding (shown in yellow) appears at the interfaces surrounding the perforated fibre bundles (shown in black) in the central (n_T-n_U) plies. The overall tensile response can be predicted by analysing the RVE, highlighted in Figure 3.14. The overall width of the RVE is *w*. The overall perimeter of the debond interfaces around the perforated fibre bundle in the RVE is $2(P + n_T h - n_U h)$. The overall cross-sectional areas of the RVE and of the unperforated region in the RVE are $n_T wh$ and $n_T wh - (n_T - n_U)Ph$, respectively. Therefore, the pseudo-yield stress, σ_{yp}, for the onset and propagation of fibre bundle debonding can be determined using the energy-based approach, used in [104] and is expressed in Eq. 3.8.

$$\sigma_{yp} = 2\sqrt{\frac{G_{IIc}E_0[P + h(n_T - n_U)][n_T w - P(n_T - n_U)]}{wPn_T h(n_T - n_U)}} \quad 3.8$$

Note that here $\sigma_{yp} < \frac{n_T w - P(n_T - n_U)}{n_T w}\sigma_0$ is essential to ensure the plateau can be observed prior to the tensile failure of the continuous unperforated part in the laminate. Hence, the coordinate of the yield point is given as $(\frac{\sigma_{yp}}{E_0}, \sigma_{yp})$, as shown in Figure 3.15. The perforated fibre bundles are assumed to be completely debonded from the remaining continuous fibres, at the end of the plateau. In the final linear-elastic stage, the tensile stress is carried by the outer continuous plies, as well as the remaining unperforated continuous fibre bundles in the perforated plies. The effective modulus of the final linear-elastic stage, E_{fp}, is therefore expressed in Eq. 3.9.

$$E_{fp} = \frac{n_T w - (n_T - n_U)P}{n_T w} E_0 \quad 3.9$$

The strain at the transition point between the plateau and final strain-hardening stages is therefore expressed as $\frac{\sigma_{yp}}{E_{fp}}$. Neglecting the excess stress in the pristine plies induced by the debonding process, the tensile strength is proportional to the overall volume fraction of the continuous fibres in the UD laminate, i.e. $\frac{n_T w - P(n_T - n_U)}{n_T w}\sigma_0$. Given the effective Young's modulus shown in Eq. 3.9, the failure strain is expressed as $\frac{\sigma_0}{E_0}$, i.e. equivalent to the failure strain of the pristine laminate, as expected. Moreover, comparison between Eq. 3.3 and Eq. 3.8 confirms that the pseudo-yield stress always becomes greater once the continuous cuts are replaced with the same number of lines of periodic perforations.

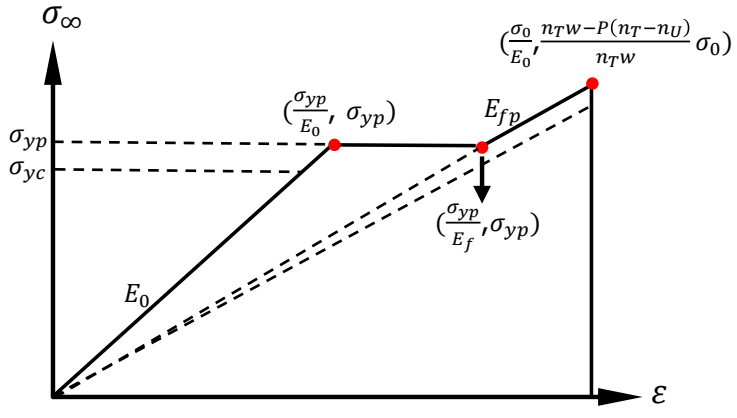


Figure 3.15 Schematc tensile stress-strain response and the coordinates of key points for a UD perforated pseudo-ductile laminate that failed by debonding of the perforated fibre bundles.

3.4 Comparison of the tensile performance of UD laminates containing cuts, cuts and interface weakening and perforations, predicted by the simplified analytical models

According to Figure 3.8 and Figure 3.10, the stress for the onset of delamination in the UD laminates containing only ply cuts is higher than that of the same laminate containing additional partially weakened interfaces. This is expected since the weakened interlaminar region has a lower mode II interlaminar fracture toughness. The partially weakened interface promotes two plateaux in the tensile stress-strain response, i.e. a more progressive failure process than in the completely pristine interface case. However preliminary experimental trials showed that it was difficult to accurately control the area of weakened interface and the interlaminar toughness weakening factor, q, in uncured prepreg materials and so the interface weakening method was not pursued.

The difference in the tensile performance of laminates containing continuous cuts and those containing periodic perforations, demonstrates the potential to adjust the tensile performance by adjusting the laminate geometry (i.e. the ply weakening geometry and the number of pristine and weakened plies). The pristine plies and the continuous part in the perforated plies result in a higher stiffness in the final linear-elastic stage than that for the same laminate containing continuous cuts. For laminates containing selected cut plies, the damage associated with pseudo-yielding is delamination between the continuous and cut plies. In laminates containing periodic perforations, if premature breakage of the continuous fibres at the perforation lines can be avoided, then pseudo-yielding occurs due to debonding around the perforated fibre bundles. The onset and propagation of damage during the yielding phase for both types of ply weakened (i.e. cut and perforated) laminates are related to the mode II fracture toughness of the material. It has been confirmed that, the yield stress for a pseudo-ductile laminate containing periodic perforations in selected plies is always higher than the yield stress for the same laminate containing continuous cuts. In addition, the tailorable geometry of the perforation profile means the 'ply perforation' strategy provides wider design space in comparison with the 'cut-ply' strategy.

It is noted that the simplified analytical models neglected the initial stiffness reduction due to the presence of any ply discontinuities. To more comprehensively understand the damage evolution in the UD laminates containing cut or perforated plies, the models are refined by considering the 'shear-lag' effect between the continuous and discontinuous blocks of plies, using a rigid perfectly-plastic interlaminar matrix shear constitutive law, as described in the following section.

3.5 Refined analytical model for the UD laminates containing continuous cuts

In the simplified analytical model, the evolution of the stress transfer zone is neglected and this results in the linear-elastic initial and final stages, as shown in Figure 3.16 (a). In the refined analytical model, the 'shear-lag' effect in the stress transfer zones between the block of continuous plies and the platelet, is considered. The interlaminar matrix is assumed as rigid perfectly-plastic. The gradual development of the stress transfer zones results in a gradual reduction of the stiffness before and after the intermediate plateau, as indicated in Figure 3.16 (b). The initial stage of the stress-strain curve is no longer linear but for practical material properties, this is almost linear and so this stage is called the 'initial almost (or approximately)-linear' stage. The final stage is also non-linear and is termed the 'final strain-hardening' stage.

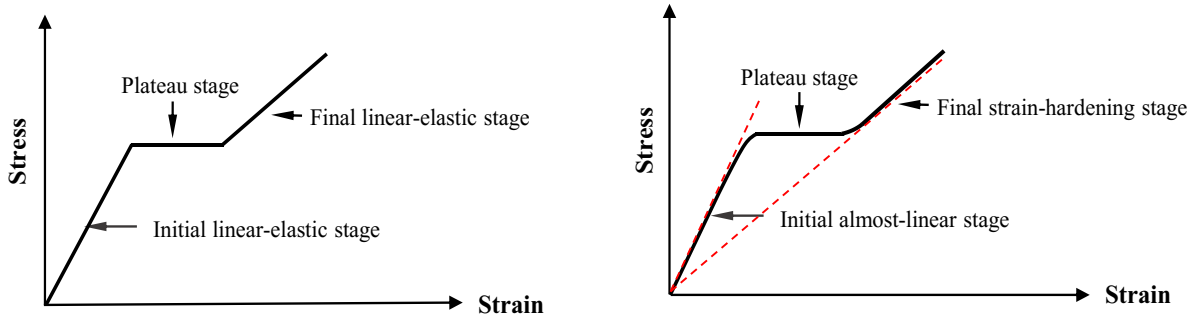
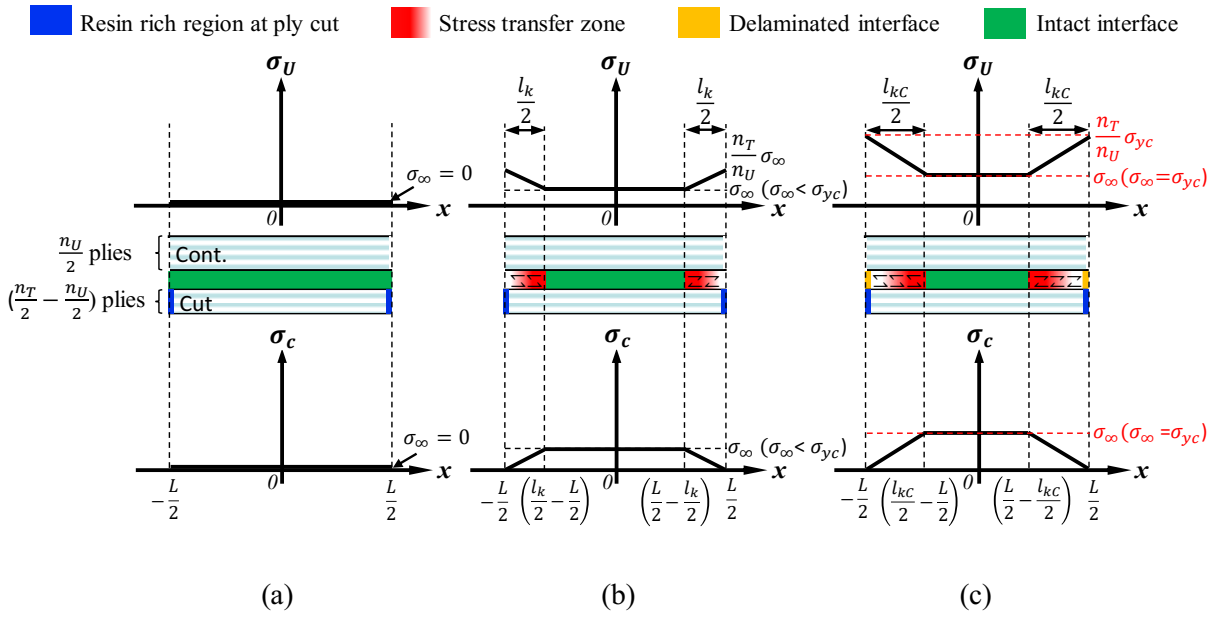


Figure 3.16 Schematic pseudo-ductile tensile stress-strain responses predicted by (a) the simplified and (b) the refined 'shear-lag' effect models.

3.5.1 Initial almost (or approximately)-linear stage

Any tensile stress transfer between the cut faces of axially adjacent platelets, shown in Figure 3.11, is neglected. The 'shear-lag' model is applied to the previously defined RVE (see Figure 3.2). Figure 3.17 shows the tensile stress distribution in the block of pristine plies and the platelet in the RVE and the evolution of the interlaminar matrix, during the initial approximately-linear stage, predicted by the refined model.

The rigid perfectly-plastic characteristic (schematically shown in Figure 3.18) of the matrix at the interface between the block of pristine plies and the platelet, provides a constant interlaminar shear stress (ILSS), τ_y, in the stress transfer zones, as shown in Figure 3.17 (b) and (c).



(a) (b) (c)

Figure 3.17 Schematic variation of tensile stress distribution in the block of continuous plies and the platelet in the RVE: (a) subjects no external stress, (b) formation and elongation of two stress transfer zones with length of $\frac{l_k}{2}$, initiated from the two ends of the platelet, under increasing average tensile stress, σ_∞ and (c) the stress transfer zones reaching the critical length, $\frac{l_{kC}}{2}$, once the average tensile stress, σ_∞, reaches the critical delamination stress, σ_{yc}.

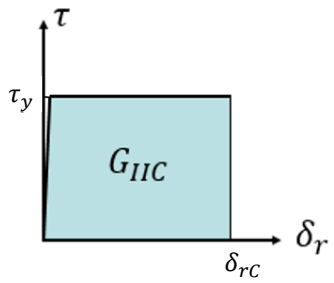


Figure 3.18 Schematic shear stress-shear displacement relation for rigid perfectly-plastic interlaminar matrix.

As the remote average stress, σ_∞, is increased from zero (see Figure 3.17 (a)), the stress transfer zones develop from the ends toward the centre of the platelet (see Figure 3.17 (b)). From equilibrium of the platelet in the stress transfer zone (shown in the enlarged diagram of Figure 3.19), the combined length of the stress transfer zones, l_k, in the platelet, is given by Eq. 3.10.

$$l_k = \frac{\sigma_\infty (n_T - n_U) h}{\tau_y} \qquad 3.10$$

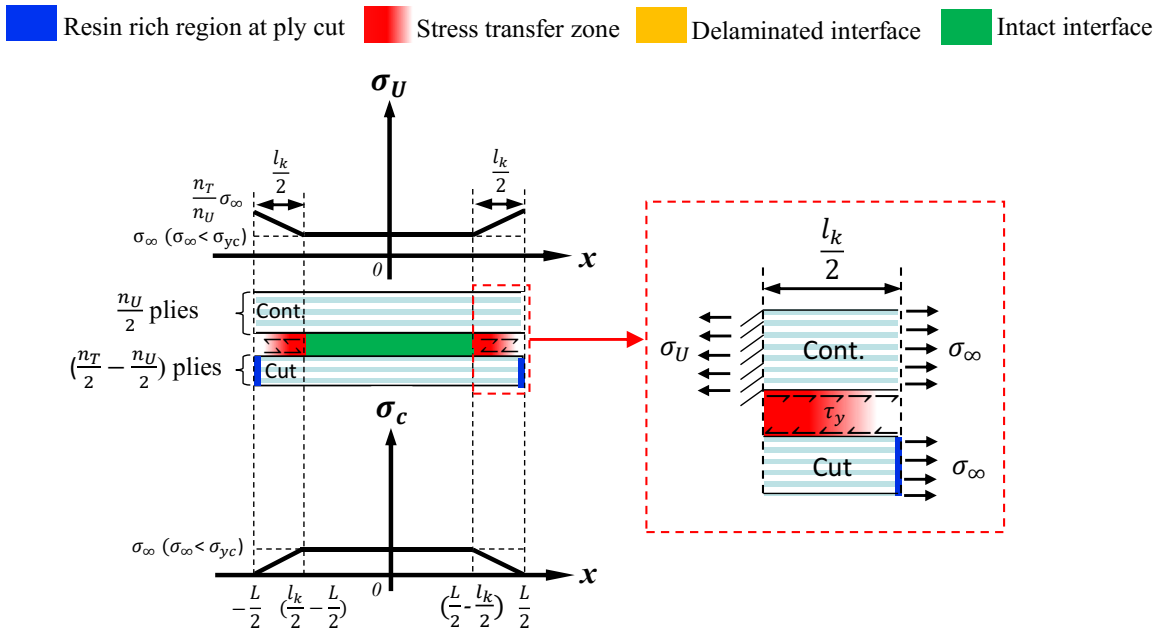


Figure 3.19 Schematic stress distribution in the continuous plies and the platelet next to the interlaminar stress transfer zone (highlighted in the RVE), at an average stress σ_∞, during the initial approximately-linear stage.

In each zone, the axial stress is assumed to be uniform across the thickness of the continuous block and also across the platelet. For a rigid perfectly-plastic interface, the axial stress varies linearly along the length of the stress transfer zones, as shown in Figure 3.17 (b) and (c).

At a certain value of the remote stress, σ_∞, the relative shear displacement between the continuous plies and the platelet at the trailing edges of the stress transfer zones will reach the critical value, δ_{rc} (see Figure 3.18), and delamination will be initiated at these positions (shown in yellow in Figure 3.17 (c)). This value of σ_∞ is the same as the critical value, σ_{yc} for delamination initiation (given by Eq. 3.3, presented earlier in the simplified model, shown in Section 3.2.1.2). As for the simplified model, σ_{yc} must satisfy Eq. 3.4 to ensure no tensile failure prior to the plateau stage in the tensile stress-stain response. At this stress, the combined length of stress transfer zones reaches its maximum value, l_{kC}, given by substituting $\sigma_\infty = \sigma_{yc}$ into Eq. 3.10. The peak stress in the continuous plies at delamination initiation is given in Figure 3.17 (c). Moreover, it is noted that to obtain the plateau (shown in Section 3.5.2) and the final strain-hardening stages (shown in Section 3.5.3), the platelet length, L, must be greater than l_{kC}.

The overall average strain of the laminate is equivalent to that of the continuous block, ε, during the growth of the stress transfer zones. ε can be formulated using the overall extension of the continuous

plies, which is equivalent to the sum of the extension of the central section adjacent to the intact interface and the extension of the overall stress transfer zone, l_k. ε in terms of increasing σ_∞, is formulated in Eq. 3.11.

$$\varepsilon = \frac{(n_T - n_U)^2 h}{2 n_U \tau_y L E_0} {\sigma_\infty}^2 + \frac{1}{E_0}\sigma_\infty \tag{3.11}$$

The equivalent overall secant modulus, E_{is}, of the RVE in the initial almost-linear stage in $\sigma_\infty \in [0, \sigma_{yc}]$, is therefore expressed as Eq. 3.12.

$$E_{is} = \frac{2 n_U \tau_y E_0 L}{2 L n_U \tau_y + (n_T - n_U)^2 h \sigma_\infty} \tag{3.12}$$

Substituting $\sigma_\infty = \sigma_{yc}$ to Eq. 3.11, the strain at the end of initial stage of the stress-strain response, associated with the onset of delamination is expressed in Eq. 3.13.

$$\varepsilon = \frac{(n_T - n_U)^2 h}{2 L E_0 n_U \tau_y} {\sigma_{yc}}^2 + \frac{1}{E_0}\sigma_{yc} \tag{3.13}$$

For a given ε (shown in Eq. 3.11), the corresponding tangent modulus, E_{it}, is determined using $\frac{1}{E_{it}} = \frac{\mathrm{d}\boldsymbol{\varepsilon}}{\mathrm{d}\boldsymbol{\sigma_\infty}}$, as shown in Eq. 3.14.

$$E_{it} = \frac{n_U \tau_y E_0 L}{L n_U \tau_y + (n_T - n_U)^2 h \sigma_\infty} \tag{3.14}$$

3.5.2 Intermediate plateau stage

When the applied overall average strain, ε, is increased above that for initiation of delamination growth (see Figure 3.20 (a)), the average tensile stress, σ_∞, remains constant as the delamination fronts and the associated stress transfer zones advance toward the mid-point of the platelet. This process is schematically shown in Figure 3.20 (b) as the gradual elongation of the delaminated zones (shown in yellow) and the contraction of the intact interface zone (shown in green). A uniform axial stress of σ_{yc} is observed in both continuous plies and the platelet next to the gradually contracting intact interface. σ_{yc} is equivalent to $\sigma_{\infty \mathrm{C}}$, shown in Eq. 3.3. The fracture toughness for the onset and propagation of the interlaminar crack is assumed to be equal to the mode II fracture toughness, G_{IIc}, and this is assumed to remain constant throughout the fracture process. (This explains why the average tensile stress, σ_∞, remains constant in the plateau stage). The zones of linearly varying axial stress in the continuous plies

and the platelet also advance with the stress transfer zones. It is worth noting that the two stress transfer zones maintain the critical length of $\frac{l_{kC}}{2}$ while translating toward the platelet mid-point. The plateau stage terminates when the two stress transfer zones eventually meet at the mid-point of the platelet, as shown in Figure 3.20 (c), at which the green zone (i.e. the intact interface) disappears.

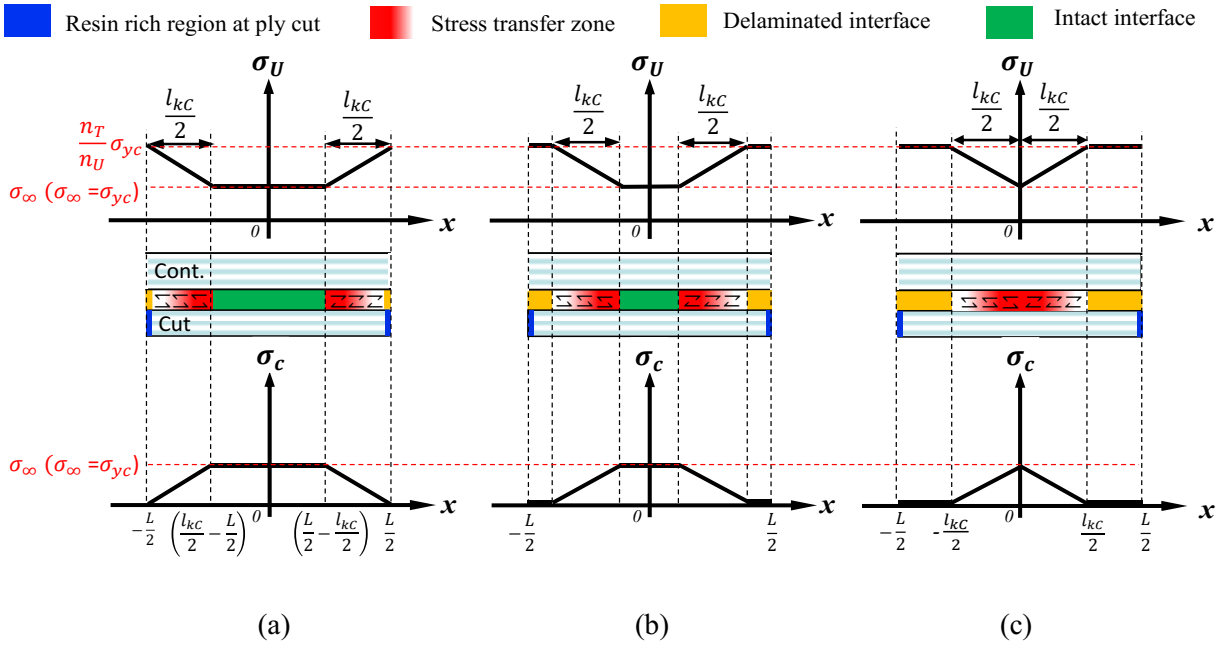


Figure 3.20 Schematics of the process of the translating of the delaminated, stress transfer and intact interlaminar zones and the associated variation of the axial stress in the continuous plies and the platelet at (a) the beginning, (b) the intermediate phase and (c) the end of the plateau stage in the tensile stress-strain response.

3.5.3 Final strain-hardening stage

To predict the response in the final strain-hardening stage (i.e. after the stress transfer zones have met at the mid-point of the platelet), propagation of the delamination fronts is assumed to occur when the shear displacement between the continuous block and the platelet, $\delta_{r,\frac{l_k}{2}}$, exceeding the critical shear displacement, δ_{rC}. The critical shear displacement of a rigid perfectly-plastic matrix (shown in Figure 3.18), δ_{rC}, can be determined by Eq. 3.15.

$$\delta_{rC} = \frac{G_{IIC}}{\tau_y} \tag{3.15}$$

As the average tensile stress, σ_∞, further increases above σ_{yc}, the stress transfer zones initiated from the two ends of the platelet gradually coalesce. The evolution of the stress transfer zones, as well as the

associated variation of the axial stress distribution in the continuous plies and the platelet, are shown in Figure 3.21.

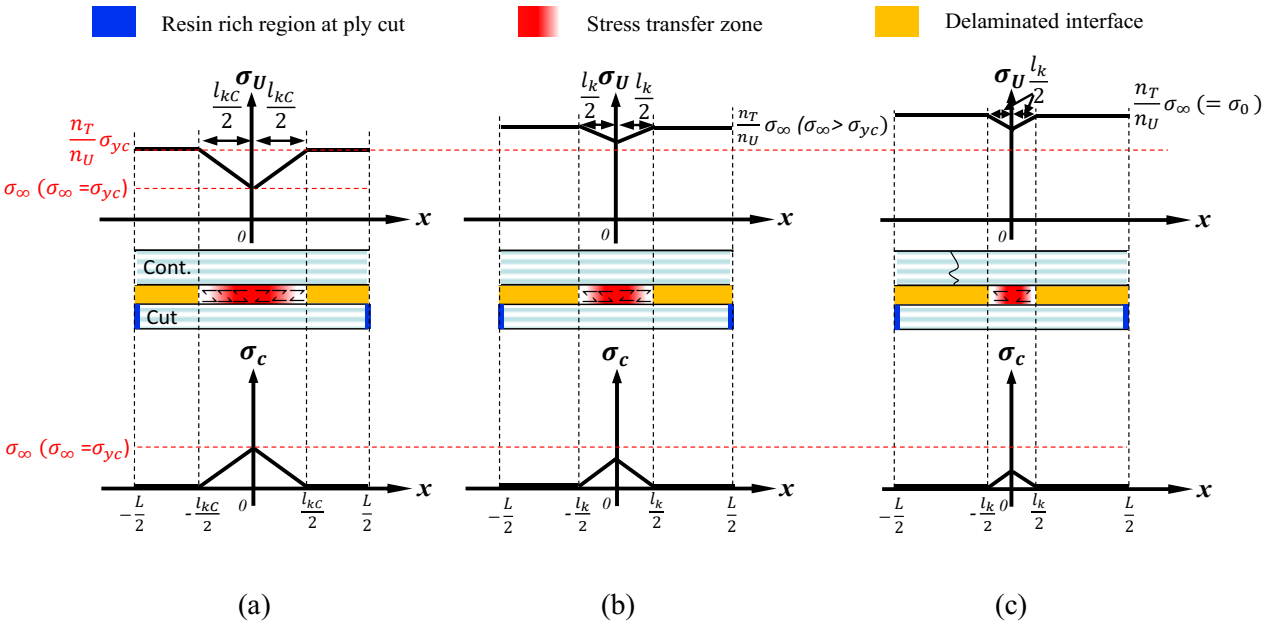


Figure 3.21 Schematic evolution of the tensile stress distribution in the continuous plies and the platelet (a) when the stress transfer zones of critical length, $\frac{l_{kC}}{2}$, just meet at the mid-point of the platelet and $\sigma_\infty = \sigma_{yc}$ (b) the combined stress transfer zone contracts as the average stress, σ_∞, is further increased above σ_{yc} and (c) ultimate failure of the continuous plies when the peak axial stress in the continuous plies, $\frac{n_T}{n_U}\sigma_\infty$, reaches the tensile strength of the material, σ_0.

For the continuous plies, the axial tensile stresses for the parts next to the stress transfer zone and the delaminated interlaminar zone, in half of the RVE (see Figure 3.21 (a) and (b)), are expressed in Eq. 3.16 and Eq. 3.17, respectively.

$$\begin{cases} \sigma_U(x) = \dfrac{n_T}{n_U}\sigma_\infty + \dfrac{(2x - l_k)\tau_y}{n_U h} & x \in [0, \dfrac{l_k}{2}] \quad \text{3.16} \\ \sigma_U(x) = \dfrac{n_T}{n_U}\sigma_\infty & x \in [\dfrac{l_k}{2}, \dfrac{L}{2}] \quad \text{3.17} \end{cases}$$

According to Eq. 3.16, the extension of the continuous plies between $x = 0$ and $x = \frac{l_k}{2}$, $\delta_{\frac{l_k}{2},U}$, is then expressed in Eq. 3.18.

$$\delta_{\frac{l_k}{2},U} = \frac{l_k n_T \sigma_\infty}{2E_0 n_U} - \frac{{l_k}^2 \tau_y}{4E_0 n_U h} \quad 3.18$$

In terms of the platelet, the axial stresses for the parts next to the stress transfer zone and the delaminated interlaminar zone, in half of the RVE, are given by Eq. 3.19 and Eq. 3.20, respectively.

$$\begin{cases} \sigma_c(x) = \dfrac{(l_k - 2x)\tau_y}{(n_T - n_U)h} & x \in [0, \dfrac{l_k}{2}] \quad 3.19 \\ \sigma_c(x) = 0 & x \in [\dfrac{l_k}{2}, \dfrac{L}{2}] \quad 3.20 \end{cases}$$

The extension of the platelet between $x = 0$ and $x = \frac{l_k}{2}$ is then calculated from Eq. 3.19 and is shown in Eq. 3.21.

$$\delta_{\frac{l_k}{2},c} = \frac{{l_k}^2 \tau_y}{4(n_T - n_U)E_0 h} \quad 3.21$$

Hence, the relative displacement between the continuous plies and the platelet between $x = 0$ to $x = \frac{l_k}{2}$, $\delta_{r,\frac{l_k}{2}}$, is determined from $(\delta_{\frac{l_k}{2},U} - \delta_{\frac{l_k}{2},c})$ (see Eq. 3.18 and Eq. 3.21) and is shown in Eq. 3.22.

$$\delta_{r,\frac{l_k}{2}} = \frac{l_k n_T}{2E_0 n_U}[\sigma_\infty - \frac{l_k \tau_y}{2(n_T - n_U)h}] \quad 3.22$$

Delamination growth occurs once $\delta_{r,\frac{l_k}{2}}$ (shown in Eq. 3.22) becomes equivalent to δ_{rC} (see Eq. 3.15), which is expressed as the quadratic equation, in terms of l_k (see Eq. 3.23).

$$n_T {\tau_y}^2 {l_k}^2 - 2(n_T - n_U)\tau_y n_T \sigma_\infty l_k h + 4hG_{IIC} n_U E_0 (n_T - n_U) = 0 \quad 3.23$$

The value of stress transfer zone length, l_k, in terms of the average tensile stress, σ_∞ ($\sigma_\infty > \sigma_{yc}$), is determined as the positive, real solution of Eq. 3.23.

The overall representative strain of the laminate in the strain-hardening stage, ε, which is equivalent to the overall strain of the continuous plies, can be determined from Eq. 3.16 and Eq. 3.17, and is shown in Eq. 3.24.

$$\varepsilon = \frac{n_T \sigma_\infty}{n_U E_0} - \frac{\tau_y {l_k}^2}{2LE_0 n_U h} \quad 3.24$$

The final strain-hardening stage is plotted according to the overall strain, ε, given in Eq. 3.24 for σ_∞ ($\sigma_\infty \in \left[\sigma_{yc}, \frac{n_U}{n_T}\sigma_0\right]$). Failure of the continuous plies occurs when the peak stress in the continuous plies reaches the tensile strength, σ_0, where the average tensile stress applied to the RVE, σ_∞, equals $\frac{n_U}{n_T}\sigma_0$. The strain at the onset of the final strain-hardening stage is obtained by substituting $\sigma_\infty = \sigma_{yc}$ into Eq. 3.24. Given Eq. 3.24, the secant modulus, E_{fs}, of the final strain-hardening stage is determined from $E_{fs} = \frac{\sigma_\infty}{\varepsilon}$, as shown in Eq. 3.25.

$$E_{fs} = \frac{2LhE_0 n_U \sigma_\infty}{(2hLn_T \sigma_\infty - \tau_y {l_k}^2)} \quad 3.25$$

The corresponding tangent modulus, E_{ft}, is determined using $\frac{1}{E_{ft}} = \frac{\mathrm{d}\varepsilon}{\mathrm{d}\sigma_\infty}$, as shown in Eq. 3.26.

$$E_{ft} = \frac{n_U E_0}{n_T} \quad 3.26$$

Eq. 3.26 indicates the tangent modulus of the final strain-hardening stage is proportional to the volume fraction of the continuous plies in the RVE.

Figure 3.21 (c) shows the interface is not fully delaminated from the continuous plies at ultimate failure. The length of the remaining un-delaminated part in the RVE at the ultimate failure point, can be calculated as the solution of Eq. 3.23, where σ_∞ is equal to $\frac{n_U}{n_T}\sigma_0$.

3.6 Refined analytical model for the UD laminates containing periodic perforations

The analytical model for a n_T-ply UD laminates containing lines of periodic perforations in the central $(n_T - n_U)$ plies, which are embedded in the middle of an even number of n_U continuous plies (as shown in Figure 3.22 (a)), is refined by considering the 'shear-lag' effect with a rigid perfectly-plastic interlaminar shear behaviour. Note that the boundaries (highlighted in Figure 3.22 (a)) between the continuous and the discontinuous fibre bundles in the perforated plies are not introduced in the perforated plies. The perforations of same length are equally spaced in both longitudinal and transverse directions, as show in Figure 3.22 (a). Lines of perforations are spaced at L apart and the perforations in adjacent lines are longitudinally aligned. Any tensile stress transfer between axially adjacent perforated bundles is neglected. The model is simplified by analysing a Representative Volume Element

(RVE) containing a central perforated fibre bundle of length, L, and width P, as shown in Figure 3.22 (b). The overall width of the RVE is w. At any cross-section of the RVE (shown in Figure 3.22 (b)), the tensile stress is assumed as uniform across the thickness of the continuous part and across the perforated fibre bundle, as shown in Figure 3.22 (c).

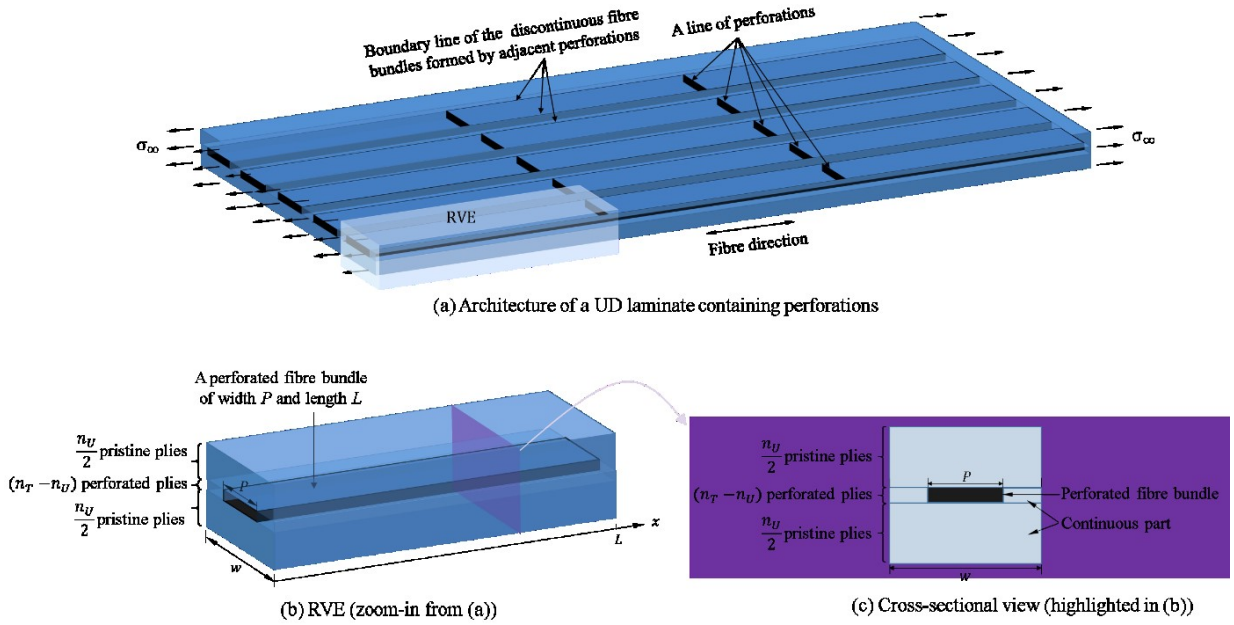


Figure 3.22 3D schematics of (a) the architecture of a UD laminate containing four lines of periodic perforations in the central perforated plies and (b) a zoom-in diagram of a RVE with a central perforated fibre bundle of length, L, with a highlighted cross-section plane and (c) the corresponding cross-sectional view of the highlighted plane.

3.6.1 Initial approximately-linear stage

The perforations promote intralaminar cracks developed at the lateral boundaries of adjacent perforated and unperforated (continuous) fibre bundles (i.e. the labelled planes abcd and efgh in the RVE, shown in Figure 3.23 (a)) and delamination at the interfaces above and below the perforated bundle (i.e. the labelled planes abfe and dcgh in Figure 3.23 (a)). The stress transfer zone on each side of the RVE is assumed to develop simultaneously on the surrounding four planes. Stress transfer zones of length $\frac{l_k}{2}$ are developed from the ends of the central perforated bundle as the average tensile stress, σ_∞, increases. The tensile stress distribution in the perforated fibre bundle and the surrounding continuous part in half of the RVE (of length $\frac{L}{2}$) are shown in Figure 3.23 (b) and (c), respectively. The interlaminar shear stress, τ_y, on the four planes surrounding the perforated bundle, is uniform throughout the stress transfer zone, due to the rigid perfectly-plastic matrix behaviour assumed here.

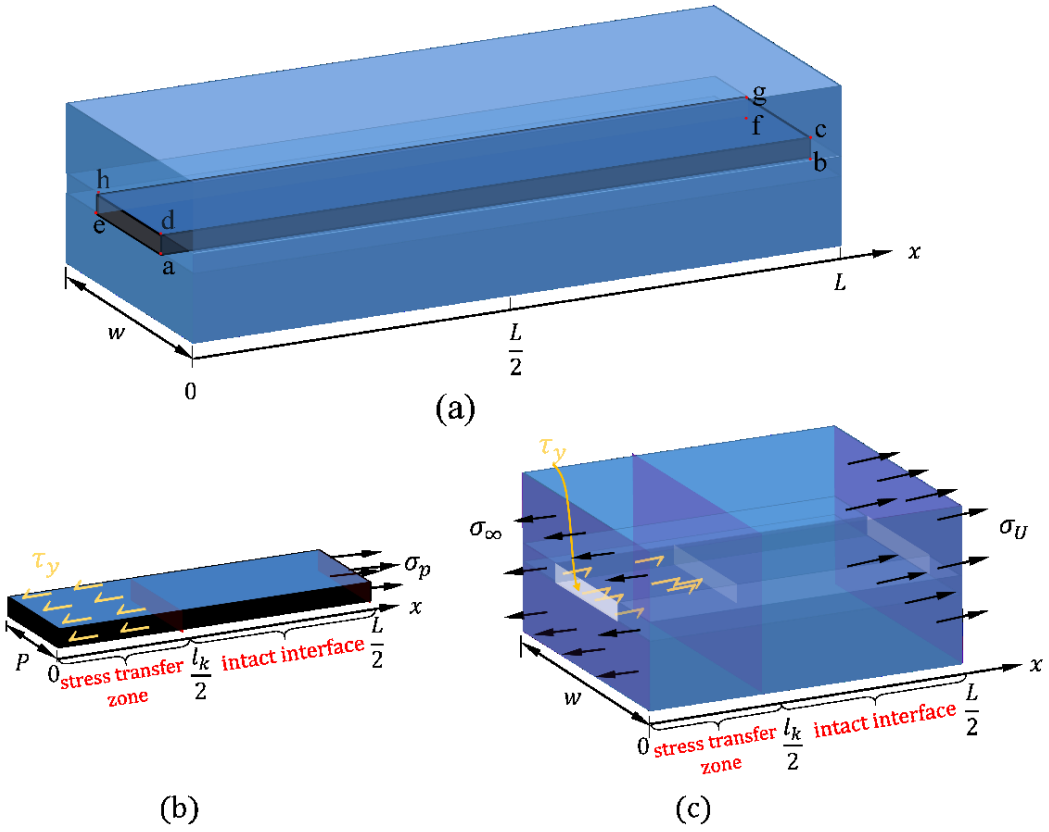


Figure 3.23 Schematic (a) RVE with labelled debonding planes surrounding the central perforated fibre bundle and the stress distribution in the (b) central perforated fibre bundle and (c) the surroudning continuous part in $x \in [0, \frac{L}{2}]$.

The combined length of the stress transfer zones in the RVE is determined from the force equilibrium of the perforated fibre bundle, shown in Figure 3.23 (b) and l_k is expressed in Eq. 3.27.

$$l_k = \frac{P(n_T - n_U)h}{\tau_y[P + (n_T - n_U)h]}\sigma_\infty \qquad 3.27$$

As the average tensile stress, σ_∞, increases, the stress transfer zones are initiated from both ends of the perforated fibre bundle and grow toward the middle of the RVE. These zones continue to grow until they reach a critical length $\frac{l_{kC}}{2}$, when σ_∞ reaches the critical stress for delamination, σ_{yp}. To obtain the plateau (shown in Section 3.5.2) and the following final strain-hardening stages (shown in Section 3.5.3), the platelet length, L must be greater than l_{kC}. The overall effective modulus of the RVE is then expressed according to the overall extension of the continuous part, i.e. sum of the extension of the continuous part next to the middle intact interface and next to the stress transfer zones. The representative average strain of the continuous part, ε, in terms of σ_∞, in the initial approximately-linear stage is formulated in Eq. 3.28.

$$\varepsilon = \frac{(n_T - n_U)^2 hP}{2[(n_T - n_U)h + P]Ln_U\tau_y E_0}\sigma_\infty^2 + \frac{1}{E_0}\sigma_\infty \qquad 3.28$$

The coordinates of the points in the initial stage, where $\sigma_\infty \in [0, \sigma_{yp}]$, is therefore determined as $(\varepsilon, \sigma_\infty)$. The overall effective secant modulus, E_{is}, of the initial stage is defined in Eq. 3.29, based on $E_{is} = \frac{\sigma_\infty}{\varepsilon}$.

$$E_{is} = \frac{2LE_0\tau_y n_U[(n_T - n_U)h + P]}{2L\tau_y n_U[(n_T - n_U)h + P] + (n_T - n_U)^2 hP\sigma_\infty} \qquad 3.29$$

The corresponding tangent modulus of the initial stage, E_{it}, is derived from $\frac{1}{E_{it}} = \frac{\mathrm{d}\varepsilon}{\mathrm{d}\sigma_\infty}$ and shown in Eq. 3.30.

$$E_{it} = \frac{LE_0\tau_y n_U[(n_T - n_U)h + P]}{L\tau_y n_U[(n_T - n_U)h + P] + Ph\sigma_\infty(n_T - n_U)^2} \qquad 3.30$$

Figure 3.24 shows the axial stress distribution in the perforated fibre bundle and in the surrounding continuous part, and the evolution of the interface between the continuous and the perforated parts in the RVE, related to the initial approximately-linear stage, predicted by the refined analytical model. The peak stress in the continuous part at debonding initiation is $\frac{n_T w}{n_T w - P(n_T - n_U)}\sigma_{yp}$, as shown in Figure 3.24 (c).

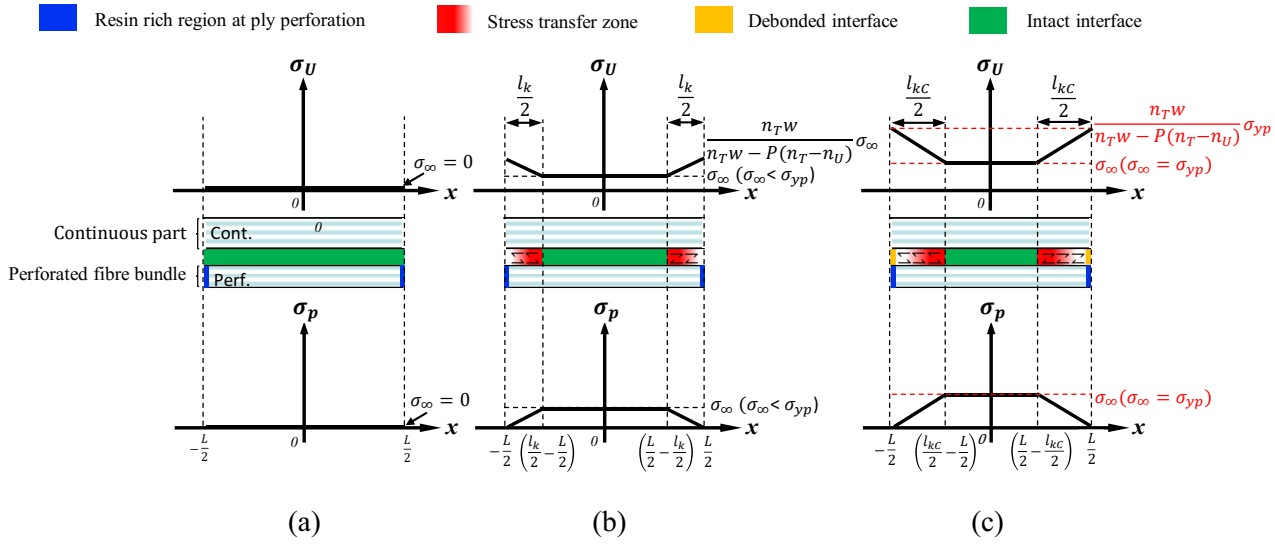


Figure 3.24 Schematic axial stress distribution in the continuous plies and the perforated fibre bundle in the RVE at (a) the beginning, (b) an intermediate phase and (c) the end of the initial approximately-linear stage of the stress-strain response of a UD laminate containing perforations.

3.6.2 Intermediate plateau stage

When the average stress, σ_∞, reaches, σ_{yp}, inter- and intra-laminar debonding growth is initiated at the ends of the perforated fibre bundle and the combined length of the stress transfer zones reaches its critical value of l_{kC}. When the applied overall average strain is increased further, the debonding fronts and the stress transfer zones advance toward the mid-point of the perforated bundle, without further increase in σ_∞ (i.e. there is a plateau in the stress-strain response). There is no change in the combined length of the stress transfer zones during this plateau stage. Figure 3.25 shows the evolution of the debonded regions, the contraction of the intact interface and distribution of the axial stress in the continuous part and the perforated fibre bundle, i.e. σ_U and σ_p, respectively.

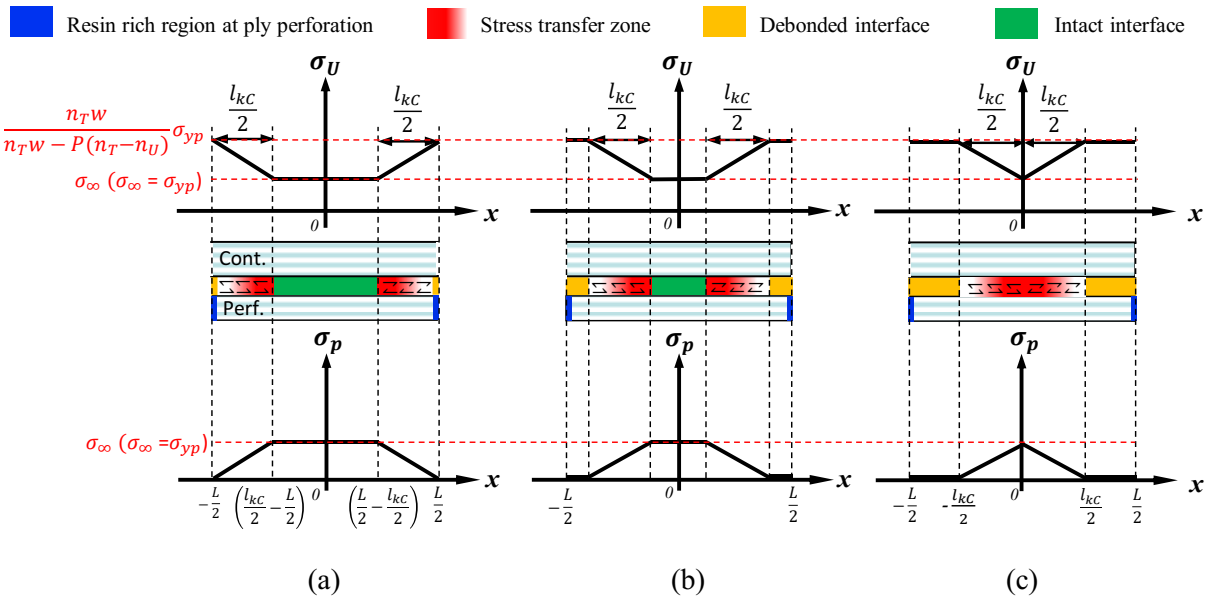


Figure 3.25 Evolution of axial stress distribution in the continuous part, the perforated fibre bundle and the interface beween the two parts in the RVE, at (a) the beginning, (b) the intermediate phase and (c) the end of the plateau stage in the tensil stress-strain response.

The fracture toughness for the onset and propagation of the inter- and intra-laminar cracks is assumed to be equal to the mode II fracture toughness, G_{IIc}, and this is assumed to remain constant throughout the fracture process. Therefore the average tensile stress, σ_∞, remains constant in the plateau stage. The pseudo-yield stress, σ_{yp}, is expressed in Eq. 3.8. The stress carried by the central perforated fibre bundle is transferred to the surrounding continuous part via the shearing of the interlaminar matrix related to stress transfer zones. The peak axial stress in the continuous part therefore occurs in the region adjacent to the debonded zones (shown in yellow) and is given by $\frac{n_T w}{n_T w - P(n_T - n_U)}\sigma_{yp}$, as indicated in Figure 3.25. The peak axial stress in the perforated fibre bundle remains at σ_{yp}. The plateau stage ends when the stress transfer zones just meet at the centre of the perforated bundle.

3.6.3 Final strain-hardening stage

In the final strain-hardening stage, the debonding process continues with increasing σ_∞, and the combined stress transfer zone contracts (see Figure 3.26). As described in the refined model for the cut ply laminates (shown in Section 3.5), it is assumed that the debonding fronts advance (see Figure 3.26 (b)), when the shear displacement between the continuous and perforated parts on each side of the RVE, $\delta_{r,\frac{l_k}{2}}$, exceeds the critical shear fracture displacement, δ_{rC}. The shear displacement at $x = \pm\frac{l_k}{2}$, (i.e. the outer edges of the stress transfer zones) can be determined by considering the difference in axial extension between the continuous and perforated parts between $x \in [0, \frac{l_k}{2}]$.

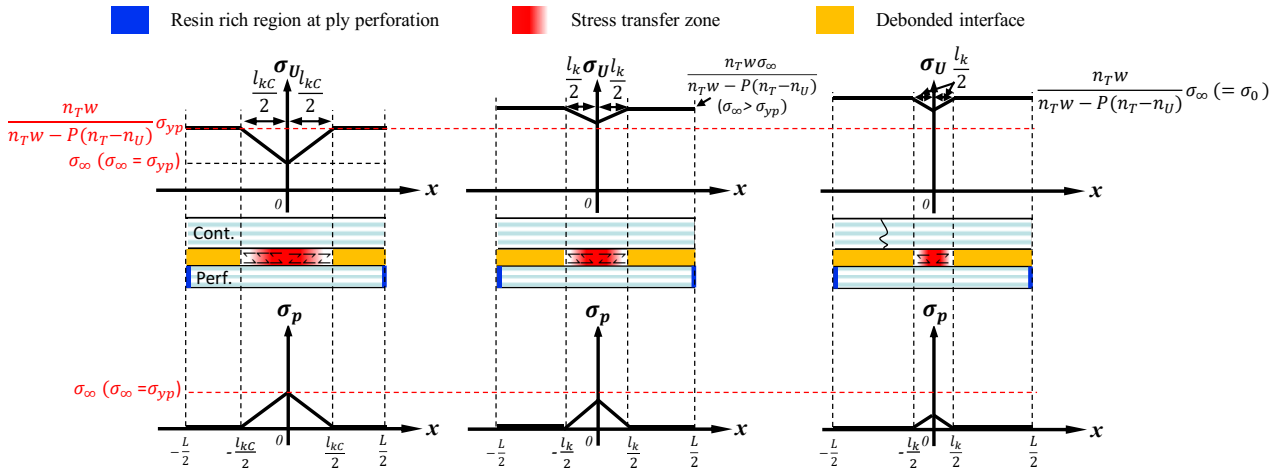


Figure 3.26 Evolution of the stress distribution in the continuous part and the central perforated fibre bundle in the RVE at (a) the beginning, (b) the intermediate phase and (c) the end of the final strain-hardening stage of the tensile stress-train response.

The axial tensile stresses in the continuous part next to the stress transfer and the intact interface zones, are expressed by Eq. 3.31and Eq. 3.32.

$$\begin{cases} \sigma_U(x) = \dfrac{\tau_y[(n_T - n_u)h + P](2x - l_k)}{wn_T h - Ph(n_T - n_u)} + \dfrac{wn_T}{wn_T - P(n_T - n_U)}\sigma_\infty & x \in \left[0, \dfrac{l_k}{2}\right] \quad 3.31 \\ \sigma_U(x) = \dfrac{wn_T}{wn_T - P(n_T - n_U)}\sigma_\infty & x \in \left[\dfrac{l_k}{2}, \dfrac{L}{2}\right] \quad 3.32 \end{cases}$$

Hence the extension of the continuous part between $x = 0$ and $x = \frac{l_k}{2}$, i.e. $\delta_{\frac{l_k}{2},U}$, for this perforated RVE, is given by Eq. 3.33.

$$\delta_{\frac{l_k}{2},U} = \frac{2wn_T h l_k \sigma_\infty - [(n_T - n_U)h + P]\tau_y {l_k}^2}{4E_0[wn_T h - Ph(n_T - n_U)]} \quad 3.33$$

The axial stresses in the perforated fibre bundle next to the stress transfer and the intact interface zones, are given by Eq. 3.34 and Eq. 3.35.

$$\begin{cases} \sigma_p(x) = \dfrac{\tau_y[(n_T - n_U)h + P](l_k - 2x)}{Ph(n_T - n_U)} & x \in \left[0, \dfrac{l_k}{2}\right] \quad 3.34 \\ \sigma_p\,(x) = 0 & x \in \left[\dfrac{l_k}{2}, \dfrac{L}{2}\right] \quad 3.35 \end{cases}$$

Therefore, the extension of the perforated fibre bundle between $x = 0$ and $x = \frac{l_k}{2}$, i.e. $\delta_{\frac{l_k}{2},p}$, is given by Eq. 3.36.

$$\delta_{\frac{l_k}{2},p} = \frac{[(n_T - n_U)h + P]\tau_y {l_k}^2}{4E_0 Ph(n_T - n_U)} \quad 3.36$$

Therefore at $x = \frac{l_k}{2}$, the relative shear displacement, $\delta_{r,\frac{l_k}{2}}$, between the continuous and perforated parts can be determined from Eq. 3.33 and Eq. 3.36 and is expressed in Eq. 3.37.

$$\delta_{r,\frac{l_k}{2}} = \delta_{\frac{l_k}{2},U} - \delta_{\frac{l_k}{2},p} \quad 3.37$$

Then setting the $\delta_{r,\frac{l_k}{2}}$ equal to δ_{rC}, the following quadratic equation 3.38 in terms of l_k, is given.

$$\frac{G_{IIc}}{\tau_y} = \frac{2wn_T h l_k \sigma_\infty - [(n_T - n_U)h + P]\tau_y {l_k}^2}{4E_0[wn_T h - Ph(n_T - n_U)]} - \frac{[(n_T - n_U)h + P]\tau_y {l_k}^2}{4E_0 Ph(n_T - n_U)} \quad 3.38$$

Rearrange Eq. 3.38 gives the quadratic equation Eq. 3.39 in terms of l_k.

$$wn_T {\tau_y}^2[(n_T - n_U)h + P]{l_k}^2 - 2wn_T Ph\tau_y\sigma_\infty(n_T - n_U)l_k + 4G_{IIC}E_0P[wn_T h - Ph(n_T - n_U)](n_T - n_U) = 0 \quad 3.39$$

Hence, for a given value of remote average stress, σ_∞ ($\sigma_\infty > \sigma_{yp}$), l_k is the positive, real solution of Eq. 3.39. For a given value of stress transfer zone length, l_k, the corresponding overall extension of the continuous part, $\delta_{L,U}$ (i.e. $x \in [\frac{-L}{2}, \frac{L}{2}]$), is determined based on Eq. 3.31 and Eq. 3.32.

$$\delta_{L,U} = \frac{2wn_T hL\sigma_\infty - [(n_T - n_U)h + P]\tau_y {l_k}^2}{2[wn_T h - Ph(n_T - n_U)]E_0} \qquad (\sigma_\infty > \sigma_{yp}) \tag{3.40}$$

The overall representative strain of the laminate, i.e. the overall strain of the continuous part, ε, in the strain-hardening stage is therefore determined as Eq. 3.41.

$$\varepsilon = \frac{\delta_{L,U}}{L} = \frac{2wn_T hL\sigma_\infty - [(n_T - n_U)h + P]\tau_y {l_k}^2}{2[wn_T h - Ph(n_T - n_U)]E_0 L} \tag{3.41}$$

Ultimate failure of the continuous part occurs when the peak stress of the continuous part, $\frac{wn_T - P(n_T - n_U)}{wn_T}\sigma_\infty$, reaches the tensile strength of the material, σ_0, as shown in Figure 3.26 (c). Using Eq. 3.41 and the l_k value, derived from Eq.3.39, the final strain-hardening part of the stress-strain curve can be plotted for a given remote average stress, σ_∞ ($\sigma_\infty \epsilon \left[\sigma_{yp}, \frac{wn_T - P(n_T - n_U)}{wn_T}\sigma_0\right]$). In addition, the secant modulus of this final strain-hardening stage, E_{fs}, for a given stress σ_∞, is determined from $E_{fs} = \frac{\sigma_\infty}{\varepsilon}$.

$$E_{fs} = \frac{2LE_0\sigma_\infty[wn_T h - Ph(n_T - n_U)]}{2wn_T h\sigma_\infty L - [P + (n_T - n_U)h]\tau_y {l_k}^2} \tag{3.42}$$

Given the overall representative strain, ε, shown in Eq.3.41, the corresponding tangent modulus, E_{ft}, is determined using $\frac{1}{E_{ft}} = \frac{\mathrm{d}\varepsilon}{\mathrm{d}\sigma_\infty}$, as shown in Eq. 3.43.

$$E_{ft} = \frac{wn_T - P(n_T - n_U)}{wn_T}E_0 \tag{3.43}$$

which indicates the tangent modulus of the final strain-hardening stage is proportional to the volume fraction of the continuous part in the RVE.

3.7 Parametric study of the tensile performance of UD laminates containing cut or perforated plies (predicted by the refined analytical models)

The properties of the carbon fibre/epoxy material are summarized in Section 3.7.1. Parametric studies on the impact of the geometric parameters on the tensile performance of the 'cut-ply' and 'perforated ply' laminates, are presented in Section 3.7.2 and 3.7.3, respectively.

3.7.1 Material

The aerospace grade M21/35%/198/T800S UD carbon fibre/epoxy prepregs produced by Hexply are used in all analytical and the experimental tests described in the following chapters. This material consists M21 toughened epoxy and Intermediate Modulus (IM) and high tensile strength grade of T800S fibres, with a cured ply thickness of 0.184 mm. The mechanical properties of a UD cured ply laminate are summarized in Table 3.1.

Table 3.1 Mechanical properties of UD cured ply M21/T800S laminates.

Elastic modulus	Tensile strength	Interlaminar shear strength (ILSS)	Mode II fracture toughness	Tensile failure strain
E_0 [GPa]	σ_0 [MPa]	τ_y [MPa]	G_{IIC} [kJ/m^2]	[%]
160[a]	2900[a]	96[b]	1.7[c]	2.0[b]

[a] Measured from pristine UD 6-ply M21/T800S specimens manufactured according to the ASTM D3039 standard [105].

[b] According to the manufacturer's data sheets [106] [107].

[c] Determined from the tensile tests of UD 4- and 6-ply M21/T800S specimens containing a single cut in the two central plies. The specimens were designed according to the ASTM D3039 standard [105]. The method to measure the mode II fracture toughness of a UD CFRP laminate was utilized in [35][37] and [108].

3.7.2 Parametric study of the tensile response of UD laminates containing continuous cuts

A parametric analysis of UD laminates containing continuous cuts was performed using the mechanical properties shown in Table 3.1. The impact of various geometric parameters, such as the platelet length, L, the absolute and the ratio between the overall number of plies and the number of pristine or continuous plies in the laminate, i.e. n_T, n_U and $\frac{n_T}{n_U}$, on the tensile performance, is shown in Figure 3.27. Five types of geometries were selected and evaluated, and the predicted stress-strain curves are shown in Figure 3.27.

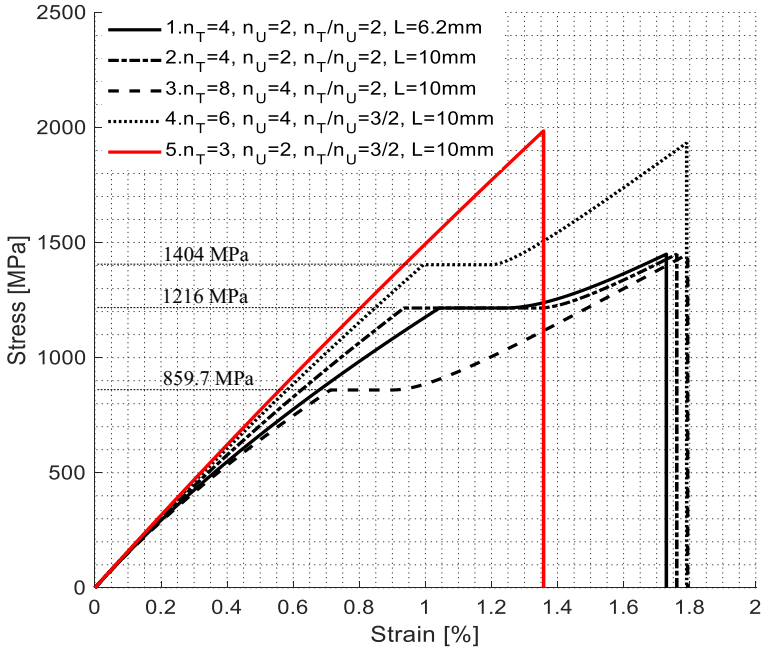


Figure 3.27 Tensile response of pseudo-ductile laminates containing ply cuts and various geometric parameters of L, n_T, n_U and $\frac{n_T}{n_U}$.

A comparison of the performances of configurations 1 and 2, with different platelet lengths but the same number of cut and pristine plies, indicates longer platelets provide less reduction of the stiffness in the initial stage of the stress-strain curve. Giving the same yielding stress at 1216 MPa, a consequently longer plateau stage is observed in the configuration with the longer platelets.

Configurations 2 and 3 have the same platelet length and the same ratio between the total number of plies and the number of pristine plies, whilst configuration 3 possessing double thicknesses of each block of the continuous and cut plies of those in configuration 2. The thicker configuration 3 gives a 29.3% lower pseudo-yield stress than that of the configuration 2 as the pseudo-yield stress is proportional to the factor of $\frac{1}{\sqrt{n_T - n_U}}$ (see Eq. 3.3), i.e. inversely proportional to the square root of the number of cut plies in a laminate. Configuration 2 and 3 also displayed great difference in the secant stiffnesses of the initial and the final strain-hardening stages, due to the difference in the length and evolution process of the stress transfer zones. The stiffness variation prior to and following the plateau was not predicted by the simplified analytical model (shown in Section 3.2.1), which neglects the development of the stress transfer zones.

Configurations 3 and 4 have the same number of pristine plies and the same platelet length, but configuration 3 contains a higher number of cut plies. Configuration 4 therefore shows a greater loss of

stiffness in the initial stage and a lower final stiffness. Configuration 3 also has a lower pseudo-yield stress (of 859.7 MPa), while the same ultimate strain as that of configuration 4.

Configurations 4 and 5 possess the same proportion of pristine and cut plies and the same platelet lengths. However, the constituent block of continuous plies and the platelet in configuration 4 are twice as thick as those in configuration 4. The thicker laminate exhibits a plateau stress of 1404 MPa and a strain-hardening stage. However, the thinner configuration behaves differently, with a continued non-linearity until ultimate failure, without any pseudo-yielding. The significant discrepancy in the tensile behaviour of the thicker configuration 4 is because the peak stress in the continuous plies reaches the critical failure stress, σ_0, before the average tensile stress reaches the pseudo-yield stress required for delamination. Therefore no delamination appears before the breakage of the uncut/pristine plies, i.e. ultimate fracture. The variation in the tensile performance of the five configurations also indicates that the pseudo-ductile performance is tailorable by adjusting the geometries of the 'cut ply' laminate.

3.7.3 Parametric study of the tensile response of UD laminates containing periodic perforations

In addition to the parameters studied for the 'cut ply' laminates, the tensile response of the 'perforated ply' laminates is also influenced by the perforation length, *P*, and the width of the RVE, *w*. Figure 3.28 presents the predicted tensile performance of two selected perforated configurations, in comparison with that of the same laminate containing continuous cuts. All selected laminates consist 4 plies in total, with 2 middle plies containing periodic perforations or continuous cuts, i.e. n_T and n_U are 4 and 2, respectively. The length of the perforated fibre bundles, *L*, is 10 mm. The selected perforation lengths, *P*, are 5 mm and 0.8 mm, with the corresponding widths of the RVE, *w*, equal to 7.5 mm and 1.2 mm, respectively. Note that the volume fractions of the continuous parts in the two perforated configurations are both 66.7%.

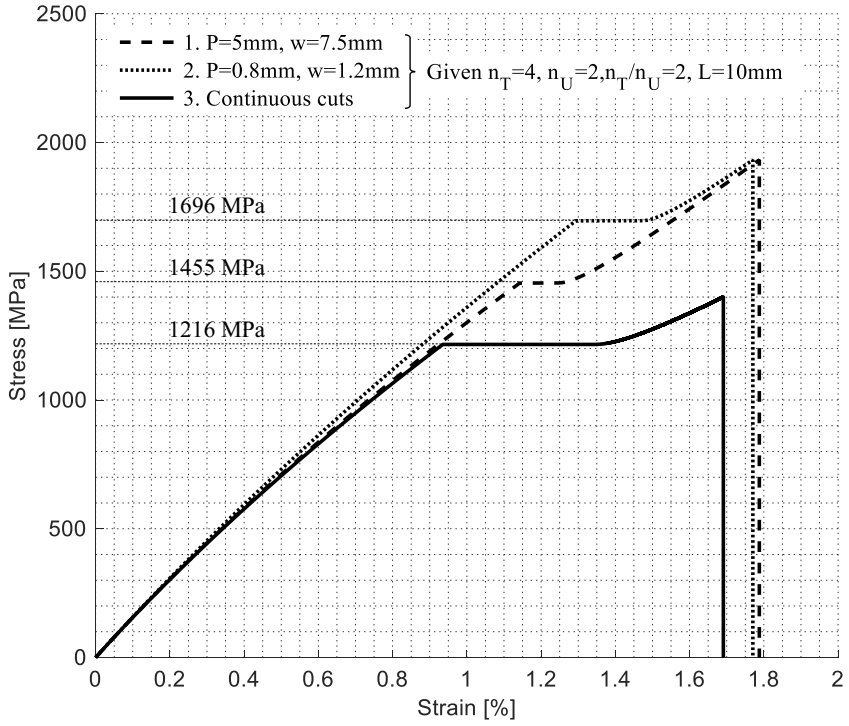


Figure 3.28 Analytical tensile stress-strain response of pseudo-ductile 'perforated ply' laminates with the same total number of plies and the number of weakened plies and different perforation geometries or continuous cuts.

Both perforated structures lose less stiffness in the initial loading stage than the 'cut-ply' one, mainly due to the higher proportion of continuous parts, the longer perforation case exhibits only a slightly higher stiffness. The yield stresses are also significantly higher in the perforated laminates, and the short perforations produce a 14.2% higher yield stress than the long perforations. This indicates that the perforation strategy gives a wider design scope for the tensile behaviour of the ply-weakened laminates. The tangent stiffnesses at the end of the final strain-hardening stages are the same for the two perforated scenarios. This is expected, as the two perforated cases have the same overall proportions of the continuous fibres, according to Eq. 3.43. The difference in the stiffness of the initial stages of the two 'perforated ply' laminates, containing the same proportion of continuous part, is because of the variation in the overall stress transfer zone area around the perforated fibre bundles.

3.8 Conclusions

The potential to achieve pseudo-ductility in UD single type of carbon fibre/epoxy material manufactured laminates using the ply weakening method, incorporated with or without partially weakened interface, was investigated using the simplified analytical models.

The simplified models neglected the stress transfer zones between continuous and weakened plies. The analyses indicated that a pseudo-yielding behaviour could be obtained with both ply weakening (using either continuous cuts or perforations) and with continuous cuts (i.e. one of the ply weakening approaches) in combination with interface weakening. In the cases of ply weakening, the simplified models predicted a stress-strain response consisting an initial linear-elastic stage, an intermediate plateau and a final linear-elastic stage. The addition of interface weakening resulted in two plateau stages. The first plateau is associated with the weakened interface and the second with the weakened ply. In addition, the simplified analytical model showed that the perforation strategy could give higher pseudo-yield stress. The simplified models also indicated that the interface weakening provides no significant benefit compared to using ply weakening only.

The ply weakening models were then refined by considering the shear stress transfer zones between the continuous and weakened (i.e. discontinuous) parts. The refined models provided better representation of the inter- and intra- laminar damage development process and the moduli variation of the approximately-linear initial and final stain-hardening stages. The ‘cut ply’ and ‘perforated ply’ strategies are predicted to have the potential to achieve an initial stiffness that is not significantly less than that of the constituent carbon fibre/epoxy material. In addition, the pseudo-ductile tensile performance is determined by the UD laminate geometric parameters, such as the absolute and relative thickness of the continuous and weakened plies, the perforation length and width of the RVE in ‘perforated ply’ laminates and the length of platelets in the ‘cut ply’ laminates. Moreover, the dominant failure mechanisms promoting pseudo-ductility are delamination or intra- and inter-laminar debonding, initiated by the cuts or perforations, respectively. The critical stress for debonding is determined by the material mode II fracture toughness. Furthermore, for a given laminate, the ‘ply perforation’ strategy has the potential to provide superior and a wider design scope for the potential pseudo-ductile tensile response, compared to the ‘ply cut’ strategy.

Chapter 4

Experimental investigation of pseudo-ductility in UD laminates containing continuous cuts

4.1 Introduction

This chapter describes an experimental investigation of the potential to achieve pseudo-ductile behaviour in UD laminates made of a single carbon fibre/epoxy material system by incorporating continuous cuts in selected plies. The detailed fabrication process, the mechanical testing procedure and the processes used to investigate the failure mechanisms are presented in Section 4.2. Section 4.3 presents the tensile behaviour achieved in static tensile tests on a range of configurations and the comparison with the stress-strain response predicted form the simplified and refined analytical models, described in Section 3.2.1 and Section 3.5, respectively. The damage mechanisms dominating the tensile performance are also analysed. Finally, conclusions of this study are presented in Section 4.4.

4.2 Experimental details

This section presents the details of the manufacture, mechanical testing and failure investigation methods used for seven cut-ply UD configurations.

4.2.1 Specimen types

Figure 4.1 shows the schematic side views of seven UD configurations.

Configurations (1) and (3) were designed to evaluate the effect of the ratio between the continuous and cut plies on the tensile response for a single cut. Configurations (2) and (5) were used to investigate the same effect in presence of distributed cuts. Configurations (3), (4) and (5) were designed to investigate the effect of increasing the number of ply cuts on the tensile response. Configurations (6) and (7) were designed to investigate the behaviour of laminates made of two sets of configurations (3) and (5), respectively.

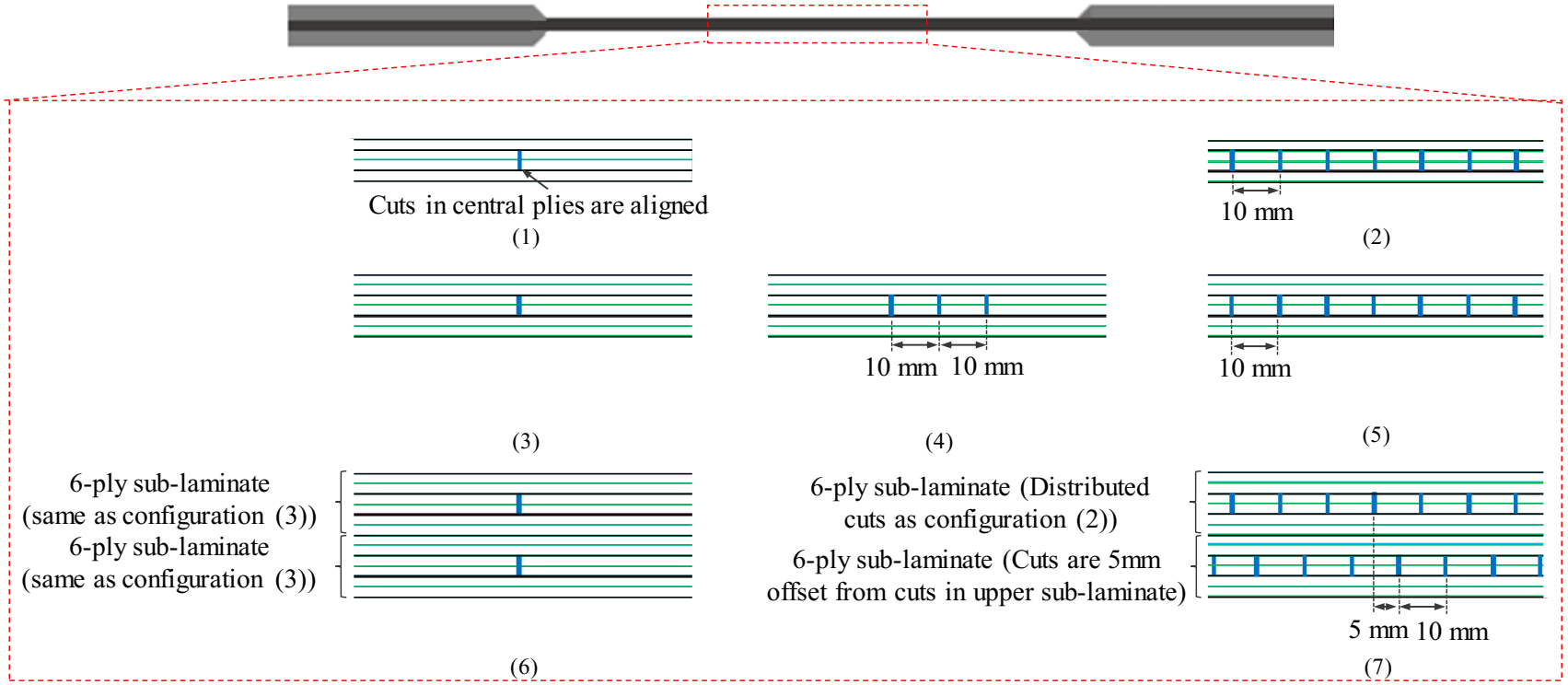


Figure 4.1 Schematic side views of seven UD configurations containing cuts: (1) 4-ply specimen with cuts in the middle of free length of the 2 middle plies; (2) 4-ply specimen with cuts in the 2 middle plies at 10 mm intervals throughout the free length; (3) 6-ply specimen with cuts in the centre of the free length of the 2 middle plies; (4) 6-ply specimen with three sets of cuts at 10 mm intervals in the middle 2 plies (at the centre of the free length); (5) 6-ply specimen with cuts in the 2 middle plies at10 mm spacing throughout the free length; (6) 12-ply specimen containing 2 sub-laminates each with the same ply cut pattern as the configuration (3) and (7) 12-ply specimen containing 2 sub-laminates each with the same ply cut pattern as the configuration (5).

4.2.2 Specimen fabrication

The specimens were manufactured with Hexply® M21/35%/198/T800S carbon fibre/epoxy prepregs. Parallel edged specimens, with the dimension shown in Figure 4.2, were fabricated according to the ASTM D3039 standard [105]. Bevel angles were implemented on the glass fibre/epoxy cross-ply end tabs, to reduce the stress concentration in the continuous plies next to the tab edges. This resulted in a free length of 138 mm. Figure 4.3 (a) shows schematically an example of the cutting patterns. In this case, the prepreg contain continuous cuts at 10 mm intervals and will produce 10 specimens of configuration 2 shown in Figure 4.2. The green lines show the outline of one specimen.

A CNC Genesis 2300 Blackman & White prepreg and textile cutting machine was used to cut the ply cuts, the rectangular ply outline and the alignment holes, shown in Figure 4.3.

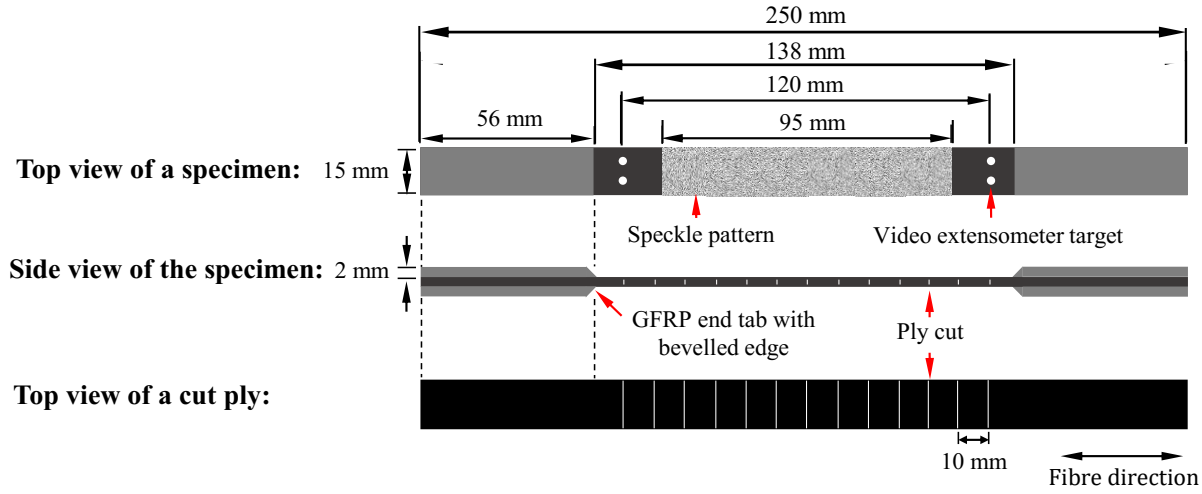
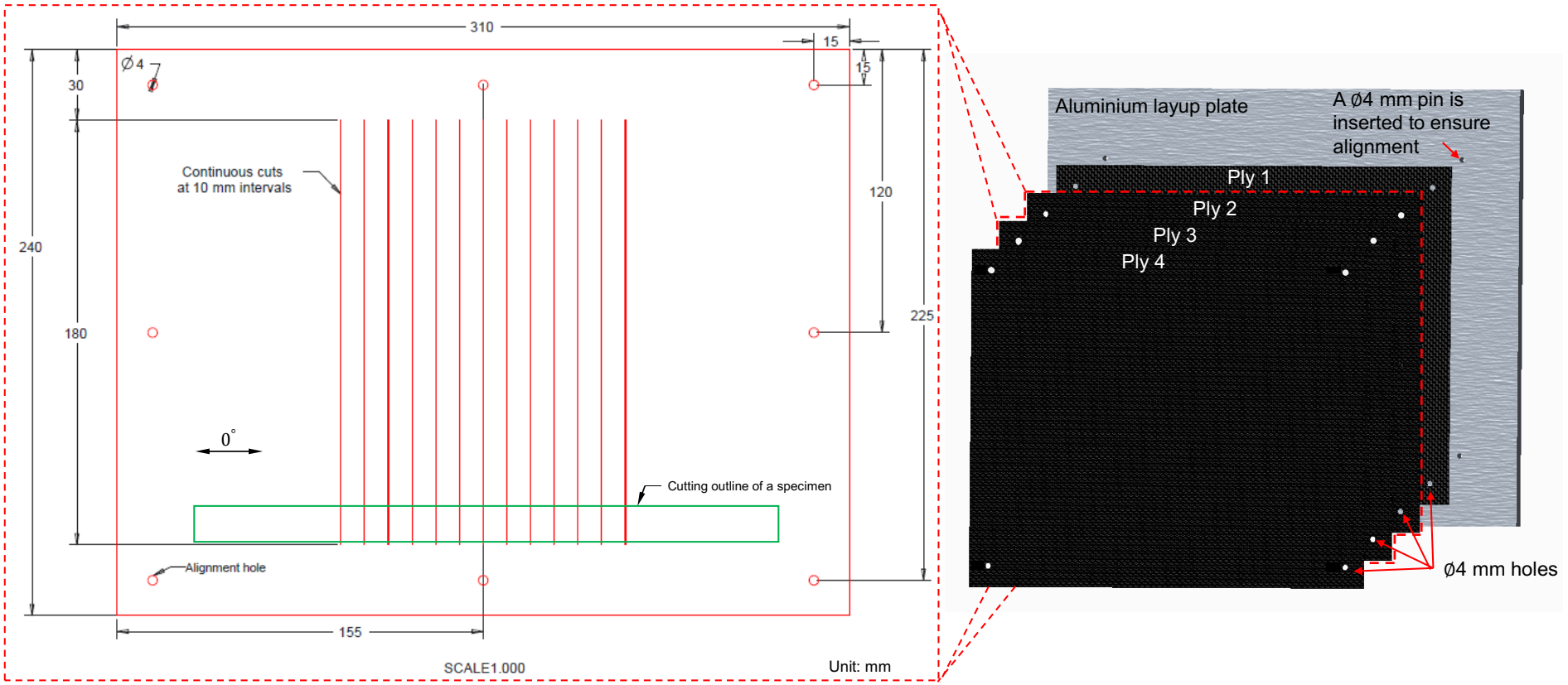


Figure 4.2 Schematic top and side views of a UD specimen with the location of speckle pattern and video extensometer target points and a schematic top view of an example cut ply containing continuous cuts at 10 mm intervals throughout the free length.



(a) (b)

Figure 4.3 Schematic diagrams of the (a) cutting profile of a prepreg containing thirteen 10 mm apart continuous cuts used to manufacture configuration (2) and (b) the alignment tool.

Pins mounted on an aluminium layup plate were used to achieve good alignment of cuts in adjacent plies during the layup process. These pins were mounted in the corresponding alignment holes in the prepreg plies, as shown in Figure 4.3 (a) and (b). After debulking on a vacuum table, the steel pins were removed and replaced with PTFE pins. The CFRP panel was then cured in an autoclave, using the manufacturer's specified cure cycle (180° at 7 bar for 120 minutes) [107]. End tab plates were adhesively bonded to the cured panels. Specimens were cut from the panels using a CNC waterjet cutter. The micrograph of a side view of a polished specimen, shown in Figure 4.4, indicates good alignment of cuts with no delamination was achieved.

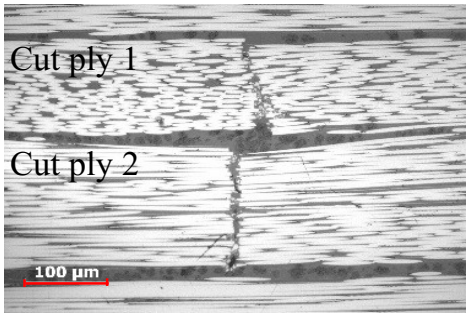


Figure 4.4 Good alignment of cuts in adjacent plies in cured panel showing no delamination.

4.2.3 Mechanical testing

4.2.3.1 **Tensile tests to ultimate failure**

At least five specimens were tested for each configuration up to ultimate failure. The tensile test was conducted in a 250 kN Instron hydraulic-controlled 5985 loading machine. Specimens were held in wedge type grips and loaded in tension with a displacement-controlled crosshead speed of 2 mm/min. An Imetrum video extensometer was used to measure the global strain at a frequency of 10 Hz for configuration (1) and 50 Hz for all other configurations, between target points set at 120 mm apart (i.e. 120 mm gauge length, as shown in Figure 4.2) prepared on specimen surface. The gauge length is shorter than the free length to avoid any strain concentrations near the end tabs. The gauge length is 18 mm shorter than the free length, which means 9 mm long regions close to each tab is not monitored by the video extensometer. The analytical tensile responses (predicted from the refined model shown in section 3.5), that obtained from the free and gauge lengths of configurations (3) to (5), are shown in Appendix 1. Results shown in Figure A-1 indicate that there is no significant differences between the tensile response of the free and gauge lengths for the three configurations.

The commercial GOM ARAMIS DIC system was used to monitor the surface strain distribution for one specimen of configuration (2) by tracking the movement of speckle pattern sprayed over a 95 mm

length of the surface (see Figure 4.2). 3D images were acquired from two ARAMIS® 3D stereo cameras with 6M pixel resolution and pixel size of 4.54 μm. A facet (or subset) size of 17×17 pixel and a 11pixel overlap (or facet distance) were used to track the movement of speckle patterns. Strain maps were captured with a frequency of 3Hz, using the DIC system.

4.2.3.2 **Interrupted tensile test and failure mechanisms characterization**

The interrupted tests with the loading-unloading-reloading cycles were used to investigate the failure mechanisms of configurations (3), (4) and (5), i.e. 6-ply laminates containing a single, three and multiple periodic cuts in the 2 middle plies. The load levels to pause the loading phase were determined based on the full stress-strain curves, obtained from the tests performed to ultimate failure. After each interruption, the specimen was removed from the loading machine and placed in a water tank of the ultrasonic C-scan machine to inspect the damage development. A Triton 1700 TT® scanning machine with a focused 10 MHz 15 mm diameter transducer was used. The scanning speed was 50 mm/s with a step size of 0.5 mm. The specimen was then placed in oven to remove moisture, before continuing the next loading cycle of the interrupted test, followed by a C-scan inspection using same scanning parameters.

4.3 Results and discussion

4.3.1 Tensile performance of 4-ply configurations

The analytical tensile stress-strain responses predicted from the simplified and refined models and the response obtained from the tests for the configurations (1) and (2), containing a single cut and multiple periodic continuous cuts, are shown in Figure 4.5 (a) and (b), respectively. The measured data is presented as discrete points to reveal the actual specimen behaviour during the static tensile loading process. The experimentally measured and the refined analytical model predicted key mechanical properties of the two configurations are summarized in Table 4.1 (at the end of this chapter).

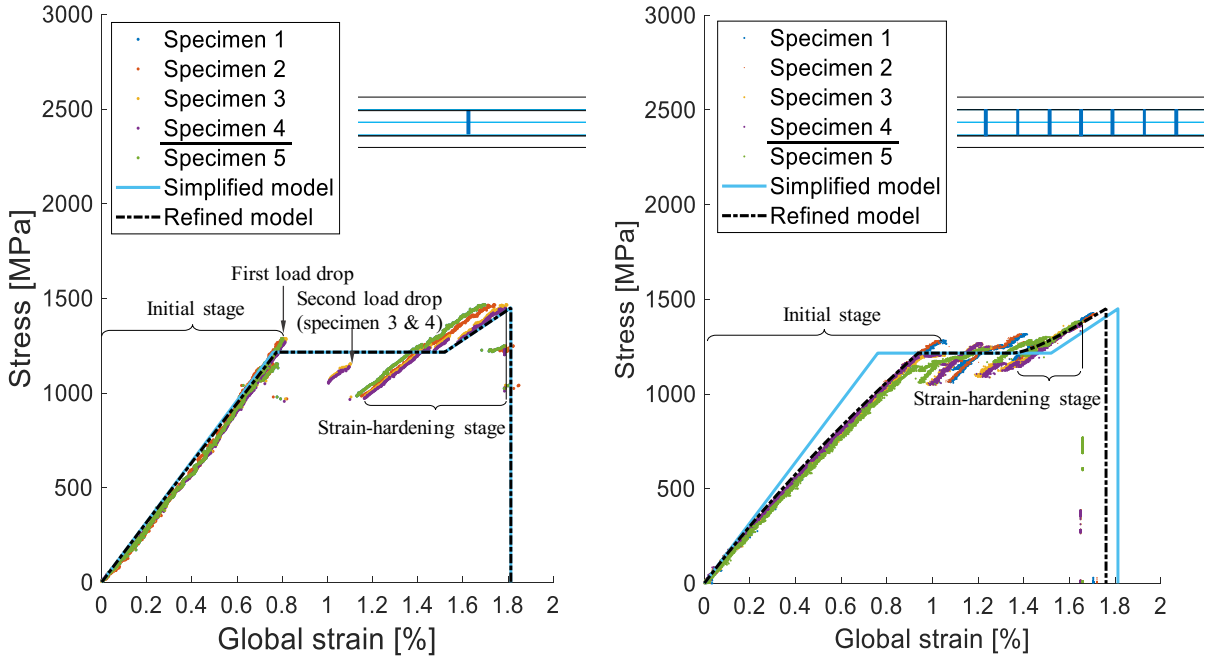


Figure 4.5 Experimental and analytical (predicted by the simplified and refined analytical models) tensile stress-strain responses of 4-ply configurations (a) (1) and (b) (2).

Figure 4.5 (a) shows no significant difference in the tensile responses predicted from the simplified and refined analytical models. The initial stage of the experimental curves is approximately linear and show good agreement with the analytical predictions. However, the experimental data does not exhibit the plateau predicted by the models. The experiments show a sudden drop in stress at a stress close to the plateau stress predicted by the models. The sudden drop in stress is almost certainly due to unstable delamination growth from the ply cut. Two specimens (specimens 3 and 4) after the initial stress drop, exhibit a short almost-linear intermediate stress-strain curve followed by another stress drop. These intermediate data points suggest that the sudden delamination growth after the initial stage did not develop throughout the entire specimen gauge length, and a second unstable delamination growth occurred at the end of the intermediate short stress-strain curve. No load drop was predicted in the analytical models, as the interlaminar fracture toughness, G_{IIC} was assumed as constant throughout the specimen.

The predictions obtained from the simplified and refined analytical models (see Figure 4.5 (b)) for configuration (2) show significant difference in the stiffnesses of the initial and the final strain-hardening stages. The refined analytical model, which considers the evolution of the stress transfer zones near the cuts, provides significantly improved agreement with the experimental results in the initial and final strain-hardening stages. The initial approximately linear stages obtained from the tensile

tests fit very well with that obtained from the refined model. The experimental results do not exhibit the analytically predicted plateau, instead the curves show a series of stress drops separated by several intermediate almost-linear stress-strain phases. The increase in the number of these intermediate phases compared to that observed for configuration (1), suggests that delamination growth does not initiate simultaneously from all cuts in configuration (2). Table 4.1 shows the average stress prior to the first sudden damage propagation is 1.07% higher than the 'plateau' stress predicted by the models. All specimens exhibit several intermediate almost-linear stress-strain phases, followed by further stress drops. This presumably indicates that the delamination damage first occurs only at some of the cuts due to a variation in toughness along the specimen. The non-linearity of these phases is due to the progressive development of the stress transfer zones at different cuts. The stiffnesses of the experimental final strain-hardening stages agree well with that predicted by the refined model.

For one configuration (2) specimen, a more detailed study of the evolution of the axial strain distribution during the loading process was performed using the DIC results. The stress-strain curve is presented in Figure 4.6 (a) with labelled initial approximately-linear, intermediate 'plateau' and strain-hardening stages. The stain contour plots of a 95 mm gauge length region and axial strain distribution curves along a common reference line for the selected stress levels in each of the three stages, are also presented in Figure 4.6. Figure 4.6 (b) to (d) display the strain distribution for five stress levels in the initial stage. Figure 4.6 (e) shows the strain distribution for four stress levels in the 'plateau' stage and Figure 4.6 (f) for the last stress level in the 'plateau' stage and two stress levels in the strain-hardening stage. The ply cut positions were indicated on each DIC strain contour plot and the axial strain distribution curve. Figure 4.6 (c) and (d) compare the DIC measured and the analytically predicted (using the refined analytical model shown in section 3.5) axial strain distribution for a representative 10 mm platelet, for stress levels 1 to 5. Such comparison is also performed for stress levels 9 to 11 and included in Figure 4.6 (e) and (f), respectively.

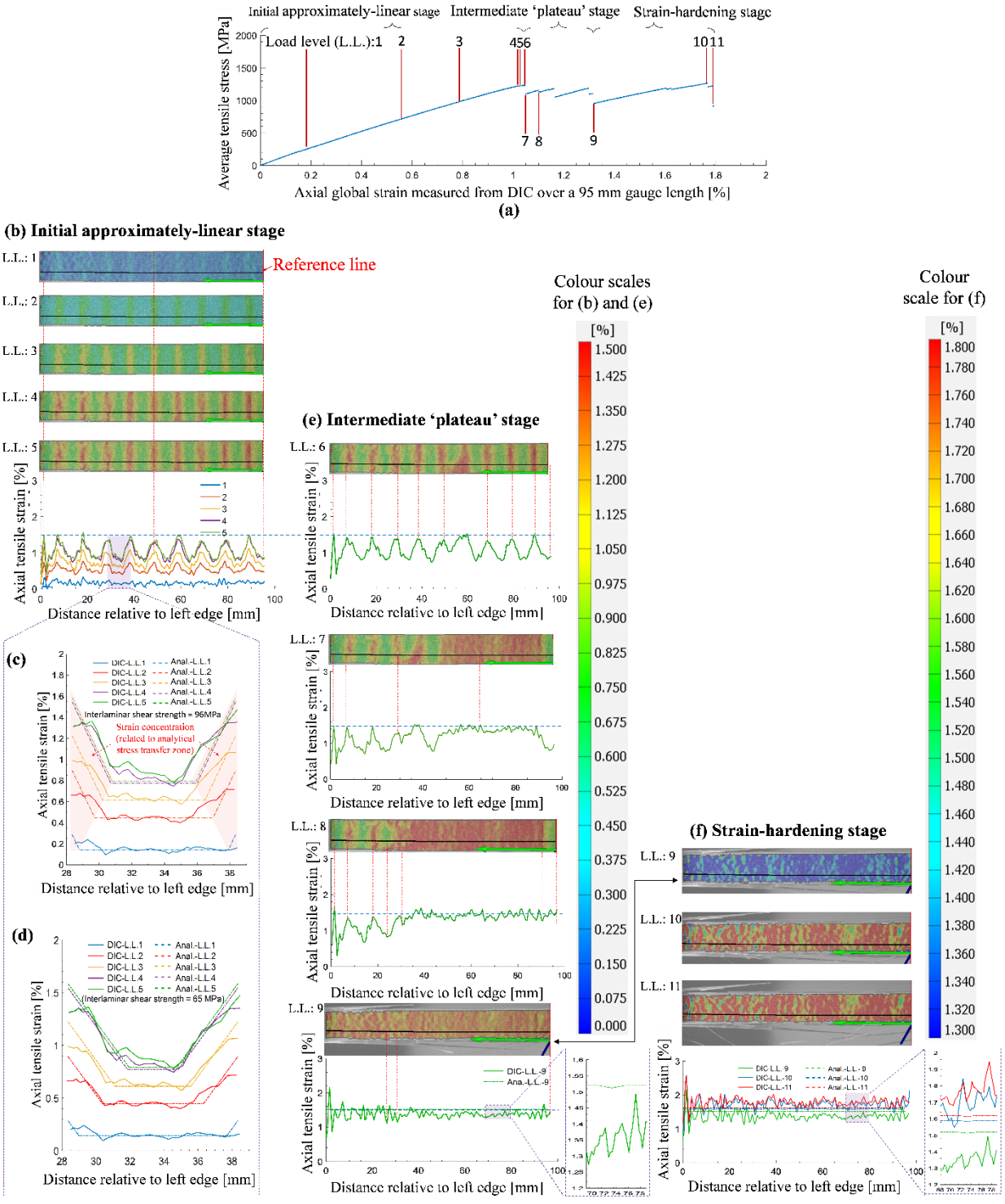


Figure 4.6 DIC strain contour plots and the corresponding axial strain distribution along a common reference line at selected stress levels of the tensile response of a configuration (2) specimen.

At stress level 1 of the initial approximately-linear stage, the axial strain distribution is relatively uniform throughout the gauge length (see Figure 4.6 (b)). Periodic strain distribution is observed at stress levels 2 to 5, with the peak strains coinciding with the internal ply cut positions. Stress transfer

zones are initiated from the ply cuts and are evident in the axial strain distributions. The strain and the stress transfer zone lengths both increase with increasing remote tensile stress.

The evolution of the axial strain distribution during the initial stage of a 10 mm long platelet (highlighted in Figure 4.6 (b)), together with the analytically predicted strain distributions are shown in Figure 4.6 (c) and (d). Except for Figure 4.6 (d), all analytically predicted distributions used the manufacturer's value of the interlaminar shear strength (ILSS) of 96 MPa. For Figure 4.6 (d), a reduced ILSS of 65 MPa was used in the analytical prediction. The results show that at the position considered in Figure 4.6 (c) and (d), a reasonable agreement is achieved between the predicted and experimental strain distributions, when the manufacturer's ILSS was used, but better agreement was obtained using the reduced ILSS. (This suggests the accuracy of the analytical prediction could be improved by 'tuning' the ILSS.)

At stress level 5, the tensile response enters to the intermediate 'plateau' stage and a short yielding stage appears between stress levels 5 and 6 (see Figure 4.6 (a)). The yielding is promoted by the onset of a 'triangular' delaminated area, initiated by the cut closest to the 60 mm axial position, as shown in the DIC strain contour plot at stress level 6 (see Figure 4.6 (e)). Presumably, the fracture toughness of this cut position is the lowest among the cuts in the gauge length. This delaminated area is associated with a locally suddenly increased trough strain and an elongated peak strain region, where the strain is close to the average of the peak strains at stress level 5 (shown as the blue dashed line in Figure 4.6 (b) and (e)).

Stress level 6 is followed by a sudden stress drop. The delamination suddenly developed to a large area, as shown in the strain contour plot and the strain distribution curve for stress level 7 (immediately after the stress drop). Delamination continues to grow in the subsequent stress levels 8 and 9. From the stress 7 to stress 9, the peak and trough strains of the delaminated area all become close to the value of the average peak strain at stress level 5 (i.e. at the end of the initial stage). Delamination is almost fully developed throughout the gauge length at stress level 9. The axial strain distribution during this 'plateau' stage shows good agreement with the analytically predicted behaviour.

At stress level 9, the 'plateau' stage transfers to the final strain-hardening stage (see Figure 4.6 (a)). A different strain scale (ranging from 1.3% to 1.8%) is used in Figure 4.6 (d) to distinguish the high and low strain regions in the strain contour plots. The axial strain distribution plots at stress level 9 to level 11, are plotted in the same diagram (see Figure 4.6 (f)). From stress level 9, the axial strain of the gauge length uniformly increases with the increasing tensile stress, as shown in the strain distribution curves. The diagram also includes the analytically predicted strain distribution, using the refined analytical model, in the gauge length at the three stress levels, for comparison. It is found that the experimental and analytical strain levels are generally in good agreement, but the small troughs shown in the predicted

curves are not captured in the DIC monitored data. Ultimate failure occurs when the axial strain at some points reached the failure strain of carbon fibre, 2.0%.

4.3.2 Tensile performance of 6-ply configurations

The experimental and analytical (predicted by simplified and refined models) tensile responses of the configurations (3), (4) and (5), which contain one cut, three cuts and thirteen cuts, respectively, are shown in Figure 4.7 and key mechanical properties are summarized in Table 4.1.

For configuration (3), containing a single central cut, the stress-strain curve displays very similar characteristics to that of configuration (1) and also shows a similar level of agreement with the analytically predicted behaviours from both the simplified and refined models.

For configuration (4), containing three cuts spaced at 10 mm intervals in the centre of the free length, the stress-strain plot is initially approximately-linear and then exhibits a sharp drop in stress, indicating unstable damage propagation. Some of the plots then exhibit a short almost-linear stress-strain curve, followed by a second sharp drop in stress. Finally, the stress-strain curves show a strain-hardening stage before ultimate failure. The curves show generally good agreement with both analytically predicted curves, but it can be seen that the stress precedimg the sudden damage propagation is slightly higher than the 'plateau' stress predicted by the models. The specimens exhibiting a short intermediate almost linear stress-strain curve, with the maximum stresses associated with the second phase of unstable damage, which are higher than the stress associated with the first phase. This presumably indicates that the damage first occurs at the weakest cut locations. For this configuration, the simplified and the refined analytical models show equally good agreement with the experimental data. Some specimens show higher stiffness of the strain-hardening stage than that predicted by the models.

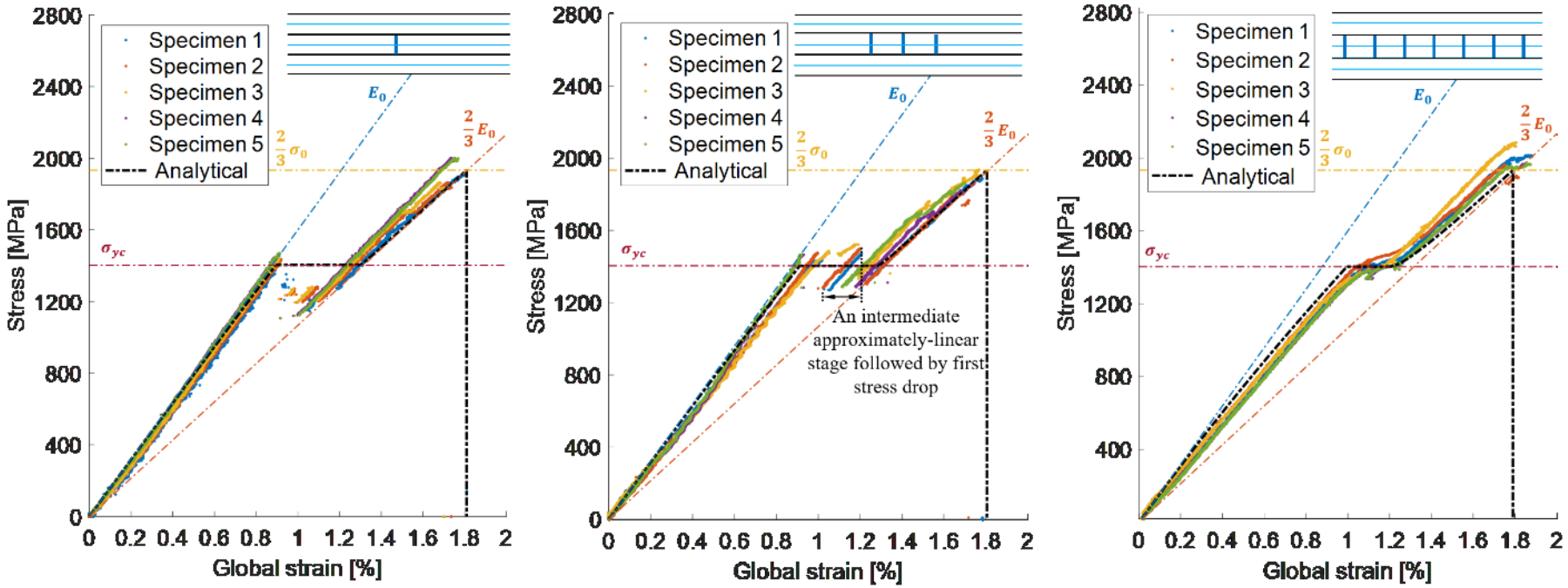


Figure 4.7 Analytical (predicted by the simplifed and refined analyticsal models) and experimental (measured by Imetrum video extensometer) tensile stress-strain responses of 6-ply (a) configuration (3), (b) configuration (4) and (c) configuration (5).

For configuration (5), containing cuts at 10 mm intervals throughout the specimen free length, the initial stage of the stress-strain curves shows a greater degree of non-linearity than observed in configurations (3) and (4). The refined analytical model shows better agreement with the experimental behaviour than the simplified model. In the 'plateau' stage, the incidence of sudden stress drops is significantly reduced compared to configurations (3) and (4). Some specimens exhibit a smooth transition between the initial and the final strain-hardening stages without any stress drops. The final strain-hardening stage shows a greater non-linearity than for configurations (3) and (4) and this is again predicted more accurately by the refined analytical model.

The tensile stress-strain curves for the series of interrupted tests and the corresponding C-scan images for a configuration (5) specimen, are presented in Figure 4.8. Delamination at the interface either above or below the two middle cut plies results in complete attenuation of the incident ultrasonic signal, which results in the white regions in the C-scan diagrams. (The strain gauge bonded to one surface also results in complete attenuation of signal.) In the first interruption, the specimen was unloaded when the average tensile stress just reaches the pseudo-yield stress level, at which delamination is predicted to begin. A small area of delamination (at the upper right corner) and smaller delamination at several cut positions are observed in the C-scan image. The second interrupted test was unloaded at a stress after a further small loss in stiffness. The C-scan image related to the second interruption shows delamination was initiated at cut positions presumably those with lower fracture toughness. With further increased remote tensile stress, the existing delamination continue propagating non-uniformly and grow significantly at some but not all cut positions (presumably those with lower fracture toughness) and further delamination initiate at other cut positions, as shown in the C-scan diagram for interruption 3. Delamination continue developing non-uniformly as the average stress is further increased, as shown in the C-scan images for the later interrupted tests during the strain-hardening stage. The stress-strain behaviour fits well with the predicted stress transfer zone evolution during the plateau and strain-hardening stages, before the ultimate failure. Un-delaminated strips remain visible in the final C-scan image. Such un-delaminated strips (and the randomly distributed un-delaminated spots) were predicted by the refined model as the stress transfer zone in the middle of the platelet, as shown in Figure 3.21 (c). Note that delamination can occur on both sides of the two middle plies and delamination on either side can result in the complete attenuation of signal, i.e. the formation of white area in the C-scan images. Experimentally, delamination is not uniformly developed throughout the entire specimen, therefore the overall area of the un-delaminated blue strips observed from the last interruption test, i.e. interruption 5, is less than expected.

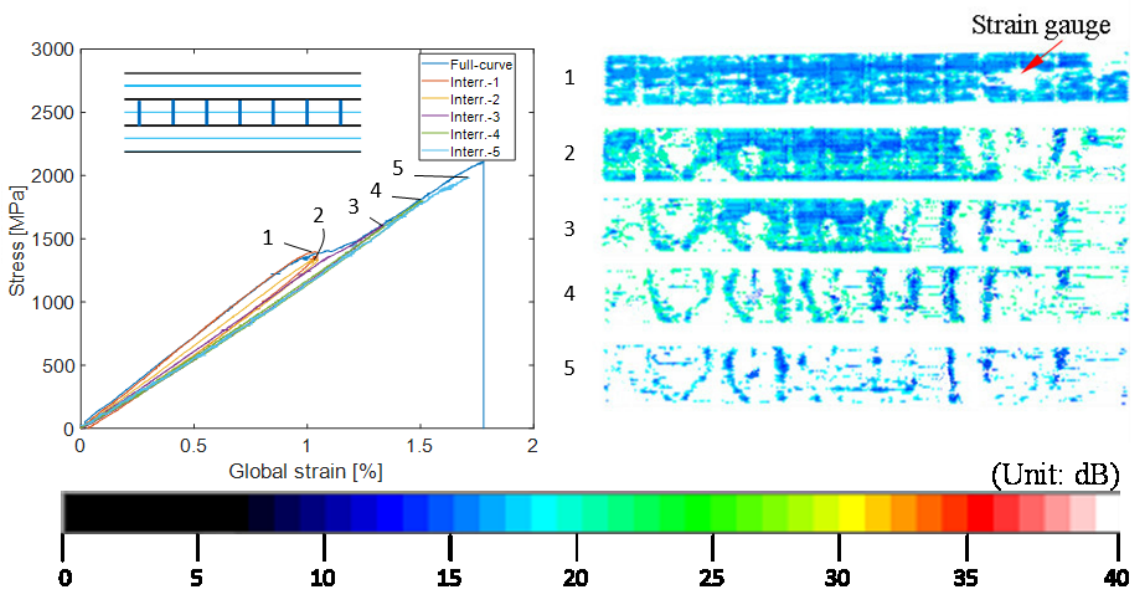


Figure 4.8 Tensile stress-strain curves (measured from 120 mm gauge length) and the corresponding ultrasonic C-scan images (showing the back-wall signal attenuation) for a series of interrupted tests on a 6-ply specimen containing thirteen cuts.

Comparing the experimental response of configurations (3), (4) and (5) containing increased number of cuts in the two middle plies, it is found that:

- Increased number of cuts provides higher reduction in stiffness during the initial stage in the tensile stress-strain response. This is expected, as theoretically more cuts lead to higher percentage of the overall length of stress transfer zones throughout the gauge length, therefore higher overall extension at a given average tensile stress. The overall stress transfer zone area for the 6-ply configuration containing 13 cuts at the end of the plateau is approximate 50.7% of the free length, which is significantly higher than that of the same laminate containing a single cut (3.9%). Therefore a more dramatic reduction of the modulus during the initial stage and consequently a higher strain at the pseudo-yield stress, σ_{yc}, for configurations with increased number of cuts.

- Shorter plateaux were observed in configurations with higher number of cuts and this characteristic is predicted by the refined analytical model (see Figure 4.7). This is due to the stress transfer zone development as described in Section 3.5.2. Configuration (3) can be regarded as containing 2 platelets, each of 60 mm long in the 120 mm long gauge length. Theoretically, the plateau stage terminates when the stress transfer zones, initiated at the central cut just moved out of the ends of the gauge length. Configuration (4) can be regarded as composed of two 10 mm and two 50 mm long platelets in the 120 mm gauge length. When the

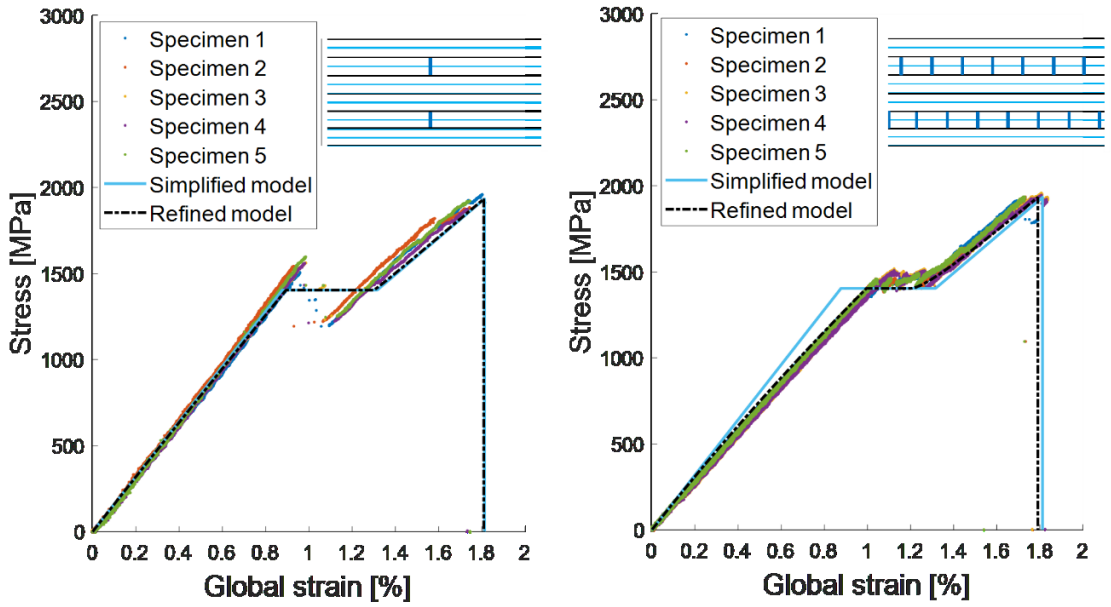
stress transfer zones in the 10 mm platelets encounter at the mid-points, the stress transfer zones in the 50 mm platelets will still be within the gauge length. The plateau in the stress-strain curve therefore continue until the stress transfer zone length in the 50 mm platelets moves out of the gauge length. In the case of configuration (5), composed only of 10 mm long platelets, the plateau is the shortest because there is only a small distance that the two stress transfer zones can travel within each platelet before they meet.

- More cuts give a higher secant modulus (measured from the zero-stress state) at the start of the strain-hardening stage. While the tangent modulus at this portion becomes lower as the number of cuts increases. This is because the overall area of the undelaminated strips formed at the end of the plateau stage increases with the number of cuts.

- Comparing the tensile performance of configurations containing 13 cuts for the 4-ply and 6-ply laminates, i.e. configurations (2) and (5). The change in yield stress and the change in plateau length is predicted well by the refined analytical model (see Table 4.1). It is shown that configuration (5), which contains higher number of pristine plies provides 15.46% higher pseudo-yield stress and 73.85% higher strain range of the plateau stage than configuration (2) (see Table 4.1).

4.3.3 Tensile performance of 12-ply configurations

The experimental and analytical stress-strain curves of the 12-ply configurations (6) and (7), composed of two sub-laminates of configurations (3) and (5), respectively, are shown in Figure 4.9.



(a) (b)

Figure 4.9 Analytical (predicted by the simplified and refined analytical models) and experimental (measured by Imetrum video extensometer) tensile responses of the 12-ply configurations (a) (6) and (b) (7).

The simplified and refined analytical models used to predict the tensile response of the 12-ply configurations are the same as those for the constituent 6-ply sub-laminates. Thereby the analytically predicted tensile responses of configurations (6) and (7) (see Figure 4.9 (a) and (b)) are the same as those for configurations (3) and (5), respectively (see Figure 4.7 (a) and (c)).

Configuration (6) contains a single cut position in each sublaminate. The reduction in stiffness of the initial and the final strain-hardening stages due to the evolution of stress transfer zone near the cut is negligible, therefore the tensile response predicted by the simplified and refined models are almost the same (see Figure 4.9 (a)). A single load drop is observed before the onset of the final strain-hardening stage in this thicker case, as was observed in the related 6-ply laminates (see Figure 4.7 (a)).

Configuration (7) contains cuts distributed at 10 mm intervals throughout the gauge length. The development of stress transfer zones, which were initiated from each cut, resulted in more severe loss in the stiffness in the initial stages. The effect of stress transfer zone on the tensile response is not considered in the simplified model, therefore a significant discrepancy in the behaviour of the initial stage is observed between the simplified and refined models predicted results. An intermediate plateau stage appears at approximately 1471 MPa (about 5 % higher than the analytically predicted stress), with small load drops. The plateau stage smoothly transforms into the final strain-hardening stage, due to the

gradual reduction in length of the stress transfer zones. This behaviour was also accurately captured by the refined analytical model. It can be seen that the overall tensile response predicted by the refined model exhibits better agreement with the experimental results.

In comparison with configuration (6), containing a single cut in the axial direction, the dramatic load drop is eliminated and instead a more progressive delamination process is achieved, as multiple dispersed cuts are introduced in the free length. In addition, the good agreement of the tensile response of the thinner (see Figure 4.7 (c)) and the thicker laminates (see Figure 4.9 (b)), implies pseudo-ductile tensile performance can be successfully transferred to thicker ones, by stacking sets of those pseudo-ductile thinner ones.

4.4 Conclusions

The concept of promoting pseudo-ductility in UD carbon fibre/epoxy materials using the 'continuous ply cuts' approach, presented analytically in Chapter 3, has been validated experimentally. This chapter presented the experimental results of the tensile response of UD laminates containing single and multiple continuous cuts in selected plies. The tensile performance and failure mechanisms of laminates containing different numbers of cuts and cut plies were compared. The experimental results were also compared with the response predicted from the simplified and refined analytical models. The findings are summarized below:

- For laminates containing a single continuous cut, the initial stage of the stress-strain response was almost identical to that of a pristine laminate. The initial stage was followed with load drops, due to the onset of unstable delamination and then a final strain-hardening stage.

- Laminates containing multiple continuous cuts exhibited a pseudo-ductile tensile behaviour. The initial stage possessed a high initial stiffness (close to that of the pristine material) but the stiffness reduces with the gradually increased load. This was followed by a relatively stable intermediate 'plateau' stage containing minor or no load-drops, leading up to a smooth transition to a final strain-hardening stage.

- The pseudo-ductility observed in the configurations with multiple lines of cuts is promoted by progressive delamination initiated at different cut positions. The minor load drops in the pseudo-ductile cases may be due to the toughness variation for cuts at different positions. The improved pseudo-ductility of the configurations containing multiple cuts comes at the cost of a loss of stiffness in the initial stage.

- For a given material system, the pseudo-ductile tensile response can be tailored by choosing the absolute and relative thicknesses of the continuous and cut plies and the length of the platelets.

- The tensile responses predicted by the refined analytical model for the UD laminates containing multiple lines of cuts, showed good agreement with the experimental results.

- The pseudo-ductility observed in a UD laminate containing multiple ply cuts can be successfully transferred to a thicker UD laminates made of several such cut-ply UD sub-laminates.

- The pseudo-ductile laminates achieved high initial stiffnesses of approximately 85% of the stiffness of a baseline pristine UD laminate and high pseudo-yield stresses of 70% to 88% of the ultimate failure strengths.

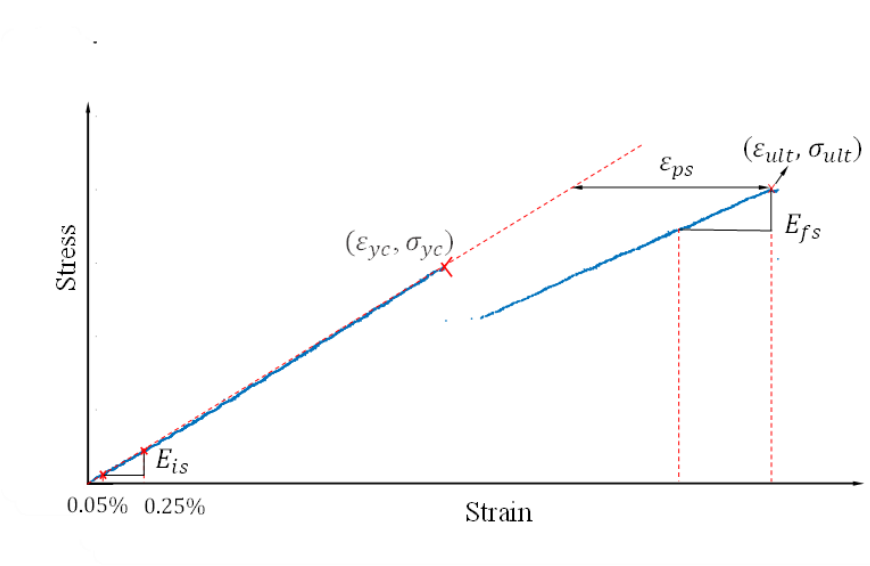
Table 4.1 Summary of the key analytical and experimental (for a 120 mm gauge length) mechanical properites of the seven types of UD laminates containing ply cuts. (Coefficient of variation, in %, is given in the parentheses).

Specimen Type	Initial modulus E_{is} [GPa]		Pseudo-yield strain and stress (ε_{yc}, σ_{yc}) * [%, MPa]		Strain-hardening modulus E_{fs} ** [GPa]		Pseudo-ductile strain ε_{ps} [%]		Ultimate failure strain and stress (ε_{ult}, σ_{ult}) *** [%, MPa]	
	Anal.	Exp.	Anal.	Exp.	Anal.	Exp.	Anal.	Exp.	Anal.	Exp.
(1) 4 ply-1 cut	159	148 (2.2%)	(0.77, 1216)	(0.85, 1284) (4.7%, 0.6%)	73	91 (4.9%)	0.90	0.71 (6.9%)	(1.81, 1450)	(1.74, 1461) (2.91%, 0.63%)
(2) 4 ply-13 cuts	148	136 (1.0%)	(0.93, 1216)	(0.87,1229) (2.8%, 4.5%)	51	59 (18.8%)	0.81	0.63 (4.1%)	(1.76, 1450)	(1.68, 1392) (1.78%, 2.45%)
(3) 6 ply-1 cut	159	150 (2.3%)	(0.89, 1404)	(0.91,1439) (1.1%, 2.4%)	107	120 (2.3%)	0.59	0.46 (9.6%)	(1.81, 1933)	(1.75, 1928) (2.79%, 3.53%)
(4) 6 ply-3 cuts	156	143 (2.8%)	(0.99, 1404)	(0.99,1449) (4.1%, 3.7%)	109	114 (7.6%)	0.58	0.43 (4.1%)	(1.81, 1993)	(1.74, 1871) (2.38%, 2.52%)
(5) 6 ply-13 cuts	153	137 (1.2%)	(0.99, 1404)	(1.11, 1406) (0.8%, 2.0%)	103	112 (3.7%)	0.51	0.38 (9.2%)	(1.79, 1993)	(1.83, 1999) (3.00%, 2.67%)
(6) 12 ply-1 cut	159	159 (3.4%)	(0.89, 1404)	(0.97, 1553) (2.1%, 2.2%)	107	117 (5.7%)	0.59	0.56 (7.2%)	(1.81, 1993)	(1.76, 1910) (1.79%, 2.06%)
(7) 12 ply-13 cuts	153	138 (4.8%)	(0.99, 1404)	(1.07, 1471) (4.2%, 2.5%)	103	112 (4.6%)	0.51	0.40 (7.8%)	(1.79, 1993)	(1.75, 1937) (2.87%, 0.89%)

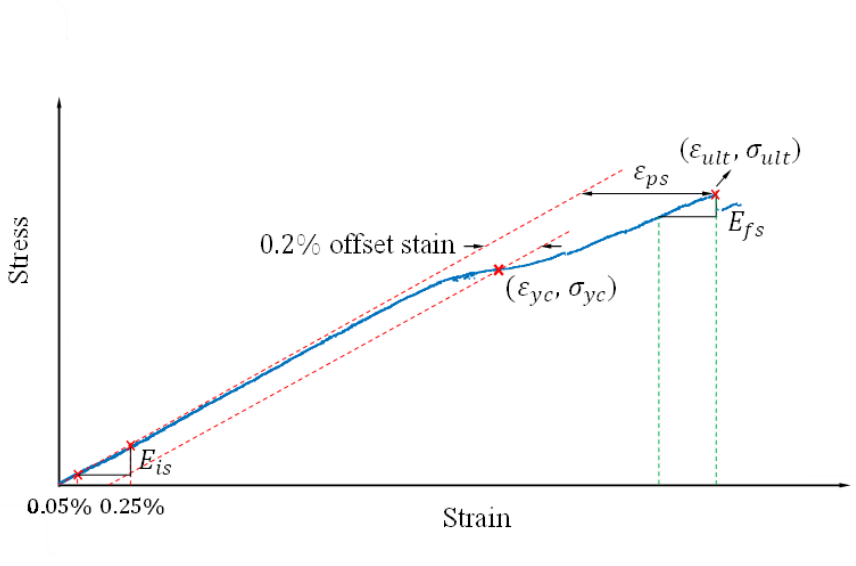
* For tensile stress-strain response containing unstable load drops immediately following the initial stage, the pseudo-yield point is determined as the point at the onset of the first load drop.

** The analytical and experimental strain-hardening stage moduli for configurations (1) to (7) are determined as the chord moduli measured from the strain range of [1.55%, 1.7%], for specimens failed at a strain greater than 1.7%; the moduli are measured from the strain ranges from 1.55% to the failure strain for specimens failed prior to the strain of 1.7%.

*** For tensile response containing load drops in the final strain-hardening stage, the ultimate failure point is determined as the maximum stress in this stage, as shown in the attached schematic stress-strain diagrams (a) and (b).



(a)



(b)

Chapter 5

Experimental investigation of pseudo-ductility in UD laminates containing ply perforations

5.1 Introduction

The analytical modelling presented in Chapter 3 showed that UD laminates containing periodic perforation patterns can provide pseudo-ductile tensile performance with higher moduli in the initial and final strain-hardening stages, higher pseudo-yield stress and higher tensile strength, compared to the same laminates containing continuous cuts. This chapter presents the experimental investigation of UD laminates incorporating perforation patterns. Section 5.2 describes the details of the investigated configurations, including the perforation geometries and distributions, the fabrication process, the mechanical testing procedure and the methods used to investigate the failure mechanisms. Section 5.3 presents the experimental results, which are compared to the tensile performance predicted by the refined analytical model (shown in Section 3.6). The conclusions of this study are summarized in Section 5.4.

5.2 Experimental details

Static tensile tests based on the ASTM D3039 standard [105] were performed on straight-edged specimens with the dimension shown in Figure 5.1. This section describes the details of the configurations of the investigated UD perforated-ply laminates, the manufacture process, the mechanical testing and failure process investigation methods.

5.2.1 Specimen types

Two groups of UD 4-ply configurations were investigated, each containing perforations in the central two plies.

The first group of configurations consist a single line of perforations, perpendicular to the fibre direction and in the middle of the free length, as schematically shown in Figure 5.1. Five perforation lengths of 50 μm, 250 μm, 500 μm, 800 μm and 5000 μm were investigated. One configuration containing a

single continuous cut was also tested for comparison. These configurations are denoted by a prefix 'S-' in Table 5.1. Each line of the periodic perforations was positioned centrally within the width of a specimen to prevent premature edge fibre splitting during the tests. In all the 'S' configurations, except 'S-800', the edge distance is equal to half the spacing between adjacent perforations (i.e. the specimen contains an integer number of unit cells), as shown in Figure 5.2. In the case of 'S-800' (and also in the 'M-800' configuration described later) the edge distance is 500 μm (rather than 300 μm, which would be the edge distance if the specimen width was modified to contain an integer number of unit cells).

The second group of configurations consist multiple lines of perforations placed at 10 mm intervals in the axial direction, as shown in Figure 5.1. The perforation pattern in the two middle plies is the same. This results in the formation of 10 mm long fibre bundles in the axial direction of each perforated ply. The three configurations investigated are denoted by 'M-800', 'M-5000' and 'M-Continuous cuts' (see Table 5.1), and the geometry of each line of perforations is the same as that described for the corresponding configuration containing the 'S-' pattern perforations. A UD configuration containing multiple continuous cuts was investigated for comparison.

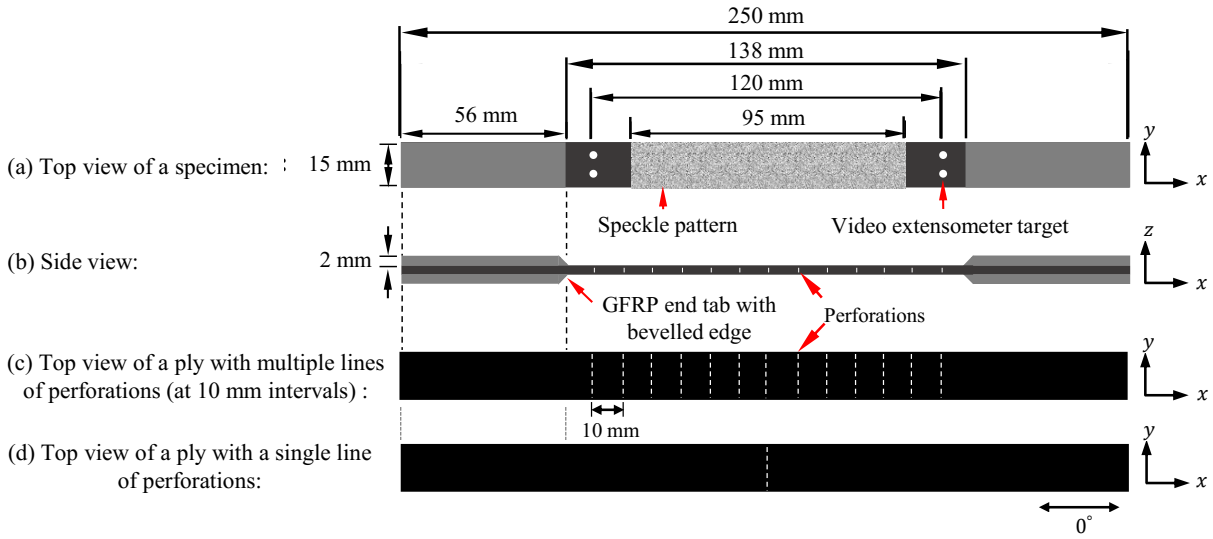


Figure 5.1 Schematic (a) top and (b) side view of a UD tensile specimen containing lines of perforations at 10 mm intervals, (c) the top views of a middle perforated ply in this specimen and (d) top view of a perforated ply containing a single line of perforations in the middle of the gauge length.

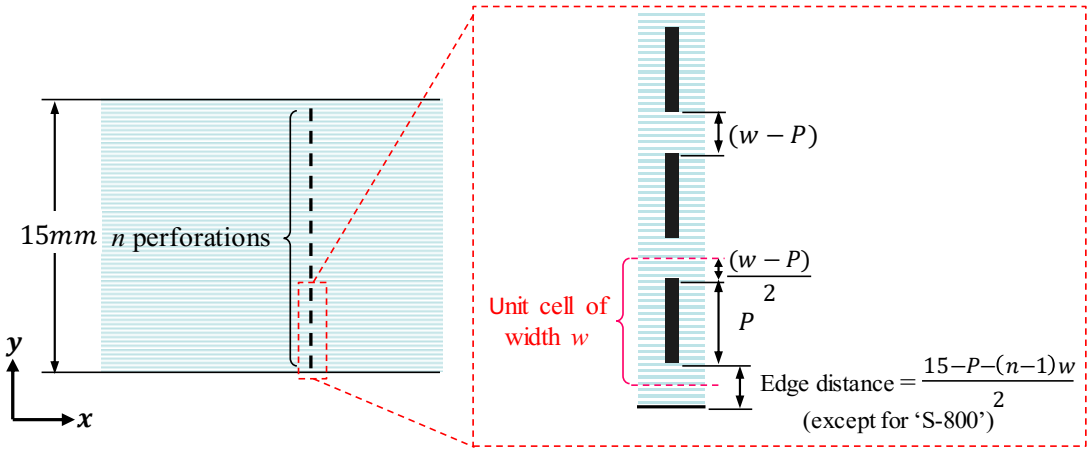


Figure 5.2 Schematic of the geometry of a line of perforations relative to a 15 mm wide specimen.

The first group of configurations were designed to evaluate the effect of increasing perforation length on the tensile response of UD laminates, containing a single line of perforations. The second group of configurations were designed to evaluate the effect of increasing perforation length on the tensile response of UD laminates, containing multiple lines of perforations. A comparison of 'S-800' with 'M-800', as well as 'S-5000' with 'M-5000', would provide an insight into how increasing the number of lines of perforations can affect the specimen behaviour.

Table 5.1 Geometry of (I) UD configurations containing a single line of perforations and (II) UD configurations containing periodic lines of perforations.

Configuration	Group I						Group II		
	(1)	(2)	(3)	(4)	(5)	(6)	(7)	(8)	(9)
Nomination	S-Continuous cut	S-50	S-250	S-500	S-800	S-5000	M-Continuous cut	M-5000	M-800
Perforation length, P [μm]	-	50	250	500	800	5000	-	5000	800
Pitch length, W [μm]	-	75	375	750	1200	7500	-	7500	1200
Perforation to pitch length ratio, P/W	-	$\frac{2}{3}$	$\frac{2}{3}$	$\frac{2}{3}$	$\frac{2}{3}$	$\frac{2}{3}$	-	$\frac{2}{3}$	$\frac{2}{3}$
Number of perforations per line, n	-	200	40	20	12	2	-	2	12

5.2.2 Specimen fabrication

The specimens were manufactured with Hexply® M21/35%/198/T800S carbon fibre/epoxy prepregs. In this case, perforations and the ply alignment holes were introduced in the prepregs using a CNC Oxford® A series/Compact laser micromachining machine, which can achieve sub-micron level control of dimensions. The laser machine working principle can be referred to [109]. The quality and geometry of the perforation is determined by the interplay of the power, the number of passes, the moving speed, the distance between the focusing lens and the prepreg milling surface, and the thermal properties of the fibres and matrix in the prepreg. Heat affected zones in the epoxy can be identified near the perforations [110]. These zones were minimized by adjusting the laser milling parameters. Preliminary research of the laser milling parameters was performed to ensure the prepreg would be completely cut through without excessive resin burning because of accumulated heat, and to achieve accurate perforation lengths within $\pm 5\mu m$ on the front and back surfaces of the 184 μm thick prepreg used here. Using these parameter values, the width of the laser-milled perforations (in the fibre direction) in the M21/T800S carbon fibre/epoxy prepreg was 12 to 15 μm (measured with an optical microscope). An example set of the resulting laser milling parameters are shown in Appendix 2.

The laser working bench was uniformly covered with a layer of double-sided tape. The backing paper side of a layer of prepreg was then fixed onto the tape layer. During this process, the prepreg was kept flat and any air bubbles between the tape and the backing paper were driven out. The release film on the top side of the prepreg was then peeled off and the prepreg could then be cut with the laser.

An example of a cutting pattern containing perforation lines and alignment holes is shown in Figure 5.3. After the laser milling is completed, the prepreg is removed from the working bench by carefully peeling off the backing paper from the adhesive tape while avoiding distortion of the perforations. Alignment holes were also introduced into prepregs used as the pristine plies of the specimens, i.e. without perforation pattern.

The laser-milled prepregs were laid up using the alignment tools that were described in Section 4.2.2 (see Figure 4.3 (b)) to maintain good alignment of perforations in adjacent perforated plies during the subsequent manufacture process. The panel was debulked and then cured in an autoclave using the manufacturer-specified curing cycle [107]. Cross-ply glass fibre/epoxy end tab plates with bevel edges to reduce the stress concentration in the continuous plies next to the tab edges were adhesively bonded to the tabbing region of the CFRP panel, giving a free length of 138 mm (see Figure 5.1). Specimens were cut from the panels using a CNC waterjet cutter. The integrity of specimens was inspected using the Ultrasonic C-scan machine.

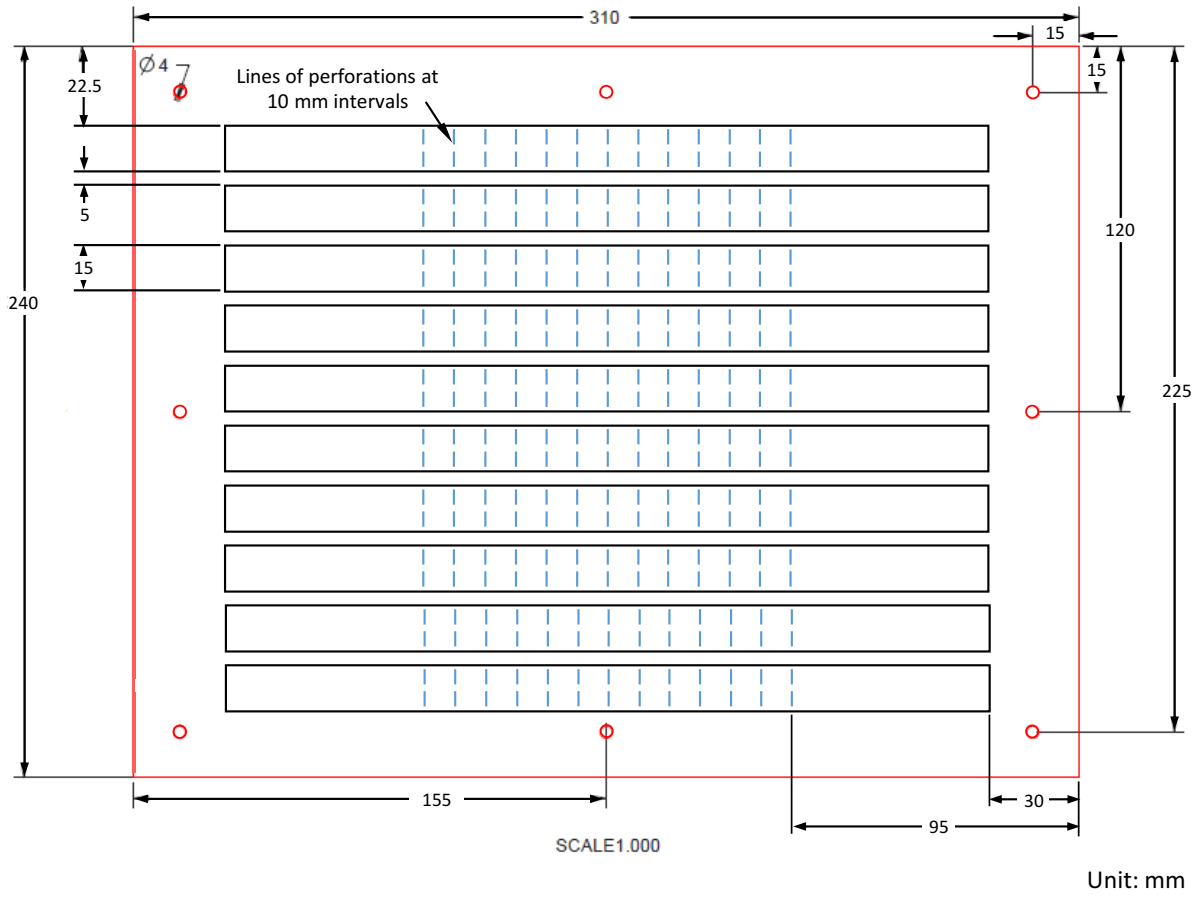


Figure 5.3 Schematic of an example perforation pattern (shown in blue) in a prepreg used to manufacture ten specimens of M-5000 configuration and the outlines of specimens (shown in black) used to separate specimens from the panel.

The X-ray computed tomograms of a specimen shown in Figure 5.4 confirm that the fabrication process achieved accurate perforation length and good alignment of the perforations in adjacent plies.

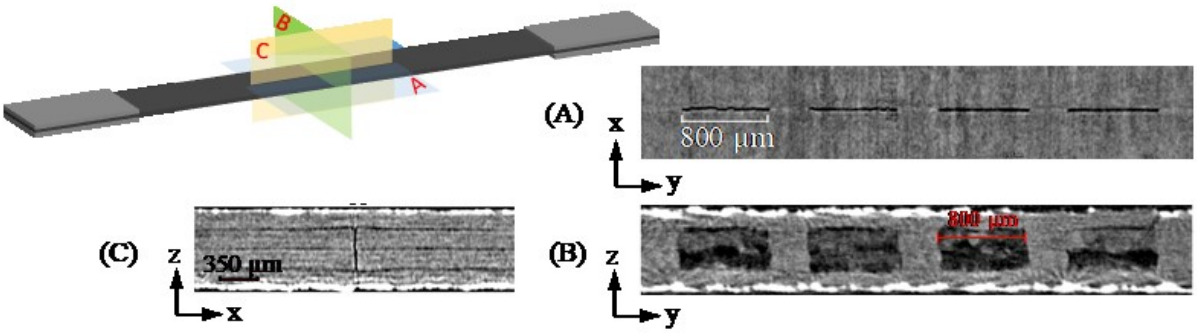


Figure 5.4 X-ray CT images of three sectional planes (A), (B) and (C) of a partially tested 4-ply UD specimen containing S-800 perforation pattern, showing the quality of periodic 800 µm long perforations and well-aligned perforations in the two middle plies.

5.2.3 Mechanical testing

5.2.3.1 Tensile test to ultimate failure

At least five specimens were tested for each configuration up to ultimate failure. The static tensile tests were performed on a 250 kN Instron hydraulic-controlled loading machine. Specimens were held in wedge type grips and loaded in tension with a displacement-controlled crosshead speed of 2 mm/min.

An Imetrum video extensometer was used to measure the global strain at a frequency of 50 Hz, between the target points set at a gauge length of 120 mm on specimen surface (see Figure 5.1). The gauge length is shorter than the free length in order to avoid the influence from potential strain concentration near the end tabs. The GOM® Digital Image Correlation (DIC) system was used to monitor the strain distribution, by tracking the speckle pattern sprayed on the same surface ply. 3D images were acquired at a frequency of 3 Hz by two ARAMIS® 3D stereo cameras with 6-mega pixel resolution and a pixel size of 4.54 μm. The subset/facet size used was 19 ×19 pixel, and the facet distance was 13 pixel.

5.2.3.2 Interrupted tensile test and failure mechanisms characterization

Interrupted tensile tests were performed to investigate the failure mechanisms and damage development processes. The loading was paused and reversed when the synchronized DIC strain maps indicated the interlaminar delamination had partially developed in the gauge length. The specimens were then removed from the Instron machine for damage characterization, performed using an optical microscope and an X-ray CT scanning machine. The resolution of the X-ray CT scanning machine is dependent on the scanning volume. For the specimens examined, the voxel resolution was 12.6 μm in the x, y and z directions. VG studio MAX 2.2 6.64 bit X-ray CT post-processing software was used to analyse the X-ray CT scanning results.

5.3 Results and discussion

5.3.1 Laminates with a single line of perforations

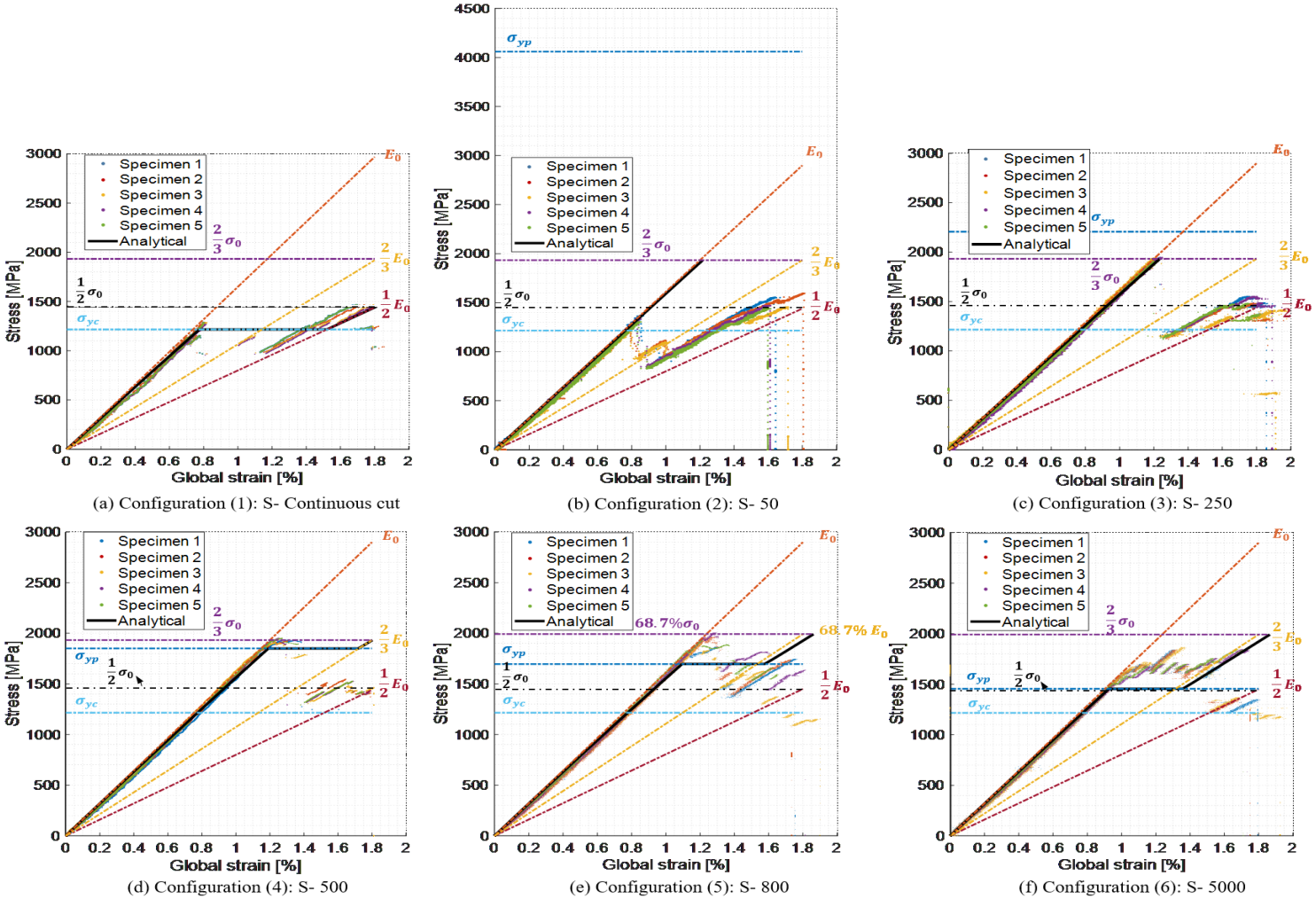
The experimental and analytical stress-strain curves for configurations (1) to (6), which contain a single cut (configuration (1)) or a single line of perforations, are shown in Figure 5.5 (a) to (f). The analytical tensile responses predicted from the refined model (shown in Section 3.6), are also presented in each diagram. The analytical models predict the tensile response over the 138 mm specimen free length (see Figure 5.1). In the experiment, the overall strain was measured using a video extensometer, monitoring the extension over a gauge length of 120 mm, which is shorter than the specimen free length. The analytically predicted response shows very little difference when the strain was calculated using this

shorter gauge length rather than the free length. The measured data is presented as discrete points to reveal the actual specimen behaviour during the tensile loading process.

Each of the stress-strain diagrams shown in Figure 5.5 and Figure 5.6 includes seven reference lines to assist the interpretation of the experimentally observed behaviour. The seven reference lines denote:

- The tensile modulus, E_0 (shown in brown), of a pristine UD baseline laminate;
- The theoretical pseudo-yield stress, σ_{yc} (shown in light blue), for the onset and propagation of delamination in a specimen containing a single continuous cut, i.e. configuration 1;
- The tensile modulus of a 4-ply laminate in which the two central plies have fully delaminated from the outer plies, $\frac{1}{2}E_0$ (shown in red);
- The theoretical pseudo-yield stress, σ_{yp} (in dark blue), for the onset and propagation of bundle debonding in the perforated configurations, i.e. configuration (2) to (6), shown in dark blue (Section 3.3.1);
- The tensile modulus of the perforated configurations, assuming complete debonding of the bundles. For configurations (2) to (4) and (6), this tensile modulus is $\frac{2}{3}E_0$ and for configuration (5), this tensile modulus is 68.7% E_0(shown in yellow);
- The theoretical stress, $\frac{1}{2}\sigma_0$ (shown in black), to cause net section failure in the cut ply configuration, i.e. in configuration (1), assuming no stress concentration due to the presence of the cut.
- The theoretical stress to cause net section failure in the perforated ply configurations (shown in purple), assuming no stress concentration due to the presence of the perforations. This is $\frac{2}{3}\sigma_0$ for configurations (2) to (4) and (6), and 68.7% σ_0 for configuration (5).

Figure 5.5 shows experimental results and analytical predictions and Figure 5.6 shows only the experimental results. Key mechanical properties extracted from the experimental and the refined model predictions for all six configurations are presented in Table 5.2.



(a) Configuration (1): S- Continuous cut

(b) Configuration (2): S- 50

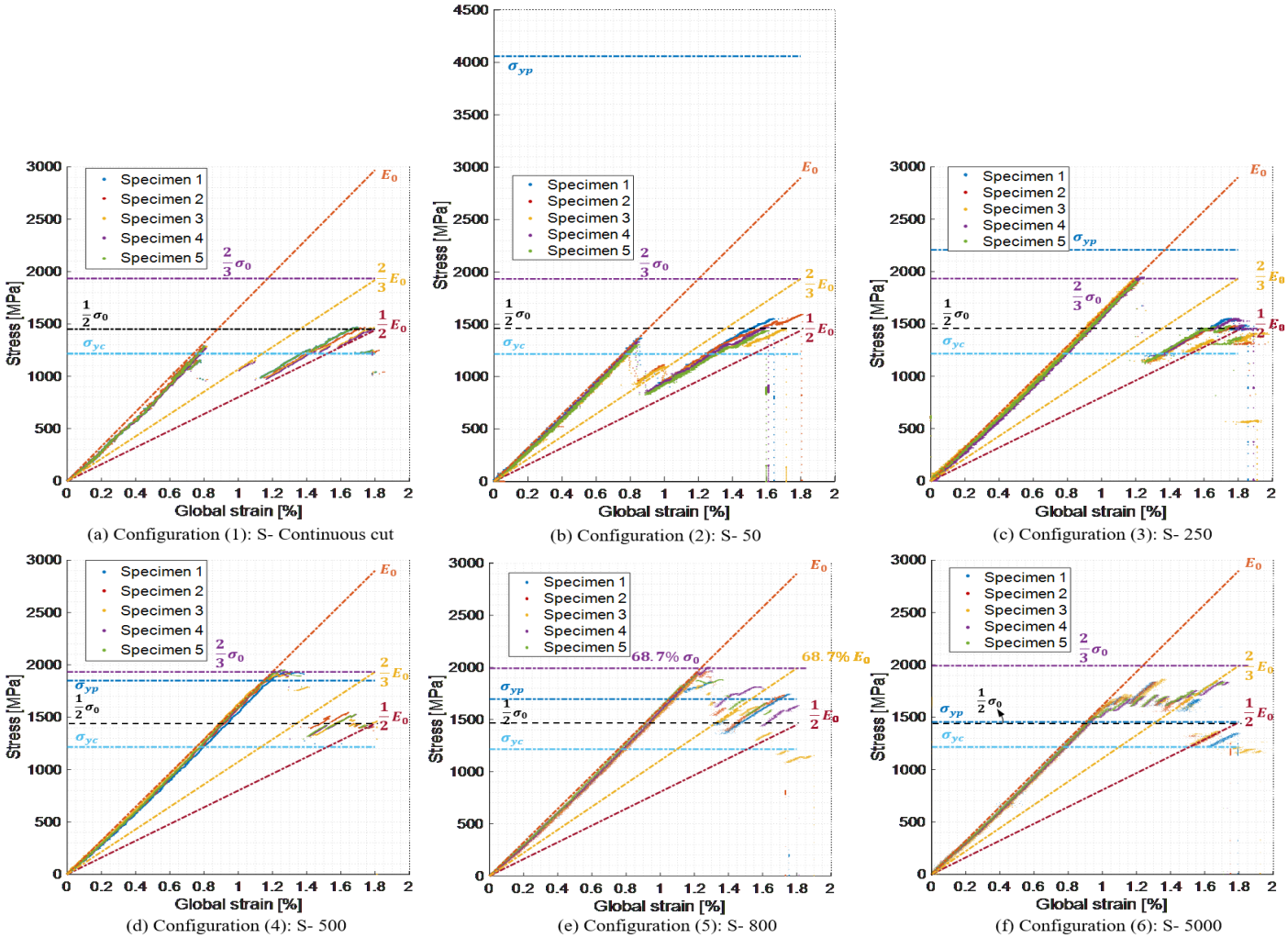
(c) Configuration (3): S- 250

(d) Configuration (4): S- 500

(e) Configuration (5): S- 800

(f) Configuration (6): S- 5000

Figure 5.5 Analytical and experimental tensile stress-strain curves of UD 4-ply configurations containing a single line of (a) S-Continuous cut and (b) S-50, (c) S-250, (d) S-500, (e) S-800 and (f) S-5000 perforation patterns, respectively.



(a) Configuration (1): S- Continuous cut

(b) Configuration (2): S- 50

(c) Configuration (3): S- 250

(d) Configuration (4): S- 500

(e) Configuration (5): S- 800

(f) Configuration (6): S- 5000

Figure 5.6 Experimental tensile stress-strain curves of UD 4-ply configurations containing a single line of (a) S-Continuous cut and (b) S-50, (c) S-250, (d) S-500, (e) S-800 and (f) S-5000 perforation patterns, respectively.

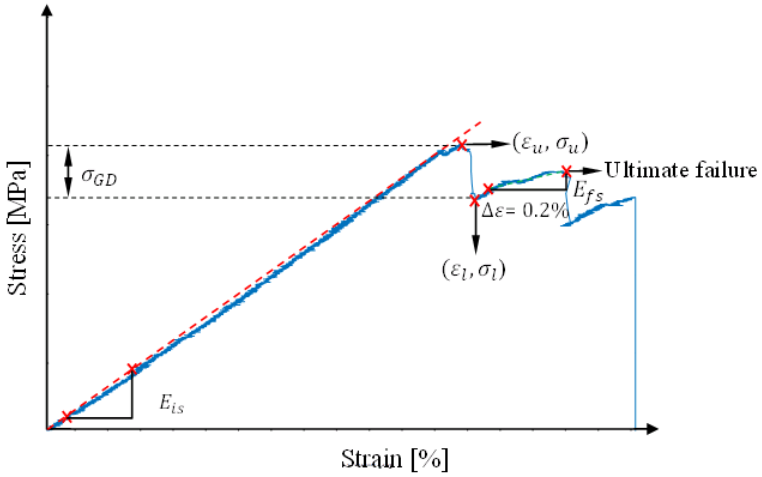
Table 5.2 Key tensile properties of UD 4-ply laminates containing a single line of continuous cut and perforations of various lengths. (Coefficient of variation, in %, is given in the parentheses.)

Specimen Type	Initial modulus E_{is} [GPa]		Pseudo-yield point/Upper point at first load drop $(\varepsilon_u, \sigma_u)$* [%, MPa]		Lower point at first load drop $(\varepsilon_l, \sigma_l)$ [%, MPa]		Stress drop amount σ_{LD} [MPa]		Strain-hardening modulus E_{ft} ** [GPa]		Ultimate failure point $(\varepsilon_{ult}, \sigma_{ult})$ *** [%, MPa]	
	Anal.	Exp.	Anal.	Exp.	Anal.	Exp.	Anal.	Exp.	Anal.	Exp.	Anal.	Exp.
(1) S-cut	158.6	153 (3.30%)	(0.77, 1216)	(0.81, 1284) (0.81%, 0.61%)	---	(0.80, 969) (2.19%, 1.84%)	---	356 (21.44%)	80	82 (5.78%)	(1.81, 1440)	(1.74, 1461) (3.04%, 0.57%)
(2) S-50	159.2	154 (1.35%)	---	(0.82, 1294) (3.62%, 4.75%)	---	(0.88, 865) (5.22%, 6.31%)	---	386 (2.48%)	---	98 (7.97%)	(1.22, 1933)	(1.67, 1501) (5.48%, 4.53%)
(3) S-250	159.1	154 (3.35%)	---	(1.22, 1930) (1.14%, 1.11%)	---	(1.29, 1174) (2.14%, 2.65%)	---	770 (2.89%)	---	89 (23.22%)	(1.23,1933)	(1.76, 1499) (10.4%, 15.4%)
(4) S-500	158.8	153 (1.70%)	(1.19, 1849)	(1.28, 1932) (5.21%, 1.39%)	---	(1.34, 1322) (3.09%, 4.47%)	---	610 (11.88%)	107	95 (14.86%)	(1.80, 1933)	(1.66, 1533) (1.98%, 0.11%)
(5) S-800	158.6	153 (2.81%)	(1.09, 1696)	(1.20, 1893) (5.93%, 3.54%)	---	(1.20, 1764) (5.21%, 7.98%)	---	129 (78.3%)	103	89 (16.26%)	(1.81, 1933)	(1.66, 1663) (5.06%, 4.53%)
(6) S-5000	158.0	153 (5.88%)	(0.94, 1454)	(1.00, 1564) (4.48%, 2.89%)	---	(1.20,1850) (2.54%, 3.92%)	---	61 (43.82%)	101	106 (22.13%)	(1.81,1933)	(1.70, 1745) (5.91%, 5.27%)

* For tensile stress-strain response containing unstable load drops immediately following the initial stage, the pseudo-yield point is determined as the point at the onset of the first load drop.

** For the analytical and experimental tensile responses without significant load drop close to failure, the ultimate failure point is defined as the point with the maximum stress; For experimental tensile responses with load drop(s) close to failure, the ultimate failure point is taken as the first point that is followed by a stress drop with more than 15% reduction in stress.

*** The analytical and experimental strain-hardening stage moduli are taken as the chord moduli defined by ultimate failure point and the point with 200$\mu\varepsilon$ lower strain, if no load drop appears in the strain-hardening stage; For the experimental tensile responses containing load drops in that 200 $\mu\varepsilon$ strain range, the modulus is defined between the point immediately following the load drop and the ultimate failure point (as shown in the example stress-strain diagram below).



5.3.1.1 **Configuration (1): a single continuous cut**

The experimental and analytical tensile responses of configurations (1), which contains a single continuous cut in the two middle plies have been presented and analysed in Chapter 4 are shown in Figure 5.5 (a). The experimental results (without analytical curve) are shown in Figure 5.6 (a)) for clarity. The experimental stiffness of the initial stage shows good correlation with that predicted by the refined model. The stiffness of the initial stage is close to that of a pristine baseline material, i.e. has a modulus close to E_0, indicating the evolution of stress transfer zones initiated from the central cut causes no significant stiffness reduction. Sudden drops in stress are observed and initially occur at stresses, which are in close agreement with the analytically predicted pseudo-yield stress. The stress at which the stress drops occur is 5.5% (on average) higher than the predicted pseudo-yield stress (see Table 5.2). These stress drops are attributed to the catastrophic unstable mode II delamination at the interfaces above and below the two central plies. The average stiffness of the final almost-linear strain-hardening stage is slightly higher than $\frac{1}{2}E_0$, indicating the two middle plies are largely but not completely delaminated from the two outer continuous plies. The ultimate fracture stresses show good agreement with $\frac{1}{2}\sigma_0$, the theoretical stress to cause net section failure.

5.3.1.2 **Configuration (2): a single line of 'S-50' perforations**

The tensile response of configuration (2) containing the shortest of 50 μm length perforations, is shown in Figure 5.5 (b) and Figure 5.6 (b). The experimental tensile response (see Figure 5.6 (b)) closely resembles that of configuration (1). The slope of the initial stage shows good agreement with the analytical prediction and the E_0 reference line. This agreement indicates that the stress transfer zones initiated from the perforations have no significant influence on the initial stage. A catastrophic load drop appeared at an average stress of 1253 MPa. The stress at the load drop is over three times lower than the analytically predicted stress, σ_{yp}, of 4059 MPa (calculated from Eq. 3.8 in Section 3.3.1), at the onset of debonding of the fibre bundles from these 50 μm perforations. Of course, such a high stress could never be reached by this material, since the net-section failure stress (i.e. $\frac{2}{3}\sigma_0$, equivalent to 1933 MPa) is much lower than the analytical σ_{yp}. The stress at the load drop is close to the stress observed at the onset of delamination in configuration (1). This suggests that the perforation line acts like a continuous cut, which requires the continuous fibres between the perforations to have broken prior to the load drop. This is confirmed in the microscopic and SEM photograph, in Figure 5.7 (a) and (b), which show that the fractures for most of the fibres in the unperforated bundles, almost coincide with the perforated planes. The cusps visible on the surface of the delaminated perforated plies (see Figure 5.7 (c)) in the regions of discontinuous and continuous fibre bundles confirm that the delamination is

dominated by mode II [111], as expected, and that failure of the perforated bundles occur before the delamination process. The continuous fibres in the perforated plies fail at a stress lower than the stress to propagate delamination growth from a continuous cut and this delamination stress is much less than the stress predicted to cause net-section failure ($\frac{2}{3}\sigma_0$). There are two possibilities to account for the failure stress of the continuous fibres in the perforated plies. Either the fibres in the unperforated regions adjacent to the laser perforated regions may have been damaged by the laser milling process or the perforations cause a significant stress concentration in the unperforated region.

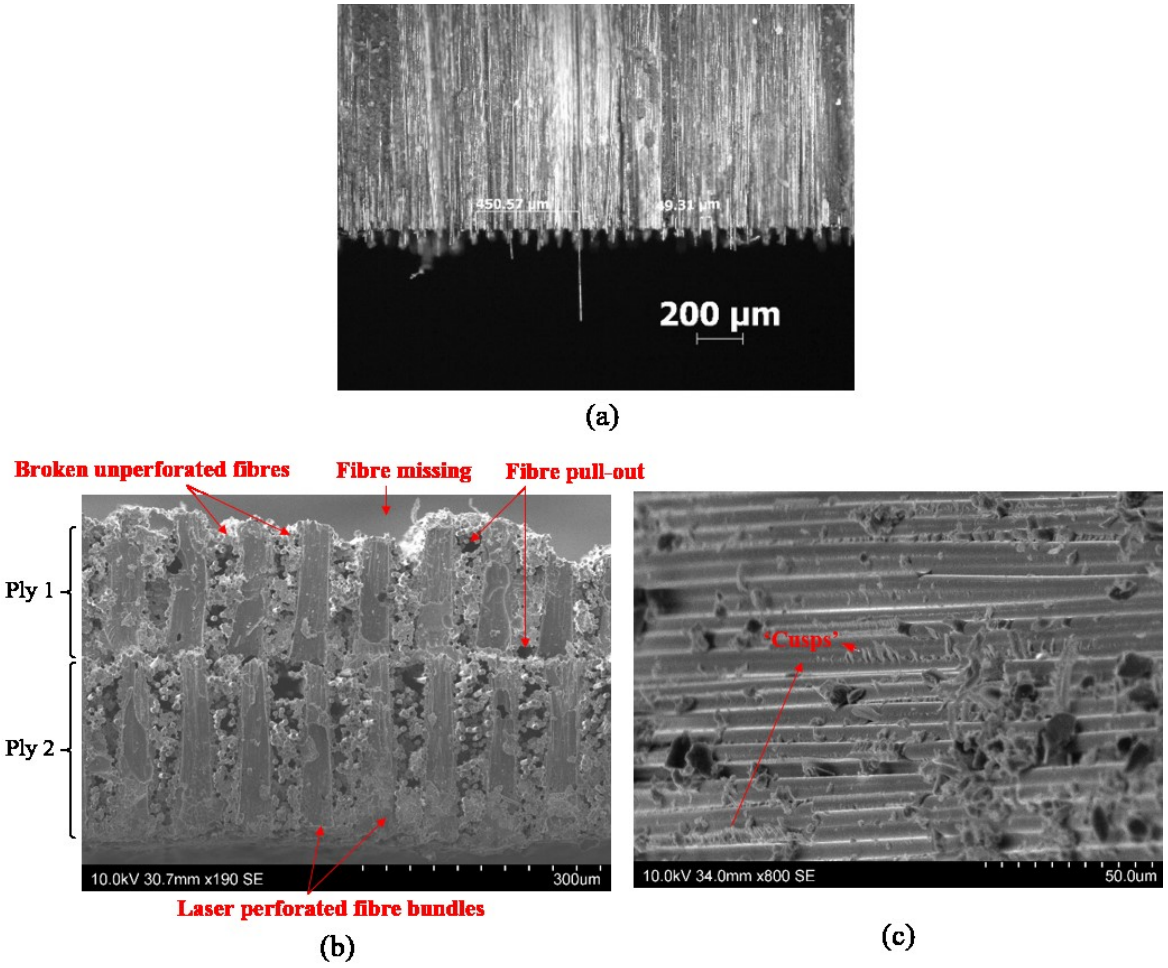


Figure 5.7 (a) Optical microscopic image of the top view and SEM topographs of (b) the cross-section of the two middle perforated plies with well-aligned 50 µm perforated fibre bundles and (c) the top view of a perforated ply, showing the typical matrix 'cusps' formed by interlaminar shearing, in a tested 'S-50' specimen.

For specimens (2) and (3), the load drop is followed by an intermediate short almost-linear stage with an average stiffness close to $\frac{2}{3}E_0$. This is because delamination initiated from the almost continuous cut developed unsymmetrically towards one of the two tabs. This intermediate load drop is followed by

another load drop, where delamination is developed towards the other tab. For the other specimens, the stress at the end of initial stage immediately dropped to the final strain-hardening stage, as delamination was propagated ideally towards both tabs.

The average stiffness and ultimate failure stress of the final strain-hardening stage of configuration (2) are both higher than those of configuration (1) (See Table 5.2). This is attributed to the continuous fibre bundles in the two perforated plies were not completely failed before the load drop. It is confirmed by the cross-sectional SEM image shown in Figure 5.7 (b), which indicates the delamination propagated inside the top perforated ply.

5.3.1.3 **Configuration (3): a single line of 'S-250' perforations**

The experimental and analytical tensile responses of configurations (3), which contains a line of 250 μm perforations in the two middle plies are shown in Figure 5.5 (c). The experimental results (without analytical curve) are shown in Figure 5.6 (c)). The experimental stiffness of the initial stage shows good correlation with that predicted by the refined model, and both present negligible reduction in stiffness.

The analytical pseudo-yield stress, σ_{yp}, (of approximately 2207 MPa) for debonding of the perforated fibre bundles in this case is still higher than the predicted stress for net section tensile failure, $\frac{2}{3}\sigma_0$. The predicted tensile response therefore shows ultimate failure at $\frac{2}{3}\sigma_0$, i.e. complete failure at the net section (and no debonding around the perforated fibre bundles). Figure 5.8 shows the strain contour plots and the axial strain distribution plots along two longitudinal section lines (captured by the DIC system) for selected load levels of specimen (4), shown in Figure 5.6 (c). The strain distribution plots contain three reference lines to assist the damage mode analysis. The reference lines are related to the theoretical strains at a specific load, P_i, and are calculated as follows:

- Assuming the load is carried by the full specimen cross section, i.e. $\varepsilon = \frac{P_i}{AE_0}$, where A is the gross cross-sectional area of the specimen;
- Assuming the load is carried only by the unperforated parts, i.e. $\varepsilon = \frac{3P_i}{2AE_0}$;
- Assuming the load is only carried by the outer continuous plies, i.e. $\varepsilon = \frac{2P_i}{AE_0}$.

Strain contour plots at loads P_1 and P_2 indicate that the stress transfer zones have been initiated from the perforation line and developed about 5mm towards each end. At load level P_3, just prior to the load drop in the load-time response, the corresponding axial strain plot shows the peak strains measured

from the two positions across the specimen width both appear at the perforated lines. The peak strains are both close to the reference strain for debonding, $\frac{3P_3}{2AE_0}$ (i.e. 1.83%). The distribution of strain outside of the stress transfer zone shows good agreement with the reference strain of $\frac{P_3}{AE_0}$ (i.e. 1.22%), indicating no damages exists in these regions. Immediately after P_3, the load suddenly drops to P_4 and it can be seen from Figure 5.6 (c) that this drop occurs close to the net section failure stress of $\frac{2}{3}\sigma_0$. The enlarged view in Figure 5.8 of the specimen edge at load level P_4, shows that the interior plies have failed at the perforation line, and have delaminated and displaced laterally, so that they appear outside of the original specimen edge. The approximately 1.67 mm gap, that has opened up at the perforation line, also indicates significant delamination of the perforated plies has occurred. The strain distribution curves at this load level show good agreement with the predicted reference strain for delamination, $\frac{2P_4}{AE_0}$ (i.e. 1.51%). This confirms that the specimen has delaminated in the 50 mm long DIC monitored region. However, the overall strain at this load level is 1.29% (see Figure 5.6 (c)) and this may suggest that roughly 70% of the gauge length is delaminated (and exhibiting a strain of 1.51%) and the rest of the gauge length is non-delaminated, and associates with an average axial strain of 0.75%. The stress-strain curve for specimen (4) in Figure 5.6 (c) shows a drop when the stress reaches σ_{yc}, (i.e. the theoretical stress for delamination growth) and the slope of the curve in the subsequent stage is very close to the reference of $\frac{1}{2}E_0$. Other specimens do not show this characteristic and remain with a high stiffness throughout the strain-hardening stage. These stiffer strain-hardening stages may be because of some continuous fibres in the perforated plies remained intact after the onset of load drop (i.e. the delamination growth in some places is not at the interface between the outer and inner plies but partially within the inner plies). This would also account for the strengths of these specimens exceeding $\frac{1}{2}\sigma_0$. The strain contour plot also shows a minor surface ply splitting. At a higher load level for specimen (4), for example P_5 in the final strain-hardening stage (see Figure 5.8), the experimental strain distribution continues to show good correlation with the reference strain for delamination, $\frac{2P_5}{AE_0}$ (i.e. 1.84%), although it is now accompanied with some edge fibre breakage, indicating the specimen is close to net section failure. The corresponding strain distribution curve shows some localized strains exceeded 2% (see Figure 5.8), close to the strain-to-failure of the fibres, at this point. At load level P_6, a wide strip of continuous plies has failed, resulting in another significant drop in the stress-strain curve before ultimate failure (see Figure 5.6 (c)).

Specimen (3) behaves quite differently compared to the other specimens of this configuration (see Figure 5.6 (c)). After the significant load drop, the elastic modulus was much less than $\frac{1}{2}E_0$. This is

because of the failure of a strip (of about 3 mm wide) of outer continuous plies in addition to the failure that occurred in the perforated plies.

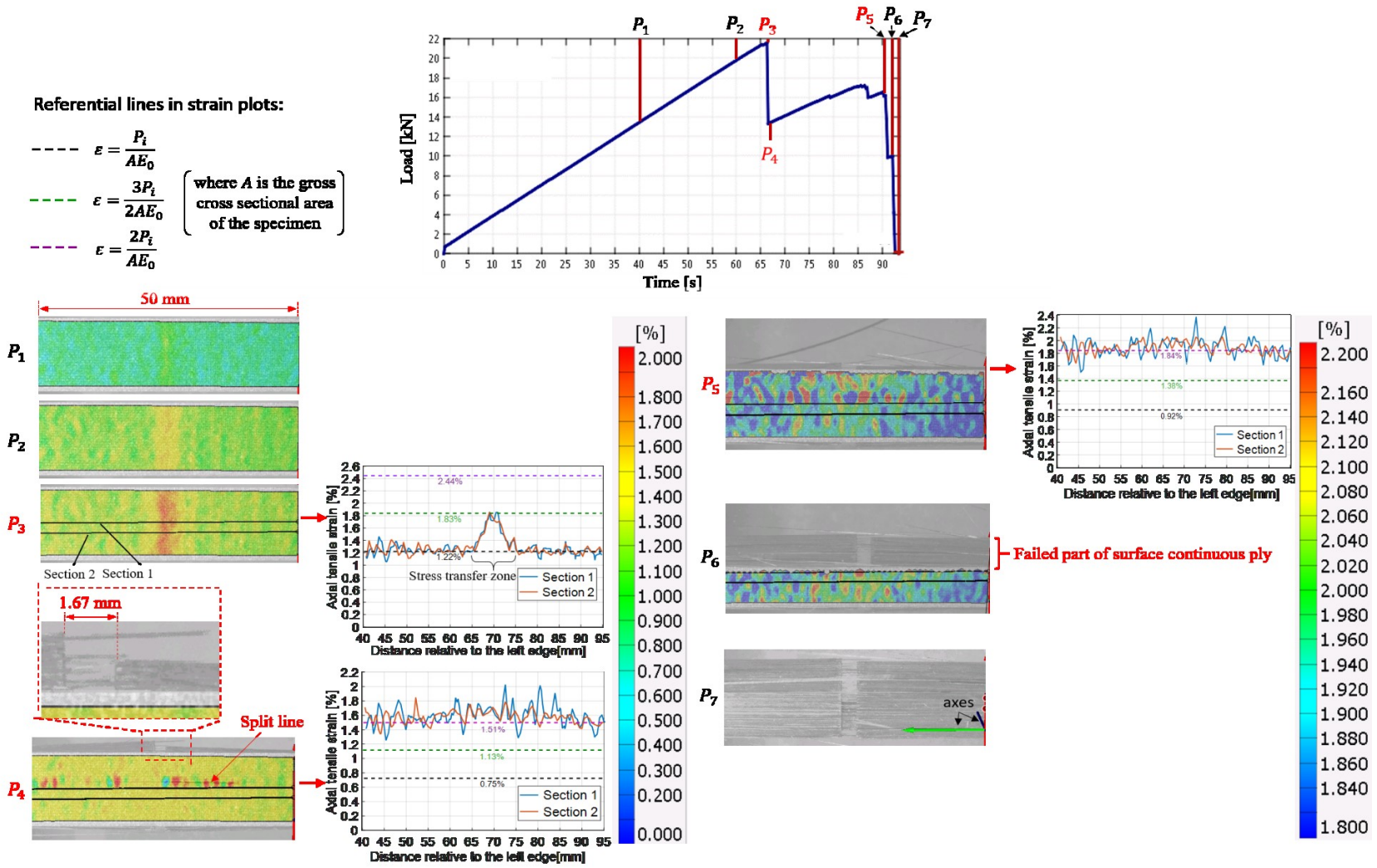


Figure 5.8 Tensile load-time diagram of specimen (4) of configuration (3) and the DIC contour plots of the 50 mm long middle part of the gauge length at seven load levels and the axial strain distribution along two section lines for P_3, P_4 and P_5 (different strain colour scale is used for P_5 to P_7).

5.3.1.4 **Configuration (4): a single line of 'S-500' perforations**

The analytical tensile response of configuration (4) (see Figure 5.5 (d)) consists an initial almost-linear stage with negligible stiffness reduction, an intermediate plateau at a pseudo-yield stresses, σ_{yp}, of 1849 MPa and a short final strain-hardening stage, prior to ultimate failure at the net section failure stress of $\frac{2}{3}\sigma_0$, i.e. 1933 MPa. Note that σ_{yp} and $\frac{2}{3}\sigma_0$ are very close in this configuration. Experimentally, shorter plateaux, as shown in Figure 5.6 (d), were obtained after the stress exceeded the analytical σ_{yp}, and just reached the net section failure stress, $\frac{2}{3}\sigma_0$. These short plateaux are followed by a significant load drop. For specimens (1) to (4), the final strain-hardening stages have an average stiffness lying approximately mid-way between $\frac{1}{2}E_0$ and $\frac{2}{3}E_0$ (see Figure 5.6 (d) and Table 5.2) and ultimate failure occurred at an average stress of 1533 MPa, which is 5.7% higher than the reference $\frac{1}{2}\sigma_0$.

Figure 5.9 shows the load-time diagram of specimen (5), shown in Figure 5.5 (d) and Figure 5.6 (d). The DIC strain contour plots and axial strain distribution plots along two section lines for six selected load levels P_1 to P_6 are also presented to assist the damage mode analysis. The strain contour plots and strain distribution curves for load levels P_1 and P_2 indicate the stress transfer zones have developed from the perforation line, with a peak strain value of about 1.5 times the average strain in the rest of the gauge length. At load level P_2, which is close to the load for net section failure and just before the load drop, the stress transfer zone has developed to about 20 mm long. The peak strain along section line 1 exceeded 2.1%, leading to the breakage of some continuous fibres and this loss of fibres would be expected to give rise to strains at the net section and outside of the stress transfer zone, which were higher than the $\frac{3P_2}{2AE_0}$ and $\frac{P_2}{AE_0}$ references, i.e. 1.84% and 1.23% respectively, as can be seen in Figure 5.9. Immediately after load level P_2, there is a sudden load drop, which arrests at P_3. The strains along the two section lines at P_3 indicate that debonding around the perforated fibre bundles appears to have developed throughout the DIC monitored region and that an additional region of delamination (between the continuous and perforated plies) has developed from the perforation line. The strain magnitudes remote from, and at the perforation line, are close to the values of $\frac{3P_3}{2AE_0}$ and $\frac{2P_3}{AE_0}$, respectively, but are slightly higher, presumably due to the fibre breakage, which is visible in the DIC image. The process of delamination indicates the breakage of some of continuous fibre bundles in the perforated plies at the perforation line. Another significant load drop to P_4 resulted in the further propagation of delamination throughout the entire free length, as shown in the strain distribution plot for this load. Severe continuous fibre breakage occurred on loading from P_4 to P_5, resulting in the axial strain along both section lines to be even higher than the reference value of $\frac{2P_5}{AE_0}$, i.e. 1.48%. Beyond P_5, further fibre failure resulted in more minor load drops and final failure. Specimens (1) to (4) show a different failure

curve with a stiffness in the strain-hardening phase, which is significantly higher than that of specimen (5) and lying between $\frac{1}{2}E_0$ and $\frac{2}{3}E_0$. It is likely that this is associated with the propagation of debonding, accompanied by some fibre breakage and incomplete delamination growth.

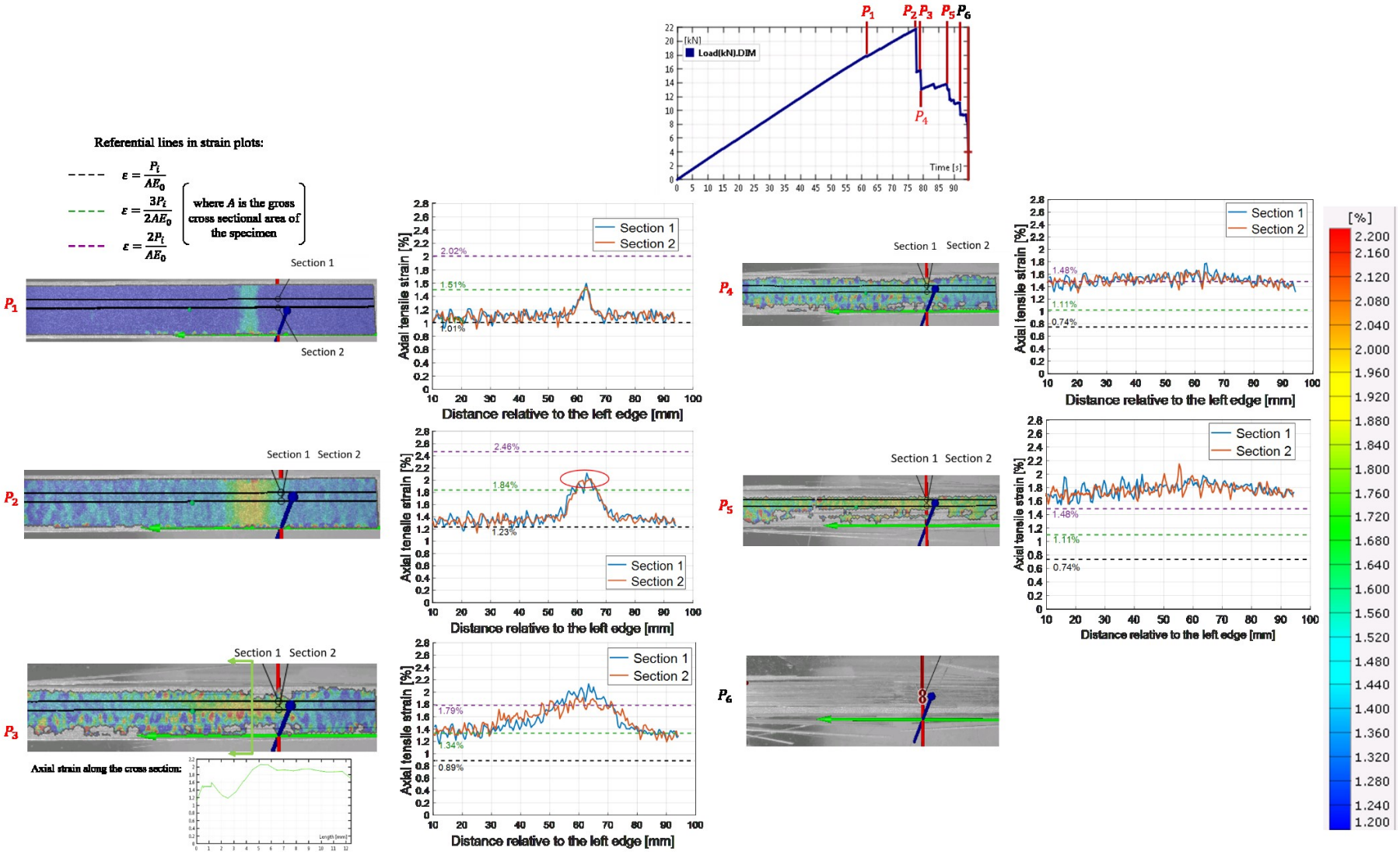


Figure 5.9 DIC images and strain distribution along two sectional lines at selected load levels for a specimen of configuration (4), i.e. 'S-500'.

5.3.1.5 **Configuration (5): a single line of 'S-800' perforations**

In the specimens of configuration (5), the non-perforated section is approximately 68.7% of the gross cross section and the reference lines in Figure 5.5 (e) and Figure 5.6 (e) were adjusted accordingly. The analytical tensile response of configuration (5) (see Figure 5.5 (e)) consists an initial almost-linear stage with negligible stiffness reduction, an intermediate plateau at a pseudo-yield stress, σ_{yp}, of 1696 MPa and a final strain-hardening stage, prior to ultimate failure at 1932 MPa, i.e. $68.7\%\sigma_0$. This configuration has lower analytical pseudo-yield stress compared to configuration (4) and therefore exhibits a shorter plateau.

Experimentally, the initial stiffness shows good agreement with the analytically predicted value, but the intermediate plateau was not observed. Instead, the initial stage continued beyond the predicted pseudo-yield stress, σ_{yp}, with specimens (2) and (4) even reaching the reference net section failure strength of $68.7\%\sigma_0$. A yielding-like behaviour with a reduction in stiffness was observed at the end of the initial stage, which is immediately followed by different numbers of load drops of varying magnitude. The tensile performance after the initial load drop consists of a series of re-loading and load drop stages with a significant variation between the individual specimens. The average stiffness of the final strain-hardening stages is 107 GPa with a very high coefficient of variation (CoV) of 16.24% (with the strain-hardening stage stiffness defined in Table 5.2). Ultimate failure appears at a stress of approximate 1662 MPa (with a CoV of 4.53%), i.e. 16.26% lower than the analytically predicted strength.

Figure 5.10 presents the strain contour plots for specimen (3) at selected load levels shown on the load-time curve. The axial strain distribution along two section lines for load levels P_2, P_3, P_4, P_6 P_7 and P_8 are also presented to help analyse the damage modes. Stress transfer zones initiated from the line of perforations can be observed from the first two strain contour plots. The peak strain of the perforated position at load P_2 (at the peak load of the load-time curve), is about 1.5 times that of the unperforated region (for both section lines) as expected. Minor breakage of fibres along the specimen bottom edge (indicated as the loss of target points in the DIC monitored area), appeared at the small load drop between $P_1$and P_2. The peak load, P_2, is followed by a small reduction in load, where an expansion of the stress transfer zone width is observed along the section line 1 and the peak strain values are close to $\frac{3P_3}{2AE_0}$ (i.e. 1.71%). This indicated that debonding has propagated along this section line. However, the stress transfer zone width is smaller for section line 2, which suggests the debonding growth is non-uniform over the width of the specimen. The debonding continues to propagate axially along the perforated fibre bundles up to load level P_4, which is just prior to a significant load drop. After the load drop, debonding gradually developed throughout the left part of the specimen, as shown in the strain contour plots and strain curves for load levels P_5, $P_6$and P_7. This debonding was accompanied by more fibre breakage on the surface continuous plies and on the specimen edges. At these load levels, strains

of the debonded region are about 1.5 times those of the pristine region, i.e. $\frac{3P_i}{2AE_0}$, as expected. At load level P_9, a wide strip of the continuous ply failed and complete failure occurred shortly after.

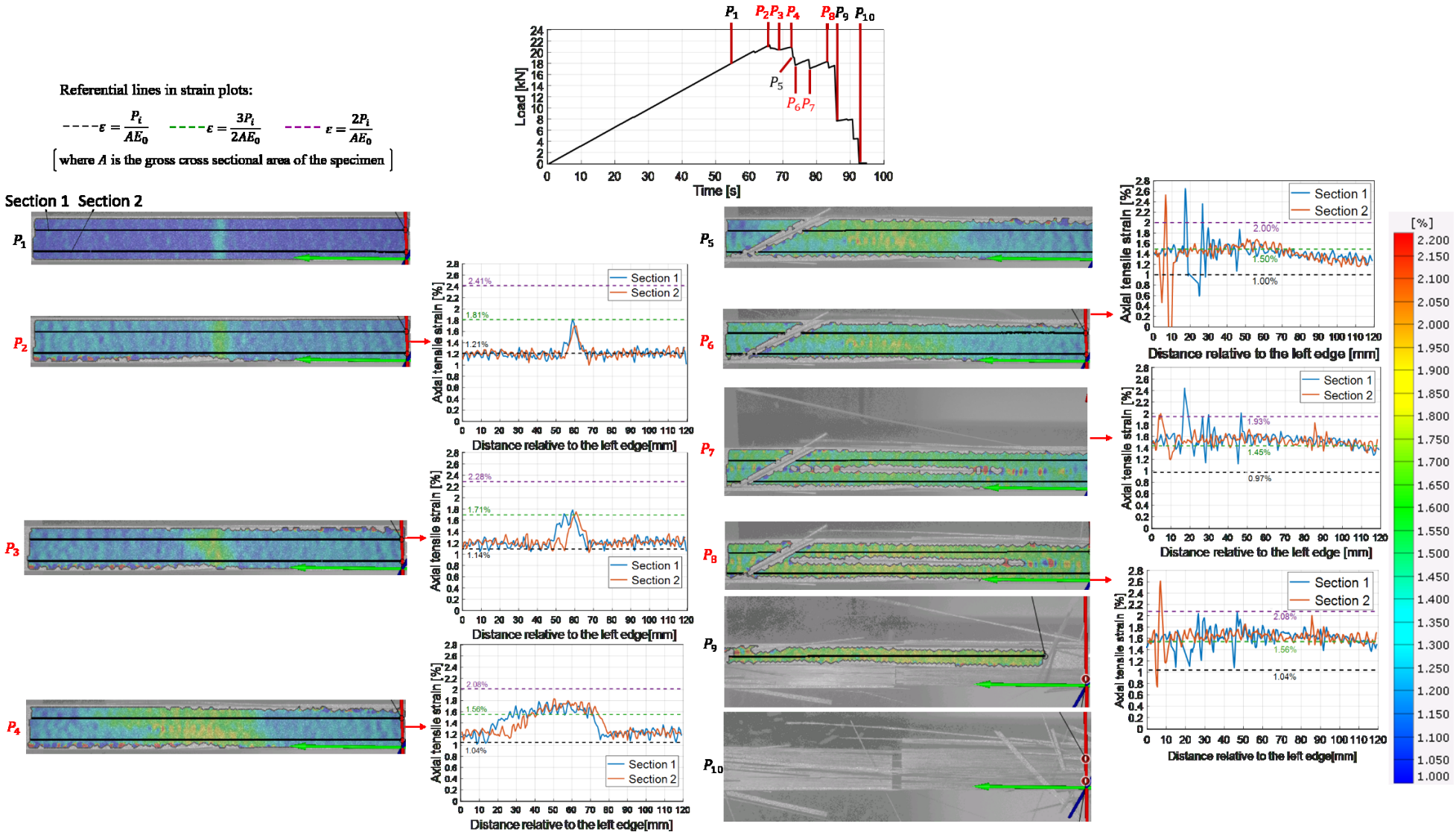


Figure 5.10 DIC images and strain distribution along two sectional lines at selected load levels for specimen (3) of configuration (5), i.e. 'S-800'.

5.3.1.6 **Configuration (6): a single line of 'S-5000' perforations**

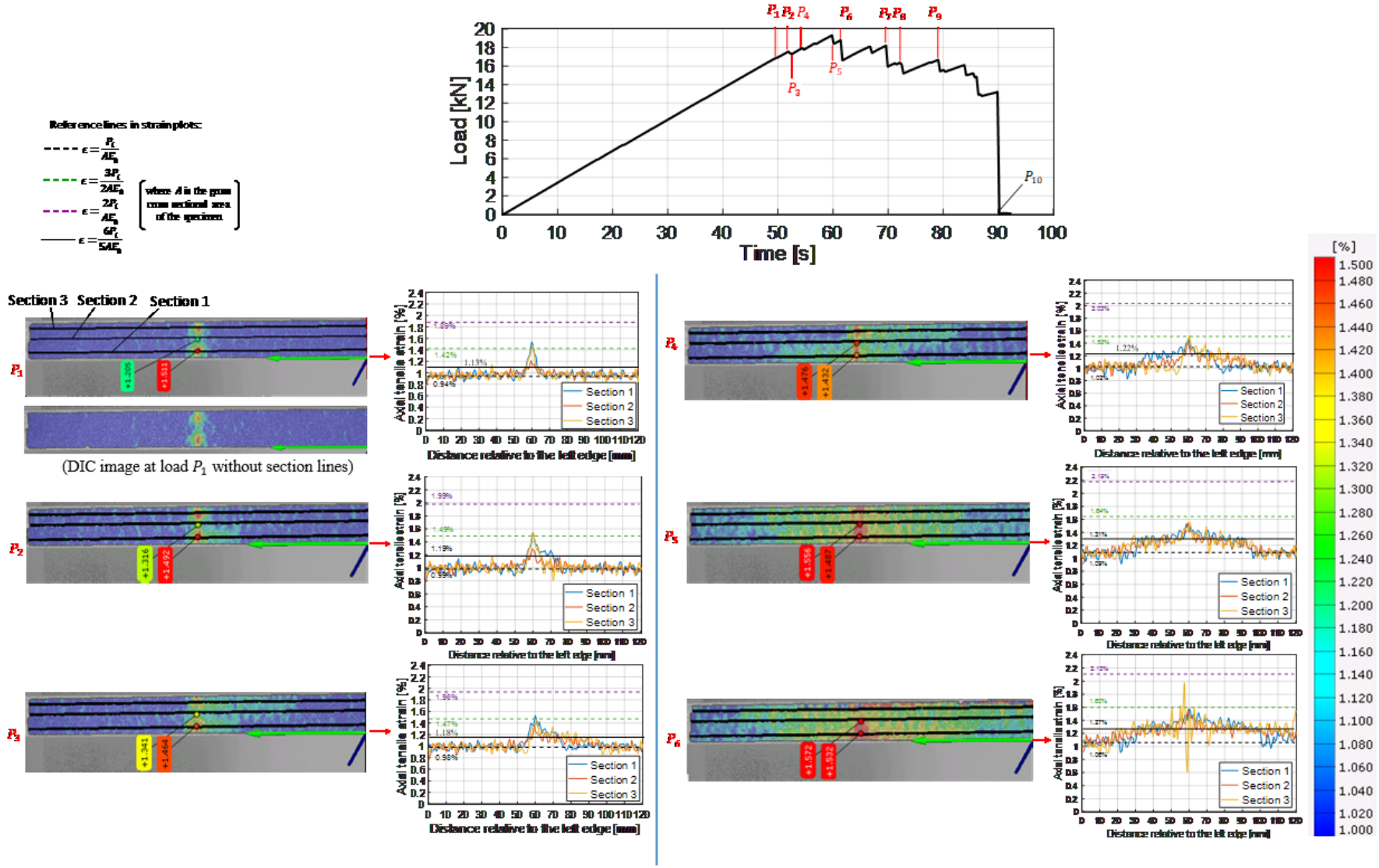
The analytical tensile response of configuration (6) (see Figure 5.5 (f)) consists an initial almost-linear stage with negligible stiffness reduction, an intermediate plateau at a pseudo-yield stresses, σ_{yp}, of 1454 MPa, and a final strain-hardening stage, with a final slope very close to $\frac{2}{3}E_0$ and an ultimate strength of $\frac{2}{3}\sigma_0$. This configuration gives a lower analytical pseudo-yield stress compared to configuration (5) and therefore exhibits a shorter plateau.

Experimentally, the initial stiffnesses of all specimens show good agreement with the analytically predicted value. After the tensile stress exceeded the analytical pseudo-yield stress, multiple load drops and re-loading stages with gradually reduced stiffness that lie between the E_0 and $\frac{2}{3}E_0$ reference lines were observed from specimens (2), (4) and (5), before entering to the final strain-hardening stage, which shows good agreement with the analytically predicted strain-hardening stiffness (see Figure 5.6 (f) and Table 5.2). Specimens (1) and (3) show very low stiffness in the final strain-hardening stage.

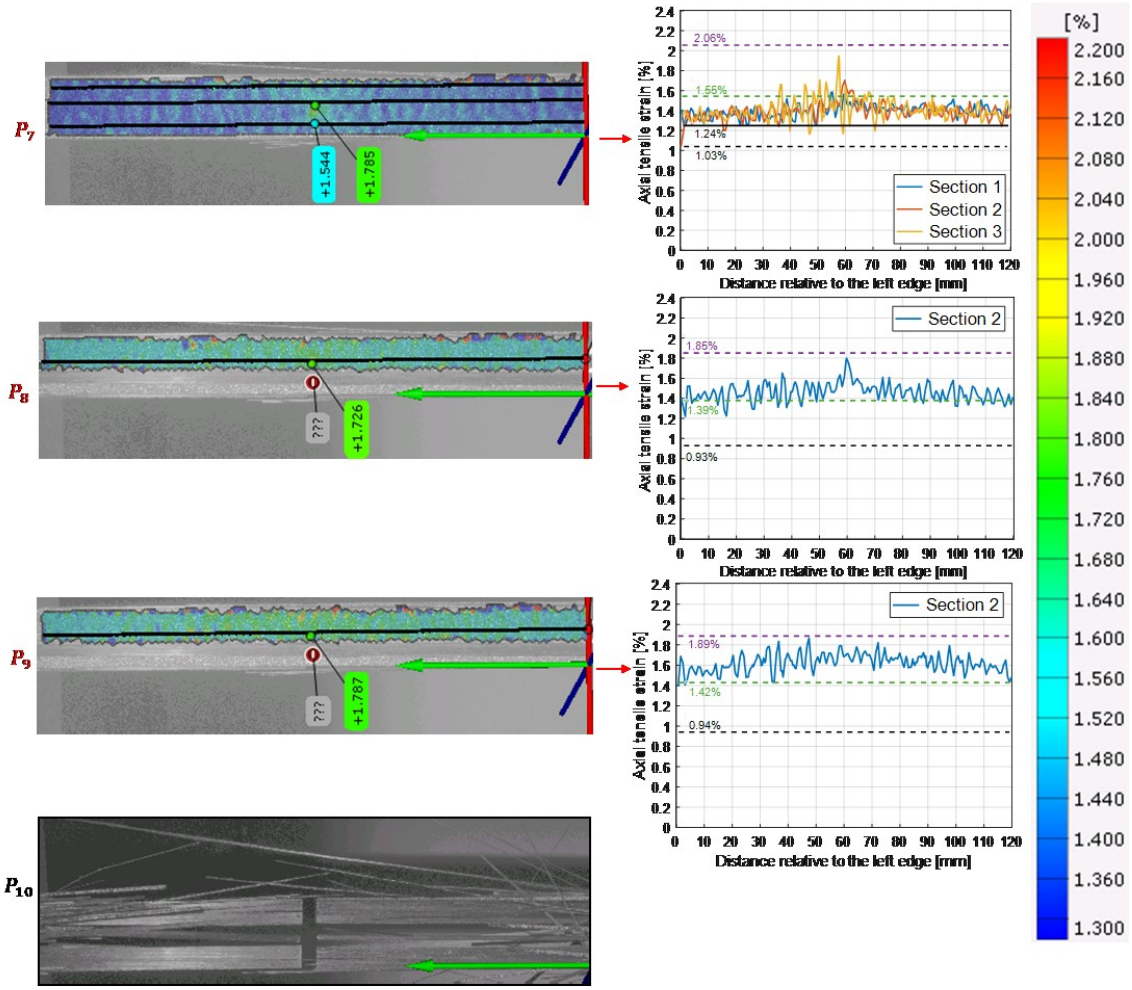
Figure 5.11 presents the strain contour plots for specimen (3) at the selected load levels P_1 to P_{10} labelled in the load-time curve. The surface axial strain distribution along three section lines for load levels P_1 to P_9 are also presented for damage mode analysis. Section lines 1 and 3 lie above perforated bundles and section line 2 lies above the unperforated section. In addition to the reference lines used earlier, one other line representing the average strain in the debonded parts if debonding only occurred along one of the two perforated fibre bundles, i.e. $\frac{6P_i}{5AE_0}$, is included in the axial strain distribution curves.

The strain contour plots for load level P_1 show stress transfer zones have been initiated from the two interior 5000 μm long perforations (see Figure 5.11 (a)). At P_2, just before a small load drop, the strain curve for section line 1 (shown in blue) indicates debonding propagated approximately 15 mm along the bottom fibre bundle. Higher strains are observed over the perforations (i.e. on sections 1 and 3) than in the unperforated middle zone (i.e. section 2). At a later load level P_3, the axial strain distribution shows good agreement with $\frac{6P_5}{5AE_0}$ over a length of approximate 7 mm (adjacent to the central stress transfer zone), indicating that a single perforated fibre bundle has debonded and over this zone. The existence of a peak strain concentration showing good agreement with $\frac{3P_5}{2AE_0}$ at the perforated cross section, also indicates that not all the fibre bundles have debonded. The strain plots at load levels P_4 and P_5 suggest that the debonded bundle is the bottom one (i.e. aligned with section 1) and the debonding propagates axially as the load increases. At load P_6, some fibre breakage appears on the upper edge of the specimen strain contour plot. At load P_7, it appears that debonding of the bottom perforated bundle has completely developed throughout the gauge length (see Figure 5.11 (b)). In the strain contour plot further fibre breakage can be seen on the specimen edges. The loss of these fibres

means the area used in the calculation of the reference strains is no longer correct and this probably accounts for why the $\frac{6P_7}{5AE_0}$ falls below the experimental strains. At load P_8, a significant load drop happened and a large amount of continuous fibres were broken, which also resulted in a greater error in the reference strain values. The strains along all the section lines surpass the reference line (due to the reduced net section area). Ultimate failure appeared when the residual continuous fibres in the specimen fractured, as shown in the DIC strain contour plot for P_{10}.


Reference lines in strain plots:
$\epsilon = \frac{P_t}{AE_s}$
$\epsilon = \frac{3P_t}{2AE_s}$
$\epsilon = \frac{2P_t}{AE_s}$
$\epsilon = \frac{6P_t}{5AE_s}$
where A is the gross cross sectional area of the specimen
Load [kN]
Time [s]
P_1 P_2 P_4 P_6 P_7 P_8 P_9
P_3
P_5
P_{10}
Section 3 Section 2 Section 1
(DIC image at load P_1 without section lines)
Axial tensile strain [%]
Distance relative to the left edge [mm]
Section 1
Section 2
Section 3
[%]

(a)



(b)

Figure 5.11 DIC images and strain distribution along three sectional lines at selected load levels ((a) P_1 to P_6 and (b) P_7 to P_{10} for specimen (3) of configuration (6), i.e. 'S-5000'.

5.3.1.7 **Summary of the failure processes of configurations (1) to (6)**

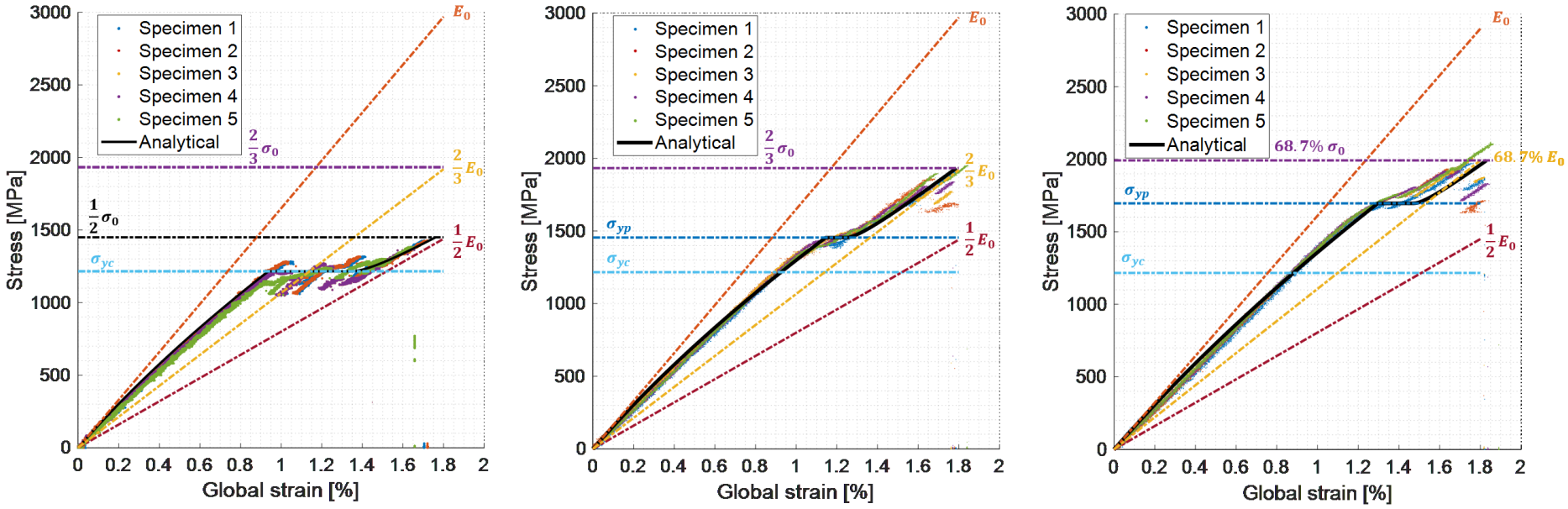
The failure processes of configurations (1) to (6) containing a single continuous cut or a line of perforations are summarized in Table 5.3.

Table 5.3 Summary of the failure processes of configurations (1) to (6), containing a single continuous cut or a line of perforations.

Configurations	**(1) S-cut**	**(2) S-50**	**(3) S-250**
Failure process	• Delamination • Failure stress is slightly higher than $\frac{1}{2}\sigma_0$	• Breakage of continuous fibre bundles in the perforated plies • Delamination • Failure stress is slightly higher than $\frac{1}{2}\sigma_0$	• Breakage of some continuous fibre bundles in the perforated plies • Delamination • Failure stress is slightly higher than $\frac{1}{2}\sigma_0$
Configurations	**(4) S-500**	**(5) S-800**	**(6) S-5000**
Failure process	• Debonding • Breakage of some continuous fibre bundles in the perforated plies • Delamination • Edge fibre splitting • Failure stress is slightly higher than $\frac{1}{2}\sigma_0$	• Debonding • Low overall stiffness of the strain-hardening stage because of significant edge fibre failure • Failure stress is very variable. The failure stresses for most specimens are much higher than $\frac{1}{2}\sigma_0$ and less than $\frac{2}{3}\sigma_0$.	• Debonding is progressively initiated from one 5000 μm perforation and then another one and propagated non-simultaneously towards the two tabs • Failure stress is close to $\frac{2}{3}\sigma_0$

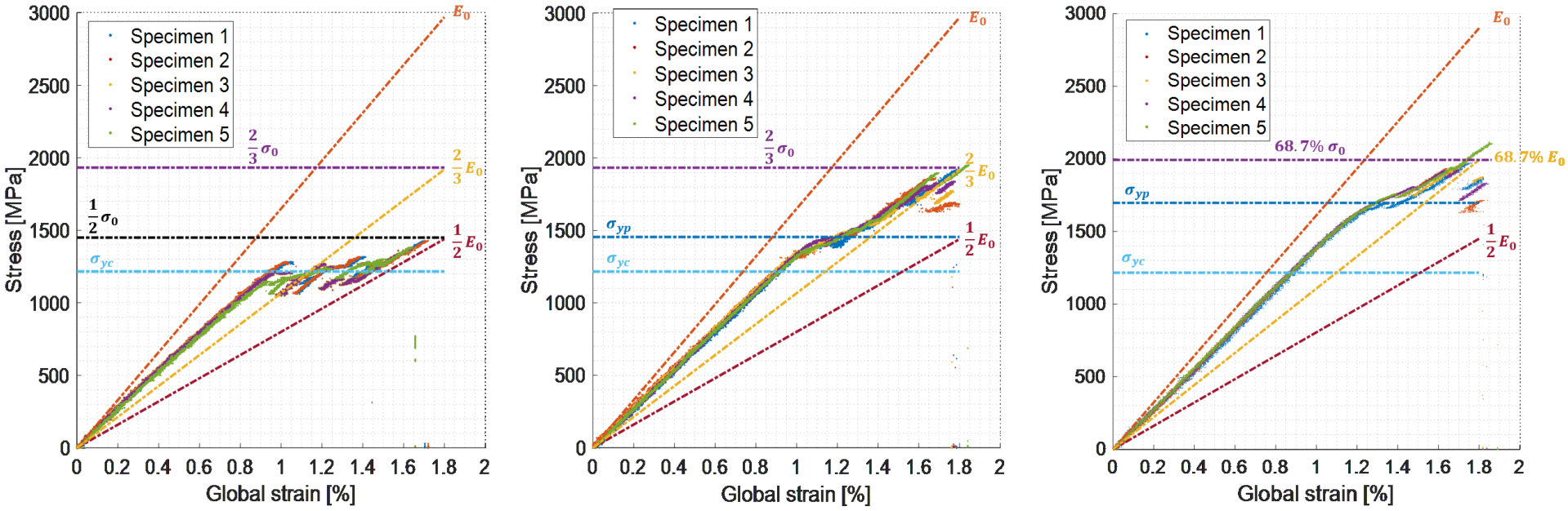
5.3.2 Laminates with multiple lines of perforations

The analytical and experimental stress-strain curves for laminates containing multiple lines of continuous cuts, 5000 µm and 800 µm perforations, i.e. configurations (7), (8) and (9), are shown in Figure 5.12 (a) to (c). The experimental curves for these three configurations (presented in Figure 5.12) are shown in Figure 5.13, without the analytical curves, for clarity. The same reference lines as those used for the single line of cut or perforation cases are shown in Figure 5.12 and Figure 5.13. Key mechanical properties are summarized in Table 5.4.



(a) M-Continuous cuts (b) M-5000 (c) M-800

Figure 5.12 Experimental and analytical stress-strain curves of three UD 4-ply configurations, i.e. (a) M- Continuous cuts, (b) M-5000 and (c) M-800, containing multiple continuous cuts or lines of perforations in the two middle plies.



(a) M-Continuous cuts (b) M-5000 (c) M-800

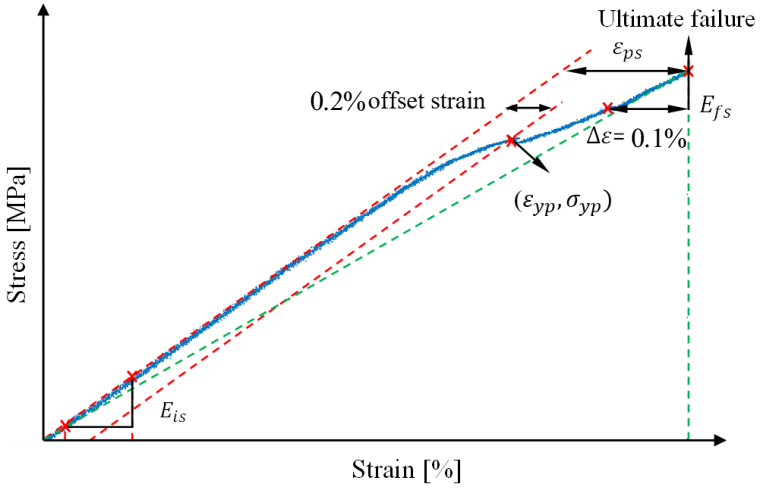
Figure 5.13 Experimental stress-strain curves of three UD 4-ply configurations , i.e. M- Continuous cuts, M-5000 and M-800, containing multiple continuous cuts or lines of perforations in the two middle plies (without the response predicted by the refined analytial model).

Table 5.4 Key tensile properties of UD 4-ply laminates containing mulitple lines of continuous cuts or perforations of various lengths. (Coefficient of variation, in %, is given in the parentheses.)

Specimen Type	Initial modulus E_{is} [GPa]		Pseudo-yield strain and stress $(\varepsilon_{yp}, \sigma_{yp})$ [%, MPa]		Strain-hardening modulus E_{fs} * [GPa]		Ultimate failure strain and stress $(\varepsilon_{ult}, \sigma_{ult})$ ** [%, MPa]		Pseudo-ductile strain ε_{ps} [%]	
	Anal.	Exp.	Anal.	Exp.	Anal.	Exp.	Anal.	Exp.	Anal.	Exp.
(7) M-Cut	147	135 (2.37%)	(0.99,1216)	(0.99, 1224) (4.32%, 4.68%)	71	77 (4.14%)	(1.76,1450)	(1.66, 1395) (2.68%, 2.20%)	0.71	0.63 (4.12%)
(8) M-5000	148	135 (2.09%)	(1.14,1455)	(1.16,1457) (1.37%,1.63%)	101	106 (7.07%)	(1.79, 1933)	(1.66, 1850) (2.81%, 3.43%)	0.49	0.42 (10.51%)
(9) M-800	151	134 (1.59%)	(1.29,1696)	(1.32,1755) (1.16%, 1.36%)	98	105 (4.73%)	(1.83, 1991)	(1.76, 1992) (4.13%, 4.15%)	0.52	0.312 (7.16%)

* The analytical and experimental strain-hardening stage moduli are measured as the chord moduli defined by ultimate failure point and the point with 100$\mu\varepsilon$ lower strain, if no load drop appeared in the final strain-hardening stage; For experimental tensile responses containing load drops in that 100 $\mu\varepsilon$ range, the chord modulus is defined between the point immediately following the load drop and ultimate failure point.

** For the analytical and experimental tensile responses without significant load drop close to failure, the ultimate failure point is defined as the point of the maximum stress; For experimental tensile responses containing load drop(s) close to failure, the ultimate failure points are determined as the onset point at the first load drop with an over 15% reduction in stress.


Ultimate failure
ε_{ps}
0.2%offset strain
E_{fs}
$\Delta\varepsilon$= 0.1%
$(\varepsilon_{yp}, \sigma_{yp})$
Stress [MPa]
E_{is}
Strain [%]

5.3.2.1 **Configuration (7): multiple continuous cuts**

Figure 5.12 (a) shows that there is good agreement between the predicated and experimental behaviour in the initial and the final strain-hardening stages. The tensile behaviour of this configuration has already been presented in Chapter 4. The results show that in the initial stage there was a gradual reduction in stiffness due to the development of the stress transfer zones from the cuts. At stress close to σ_{yc}, a series of load drops with intermediate re-loading stages were observed. The load drops were caused by unstable delamination growth, which was arrested when it reached the stress transfer zone initiated from the adjacent cut, which associates with a higher fracture toughness. A final strain-hardening stage is observed and this occurs when the leading edges of the stress transfer zones for each cut have just reached and started to coalesce with those of the neighbouring cuts. During the strain-hardening stage the tangent stiffness gradually increases as the coalesced stress transfer zones shorten. The final stiffness is close to $\frac{1}{2}E_0$ and the ultimate stress is very close to $\frac{1}{2}\sigma_0$.

5.3.2.2 **Configuration (8): multiple lines of 'S-5000' perforations ('M-5000')**

Figure 5.12 (b) shows good correlation between the experimental and analytically predicted tensile behaviour of configuration (8), containing multiple lines of 'S-5000' perforations at 10 mm intervals. Experimentally, the tensile stress-strain response consists an initial approximately-linear stage with gradually reducing stiffness, an intermediate rising 'plateau' initiated at a stress slightly lower than the analytically predicted σ_{yp} and gradually reducing stiffness, followed by a strain-hardening stage with an average final stiffness close to $\frac{2}{3}E_0$. There are smooth transitions preceding and following the intermediate 'plateau' with very small, if any, load drops are observed from these specimens. This is in marked contrast to the specimens of configuration (7), which showed multiple load drops before entering the final strain-hardening stage. The average maximum stress of the specimens is 1850 MPa, which is within 5% of the predicted failure stress.

For this configuration there are only two perforations across the width of the specimen at each perforated cross-section.

The failure mechanisms of this configuration are analysed with the DIC strain contour plots and corresponding axial strain distribution curves along three sectional lines, i.e. section 1, section 2 and section 3, at selected load levels P_1 to P_9 (see Figure 5.14) for specimen (5). As shown in Figure 5.14, section line 2 is over the upper row of perforations and section line 3 is over the lower row of perforations, while section line 1 is placed in the unperforated gap between the two rows of perforations. Two strain colour scales are used to clearly visualise the strain distribution at different load levels. On

each of the axial strain curves, three reference lines representing $\frac{P_i}{AE_0}$, $\frac{3P_i}{2AE_0}$ and $\frac{2P_i}{AE_0}$, where A denotes the gross cross sectional area of the specimen, are also presented to assist the interpretation of the loading process.

The axial strain distributions along section lines 2 and 3 for load P_1 indicate stress transfer zones have almost uniformly initiated from each perforation, with the strain values at peaks and troughs close to $\frac{3P_1}{2AE_0}$ and $\frac{P_1}{AE_0}$, respectively. At load level P_1, the strain along section line 1 (between perforation rows) is fairly uniform. At higher load P_2, section 1 strain distribution is starting to show peak values corresponding to the peaks in the strain distributions for section lines 2 and 3. At this load level, the axial strain curves indicate growth of the stress transfer zone length. At load levels P_3 and P_4, which are in the rising 'plateau' stage of the load-time curve, the DIC strain contour plots show debonding around the perforated fibre bundles grow from perforations at a few different locations, presumably those with relatively lower fracture toughness. Higher load is required to initiate debonding growth at other locations (with higher toughness). This accounts for the gradually rising 'plateaux' observed in the experimental stress-strain curves of Figure 5.13 (b). The average axial strains at section lines 1, 2 and 3, in the debonded regions (marked as I, II, III and IV) become close to $\frac{3P_i}{2AE_0}$, where P_i is equal to P_3 and P_4, as shown in the corresponding axial strain distribution curves. At other locations, the minimum strains (i.e. trough strains) coincide with $\frac{P_i}{AE_0}$ (for $P_i = P_3$ and P_4), indicating no debonding at these positions. At load level P_5, the strain-hardening stage has already started. The axial strain plot indicate debonding has occurred at all perforations. The debonded regions now occupy most but not all the specimen length. The strains of these debonded regions are in good agreement with $\frac{3P_5}{2AE_0}$ and these indicate positions where the debonding process is not yet complete. However, unlike at load level P_4, the strain values at these minima area are significantly higher than $\frac{P_5}{AE_0}$. This indicates that all the stress transfer zones initiated from adjacent perforations have already coalesced. This behaviour is predicted by the analytical model (see Figure 3.26 of Chapter 3). The analytically predicted minimum strain is shown on enlarged axial strain curves for load levels P_5 and P_6 in Figure 5.15 (a) and (b), respectively. Load level P_6 is at a later point of the strain-hardening stage in the load-time diagram. In both diagrams shown in Figure 5.15, the predicted minimum strains show reasonable agreement with the experimental minimum values and become close to $\frac{3P_i}{2AE_0}$, as the load is increased. The breakage of unperforated continuous fibres on the specimen edge attributes to a small load drop immediately after load P_7. The fibre breakage results in the significant undulation of the axial strain of section line 1, as shown in the axial strain curves for P_8 and P_9. The specimen is completely failed immediately after load level P_9.

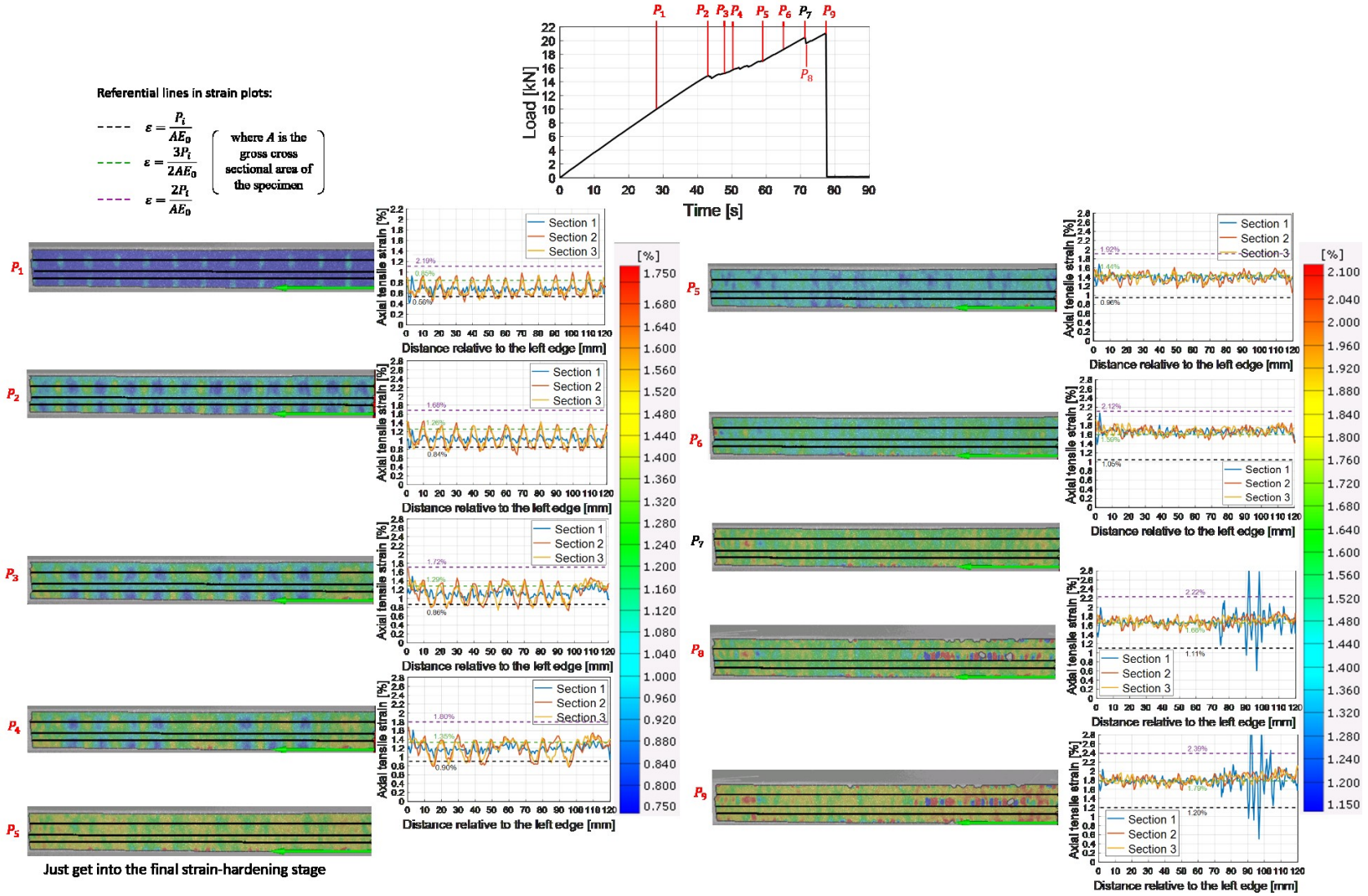
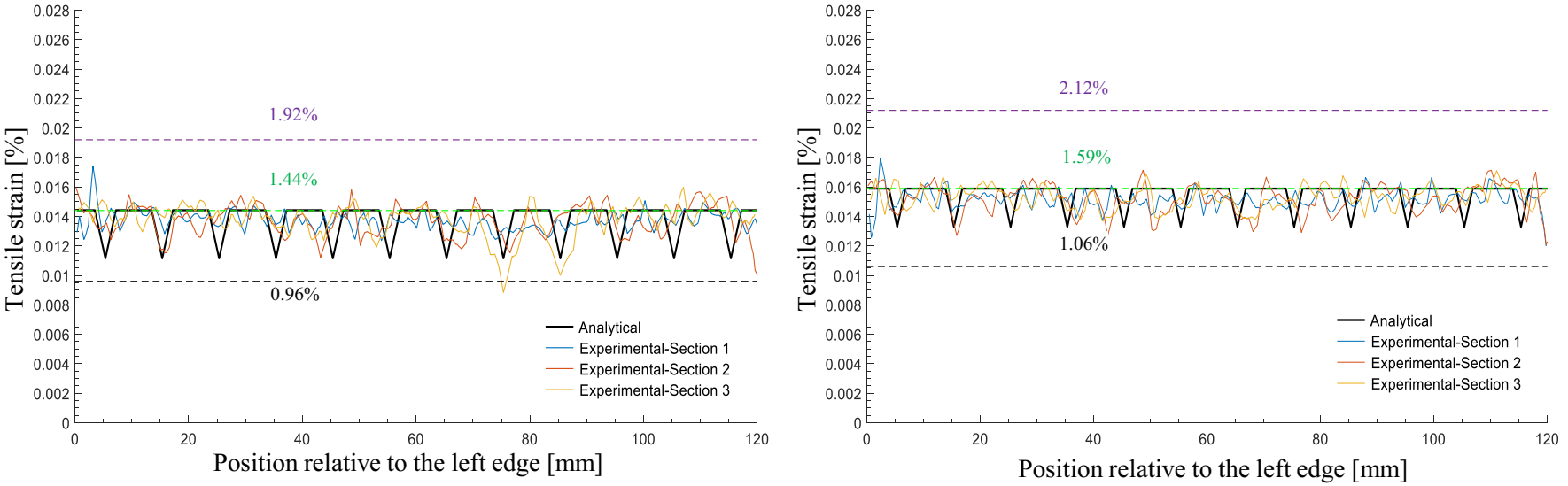


Figure 5.14 DIC images and strain distribution along three sectional lines at selected load levels for specimen (5) of configuration (8).



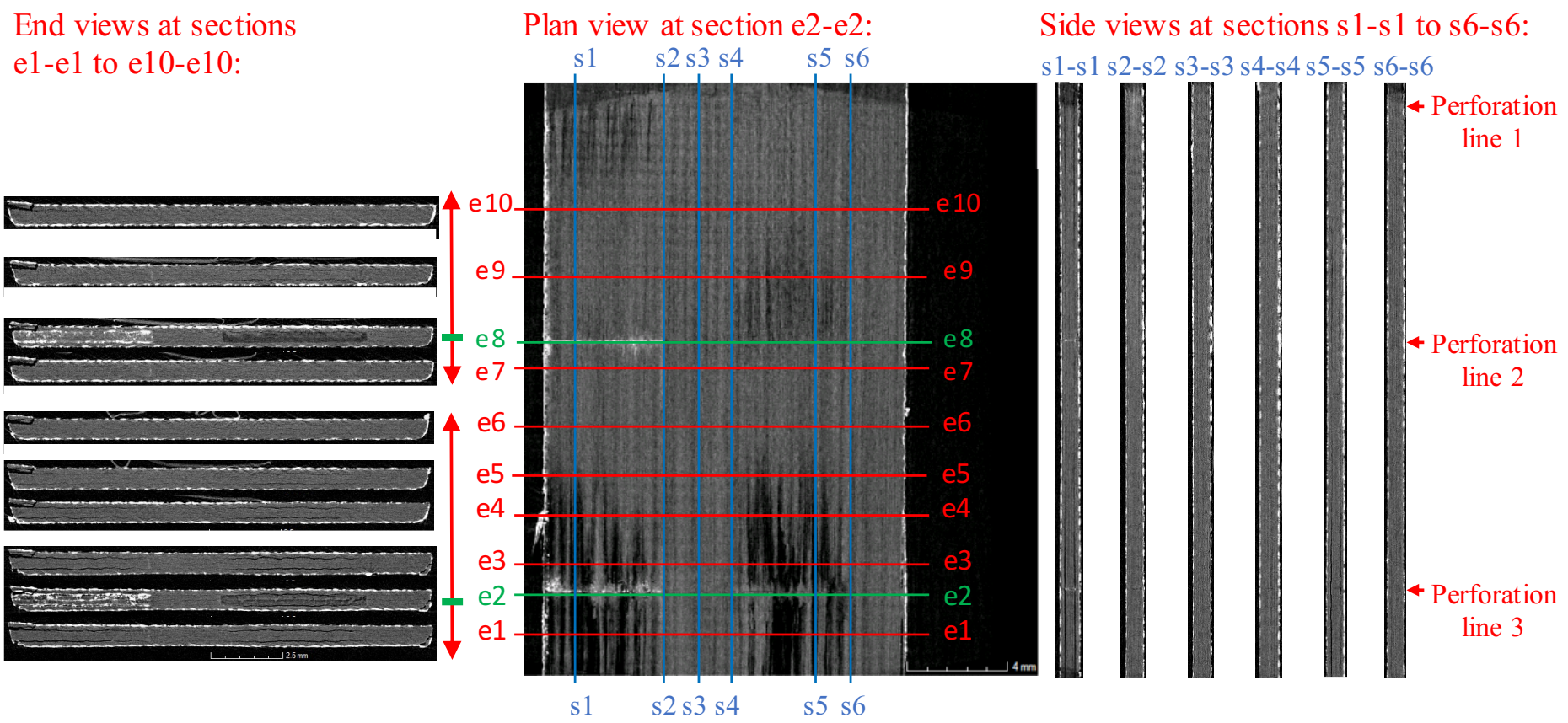
(a) (b)

Figure 5.15 Experimental (along section lines 1, 2 and 3) and analytical axial strain distribution (predicted by the refined analytical model presented in Chapter 3) for load levels P_5 and P_6, shown in Figure 5.14.

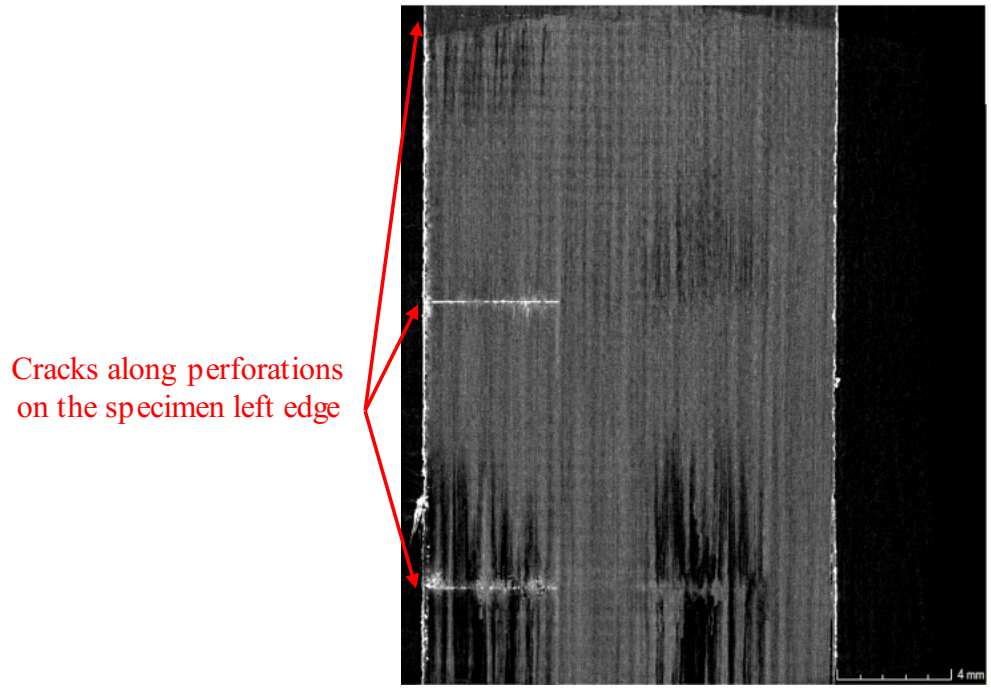
The failure mechanisms of the specimens containing multiple lines of 5000 μm perforations were also confirmed by X-ray CT scanning images of a specimen tested to 1540 MPa, close to failure, where debonding is expected to have propagated along the perforated fibre bundles. The specimen was scanned with the X-ray CT method over a region containing three lines of perforations, as shown in Figure 5.16. The resulting images at selected positions are shown in Figure 5.16 (a). Note one row of the 5000 μm perforations in the axial direction are along the specimen left edge. X-ray opaque penetrant was applied to the specimen but only penetrated into the cracks from this edge, as can be seen from the plan view.

The two end views at the lower two perforation lines, i.e. sections e2-e2 and e8-e8 (highlighted in green), show cracks around the two 5000 μm perforated fibre bundles. The end views for the sections close the lowest perforation line e2-e2, i.e. sections e1-e1 and e3-e3 to e6-e6, indicate interlaminar cracks were initiated from both 5000 μm perforations on section e2-e2 and the width of the interlaminar cracks reduces as moving away from the perforations. The end views near the two 5000 μm perforations on the upper most section line e8-e8, i.e. sections e7-e7, e9-e9 and e10-e10, indicate interlaminar cracks were initiated and propagated along the perforated fibre bundle on the right but have not propagated along the left perforated fibre bundle. The outline of interlaminar and intralaminar cracks can be inferred from the end view e8-e8, but it is likely that there are not cracks, instead, just the opaque penetrant collected at the edge of the laser cut perforation. This difference indicates debonding propagated non-uniformly along different perforated fibre bundles.

The side view at section s1-s1, lying within the perforated fibre bundles on the left of the specimen shows interlaminar cracks initiated from the top and bottom perforations, but not from the middle perforation. The side view at section s5-s5, lying within the perforated fibre bundles on the right shows interlaminar cracks were initiated from the middle and bottom perforations. Side views on the other sections, i.e. s2-s2 to s4-s4 and s6-s6, show no interlaminar crack, indicating interlaminar cracks only propagate along the fibre bundles that were perforated.


End views at sections
e1-e1 to e10-e10:
Plan view at section e2-e2:
Side views at sections s1-s1 to s6-s6:
s1
s2 s3 s4
s5 s6
e10
e9
e8
e7
e6
e5
e4
e3
e2
e1
s1-s1 s2-s2 s3-s3 s4-s4 s5-s5 s6-s6
Perforation line 1
Perforation line 2
Perforation line 3

(a)



(b)

Figure 5.16 (a) X-ray CT images at selected sections of a specimen containing multiple lines of 5000 μm perforations, i.e. configuration 'M-5000', tested to a stress, where debonding around the perforated fibre bundles has occurred and (b) the plan view at section e2-e2.

5.3.2.3 **Configuration (9): multiple lines of 'S-800' perforations ('M-800')**

Figure 5.12 (c) shows that there is good agreement between the experimental and analytically predicted tensile behaviour of configuration (9). Experimentally, the tensile stress-strain curves consist an initial approximately-linear stage with gradually reduced stiffness, an intermediate rising 'plateau' with an onset stress slightly lower than the analytical σ_{yp} and a strain-hardening stage with an average final stiffness close to the reference value of $68.7\%E_0$. The magnitude of 68.7% used in the predicted strength value, arises because in these 800 μm perforation specimens the net section area at the perforation line is 68.7% of the gross area (see Figure 5.2). Except for specimen (1), which presents a small load drop in the plateau stage, all other specimens show smooth transitions prior to and after the intermediate rising 'plateau' stage. The average maximum stress observed in these specimens is 1992 MPa, which is remarkably close to the net section failure stress of $68.7\%\sigma_0$.

DIC contour plots and the strain distribution curves for the axial strain along three section lines on specimen (3), for seven selected load levels P_1 to P_7, are shown in Figure 5.17. (The section lines are placed at three randomly selected positions as the strains at the perforated and spacing positions are cannot be distinguished from the employed DIC camera system.) The reference strain lines on the axial strain curves are $\frac{P_i}{AE_0}$, $\frac{P_i}{68.7\%AE_0}$ and $\frac{2P_i}{AE_0}$. The DIC strain contour plots and the related axial strain plots for load levels P_1 and P_2 show the stress transfer zones developed almost uniformly from the perforated cross-sections, with the peak values close to $\frac{P_i}{68.7\%AE_0}$ and trough values close to $\frac{P_i}{AE_0}$, where P_i is equal to P_1 and P_2, respectively. At load level P_3, the strain values at the peaks are close to $\frac{P_3}{68.7\%AE_0}$ but the values at the troughs are now significantly higher than $\frac{P_3}{AE_0}$, which indicates that the stress transfer zones initiated from adjacent perforations have already started to coalesce and therefore debonding has already initiated at the perforated fibre bundles, as predicted by the refined analytical model (see Figure 3.26 (b)). At the subsequent load levels P_4 to P_6, it is seen that the trough strain values become increasingly greater than $\frac{P_i}{AE_0}$ (i = 4, 5 and 6, respectively), indicating the continued shortening of the coalesced stress transfer zones. At load levels P_3 to P_6, some minor fibres failure occurs at the edges of the specimen. At P_8, this fibre failure becomes more significant as indicated by the peak strains, which are markedly higher than the reference value of $\frac{P_8}{68.7\%AE_0}$.

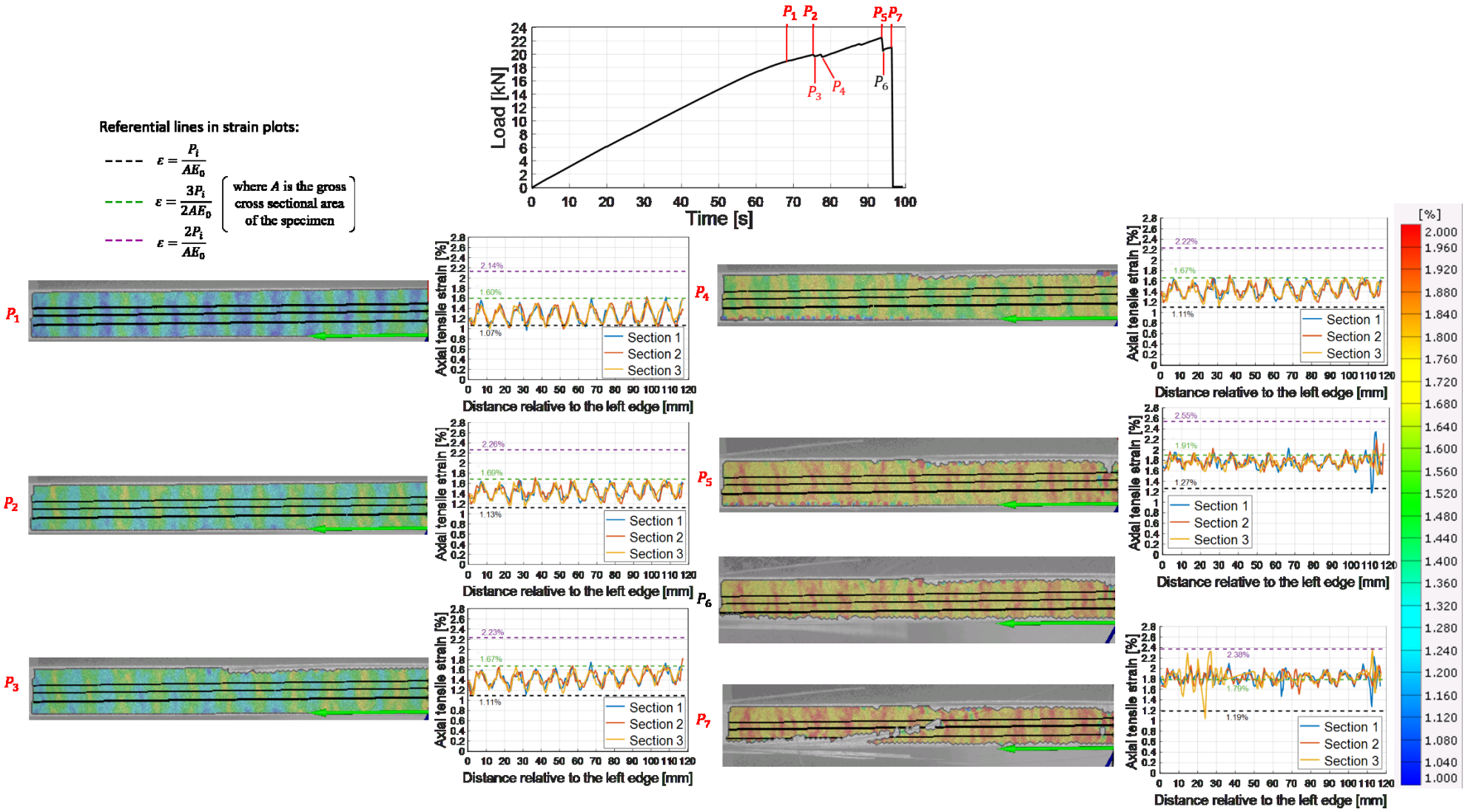
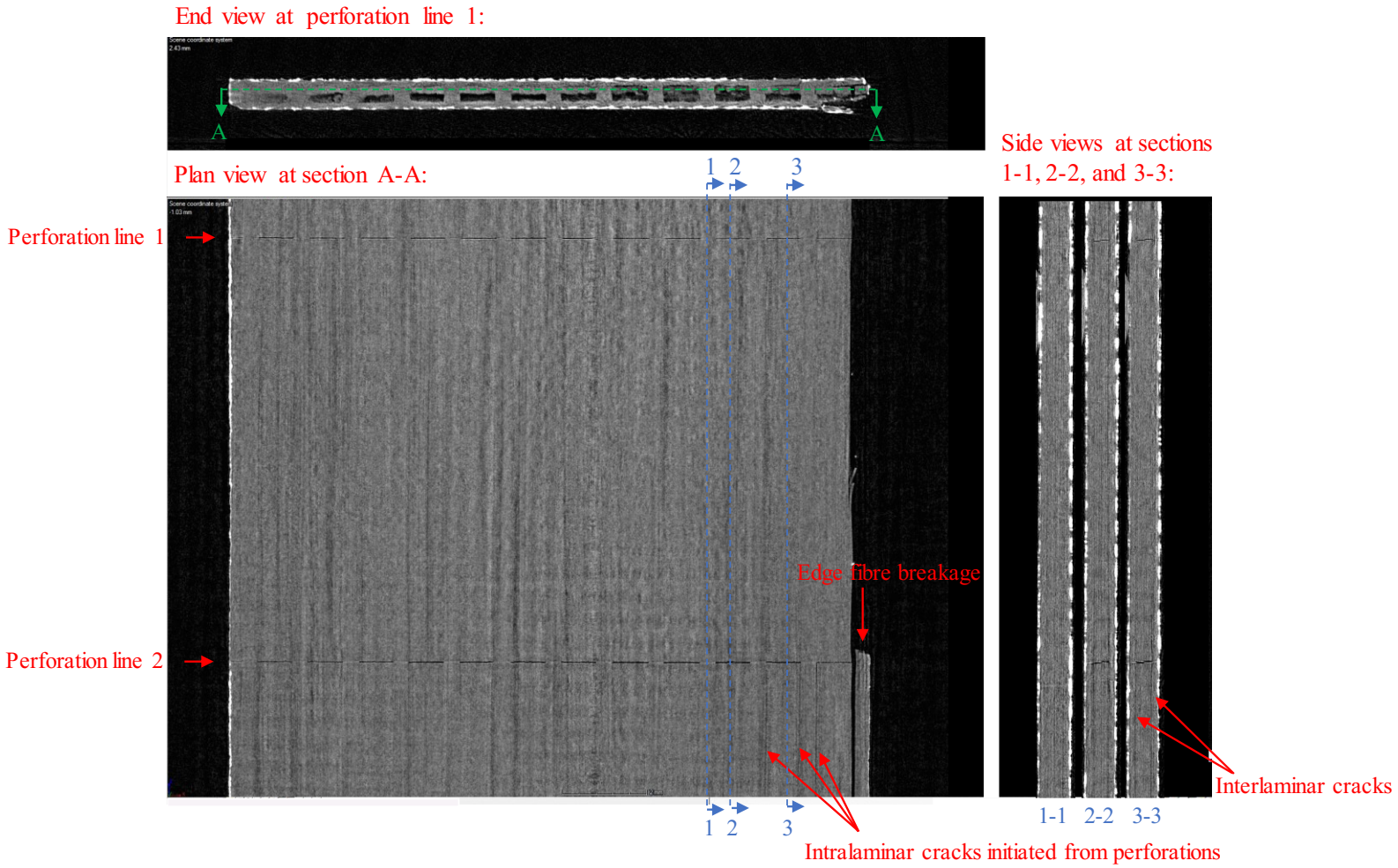


Figure 5.17 DIC images and strain distribution along three sectional lines at selected load levels for specimen (3) of configuration (9).

The failure mechanism of perforated fibre bundle debonding was also confirmed by the X-ray CT scanning images and the cross-sectional optical microscope images of a specimen, for which the test was halted at an average stress of 1853 MPa, close to ultimate failure. After removing the specimen from the test machine, the specimen was scanned with an X-ray CT machine. The resulting images at selected positions within the same specimen are shown in Figure 5.18 (a). A polished cross section cut from the specimen at 3 mm from a perforation line was prepared and inspected using an optical microscope, as shown in Figure 5.18 (b) and (c).

The X-ray CT plan view (lying within the perforated plies) shows intralaminar cracking has propagated along the sides of the perforated fibre bundles from the perforations. The X-ray side view at section 1-1 (between adjacent perforated fibre bundles) indicates no interlaminar cracking. The side views at sections 2-2 and 3-3 indicate, at this stress, interlaminar cracks have propagated from the perforations. The optical microscopic image of the polished section shows debonding cracks formed around the perimeters of the 800 μm perforated bundles (in Figure 5.18 (b)). These cracks have been highlighted in red for all the debonded fibre bundles in the Figure 5.18 (c), which shows the entire cross-section.


End view at perforation line 1:
A
A
Plan view at section A-A:
1 2 3
Side views at sections
1-1, 2-2, and 3-3:
Perforation line 1
Perforation line 2
Edge fibre breakage
Interlaminar cracks
1 2 3
1-1 2-2 3-3
Intralaminar cracks initiated from perforations

(a)

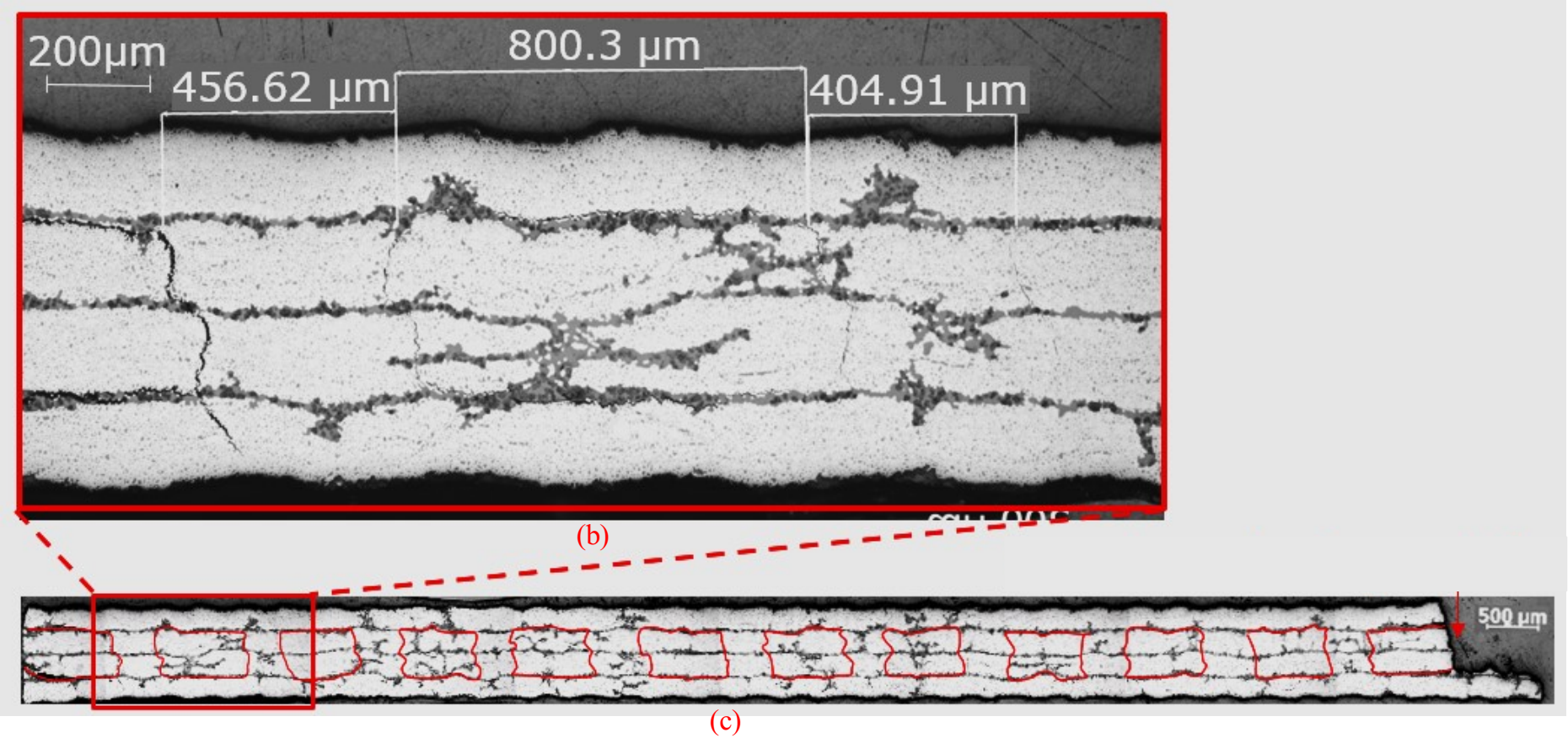


Figure 5.18 (a) X-ray CT images of the top and side views, (b) and (c) the cross-sectional optical micrographs, of a ‘M-800’ specimen tested close to failure.

5.3.2.4 **Comparison of the tensile performance of configurations (7) to (9), containing multiple continuous cuts or lines of perforations:**

The failure processes of configuration (7), i.e. the 'M-cut' configuration, containing multiple continuous cuts; configuration (8), i.e. the 'M-5000' configuration, containing multiple lines of 5000 μm perforations and configuration (9), i.e. the 'M-800' configuration, containing multiple lines of 800 μm perforations, are summarized in Table 5.5. The three configurations achieved high initial stiffnesses of approximately 85% of the stiffness of the baseline pristine material and high pseudo-yield stresses of 78% to 88% of the ultimate failure strengths.

In contrast to the configuration (7), containing continuous cuts, which exhibited significant load drops during the 'plateau' stage (see Figure 5.12 (a)), configurations (8) and (9) (see Figure 5.12 (b) and (c)) show a rising 'plateau' with almost no load drops and smooth transitions to the adjacent stages of the stress-strain curves. The potential reasons are explained below.

Theoretically, the onset of debonding or delamination for each cut or perforated position is related to the local interlaminar and intralaminar fracture toughness. The values of these toughness will vary with position. This is possibly due to material variability, but the manufacturing process used here (e. g. laser milling to introduce the perforations) may also have caused additional variation. As the number of cuts or perforations are increased, the probability of a larger variation in the toughness values at these cuts /perforations will also be increased. The number of cuts/perforations in the three configurations (7), (8) and (9) are 13, 26 and 156, respectively. Therefore configurations (8) and (9) potentially have a greater variation in fracture toughness values at different perforations. During the 'plateau' stage, those positions with the lowest fracture toughness start to debond or delaminate at first. As the remote tensile stress increases, debonding/delamination will be successively initiated at locations with the next lowest fracture toughness. This results in a 'rising plateau' and smooth transitions in advance of and following the 'rising plateau' stage in the stress-strain responses.

Also, if the debonding/delamination process was unstable, then in the cut ply case there is a potential for a larger sudden growth in delaminated area (and therefore a greater load drop) than in the perforated ply cases.

Another factor that may contribute to the rising 'plateau' could be an increasing toughness as the debonding/delamination growth advances. This is particularly possible for the intralaminar toughness, which is likely to increase with crack growth due to increasing fibre bridging.

The perforation strategy provides the possibility to tailor the initial stiffness, pseudo-yield stress, the final strain-hardening stiffness and the ultimate failure strength.

Table 5.5 Summary of the failure process of configurations (7), i.e. 'M-cut', containing mulitple lines of continuous cuts, and configurations (8) and (9), i.e. 'M-5000' and 'M-800', containing multiple lines of 5000 μm and 800 μm perforations, respectively.

Configurations	**(7) M-cut**	**(8) M-5000**	**(9) M-800**
Failure process	• Gradual loss of stiffness in the initial stage • Unstable **delamination** accompanied with small load drops • Average failure stress is close to $\frac{1}{2}\sigma_0$ ($\pm$3.8%) • Average stiffness at ultimate failure is close to $\frac{1}{2}E_0$ ($\pm$ 4.5%)	• Gradual loss of stiffness in the initial stage • Stable **debonding** around 5000 μm perforations with very few load drops • Average failure stress is close to $\frac{2}{3}\sigma_0$ ($\pm$ 0.01%) • Average stiffness at ultimate failure is slightly higher than $\frac{2}{3}E_0$ ($\pm$1.1%)	• Gradual loss of stiffness in the initial stage • Stable **debonding** around 800 μm perforations with very small load drops • Average failure stress is close to 68.7% σ_0 ($\pm$ 0.04%) • Average stiffness at ultimate failure is close to 68.7% E_0 ($\pm$ 4.9%)

5.3.3 Comparison of the configurations containing a single and multiple lines of cuts or perforations

In this section, the tensile performance of configuration (1) containing a single continuous cut is compared with that of configuration (7) containing multiple continuous cuts. Comparison of configurations (5) and (9), i.e. containing a single line and multiple lines of 800 μm perforations, as well as configurations (6) and (8), i.e. containing a single line and multiple lines of 5000 μm perforations, is also presented.

The load drops in the stress-strain curves of configuration (1), containing a single continuous cut (shown in Figure 5.5 (a)) were replaced with less significant drops in the intermediate 'plateau' stage (see Figure 5.12 (a)), when the single continuous cut was replaced with multiple cuts. Such variation in tensile response is also observed in the configurations with the 800 μm and 5000 μm perforations. This change in response is related to the evolution of the stress transfer zones. For specimens with a single cut or perforation line, once debonding or delamination occurs, the leading edges of the stress transfer zones together with the associated stress transfer zone are free to propagate to the ends of the specimen. In the experiment, this propagation of debonding/delamination is unstable and therefore accompanied by significant load drops and sudden release of large amount of strain energy. For those specimens with multiple lines of cuts or perforations, the propagating stress transfer zones are suppressed once encountering the stress transfer zones initiated from the adjacent cuts or perforations. Thus, the debonding or delamination can only propagate a short distance, and the associated amount of released strain energy is dramatically reduced, compared to the single line of cut and perforations cases. The load drops in the experimental tests for the specimens with multiple cuts or lines of perforations were therefore significantly reduced. Due to the variation in fracture toughness, discussed earlier, this 'arresting' mechanism will occur first at the locations of the lowest toughness. Debonding/delamination and the 'arresting' mechanism will occur at other tougher locations as the load is further increased. Such a progressive process promotes less significant, or even no, load drops in configurations with multiple lines of cuts or perforations.

Note that these stable intermediate 'plateau' stages were achieved at the expense of a more severe reduction in stiffness of the initial stages of the stress-strain curves. This is due to the formation of a larger total area of stress transfer zones than in those specimens containing a single cut or perforation line.

Table 5.6 Comparison of the failure process of configurations containing multiple continuous cuts or lines of 5000 μm or 800 μm perforations , i.e. configurations 'M-cut', 'M-5000' and 'M-800' 'M-cut', with the corresponding configurations containing a single continuous cut or line of perforations, i.e. configurations 'S-cut', 'S-5000' and 'S-800', respectively.

Configurations	'M-cut' performance relative to 'S-cut'	'M-5000' performance relative to 'S-5000'	'M-800' performance relative to 'S-800'
Failure process	• More severe loss in stiffness of the initial stage • Higher numbers but less severe load-drops due to multiple cuts • Unstable delamination is arrested due to interaction with adjacent stress transfer zone. • Stress for plateau is same for both cases • Ultimate failure stress is similar for both cases • Better agreement with the refined analytical model predicted response	• More severe loss in stiffness of the initial stage • No significant load drops • Much smoother transitions between adjacent stages in the stress-strain curves • Experimental response has reduced scatter and in better agreement with the refined analytical model predicted response	• More severe loss in stiffness of the initial stage • No significant load drops • Much smoother transitions between adjacent stages in the stress-strain curves • Experimental response has reduced scatter and in better agreement with the refined analytical model predicted response

5.4 Conclusions

This chapter presented experimental results of the tensile performance of UD laminates containing a single line and multiple lines of perforations with several different geometries in selected plies. Perforations were precisely and uniformly introduced into prepregs using a laser milling technique. The tensile performance and the failure mechanisms of the perforated laminates were compared with those specimens containing a single and multiple lines of continuous cuts, and with the behaviour predicted by the refined analytical model. The conclusions are summarized below:

- For laminates containing a single continuous cut or a single line of perforations, the initial stage of the stress-strain response was almost identical to that of a pristine laminate. The initial stage was followed with load drops, due to the suddenly developed unstable delamination or debonding (accompanied with some breakage of continuous fibres) and then a final strain-hardening stage exhibiting considerable scatter.

- Laminates containing multiple continuous cuts or lines of perforations exhibited a pseudo-ductile tensile performance. The initial stage possessed a high initial stiffness (close to the pristine material) but the stiffness gradual reduced with increasing load. This was followed by a stable intermediate rising 'plateau' stage, with a smooth transition to a final strain-hardening stage. The tensile performance of the configurations with multiple cuts or perforation lines exhibited considerably less scatter than that of the configurations with a single line of cut or perforations.

- The pseudo-ductility observed in the configurations with multiple lines of perforations is promoted by debonding around the perforated fibre bundles. The stability of the rising 'plateau' stage in the pseudo-ductile cases may be due to the toughness variation, interaction of the stress transfer zones and fibre bridging at intralaminar cracks. The improved pseudo-ductility of the configurations containing multiple cuts and lines of perforations comes at the cost of the loss of stiffness observed in the initial stage.

- The ply perforation strategy provides the possibility for more tailorable pseudo-ductile tensile response, compared to the 'cut-ply' strategy.

- The tensile responses predicted by the refined analytical model for the UD laminates containing multiple lines of perforations, showed good agreement with the experimental results.

Chapter 6

Experimental investigation of pseudo-ductility in multi-directional laminates containing ply cuts or perforations

6.1 Introduction

Chapter 4 and Chapter 5 have shown that pseudo-ductile tensile response can be achieved in UD laminates containing ply cuts or perforations in the middle plies. The ply cuts triggered progressive delamination, which provides an intermediate plateau stage in the tensile response. The ply perforations promoted progressive debonding providing a stable rising 'plateau' stage in the tensile response. This chapter presents an investigation on the potential to transfer the pseudo-ductility observed in the UD laminates to multi-directional laminates that possess wider application scope in engineering structures, by introducing continuous cuts or perforations into selected plies. The multi-directional laminates consist two 0° plies placed in the middle of two blocks of quasi-isotropic (QI) sub-laminates. Evenly spaced continuous cuts or lines of perforations were introduced perpendicular to the fibre direction of the two middle 0° plies.

This chapter is organized as follows: section 6.2 presents the design criteria (see section 6.2.1), the fabrication process (see section 6.2.2) and tensile testing method (see section 6.2.3). The tensile testing results are presented in section 6.3. The tensile responses of these configurations are compared in section 6.3.1. The failure mechanisms of these configurations are presented in section 6.3.2. The effects of the laminate layup, the geometry of the ply cuts and perforations on the tensile response, are also analysed in this section. The conclusions are drawn in section 6.4.

6.2 Experimental details

Static tensile tests on straight-edged tensile specimens were performed based on the CRAG 302 standard [112]. This section presents the details of criteria considered to design the layup, the ply cuts and perforation patterns in the multi-directional configurations, as well as the manufacture process, the mechanical testing and failure process investigation methods.

6.2.1 Specimen design details

In order to replicate the pseudo-ductility mechanisms achieved in the UD laminates, the multi-directional configurations were designed by simply replacing the two outer continuous 0° plies in the pseudo-ductile $[0°/0_c^\circ]_s$ and $[0°/0_p^\circ]_s$ UD laminates (presented in Chapter 4 and Chapter 5), with two blocks of multi-directional sub-laminates, as shown in Figure 6.1. (The subscripts 'c' and 'p' denote cuts and perforated plies, respectively.)

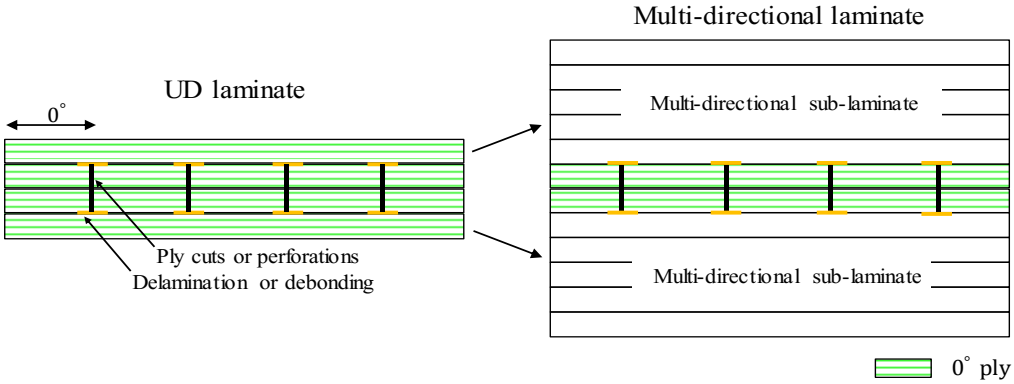


Figure 6.1 Schematic layups of the UD 4-ply laminate and the multi-directional laminate.

6.2.1.1 **Pseudo-yield stress for laminates containing continuous cuts**

The pseudo-yield stress must be lower than the ultimate failure stress to achieve a pseudo-ductile response. The pseudo-yield stress for the onset and propagation of delamination, σ_{ycM}, was predicted according to the proposed LEFM-based method [104]. Delamination is initiated by the cuts, once the average tensile stress reaches the critical pseudo-yield stress, σ_{ycM}. At this moment, the mode II strain energy release rate, G_{II} becomes equal to the mode II interlaminar fracture toughness, G_{IIC}. G_{IIC} is assumed as constant for delamination (and debonding shown in section 6.2.1.2) initiation and propagation. The expression of σ_{ycM} for delamination is a modification of the UD laminate pseudo-yield stress expression (see Eq. 3.3) and is given in Eq. 6.1.

$$\sigma_{ycM} = 2\sqrt{\frac{G_{IIC} n_U E_{0M} E_{1M}}{{n_T}^2 h E_{0M} - n_T n_U h E_{1M}}} \tag{6.1}$$

In this equation, n_T and n_U are the total number of plies and the number of continuous plies in the entire multi-directional laminate; h is the ply thickness; E_{0M} is the longitudinal tensile elastic modulus of the pristine multi-directional laminate; E_{1M} is the longitudinal tensile elastic modulus of the two outer continuous sub-laminates. E_{0M} and E_{1M} were predicted using Classical Laminate Analysis (CLA).

The tensile stress to cause failure of the outer multi-directional sub-laminates in the cut-ply configuration, was estimated using the Ten-Percent Rule [113], assuming the middle cut plies are completely separated from the multi-directional sub-laminates after delamination.

6.2.1.2 **Pseudo-yield stress for laminates containing lines of perforations**

As for the perforated-ply laminates, the pseudo-yield stress, σ_{ypM}, is required to be lower than the ultimate failure stress, to achieve a pseudo-ductile response. The pseudo-yield stress, σ_{ypM}, was predicted by considering an RVE, as shown in Figure 6.2.

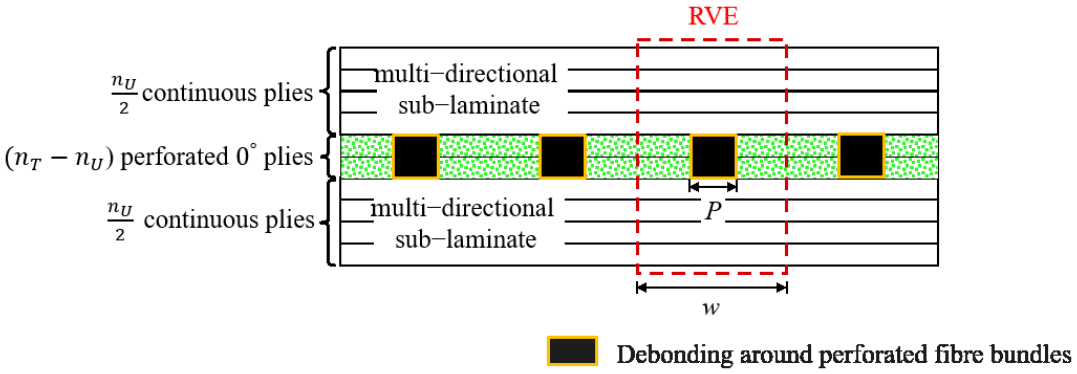


Figure 6.2 Schematic cross-section of a multidirectional perforated-ply configuration showing the RVE.

Debonding around the perforated fibre bundles occurs once the mode II strain energy release rate, G_{II} reaches the mode II fracture toughness, G_{IIC}. The fracture toughness values for the initiation and propagation of inter- and intra-laminar cracks around the fibre bundles are assumed to be the same and both equal to G_{IIC}. The expression of the pseudo-yield stress for debonding, σ_{ypM}, was a modification of the pseudo-yield stress derived for the UD laminates (see Eq. 3.8). The pseudo-yield stress, σ_{ypM}, is given by Eq. 6.2.

$$\sigma_{ypM} = 2\sqrt{\frac{2G_{IIC}E_{0M}E_{1M}[P + h(n_T - n_U)][n_T w - P(n_T - n_U)]}{{n_T}^2 w^2 h(E_{0M} - E_{1M}) + n_T w h(n_T - n_U)PE_{1M}}} \qquad 6.2$$

In this equation, E_{0M} is the longitudinal tensile elastic modulus of a completely continuous and pristine multi-directional laminate and was calculated from *Classical Laminate Analysis* (CLA); E_{1M} is the longitudinal tensile elastic modulus of the continuous part in the laminate and was calculated using *Classical Laminate Analysis* (CLA) and the *Rule of Mixtures* (RoM).

The tensile stress to cause ultimate failure of the perforated-ply configuration was also estimated using the Ten-Percent Rule [113], assuming the perforated fibre bundles are completely separated from the residual continuous part. Note the perforation strategy provides a higher volume of continuous 0° plies than the cut-ply strategy in the same laminate, therefore it gives a higher ultimate failure stress.

6.2.1.3 **Layups and investigated configurations**

In this experimental investigation, the outer multi-directional sub-laminates on either side of the two middle 0_c° or 0_p° plies were chosen to be quasi-isotropic, with a layup of $[90°/0°/+45°/-45°]$ (with the 90° plies as the outermost plies of the entire laminate).

To help avoid free edge delamination, this QI layup was selected with the following considerations:

- Each fibre direction within the layup consists of a single ply, in order to reduce the potential of free-edge delamination, which often occurs in laminates with excessive number of plies placed successively in the same direction.
- 90° plies were used as the outermost plies of the entire multi-directional laminate. This ensures a compressive interlaminar stress at the free edge, so as to reduce the risk of free-edge delamination.

This QI layup provides a resulting layup of the entire multi-directional laminate as $[90°/0°/+45°/-45°/0°]_s$.

Three configurations designed with this layup are shown in Table 6.1. Configuration (1) is the baseline configuration containing no cut or perforation. Configuration (2) contains continuous cuts in the two middle 0_c° plies, with the layup represented as $[90°/0°/+45°/-45°/0_c^\circ]_s$. 50% volume fraction of the 0° plies in this laminate is continuous, as shown in Table 6.1. Configuration (3) contains perforations with the pattern of '5P-5S', where P and S represent the lengths (in mm) of perforations and spacing between adjacent perforations in a perforation line, respectively. The layup of this perforated-ply case is $[90°/0°/+45°/-45°/0_p^\circ]_s$. The failure mechanisms of the two cut- and perforated-ply configurations with the same layup were compared.

The '5P-5S' perforation pattern was also investigated with a modified layup of [90°/+45°/-45°/0°/0_p°]s (configuration 4) to eventually achieve distinct 'yielding' in the tensile response, using this ply-perforation strategy. In this layup, the continuous 0° plies have been placed adjacent to the middle 0_p° plies to create $0°/0_p^\circ$ interfaces for delamination, like those in the UD pseudo-ductile [0°/0_p°]s perforated

configurations (reported in Chapter 5). The perforated configurations (3) and (4) provide 75% volume fraction of continuous 0° plies in the laminate.

6.2.1.4 **Predicted pseudo-yield stresses for cut- and perforated-ply configurations**

Table 6.1 also contains the predicted pseudo-yield stress and the estimated ultimate stress. The material system for this investigation is Hexply® M21/35%/198/T800S carbon fibre/epoxy UD prepregs with a cured ply thickness of 0.184 mm. The pseudo-yield stresses were calculated using the properties of a UD lamina given in Table 6.2 and equations 6.1 and 6.2. E_{0M} was determined to be 80 GPa, E_{1M} for the cut and perforated ply configurations were calculated to be 60 GPa and 71 GPa, respectively. As mentioned earlier, the ultimate stresses were calculated using the Ten-percent Rule, with the ply tensile strength given in Table 6.2. It can be seen from Table 6.1 that for all cut and perforated ply configurations the estimated ultimate stress is greater than the predicted pseudo-yield stress and therefore they are expected to exhibit pseudo-ductility.

Table 6.1 Summary of the investigated multi-directional configurations.

Configuration number	Layup	Configuration Name	Volume fraction of continuous 0° plies in the laminate	Predicted pseudo-yield stress [MPa]	Estimated ultimate failure stress [MPa]
(1)	$[90°/0°/+45°/-45°/0°]_s$	Pristine	100%	---	1334
(2)		Cut	50%	668	943
(3)		Perforated	75%	799	1073
(4)	Modified layup $[90°/+45°/-45°/0°/0°]_s$	Perforated	75%	799	1073

Table 6.2 Mechanical properties of a UD M21/T800S lamina

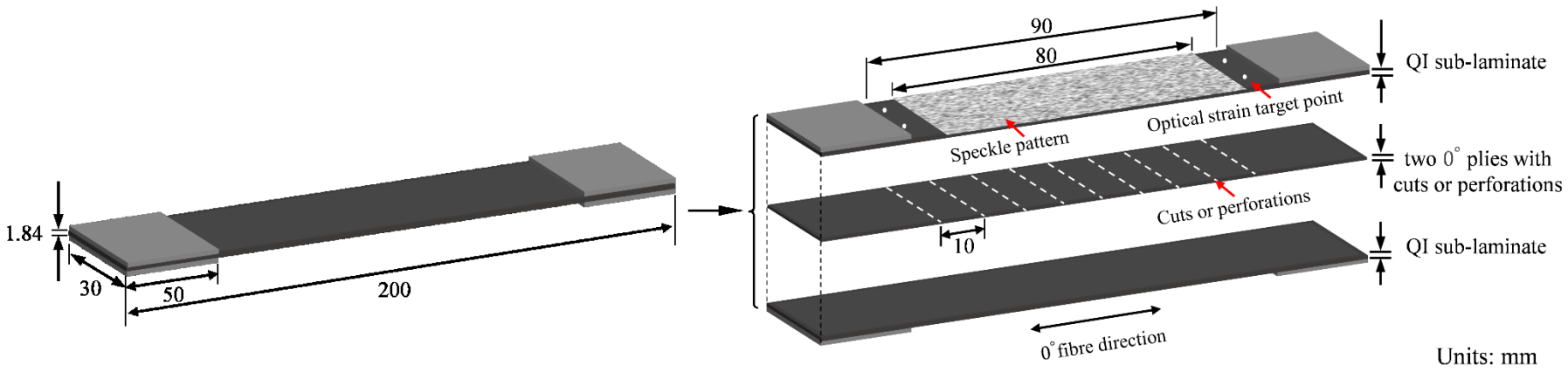
Elastic modulus E_{11} [GPa]	Transverse modulus E_{21} [GPa]	Shear modulus G_{12} [GPa]	Poisson's ratio υ_{12}	Tensile strength in 0° direction σ_0 [MPa]	Mode II interlaminar fracture toughness G_{IIC} [kJ/m^2]
160	8.1	4.8	0.33	2900	1.7

Note all properties except G_{IIC} are from the manufacturer's data sheet [107]. G_{IIC} was determined from the tensile tests of UD 4- and 6-ply M21/T800S specimens containing a single cut in the two central plies. The method to measure the mode II fracture toughness of a UD CFRP laminate was utilized in [35][37] and [108].

6.2.2 Specimen fabrication

Straight-edged tensile specimens were manufactured with dimensions shown in Figure 6.3 (a). The cuts and lines of perforations are perpendicular to the 0° fibre direction and are introduced at 10 mm intervals in the free length of the two middle 0° plies, as shown in Figure 6.3 (b). The cuts and perforations at the same positions of the two middle 0° plies were well aligned in the through-thickness direction.

The specimen manufacture method was the same as that for the UD specimens (shown in Chapter 4 and Chapter 5). Ply cuts were introduced into prepregs using the prepreg cutter. Perforations were introduced in the prepregs using the laser milling method. For the '5P-5S' perforation pattern, the transverse lines of perforation lines were symmetrically positioned within the middle of the specimen with continuous fibres at the outer edges, as shown in Figure 6.4.



(a) (b)

Figure 6.3 Schematic of the multi-directional specimen containing cuts or perforations.

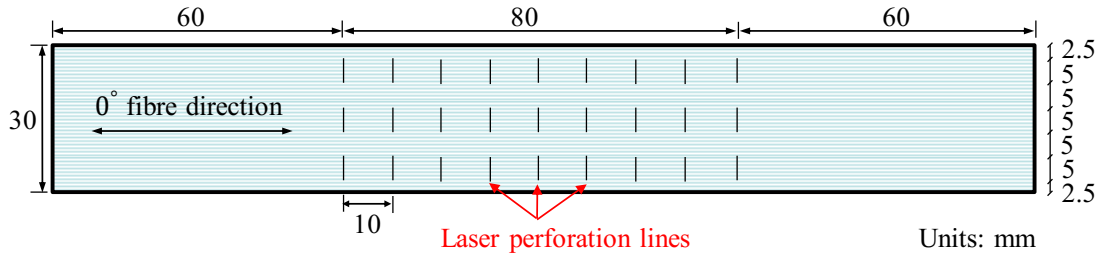


Figure 6.4 Schematic showing the position of the '5P-5S' perforation pattern within a specimen.

6.2.3 Mechanical testing

Static tensile tests were performed on a 250 kN Instron machine, equipped with hydraulic wedge type grips. The uniaxial tensile loading was applied at a crosshead-displacement speed of 2 mm/min. Five specimens were tested for each configuration. Four specimens were tested to ultimate failure and for one specimen the test was stopped prior to failure to investigate the failure mechanisms. The global strain was measured by an Imetrum video extensometer over a 90 mm gauge length. The full strain field over a gauge length of 80 mm was monitored with a GOM Digital Image Correlation (DIC) system. The DIC results were post-processed with different facet sizes and facet distances. Results for 19 pixel facet size and 15 pixel facet distance are presented in the following content. The placement of the optical strain gauge target points and DIC speckle pattern on a specimen surface is schematically shown in Figure 6.3. Ultrasonic C-scan inspection, X-ray scanning and optical microscopic inspection were performed on some of the interrupted test specimens, to assist the analysis of the damage mechanisms.

6.3 Results and Discussion

6.3.1 Tensile response of multi-directional configurations (1) to (4)

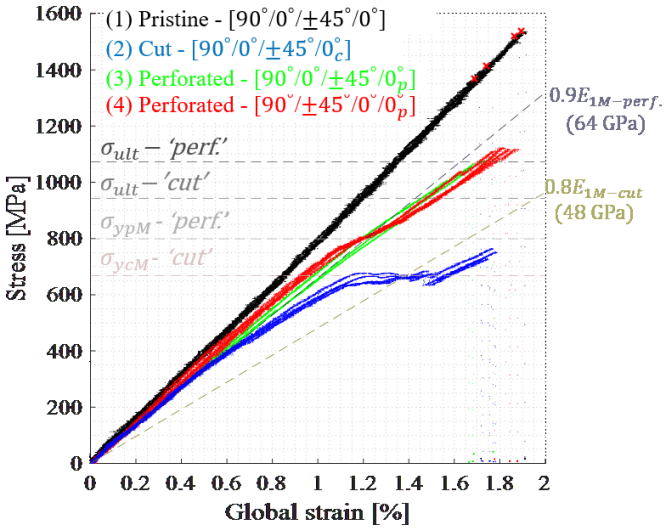
The tensile responses of the multi-directional configurations are shown in Figure 6.5 (a) and the mechanical properties are summarized in Table 6.3. Results show that only the cut-ply configuration with the layup of [90°/0°/+45°/-45°/0°_{c}]s and the perforated configuration with the modified layup of [90°/+45°/-45°/0°/0°_{p}]s behaved with a distinct 'yielding' in the tensile response. The tensile stress-strain responses of these two configurations, i.e. configurations (2) and (4), are shown in Figure 6.5 (b), together with that of the pristine baseline configuration, for comparison. For clarity, the tensile responses of the perforated configuration with no distinct 'yielding', i.e. configuration (3), is shown in Figure 6.5 (c), again with the baseline response. Figure 6.5 (a) to (c) also include the following reference lines:

- The analytical pseudo-yield stress, σ_{ycM}-'cut', for the cut-ply configuration with the layup of [90°/0°/+45°/-45°/0°_{c}]s;
- The analytical pseudo-yield stress, σ_{ypM}-'perf.', for the perforated-ply configurations with the layups of [90°/0°/+45°/-45°/0°_{p}]s and the modified one of [90°/+45°/-45°/0°/0°_{p}]s;
- The estimated ultimate tensile strength, σ_{ult}-'cut', of the cut-ply configuration with the layup of [90°/0°/+45°/-45°/0°_{c}]s;

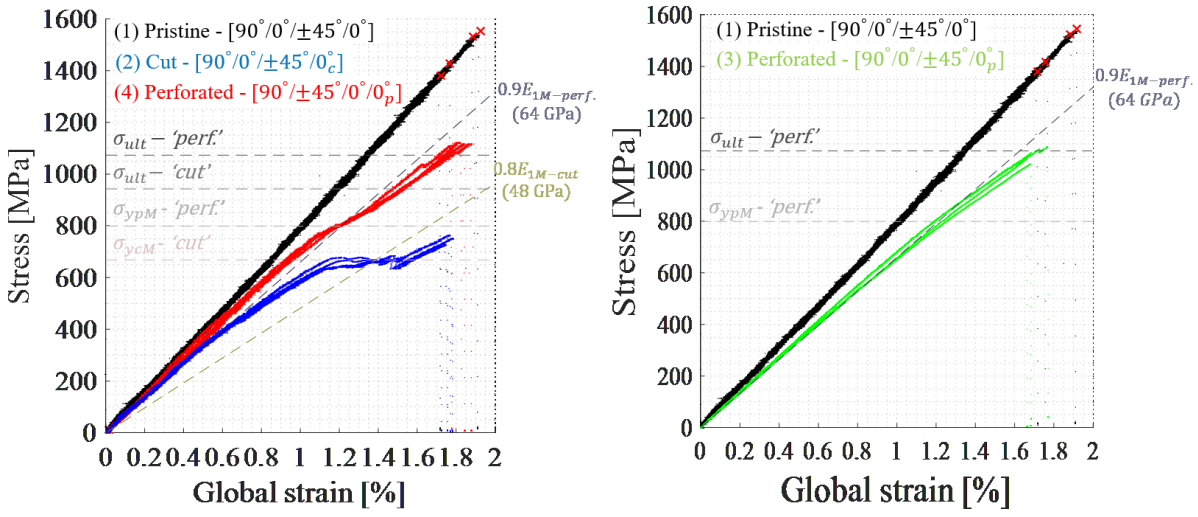
- The estimated ultimate tensile strength, σ_{ult}-'perf.', of the two perforated configurations, with different layups;

- Effective elastic modulus of the cut-ply configuration with the two middle plies completely separated from the outer continuous QI sub-laminates (This is given by 0.8 E_{1M-cut} and equal to 48 GPa);

- Effective elastic modulus of the perforated-ply configurations with the perforated 0° fibre bundles completely separated from the continuous part (This is given by 0.9 $E_{1M-perforated}$ and is equal to 64 GPa).



(a)



(b) (c)

Figure 6.5 Tensile stress-strain responses of the multi-directional configurations.

Table 6.3 Key experimental mechanical properties of the multi-directional configurations (Coefficient of variation, in %, are given in the parentheses).

Configuration	Initial Stiffness E_{0M} [GPa]	Pseudo-yield stress σ_{ycM} or σ_{ypM}* [MPa]		Strain-hardening stage modulus E_{1M}** [GPa]		Ultimate failure strain ε_{ult} [%]	Ultimate failure Stress σ_{ult} [MPa]	
	Exp.	Anal.	Exp.	Anal.	Exp.	Exp.	Anal.	Exp.
(1) Pristine - $[90°/0°/+45°/-45°/0°]_s$	80 (2.68%)	---	---	80	80 (8.39%)	1.81 (4.83%)	1334	1462 (5.12%)
(2) Cut - $[90°/0°/+45°/-45°/0_c^{\circ}]_s$	66 (2.13%)	688	654 (2.07%)	48	36 (0.81%)	1.76 (1.57%)	943	746 (2.55%)
(3) Perforated - $[90°/0°/+45°/-45°/0_p^{\circ}]_s$	69 (4.40%)	799	---	64	60 (8.22%)	1.49 (1.84%)	1073	949 (3.01%)
(4) Perforated - $[90°/+45°/-45°/0°/0_p^{\circ}]_s$	71 (7.39%)	799	796 (7.80%)	64	56 (6.03%)	1.83 (2.60%)	1073	1117 (3.17%)

* Determined using the method described in Appendix 3.

** The chord modulus close to failure were measured between the ultimate failure point and the point with $1000\mu\varepsilon$ lower strain.

The pristine configuration, i.e. configuration (1) is linear-elastic with an average modulus of 80 GPa and failed in a brittle manner, with an average tensile strength of 1462 MPa (see Table 6.3). The failure points on the stress-strain plots are highlighted with red crosses in Figure 6.5.

The cut-ply configurations (2), retained 82.5% of the initial stiffness of the pristine baseline configuration (as measured over the strain interval of 0.05% to 0.25%) (see Table 6.3). There is a gradual loss in stiffness in the initial stage and this is followed by an intermediate flat plateau at an average stress of 654 MPa. Finally, there is a strain-hardening stage with the final secant modulus of 36 GPa (measured over the final 0.1% strain range) and failure occurs at 746 MPa (see Figure 6.5 (a) and (b)). The experimental pseudo-yield stress shows good agreement with the analytically predicted value. The stiffness of the final strain-hardening stage is much lower than the $0.8E_{1M-cut}$ reference value, i.e. 48 GPa, shown as the blue line. The overestimated reference value is probably because of damage in the off-axis plies in the experimental tests, which is not considered when determining the reference value. The failure stress is lower than the value estimated by the Ten-Percent Rule, but this rule is only an approximation and does not consider the complete failure process.

Configuration (3) contains the '5P-5S' perforation pattern and the same layup as configuration (2). No distinct pseudo-ductile 'yielding' was observed, instead the specimens exhibited a gradual loss in stiffness as the tensile stress increased and failure occurred at an average stress of 945 MPa (see Figure 6.5 (c)).

The pseudo-ductile performance with a distinct 'yielding' behaviour was also achieved in configuration (4), containing '5P-5S' perforation pattern in the modified layup, as shown in Figure 6.5 (a) and (b). In comparison with the cut-ply configuration, this perforated case exhibits the following characteristics:

- The stiffness reduction in the initial non-linear stage prior to the onset of pseudo-yielding is much smaller, due to the 25% lower volume fraction of continuous 0° plies and the shorter stress transfer zones than in the cut-ply configuration (see Figure 6.5 (b)).

- The initial stage is followed by a rising 'plateau' stage with a pseudo-yield stress of 796 MPa, which is approximately 150 MPa higher than the cut-ply configuration (see Table 6.3). In addition, the pseudo-yield stress shows good agreement with the analytically predicted value.

- The 'plateau' smoothly transformed into the final strain-hardening stage, which has a secant modulus of 56 GPa (measured close to failure). This modulus is 56% higher than that for the cut-ply case. Moreover, this secant modulus is about 12% lower than the 0.9 $E_{1M-perforated}$ reference value of 64 GPa, but this reference value does not consider the damage in the off-axis plies;

- The average failure stress is 1117 MPa, which is approximately 370 MPa higher than that of the cut-ply case and is close to the estimated reference value.

Configurations (3) and (4) have the same '5P-5S' perforation pattern but only configuration (4), with the modified layup, exhibits distinct pseudo-yielding, indicating the layup significantly influences the pseudo-yielding behaviour.

6.3.2 Failure mechanisms

6.3.2.1 **Configuration (1) (Pristine-[90°/0°/+45°/-45°/0°]s)**

The tensile stress-strain curve and DIC strain contour plots at four selected stress levels of a baseline specimen is shown in Figure 6.6. These contour images, captured with 19 pixel facet size and 11 pixel facet distance by the DIC system together with carefully selected strain ranges (i.e. colour scales), reveal that transverse cracks (see Figure 6.7) appeared on the surface 90° ply with the increasing stress. The axial strain distribution along the section line at four stress levels are shown in Figure 6.8. The axial strain distribution plots present high levels of fluctuation. The fluctuation in the axial strains is due to cracking in surface 90° plies. The strain distribution fluctuation is reduced when the higher DIC facet distance of 15 pixels is used, as shown in Figure 6.9. This is because a lower facet distance is more sensitive to the surface ply cracks. (In the subsequent analysis of the damage mechanisms of the non-pristine configurations, the axial strain distributions were obtained using the 15 pixel facet distance.) The average strain of each plot is slightly higher than the corresponding reference values, indicated by the black lines for each stress level. This is because of cracking in the off-axis plies (i.e. $\pm$45° and 90° plies) was not considered in the reference value calculation.

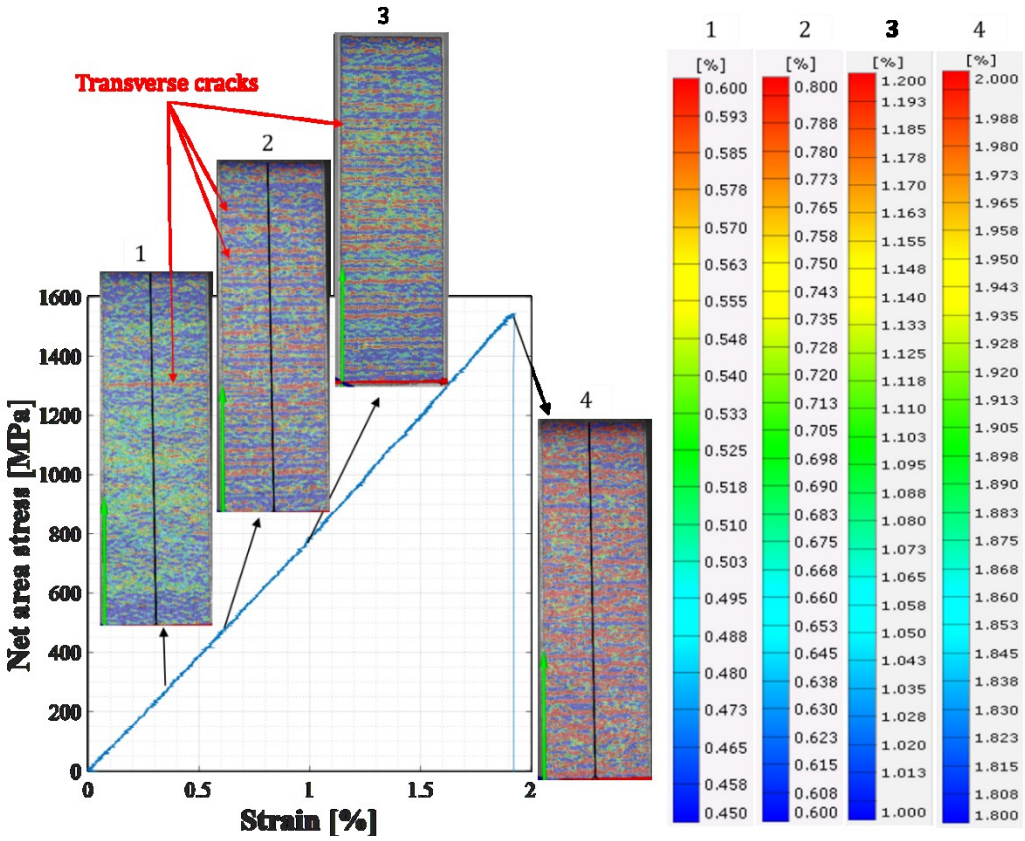
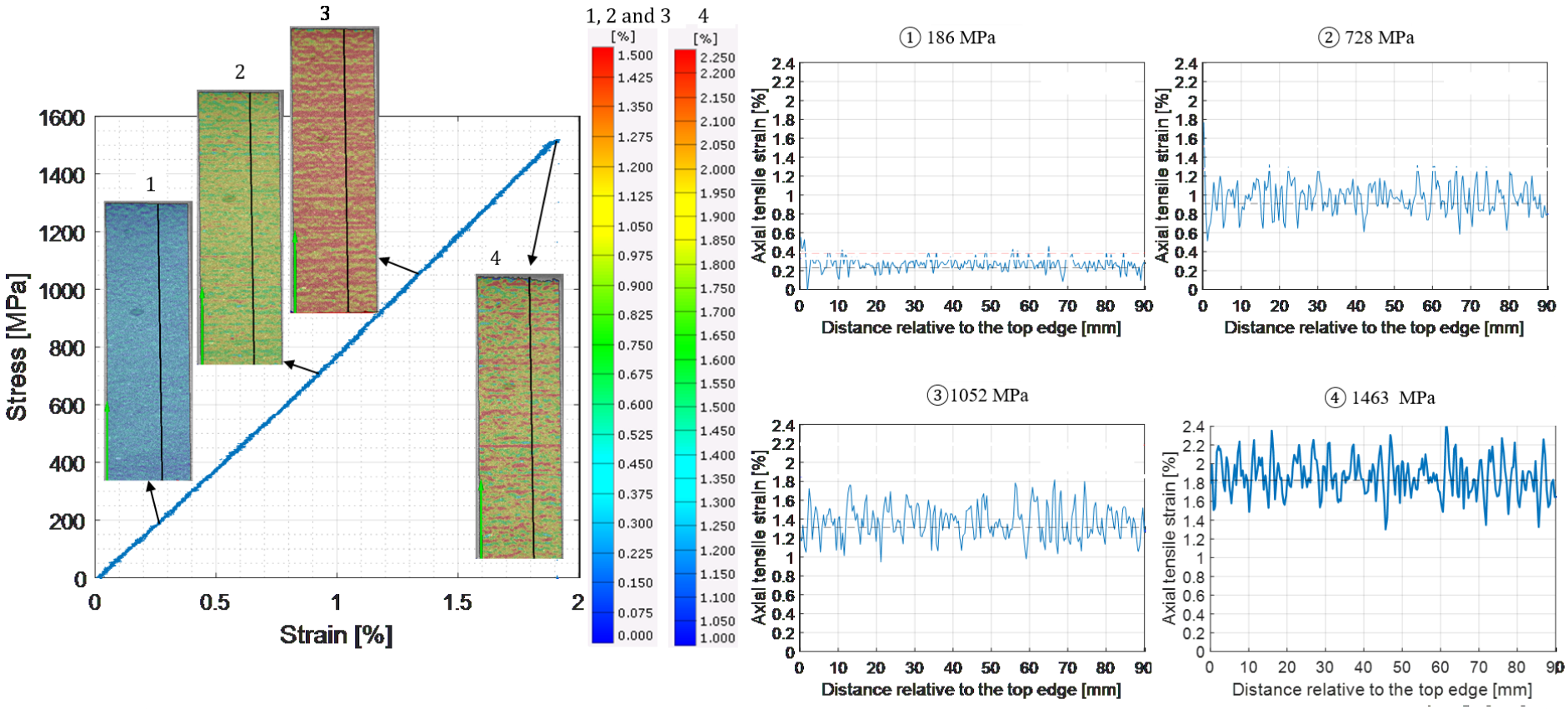


Figure 6.6 Tensile stress-strain curve and DIC strain contour plots (under different colour scales) at selected load levels.



Figure 6.7 Transverse cracks in the surface 90° ply of a partially tested pristine baseline specimen.



Reference line in strain plots:

------ $\varepsilon = \frac{P_i}{A_0 E_{0M}}$ (pristine)

- P_i (i = 1 to 4) is the remote tensile load for stress levels 1 to 4, respectively;
- A_0, E_{0M} are the gross cross-section area and tensile modulus of a pristine specimen.

Figure 6.8 Axial strain distribution plots at selected stress levels for the pristine baseline configuration (DIC facet size:19 pixel and facet distance: 11 pixel).

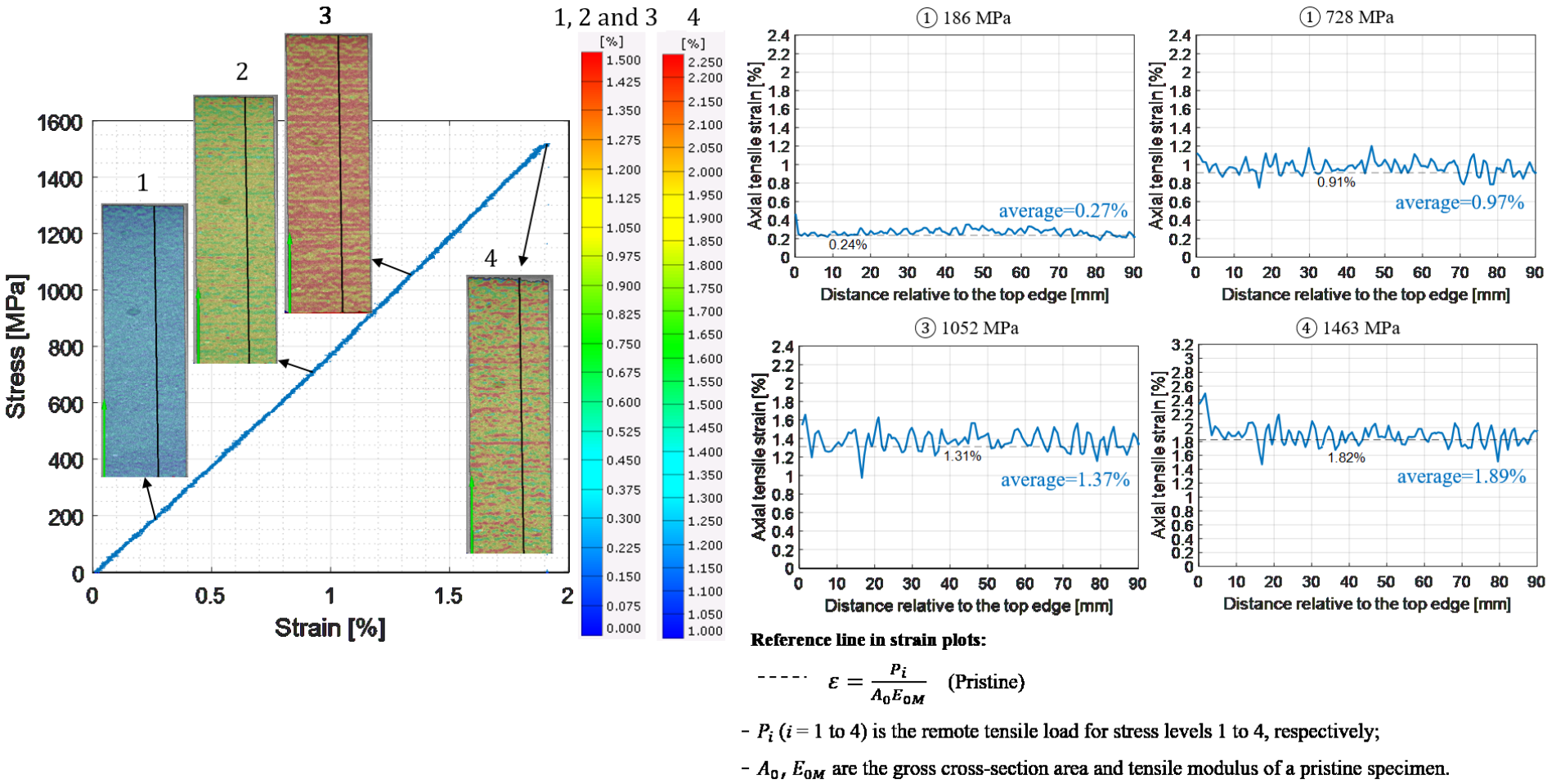


Figure 6.9 Axial strain distribution plots at selected stress levels for the pristine baseline configuration (DIC facet size:19 pixel and facet distance: 15 pixel).

6.3.2.2 **Configuration (2) (Cut-[90°/0°/+45°/-45°/0°c]s)**

The DIC strain contour plots of a cut-ply specimen at six selected stress levels in the tensile response are shown in Figure 6.10. The first two contour plots show high strain regions gradually appeared in the vicinity of the ply cut positions, prior to the plateau stage in the tensile stress-strain response. These high strain regions (shown in red for stress levels 3 to 6) gradually expand during the plateau and the final strain-hardening stages. The axial strain distribution along the longitudinal section line (shown in the contour plots) for each of the selected stress level, is shown in Figure 6.11. The positions of the cuts are labelled in each axial strain distribution plot.

At stress level 1 (170 MPa), DIC again shows significant fluctuations. The axial strain plot oscillates between the pristine and fully-delaminated reference values but does not show a periodic behaviour aligned with the cut positions. This is probably due to the noise in the DIC measurement at these low strains and the difficulty for the DIC to detect strain changes over the very short stress transfer zones at this low stress level. (The UD specimens with the same cut pattern, showed a similar behaviour at a low strain level (see Figure 4.6). At stress level 2 (500 MPa), the periodic behaviour of the axial strain is now more visible, because of the higher applied tensile strain and the longer stress transfer zones. The peak values are close to the reference line for the fully-delaminated behaviour and the trough values are close to the reference line for the pristine reference.

During the plateau stage (stress levels 3, 4 and 5), there is a zone in which the trough strain values are significantly higher than the pristine reference value and the peak strain values significantly exceed the reference value for fully-delaminated behaviour. This zone indicates delamination has occurred and the length of this zone increases with increasing applied strain, as shown in the highlighted region in the axial strain distribution plots. This is unlike the axial strain distribution observed in the UD cut ply case (see Figure 4.6). As noted earlier, this difference is probably due to cracking in the off-axis plies.

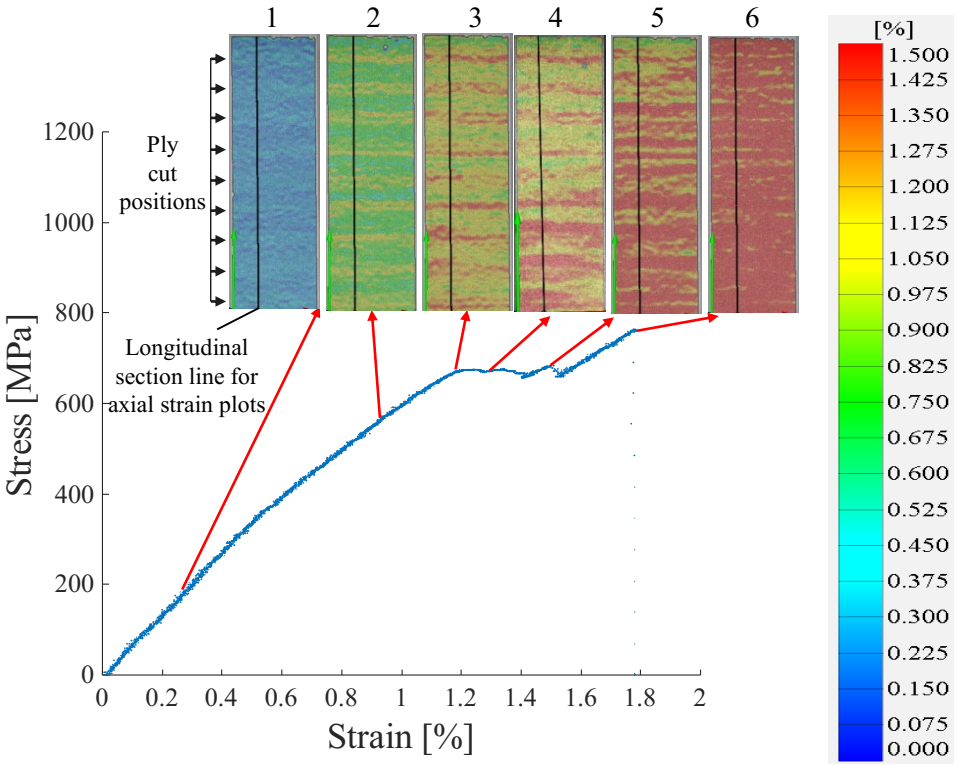
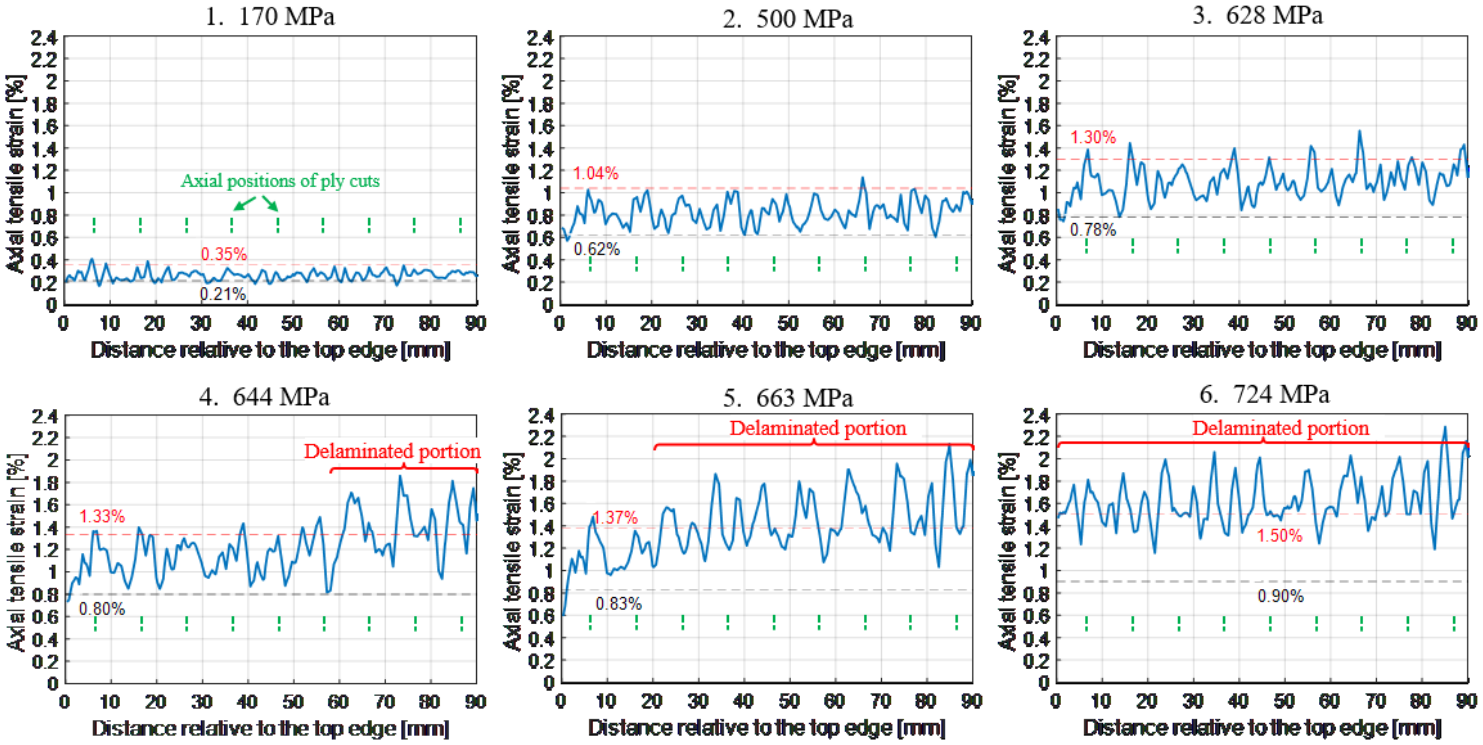


Figure 6.10 Tensile response of a cut-ply multidirectional spcimen and the DIC strain contour plots at six stress levels.



Reference lines in strain plots:

- - - - - $\varepsilon = \frac{P_i}{A_0 E_{0M}}$ (pristine) - - - - - $\varepsilon = \frac{P_i}{A_{del} E_{1M_del}}$ (delaminated)

- P_i ($i = 1$ to 6) is the remote tensile load for stress levels 1 to 6, respectively;
- A_0 and A_{del} are the cross-sectional areas of a pristine baseline specimen and of the continuous part (i.e. the outer QI sub-laminates) in the cut-ply specimen;
- E_{0M} and E_{1M_del} are the tensile moduli of a pristine baseline specimen and of the continuous part (i.e. the outer QI sub-laminates) in the cut-ply specimen.

Figure 6.11 Axial strain distribution along the longitudinal section line shown in the DIC strain contour plots for the cut-ply multidirectional spcimen shown in Figure 6.10.

The damage modes of this cut-ply configuration were investigated using a specimen tested to a stress of 670 MPa, which is slightly higher than the average pseudo-yield stress (see Figure 6.12). At this stress, delamination between the 0_c° and outer QI continuous sub-laminates is expected to have occured. The DIC strain contour plot at the stress, at which the test was halted, is also shown in Figure 6.12. Optical microscopic images of a polished cross-section at about 3.5 mm away from a cut position (labelled in the DIC image in Figure 6.12), is displayed in Figure 6.13. The zoom-in image of a part to the left of this cross-section shows delamination at the interfaces above and below the two middle 0_c° plies. It confirms that the delamination occurred at the expected interfaces and promoted the distinct 'pseudo-yield' and the intermediate plateau in the stress-strain response. In addition, many inclined cracks occurred in the -45° plies next to the middle 0_c° plies, presumably because of the high interlaminar shear stress acting at the -45°/0_c° interfaces in the vicinity of the cuts. These off-axis ply cracks also exist in the region, in which delamination has not yet developed, as shown in the zoom-in image on the right. Note that the left zoom-in image shows the delamination crack at the bottom -45°/0_c° interface linking up with a -45° ply crack and migrating to the adjacent +45°/-45° interface. Presumably, this minor delamination also occurred in other specimens tested to failure, however, the tensile response shown in Figure 6.5 implies the +45°/-45° delamination does not have a significant influence on the pseudo-ductility. The off-axis cracks and the potential minor delamination may also contribute to the experimental stiffness of the final strain-hardening stage being lower than that of the reference stiffness of $0.8E_{1M-cut}$, shown in Figure 6.5.

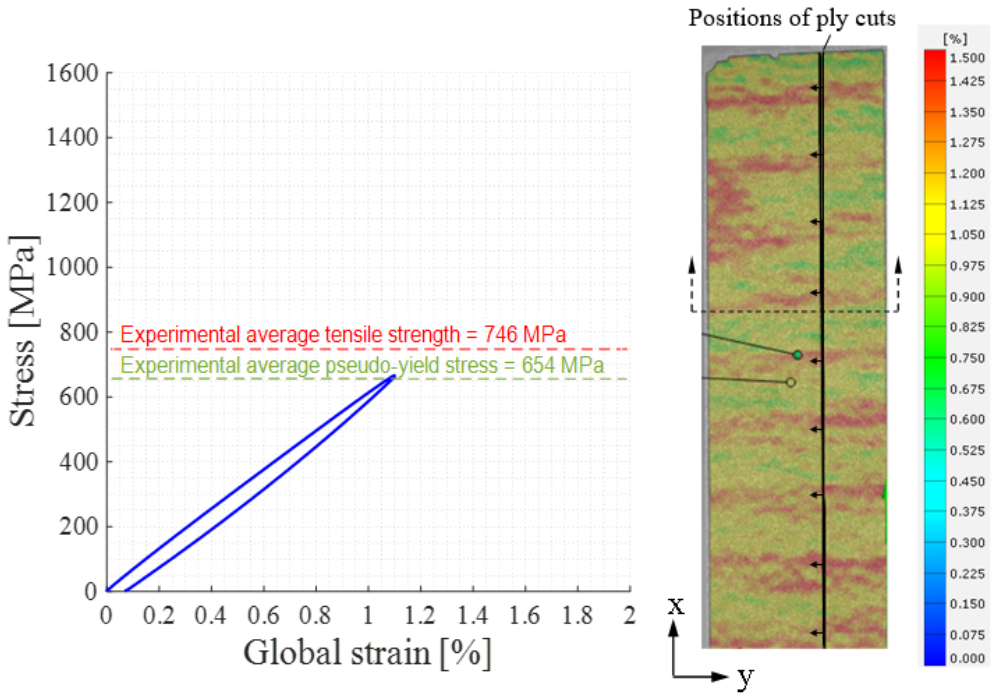


Figure 6.12 The tensile stress-strain curve of a multi-directional cut-ply specimen tested to 654 MPa and the DIC strain contour plot at 654 MPa.

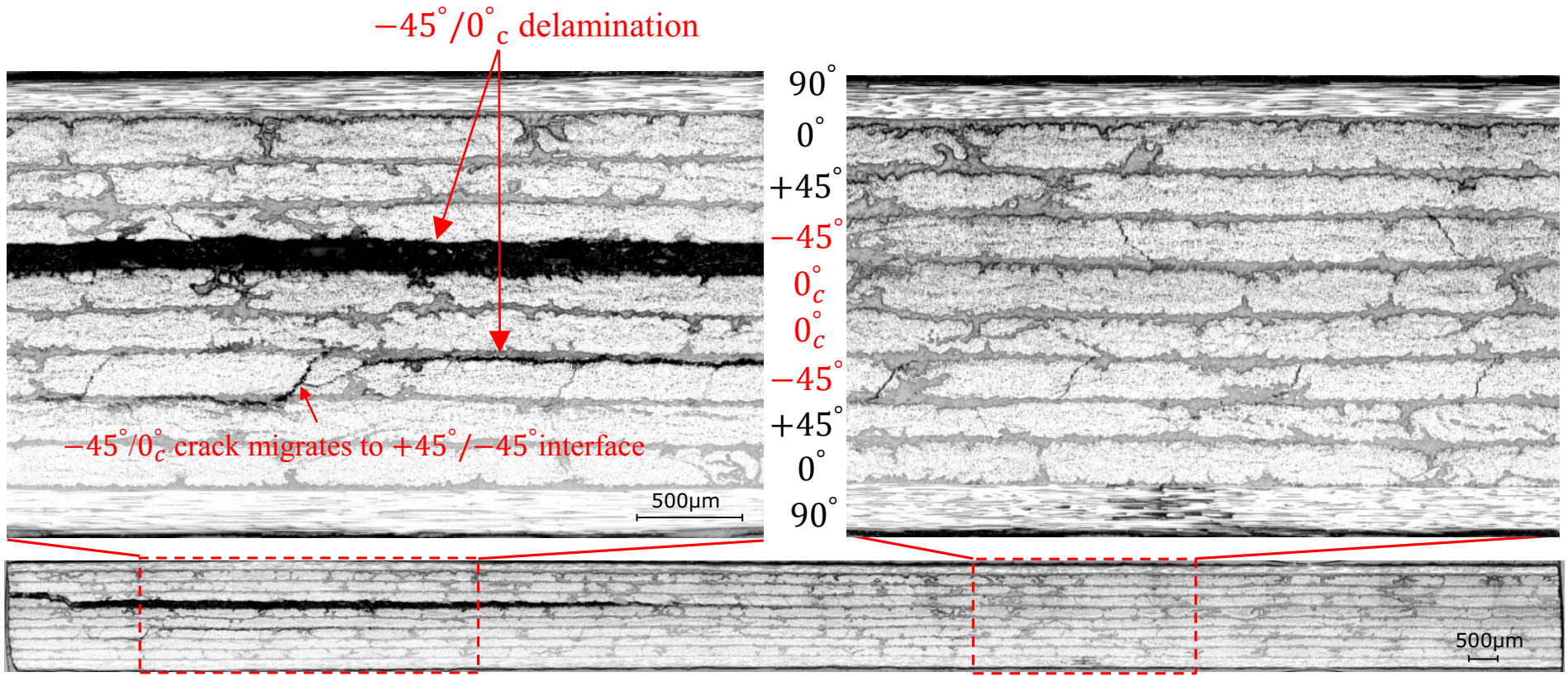


Figure 6.13 Microscopic images of the polished cross-section (3.5mm from the cut postion) of the specimen shown in Figure 6.12.

6.3.2.3 **Configuration (3) ('5P-5S'-[90°/0°/+45°/-45°/0°p]s)**

Figure 6.14 shows the tensile response and the DIC strain contour plots at four selected stress levels of a specimen containing '5P-5S' perforations and the original layup. The axial strain distribution plotted along the section line (aligned with the central line of perforations in the gauge length) are shown in Figure 6.15. The perforation positions are also labelled in these strain plots. The normalized axial strain distribution curves (defined as the axial strain divided by the strain for a pristine specimen), for the four stress levels are plotted together in Figure 6.16, for comparison.

The axial strain distribution is periodic for all the selected stress levels, with the peak strains appearing in the vicinity of perforation positions (see Figure 6.15). At the first stress level, most of the trough strains align along the reference line for a pristine specimen. The peak strains are approximately 0.19% (in strain) on average higher than the reference value for debonding behaviour. This peak strain difference is presumably because of the onset of cracks in the off-axis plies (as will be seen in the subsequent microscopic images). Figure 6.16 shows that the normalized axial strain distribution for the four stress levels are almost identical and exhibit negligible growth of the stress transfer zone length for increased remote tensile stress. In addition, it is worth noting that there are small increments in some of the trough strains, but these increments are not as significant as those for the pseudo-ductile perforated counterpart, i.e. configuration (4), at the similar stress levels (as will be seen in Figure 6.22 (a)). These findings suggest no significant debonding occurred at all, prior to ultimate failure.

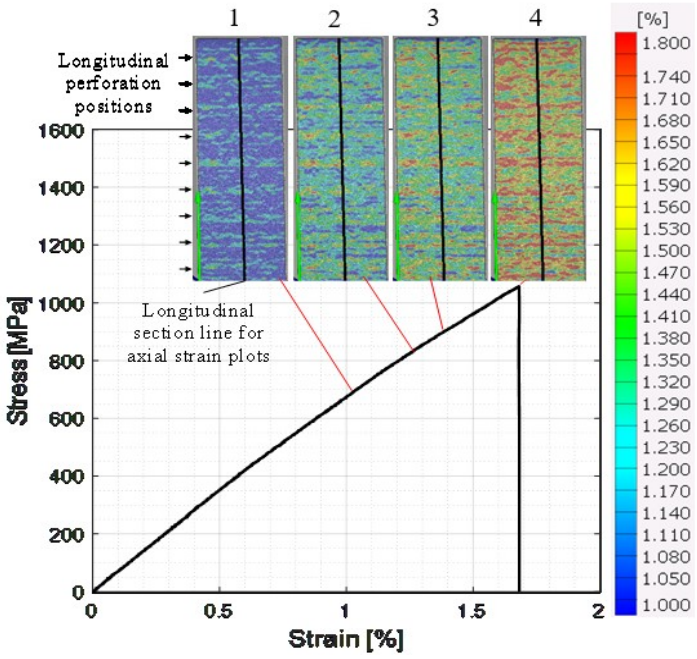
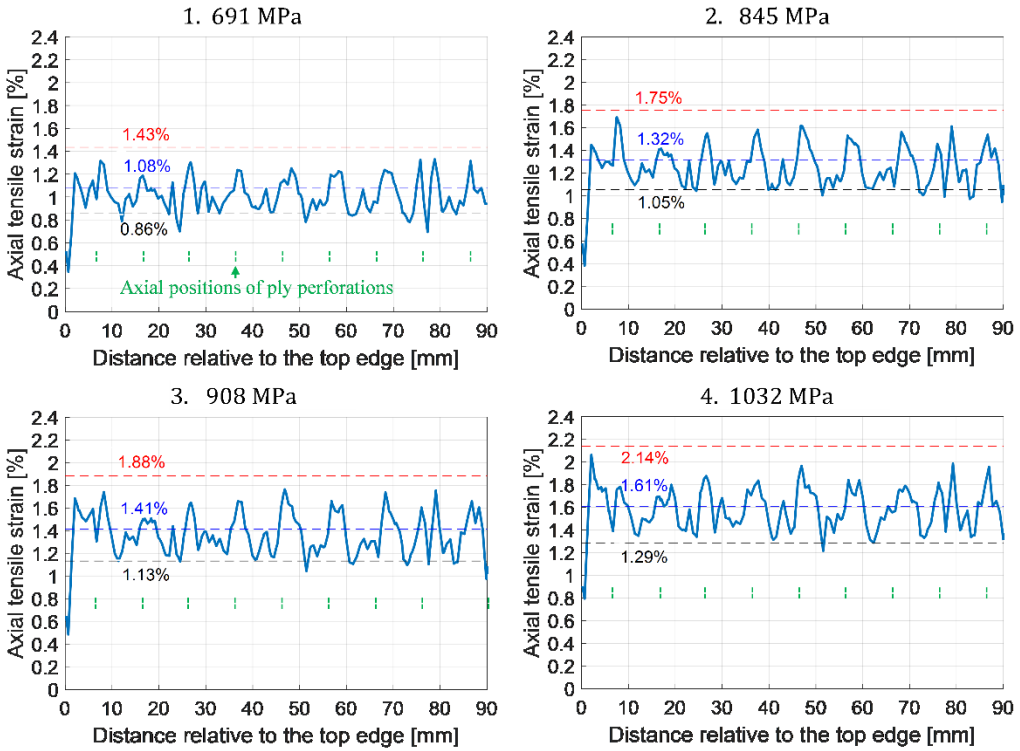


Figure 6.14 Tensile response of a perforated specimen with the [90°/0°/±45°/0°_{p}]s layup and DIC strain contour plots (measured with 19 pixel facet size and 15 pixel facet point distance) at four selected stress levels.

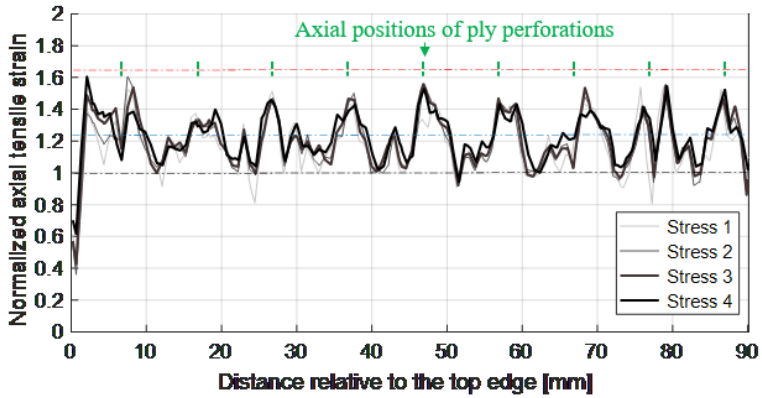


Reference lines in strain plots:

----- $\varepsilon = \frac{P_i}{A_0 E_{0M}}$ (pristine) ----- $\varepsilon = \frac{P_i}{A_{deb} E_{1M_deb}}$ (debonded) ----- $\varepsilon = \frac{P_i}{A_{del} E_{1M_del}}$ (delaminated)

- P_i (i = 1 to 4) is the tensile load for stress levels 1 to 4, respectively;
- A_0, A_{del} and A_{deb} are the cross-sectional areas of a pristine baseline specimen, the continuous outer QI sub-laminates of a cut-ply specimen and the continuous unperforated part of a perforated-ply specimen, respectively;
- E_{0M}, E_{1M_del} and E_{1M_deb} are the tensile moduli of a pristine baseline specimen, the continuous outer QI sub-laminates of a cut-ply specimen and the continuous unperforated part of a perforated-ply specimen, respectively;

Figure 6.15 Axial strain distribution along the longitudinal section line shown in the DIC strain contour plots of the spcimen ('5P-5S'- [90°/0°/±45°/0°$_p$]s) shown in Figure 6.14.



Reference lines in normalized axial strain plots:

$\hat{\varepsilon}_0 = 1$ (pristine) $\quad \hat{\varepsilon}_{deb} = \frac{A_0 E_{0M}}{A_{deb} E_{1M_deb}}$ (debonded) $\quad \hat{\varepsilon}_{del} = \frac{A_0 E_{0M}}{A_{del} E_{1M_del}}$ (delaminated)

- A_0, A_{del} and A_{deb} are the cross-sectional areas of a pristine baseline specimen, the continuous outer QI sub-laminates of a cut-ply specimen and the continuous unperforated part of a perforated-ply specimen, respectively;
- E_{0M}, E_{1M_del} and E_{1M_deb} are the tensile moduli of a pristine baseline specimen, the continuous outer QI sub-laminates of a cut-ply specimen and the continuous unperforated part of a perforated-ply specimen, respectively.

Figure 6.16 Aixal strain distirbution normalized by the tensile strain of a pristine specimen at the four stress levels for the specimen ('5P-5S'-[90°/0°/±45°/$0°_p$]s) shown in Figure 6.14.

The failure mechanisms of this perforated configuration were also investigated using a specimen loaded to 940 MPa (see Figure 6.17), very close to the average experimental tensile strength of 949 MPa (see Table 6.3), for this configuration. The micrographs of a polished cross-section at approximately 1.5 mm away from a transverse line of perforations are shown in Figure 6.18 (i). Note that a length of about 2.5 mm was cut off from the left end of the sample to fit the diameter of the potting tool, which was used to prepare the specimen for microscope inspection. Cracks around the three perforated 0°_{p} fibre bundles are highlighted in the overall cross-section view (see Figure 6.18 (ii)). The earlier stress-strain plot (see Figure 6.14) shows little sign of pseudo-yielding and therefore implies that no significant debonding has occurred (as indicated by the absolute and normalized axial strain distribution plots of Figure 6.15 and Figure 6.16). This suggests that the debonding observed in the microscopic sections of Figure 6.18 did not extend very far from the perforation plane but this requires further investigation.

A long crack has initiated from the left bottom corner of the debonded perforation on the right and propagates along the -45°/$0°_{p}$ interface and partially migrated into the adjacent $-45°$ ply. In addition, delamination is observed at the bottom 0°/+45° interface in the left half of the overall section view.

In addition, the three enlarged images of the left and middle perforations show many ±45° cracks (see Figure 6.18 (iii-v)). The cracks in the off-axis plies next to the perforated bundles are denser than those next to the continuous bundles in the 0°_{p} plies (see Figure 6.18 (iii & v)). This is possibly resulted from the interlaminar shear stress acting in the stress transfer zone adjacent to the perforations. The much denser -45° cracks in the vicinity of the perforations may have caused the high peak strains, which significantly exceed the 'debonded' reference strain value, shown in Figure 6.15 and Figure 6.16.

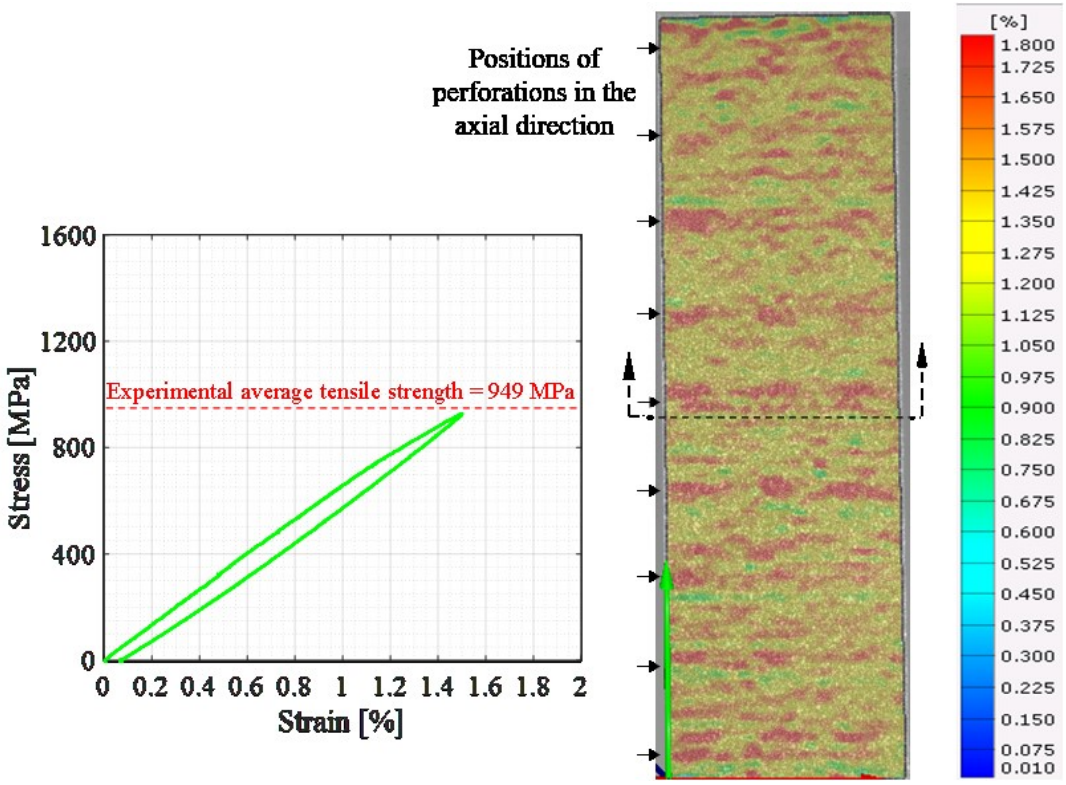


Figure 6.17 Tensile stress-strain response of a '5P-5S' pattern perforated specimen with the layup of $[90°/0°/\pm45°/0°_p]$s tested to a stress close to failure and the DIC strain contour plot at the maximum stress.

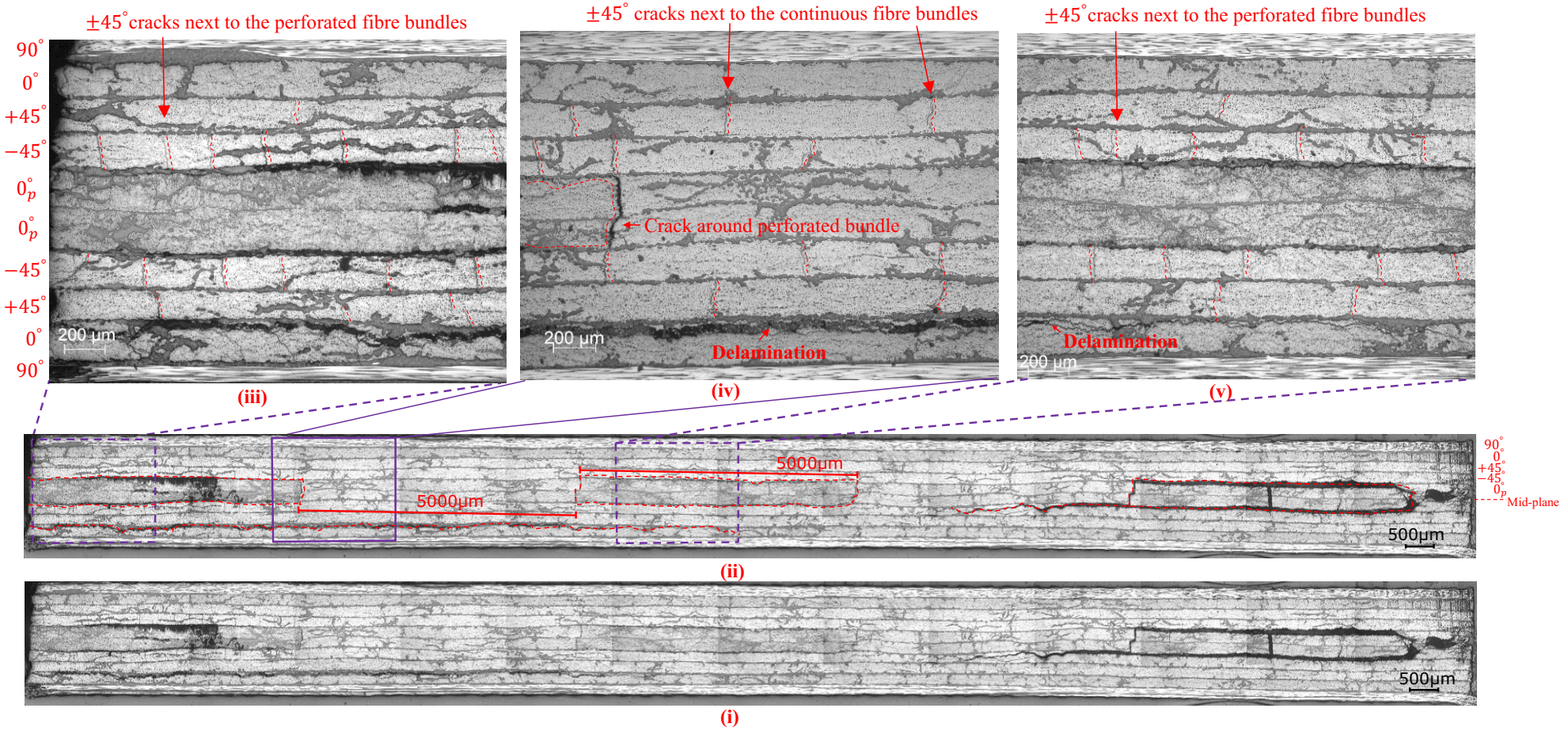


Figure 6.18 Microscopic images of a polished cross-section of the '5P-5S' pattern perforated specimen (with the layup of [90°/0°/±45°/0°_{p}]s) specimen shown in Figure 6.17.

6.3.2.4 **Configuration (4) ('5P-5S'-[90°/+45°/-45°/0°/0°p]s)**

As seen earlier in Figure 6.5 (a) and (b), a pseudo-ductile tensile response with a distinct intermediate 'yielding' and a final strain-hardening stage, was achieved after moving the continuous 0° plies (in configuration (3)) to the position adjacent to the middle $0°_p$ perforated plies.

The pseudo-ductile tensile response of a specimen tested to failure and the DIC strain contour plots at six selected stress levels, are shown in Figure 6.19. The axial strain distribution curves along a longitudinal section line (along the central line of perforations in the gauge length) are presented in Figure 6.20.

At the first stress level, the strain oscillates between the pristine and fully-delaminated reference values, but does not show an obvious periodic behaviour, relative to the cut positions. This non-periodic behaviour is probably because of off-axis ply cracking, developed in the vicinity of the perforated positions, which resulted in strains that are higher than the reference value for a debonded specimen, and masked the expected periodic behaviour. At stress level 2, the axial strain distribution is more periodic. Most of the peak strains, at the perforation positions become close to the reference line for a delaminated specimen and the trough strains are close to the reference line for a pristine specimen.

At stress level 3, the tensile response transfers to the short 'yielding' stage (see Figure 6.19). Debonding initiated from the perforations is expected to develop along the perforated fibre bundles, during this yielding stage. Stress levels 4 is close to level 3. The axial strain distributions for these two stress levels are similar, with all the peak strains exceeding the reference values for delamination. It can be seen that the trough strains in the highlighted regions become slightly higher than the reference for a pristine specimen, at these two stress levels. It may indicate debonding has initiated from the adjacent perforations and propagated a short distance.

Stress level 5 is in the final strain-hardening stage (see Figure 6.19), where debonding is expected to have further propagated longitudinally. Some of the peak strains now lie significantly above the reference line for a delaminated specimen. Compared to the previous stress level, the high trough strain regions have increased significantly and the trough strain values in these regions have become close to the reference strain for a debonded specimen. This indicates debonding has propagated further, forming these longer highlighted high strain regions. The high trough strain regions grow further as the stress is increased to level 6 (the ultimate failure point).

The axial strain distribution curves at each stress level, normalized by the tensile strain for a pristine specimen, are plotted together in Figure 6.21, to reveal the axial strain variation, during the test. Compared to the non-pseudo-ductile case, with the layup of [90°/0°/±45°/$0°_p$]s (see Figure 6.16), this

pseudo-ductile configuration, with the modified layup of [90°/±45°/0°/0°$_p$]s (see Figure 6.21), exhibits more significant increase in the trough strains during the loading process.

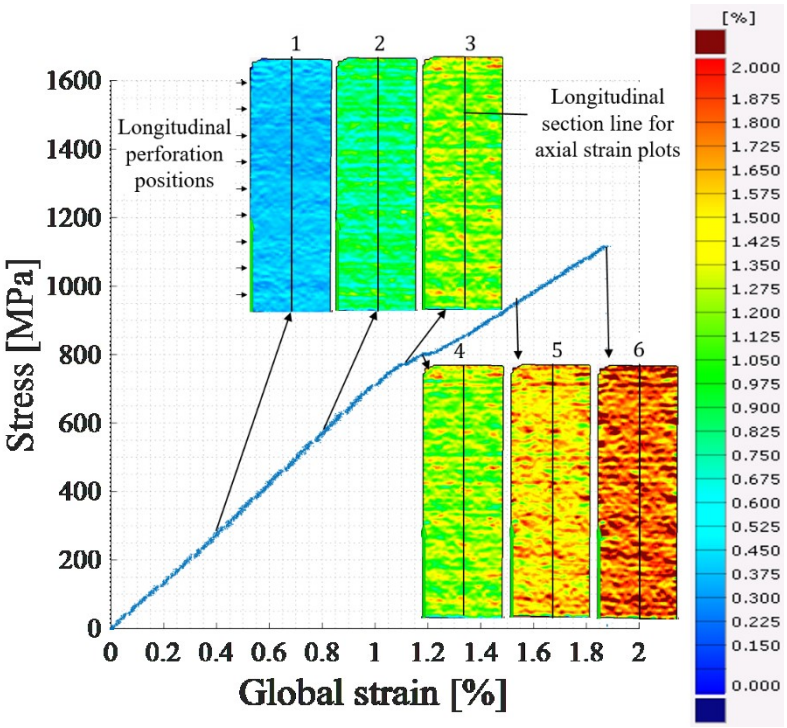
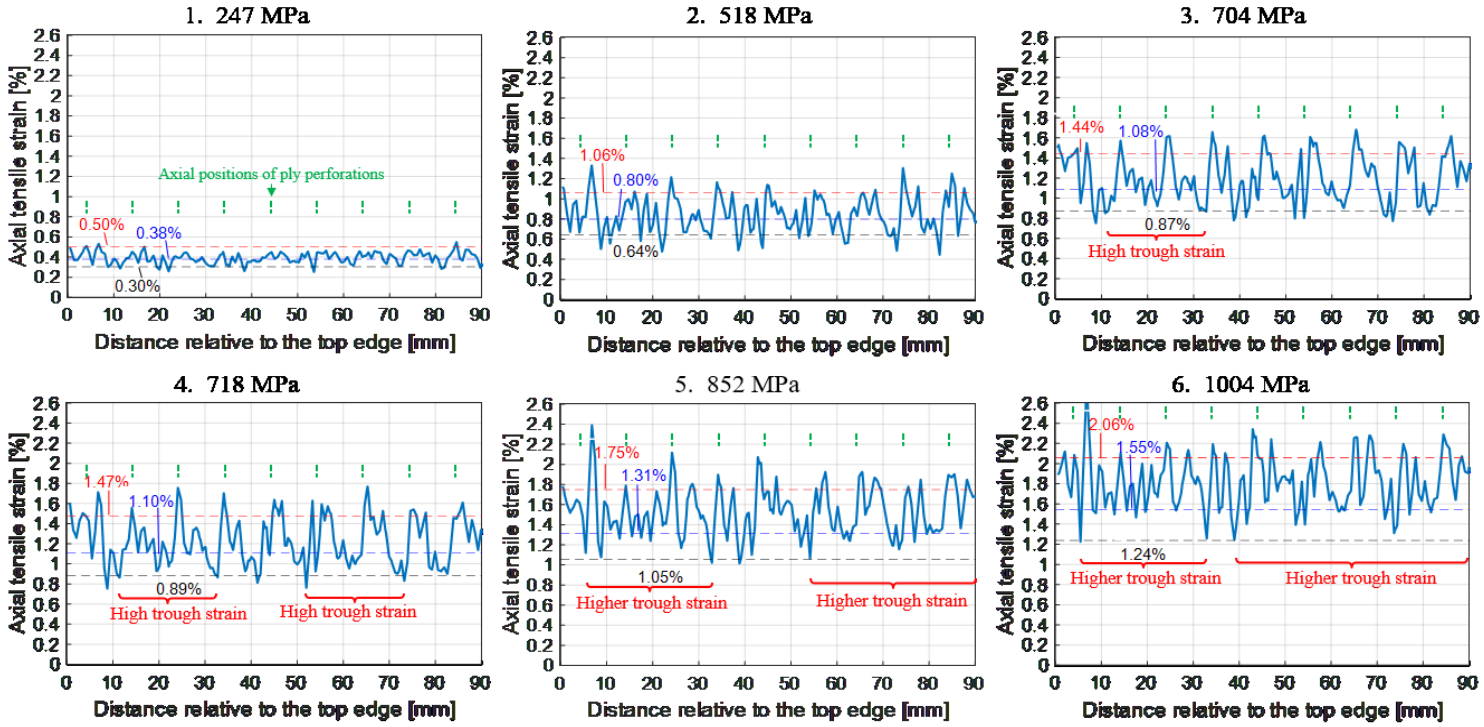


Figure 6.19 Tensile stress-strain response of a '5P-5S' pattern perforated specimen with the modified layup of [90°/±45°/0°/0°$_p$]s and the DIC strain contour plots (measured with 19 pixel facet size and 15 pixel facet point distance) at six selected stress levels.

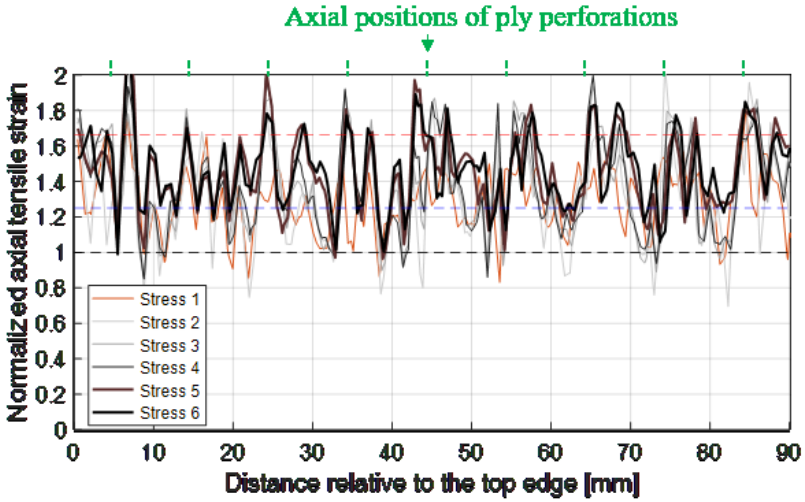


Reference lines for in strain plots :

------ $\varepsilon = \frac{P_i}{A_0 E_{0M}}$ (pristine) ------ $\varepsilon = \frac{P_i}{A_{deb} E_{1M_deb}}$ (debonded) ------ $\varepsilon = \frac{P_i}{A_{del} E_{1M_del}}$ (delaminated)

- P_i ($i = 1$ to 6) is the remote tensile load for stress levels 1 to 6, respectively;
- A_0, A_{del} and A_{deb} are the cross-sectional areas of a pristine baseline specimen, the continuous outer QI sub-laminates of a cut-ply specimen and the continuous unperforated part of a perforated-ply specimen, respectively;
- E_{0M}, E_{1M_del} and E_{1M_deb} are the tensile moduli of a pristine baseline specimen, the continuous outer QI sub-laminates of a cut-ply specimen and the continuous unperforated part of a perforated-ply specimen, respectively;

Figure 6.20 Axial strain distribution plots along the longitudinal section line shown in the DIC strain contour plots in Figure 6.19 (for the '5P-5S'-[90°/±45°/0°/0°$_p$]s specimen).



Reference lines in normalized axial strain plots:

$\hat{\varepsilon}_0 = 1$ (pristine) $\quad \hat{\varepsilon}_{deb} = \frac{A_0 E_{0M}}{A_{deb} E_{1M_deb}}$ (debonded) $\quad \hat{\varepsilon}_{del} = \frac{A_0 E_{0M}}{A_{del} E_{1M_del}}$ (delaminated)

- A_0, A_{del} and A_{deb} are the cross-sectional areas of a pristine baseline specimen, the continuous outer QI sub-laminates of a cut-ply specimen and the continuous unperforated part of a perforated-ply specimen, respectively;
- E_{0M}, E_{1M_del} and E_{1M_deb} are the tensile moduli of a pristine baseline specimen, the continuous outer QI sub-laminates of a cut-ply specimen and the continuous unperforated part of a perforated-ply specimen, respectively.

Figure 6.21 Axial strain distribution (at stress levels 3 to 6, shown in Figure 6.20) normalized by the tensile strain of a pristine specimen, for the '5P-5S'-[90°/±45°/0°/$0°_p$]s specimen.

The damage modes of the pseudo-ductile perforated configuration have been investigated using a specimen loaded to 875 MPa (see Figure 6.22). This stress is slightly higher than the stresses related to the 'yielding' behaviour in the tensile response, and so it is expected that debonding has propagated from the 5 mm perforations. The DIC strain contour plot at this maximum loading stress and the corresponding axial strain distribution along the longitudinal section line (over the middle line of perforations), are shown in Figure 6.22. The trough values in the 0-25mm, 40-55 mm and 80-90 mm regions exceed the reference strain for a pristine specimen, indicating that significant debonding has occurred in these regions.

The ultrasonic C-scan and X-ray scanning images of this specimen are presented in Figure 6.23. The perforation positions within the perforated $0°_{\mathrm{p}}$ plies on the X-ray and ultrasonic C-scan diagrams, are marked in black and red, respectively.

The ultrasonic C-scan image of the signal amplitude reflected from the specimen back surface is presented in Figure 6.23 (a). The image indicates pockets of delamination, forming a grid pattern, presumably at the $0°/0°_{p}$ interfaces.

The X-ray image, presented in Figure 6.23 (b), shows longitudinal intralaminar cracks (presumably in the $0°_{p}$ plies) have initiated from the edges of most of the perforations and developed to different extents in the axial direction. Dense matrix cracks are identified in the -45° plies. A zoom-in image of the perforation at the bottom right corner shows dense cracks, distributed along the path of the longitudinal intralaminar cracks. The longitudinal intralaminar cracks (parallel to the incident ultrasonic signal) and any fibres bridging along these cracks will scatter the incident ultrasonic signal, leading to a greater loss of the signal amplitude at the boundaries of the perforated fibre bundles. The length of delamination (interlaminar cracks) is similar to that of the longitudinal intralaminar cracks, developed from the same perforations, implying that debonding around the perforated fibre bundles has occurred. The X-ray and ultrasonic C-scan images show that the debonding has not propagated to the same distance at all perforations, in the longitudinal direction, presumably due to material variability.

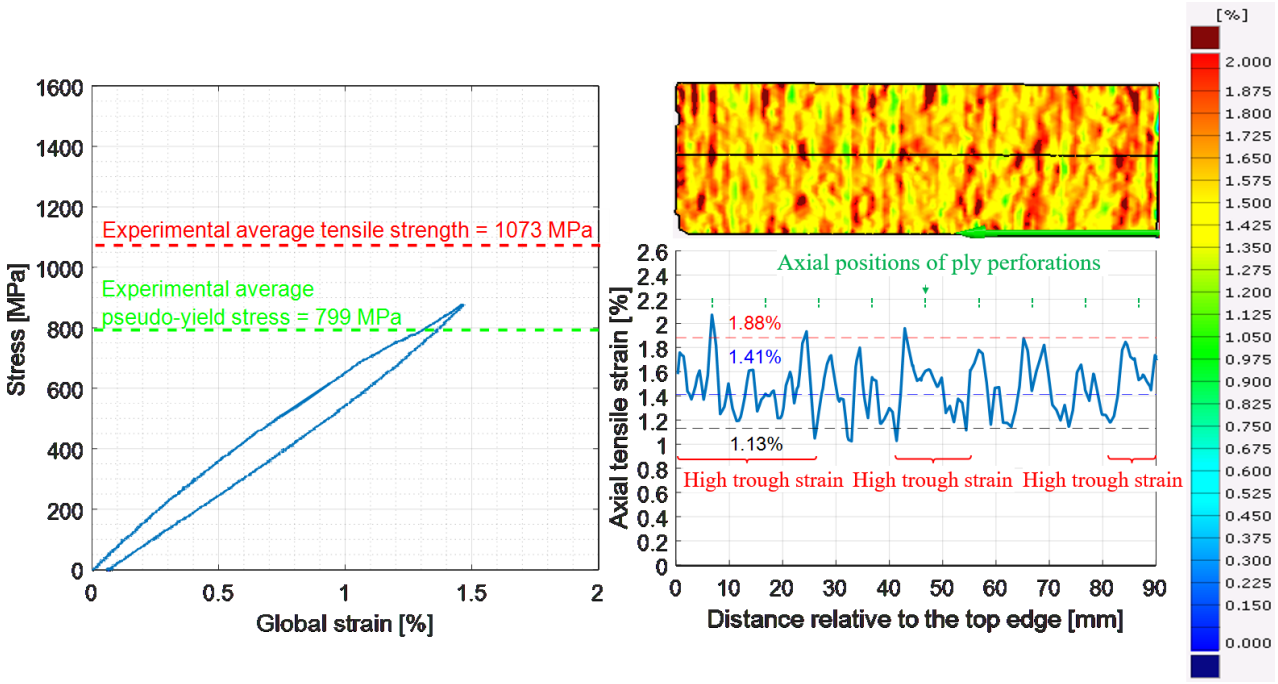


Figure 6.22 Tensile stress-strain response of a '5P-5S'-[90°/±45°/0°/0°$_p$]s specimen, tested to 875 MPa and the DIC strain contour image and the axial strain distribution curve at 875 MPa.

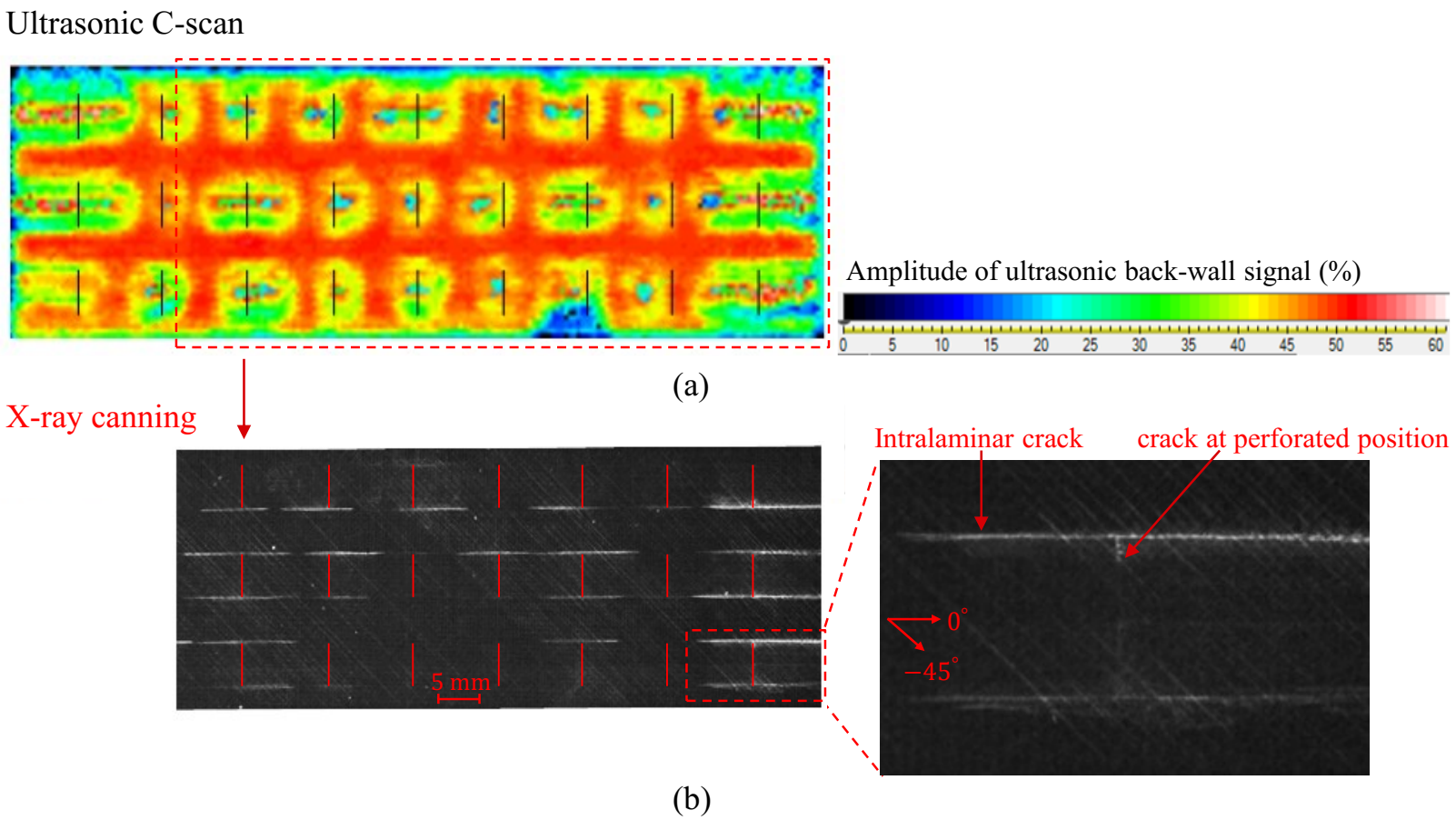


Figure 6.23 Ultrasonic C-scan and X-ray scanning images of a specimen containing '5P-5S' perforation pattern and the layup of [90°/±45°/0°/0°$_p$]s tested to 875 MPa.

6.3.2.5 **Comparison of the tensile performance of the multi-directional configurations**

The multi-directional configurations containing continuous cuts with the original layup of $[90°/0°/\pm45°/0_c^\circ]_S$ (configuration (2))) and containing the '5P-5S' perforations with the modified layup of $[90°/\pm45°/0°/0_p^\circ]_S$ (configuration (4)), both exhibited pseudo-ductility. High initial stiffnesses (83 and 89% of the baseline pristine multi-directional laminate) and high pseudo-yield stresses (88% and 72% of the ultimate failure strengths) were achieved in configurations (2) and (4), respectively, as shown in Table 6.3. The '5P-5S' perforated configuration with the original layup showed no distinct 'yielding' in the tensile response. The failure mechanisms of these ply weakened configurations are summarized in Table 6.4.

Table 6.4 Summary of the failure mechanisms of the multi-directional configurations.

Configurations	Configuration (2) - Cuts $([90°/0°/+45°/-45°/0_c^\circ]_s)$	Configuration (3) - '5P-5S' $([90°/0°/+45°/-45°/0_p^\circ]_s)$	Configuration (4) - '5P-5S' $([90°/+45°/-45°/0°/0_p^\circ]_s)$
Failure mechanisms	• Relatively sparse matrix cracking in the $-45°$ plies • Delamination at the expected $-45°/0_c^\circ$ interfaces • Minor delamination migrated to the $+45°/-45°$ interfaces	• Much denser matrix cracking than that in configuration (2). This cracking is denser in the $-45°$ plies next to the 0_p° perforated bundles than those next to the unperforated bundles in the 0_p° plies • Debonding around the 0_p° fibre bundles but did not propagate long distance • Unexpected delamination at the $0°/+45°$ interface	• Matrix cracking in the $-45°$ plies, in the vicinity of the significantly debonded fibre bundles. These cracks are relatively sparse than those in configuration (3). • Debonding (inter- and intralaminar cracks) around the perforated 0_p° fibre bundles

The strain range related to the delamination process of the cut plies (i.e. the intermediate flat plateau stage) is much greater than that for the debonding of the perforated bundles (i.e. the intermediate rising 'plateau' stage) for the pseudo-ductile case. This is because, analytically, the change in stiffness caused by the delamination of the 0_c° cut plies is more significant than the stiffness variation due to the debonding of the 0_p° perforated bundles.

As already noted the original layup achieved the pseudo-ductility with the continuous cuts strategy, but this achievement did not happen with the '5P-5S' perforations. For the '5P-5S' perforations in the

original layup, a much greater density of cracking in the adjacent $\pm 45°$ plies was observed than in the cut configuration. This was probably caused by the stress concentration associated with the edges of the perforations. The energy required to drive both the dense cracking of the $\pm 45°$ plies and the debonding of the perforated bundles will have been remarkably increased (compared to driving the debonding alone) and it appears that this prevented any significant debonding and the associated pseudo-ductile behaviour. When the perforated 0_p° plies were confined between continuous 0° plies in the modified layup, the effect of these stress concentrations will have been much reduced and so the debonding process could propagate as intended.

6.4 Conclusions

This chapter investigated the potential to transfer the pseudo-ductility observed in the UD laminates to multi-directional laminates, using the 'ply weakening' strategy. The multi-directional laminates consist two central 0° plies, embedded between two blocks of continuous QI sub-laminates. It was shown that the brittleness observed in the conventional continuous multi-directional laminates could be overcome by introducing continuous cuts or lines of perforations in the central 0° plies. In the case of the perforations, the orientation of the plies adjacent to the perforated plies is critical.

Chapter 7

Conclusions and future work

7.1 Conclusions

The research presented in this thesis has demonstrated that it is possible to promote pseudo-ductility and a progressive failure process in conventional brittle UD and multi-directional laminates made of a single type of CFRP material, using a ply weakening strategy. Pseudo-ductile tensile stress-strain responses were achieved, which consisted of an initial approximately-linear stage, with high initial stiffness, followed by a metal-like intermediate plateau and a final strain hardening stage. The key findings of chapters 3 to 6 are summarized below.

Chapter 3: The potential to achieve pseudo-ductility in UD laminates, using ply weakening (via introducing continuous ply cuts or periodic perforations, perpendicular to the fibre direction in selected plies) and interface weakening methods, was investigated using a Linear Elastic Fracture Mechanics (LEFM)-based simplified analytical model. Both ply weakening methods were predicted to achieve a tailorable and progressive pseudo-ductile tensile failure process. The intermediate plateau in the stress-strain response was due to delamination of the cut plies or debonding of the perforated fibre bundles. In this model, the criterion for the onset of delamination or debonding is determined by mode II fracture toughness. When used in conjunction with the ply weakening approach, the interface weakening was shown to introduce another plateau stage at a lower stress level. The ply weakening model was then refined by considering the evolution of the interlaminar stress transfer zones between the continuous and discontinuous plies. In contrast to the simplified prediction model, the refined model predicts a gradual change in stiffness in both the initial and final strain-hardening stages. A parametric study showed that the absolute and relative thickness of the continuous and weakened plies, and geometric parameters of the platelets or fibre bundles (such as the lengths of the platelets and perforated fibre bundles, the aspect ratio of the perforated and un-perforated fibre bundles, formed by cuts or perforations) dominate the resulting pseudo-ductile properties, for a given material. The 'ply perforation' strategy has showed the potential to provide superior and a wider design space to manipulate pseudo-ductile properties, compared to the 'ply cut' counterpart.

Chapter 4: An experimental investigation was conducted on the tensile response of UD laminates containing different numbers of continuous cuts and different proportions of continuous and cut plies. DIC and ultrasonic C-scan were employed to examine the development of failure mechanisms at different loads. The results demonstrated that laminates with low number of cuts often suffer from

significant load drop(s) after the initial almost-linear stage, due to unstable delamination growth. The load drops issue was resolved by introducing a sufficient number of cuts, to achieve a stable intermediate plateau stage, at the expense of a slightly higher reduction in stiffness during the initial stage of the stress-strain response. Compared to the laminates containing a single cut, multiple cuts promoted progressive delamination initiated at different cut positions, providing a more stable plateau in the tensile response. For the pseudo-ductile cases with stable plateau stress-strain behaviour, the DIC results demonstrated that the evolution of stress transfer zones showed good agreement with that predicted by the refined analytical model. In addition, the refined models provided a more accurate representation of the experimental stress-strain behaviour of those pseudo-ductile cases, especially for the elastic modulus variation of the initial and final strain-hardening stages.

Chapter 5: An experimental investigation was performed on UD laminates containing various perforation patterns. The laminates containing a single line of laser-milled perforations (with different patterns) retained an initial stiffness almost identical to that of the pristine baseline. The approximately-linear initial stage was followed by unstable load drops and considerable scatter in the tensile behaviour. This behaviour was shown to be caused by unstable delamination or debonding from the perforated positions, accompanied by breakage of the continuous fibres. A desirable pseudo-ductile tensile response with an intermediate 'rising plateau' was achieved with laminates containing multiple lines of perforations. X-ray CT images and axial strain distribution on DIC strain maps proved that the stable intermediate plateau was promoted by the progressive debonding of the perforated fibre bundles. 'Fibre bridging' at the intralaminar cracks, the variation of fracture toughness at perforated positions and interaction of stress transfer zones, contributed to the stable 'rising plateau'. The experimental tensile responses of these pseudo-ductile UD perforated laminates showed good agreement with the predicted results, proposed from the refined analytical model. The experimentally observed evolution of the axial strain distribution during the entire loading process, determined from DIC data, showed good agreement with that predicted by the refined analytical model.

Chapter 6: Preliminary experimental tests confirmed that it is possible to achieve pseudo-ductility in a multi-directional laminate using the ply cut and perforation strategies. This was achieved by introducing continuous cuts or lines of perforations normal to the fibre direction of two central 0° plies, which were embedded between two blocks of continuous QI sub-laminates.

A pseudo-ductile response with a relatively long and stable intermediate plateau was attained in the configuration containing continuous cuts. The evolution of axial strain distribution (captured from DIC system) and microscopic images indicated that progressive delamination of the discontinuous cut plies, initiated by the dispersed cuts, caused the plateau. Pseudo-ductile response with a distinct but short intermediate 'yielding' behaviour was obtained from the perforated configuration with a modified QI

sub-laminate layup, in which continuous 0° plies were positioned on both sides of the perforated plies. X-ray and Ultrasonic C-scan results confirmed that the 'yielding' was associate with the debonding of the dispersed perforated fibre bundles. Cracking in the off-axis plies was observed in all ply-weakened configurations.

The main achievements of this PhD project are summarized below:

- Tailorable pseudo-ductility with high initial stiffness and high pseudo-yield stress in CFRP UD and multi-directional composites have been achieved by a ply weakening approach;
- The analytical models have been developed and showed good agreement with the experimental results.

7.2 Recommendations for future work

- In this thesis, the ply weakenings, i.e. continuous cuts and perforations, were placed in the perpendicular to the fibre direction of selected plies. The effect of ply weakening in other directions relative to the fibres on the tensile performance can be investigated.

- Conventional continuous laminates frequently fail catastrophically due to the presence of stress concentrations (e.g. open-holes or notches). The influence of patterns of perforations introduced in high stress zones could be investigated to determine if it is possible to reduce the notch sensitivity of a laminate.

- Thin-ply carbon prepregs can be a candidate material for future ply weakening strategy investigation. It would be interesting to investigate if a pseudo-ductile multidirectional laminate can be created by using UD thin-ply sub-laminates, in which selected internal 0° plies have been cut or perforated. It may be necessary to also use interface weakening on the cut or perforated plies to ensure the pseudo-yielding behaviour occurs prior to ultimate failure.

- The performance of the ply weakening laminates should be investigated in other loading modes, such as impact and fatigue.

References

[1] M. R. Wisnom, B. Khan, and S. R. Hallett, "Size effects in unnotched tensile strength of unidirectional and quasi-isotropic carbon/epoxy composites," *Compos. Struct.*, 2008.

[2] M. R. Wisnom and S. R. Hallett, "The role of delamination in strength, failure mechanism and hole size effect in open hole tensile tests on quasi-isotropic laminates," *Compos. Part A Appl. Sci. Manuf.*, 2009.

[3] M. R. Wisnom, "Size effects in the testing of fibre-composite materials," *Compos. Sci. Technol.*, 1999.

[4] K. E. Jackson, S. Kellas, and J. Morton, "Scale Effects in the Response and Failure of Fiber Reinforced Composite Laminates Loaded in Tension and in Flexure," *J. Compos. Mater.*, 1992.

[5] H. Diao, P. Robinson, M. R. Wisnom, and A. Bismarck, "Unidirectional carbon fibre reinforced polyamide-12 composites with enhanced strain to tensile failure by introducing fibre waviness," *Compos. Part A Appl. Sci. Manuf.*, vol. 87, pp. 186–193, 2016.

[6] S. Pimenta and P. Robinson, "Wavy-ply sandwich with composite skins and crushable core for ductility and energy absorption," *Compos. Struct.*, vol. 116, no. 1, pp. 364–376, 2014.

[7] J. D. Fuller, M. Jalalvand, and M. R. R. Wisnom, "Pseudo-ductility by fragmentation of central unidirectional plies in thin CFRP angle-ply laminates," *ECCM-16th Eur. Conf. Compos. Mater.*, no. June, pp. 22–26, 2014.

[8] J. D. Fuller and M. R. Wisnom, "Pseudo-ductility and damage suppression in thin ply CFRP angle-ply laminates," *Compos. Part A Appl. Sci. Manuf.*, vol. 69, pp. 64–71, 2015.

[9] J. D. Fuller, M. Jalalvand, and M. R. Wisnom, "Combining fibre rotation and fragmentation to achieve pseudo-ductile CFRP laminates," *Compos. Struct.*, 2016.

[10] J. D. Fuller, M. Jalalvand, and M. R. Wisnom, "Analytical modelling of pseudo-ductility in angle-ply CFRP laminates with central unidirectional plies," *20th Int. Conf. Compos. Mater. ICCM-20*, 2015.

[11] X. Wu, J. D. Fuller, M. L. Longana, and M. R. Wisnom, "Reduced notch sensitivity in pseudo-ductile CFRP thin ply angle-ply laminates with central 0° plies," *Compos. Part A Appl. Sci. Manuf.*, vol. 111, no. July 2017, pp. 62–72, 2018.

[12] A. Bismarck *et al.*, “Exploring Routes To Create High Performance Pseudo-Ductile Fibre Reinforced Composites,” *20th Int. Conf. Compos. Mater. ICCM-20*, 2015.

[13] M. R. Wisnom, “Mechanisms to create high performance pseudo-ductile composites,” *IOP Conf. Ser. Mater. Sci. Eng.*, vol. 139, no. 1, 2016.

[14] M. R. Wisnom, G. Czél, Y. Swolfs, M. Jalalvand, L. Gorbatikh, and I. Verpoest, “Hybrid effects in thin ply carbon/glass unidirectional laminates: Accurate experimental determination and prediction,” *Compos. Part A Appl. Sci. Manuf.*, vol. 88, pp. 131–139, 2016.

[15] F. Bouville, E. Maire, S. Meille, B. Van De Moortèle, A. J. Stevenson, and S. Deville, “Strong, tough and stiff bioinspired ceramics from brittle constituents,” *Nat. Mater.*, 2014.

[16] T. P. Niebel, F. Bouville, D. Kokkinis, and A. R. Studart, “Role of the polymer phase in the mechanics of nacre-like composites,” *J. Mech. Phys. Solids*, 2016.

[17] “Corrigendum: Strong, tough and stiff bioinspired ceramics from brittle constituents (Nature Materials (2014) 13 (508-514) DOI: 10.1038/nmat3915),” *Nature Materials*. 2017.

[18] S. Tapse and S. Anup, “Bio-inspired composites with functionally graded platelets exhibit enhanced stiffness,” *Bioinspiration and Biomimetics*, 2018.

[19] U. G. K. Wegst, H. Bai, E. Saiz, A. P. Tomsia, and R. O. Ritchie, “Bioinspired structural materials,” *Nat. Mater.*, 2015.

[20] F. Pinto, M. Meo, and F. Rizzo, “Bioinspired pseudo-ductile composite laminates with hierarchical energy absorption mechanism,” *Bioinspiration, Biomimetics, Bioreplication VIII*, no. March, p. 13, 2018.

[21] F. Pinto, M. Meo, and F. Rizzo, “Bioinspired pseudo-ductile composite laminates with hierarchical energy absorption mechanism,” in *Bioinspiration, Biomimetics, and Bioreplication VIII*, 2018.

[22] R. Malkin, M. Yasaee, R. S. Trask, and I. P. Bond, “Bio-inspired laminate design exhibiting pseudo-ductile (graceful) failure during flexural loading,” *Compos. Part A Appl. Sci. Manuf.*, vol. 54, pp. 107–116, 2013.

[23] F. De Luca, R. Menzel, J. J. Blaker, J. Birkbeck, A. Bismarck, and M. S. P. Shaffer, “Nacre-nanomimetics: Strong, Stiff, and Plastic,” *ACS Appl. Mater. Interfaces*, vol. 7, no. 48, pp. 26783–26791, 2015.

[24] J. Wang, Q. Cheng, and Z. Tang, “Layered nanocomposites inspired by the structure and mechanical properties of nacre,” *Chemical Society Reviews*. 2012.

[25] J. Summerscales and D. Short, “Carbon fibre and glass fibre hybrid reinforced plastics,” *Composites*, 1978.

[26] D. Short and J. Summerscales, “Hybrids - a review. Part 2. Physical properties,” *Composites*, 1980.

[27] T. P. Sathishkumar, J. Naveen, and S. Satheeshkumar, “Hybrid fiber reinforced polymer composites - A review,” *Journal of Reinforced Plastics and Composites*. 2014.

[28] Y. Swolfs, L. Gorbatikh, and I. Verpoest, “Fibre hybridisation in polymer composites: A review,” *Compos. Part A Appl. Sci. Manuf.*, 2014.

[29] M. R. Sanjay, G. R. Arpitha, and B. Yogesha, “Study on Mechanical Properties of Natural - Glass Fibre Reinforced Polymer Hybrid Composites: A Review,” in *Materials Today: Proceedings*, 2015.

[30] G. Kretsis, “A review of the tensile, compressive, flexural and shear properties of hybrid fibre-reinforced plastics,” *Composites*. 1987.

[31] Z. G. WEI, R. Sandstroröm, and S. MIYAZAKI, “Shape memory materials and hybrid composites for smart systems Part II Shape-memory hybrid composites,” *J. Mater. Sci.*, 1998.

[32] M. N. Gururaja and H. Rao, “A Review on Recent Applications and Future Prospectus of Hybrid Composites,” *Int. J. Soft Comput. Eng.*, 2012.

[33] M. Jalalvand, G. Czél, and M. R. Wisnom, “Numerical modelling of the damage modes in UD thin carbon/glass hybrid laminates,” *Compos. Sci. Technol.*, 2014.

[34] M. Jalalvand, G. Czél, and M. R. Wisnom, “Parametric study of failure mechanisms and optimal configurations of pseudo-ductile thin-ply UD hybrid composites,” *Compos. Part A Appl. Sci. Manuf.*, 2015.

[35] M. Jalalvand, G. Czél, and M. R. Wisnom, “Damage analysis of pseudo-ductile thin-ply UD hybrid composites - A new analytical method,” *Compos. Part A Appl. Sci. Manuf.*, 2015.

[36] G. Czél and M. R. Wisnom, “Demonstration of pseudo-ductility in high performance glass/epoxy composites by hybridisation with thin-ply carbon prepreg,” *Compos. Part A Appl. Sci. Manuf.*, vol. 52, pp. 23–30, 2013.

[37] W. Cui, M. R. Wisnom, and M. Jones, “An Experimental and Analytical Study of Delamination of Unidirectional Specimens with Cut Central Plies,” *J. Reinf. Plast. Compos.*, vol. 13, no. 8, pp. 722–739, 1994.

[38] W. Cui, M. R. Wisnom, and M. L. Jones, “Effect of Through Thickness Tensile and Compressive Stresses on Delamination Propagation Fracture Energy,” *J. Compos. Tech-nology Res. JCTRER*, vol. 16, no. 4, pp. 329–335, 1994.

[39] M. Fotouhi, P. Suwarta, M. Jalalvand, G. Czel, and M. R. Wisnom, “Acoustic emission based method to characterise the damage modes in UD thin carbon/glass hybrid laminates,” in *ECCM 2016 - Proceeding of the 17th European Conference on Composite Materials*, 2016.

[40] M. Fotouhi, P. Suwarta, M. Jalalvand, G. Czel, and M. R. Wisnom, “Detection of fibre fracture and ply fragmentation in thin-ply UD carbon/glass hybrid laminates using acoustic emission,” *Compos. Part A Appl. Sci. Manuf.*, 2016.

[41] M. Fotouhi, P. Suwarta, M. Jalalvand, G. Czél, and M. R. Wisnom, “Acoustic emission monitoring of thin ply hybrid composites under repeated quasi-static tensile loading,” *FME Trans.*, 2018.

[42] H. G. Harris, W. Somboonsong, and F. K. Ko, “New Ductile Hybrid FRP Reinforcing Bar for Concrete Structures,” *J. Compos. Constr.*, 1998.

[43] J. Aveston and A. Kelly, “Tensile First Cracking Strain and Strength of Hybrid Composites and Laminates,” *Philos. Trans. R. Soc. A Math. Phys. Eng. Sci.*, 1980.

[44] M. Arrington and B. Harris, “Some properties of mixed fibre cfrp,” *Composites*, vol. 9, no. 3, pp. 149–152, 1978.

[45] K. D. Jones and A. T. DiBenedetto, “Fiber fracture in hybrid composite systems,” *Compos. Sci. Technol.*, vol. 51, no. 1, pp. 53–62, 1994.

[46] R. Amacher *et al.*, “Toward Aerospace Grade Thin-Ply Composites,” *Proc. ECCM-17, 17th Eur. Conf. Compos. Mater.*, no. November, pp. 26–30, 2016.

[47] R. Amacher, J. Cugnoni, J. Botsis, L. Sorensen, W. Smith, and C. Dransfeld, “Thin ply composites: Experimental characterization and modeling of size-effects,” *Compos. Sci. Technol.*, 2014.

[48] G. Czél, M. Jalalvand, and M. R. Wisnom, “Design and characterisation of advanced pseudo-ductile unidirectional thin-ply carbon/epoxy-glass/epoxy hybrid composites,” *Compos. Struct.*, 2016.

[49] G. Czél, M. Jalalvand, M. R. Wisnom, and T. Czigány, “Design and characterisation of high performance, pseudo-ductile all-carbon/epoxy unidirectional hybrid composites,” *Compos. Part B Eng.*, vol. 111, pp. 348–356, Feb. 2017.

[50] G. Czél *et al.*, "Pseudo-ductility and reduced notch sensitivity in multi-directional all-carbon/epoxy thin-ply hybrid composites," *Compos. Part A Appl. Sci. Manuf.*, vol. 104, pp. 151–164, 2018.

[51] G. Czél, T. Rév, M. Jalalvand, M. Fotouhi, and M. R. Wisnom, "Demonstration of pseudo-ductility in quasi-isotropic laminates comprising thin-ply UD carbon/epoxy hybrid sub-laminates," in *ECCM 2016 - Proceeding of the 17th European Conference on Composite Materials*, 2016.

[52] M. Fotouhi, M. Jalalvand, and M. R. Wisnom, "High performance quasi-isotropic thin-ply carbon/glass hybrid composites with pseudo-ductile behaviour in all fibre orientations," *Compos. Sci. Technol.*, 2017.

[53] M. R. Jalalvand, M., Czel, G., & Wisnom, "Multi-directional hybrid laminates-studying the effect of fragmentation and dispersed delamination on stress-strain curves of unnotched laminates using analytical modelling . In Proceedings of the 20th International Conference on Composite Materials (ICC," 2015.

[54] M. Jalalvand, M. Fotouhi, and M. R. Wisnom, "Orientation-dispersed pseudo-ductile hybrid composite laminates – A new lay-up concept to avoid free-edge delamination," *Compos. Sci. Technol.*, vol. 153, pp. 232–240, 2017.

[55] M. Jalalvand, M. Fotouhi, G. Czél, and M. R. Wisnom, "Avoiding free edge delamination in quasi-isotropic pseudo-ductile hybrid laminates - By material dispersion or layer angle dispersion?," *ECCM 2016 - Proceeding 17th Eur. Conf. Compos. Mater.*, no. June, pp. 26–30, 2016.

[56] R. Muñoz, F. Martínez, R. Seltzer, C. González, and J. Llorca, "Mechanical behaviour of hybrid 3D woven composites under static and impact loadings," *ECCM16 - 16th Eur. Conf. Compos. Mater.*, 2014.

[57] W. M. Diao H, Bismarck A, Robinson P, "Pseudo-ductile behaviour of unidirectional fibre reinforced polyamide-12 composite by intra-tow hybridization," in *Proceedings of ECCM 15 Conference*, 2012.

[58] Y. Swolfs, R. M. McMeeking, I. Verpoest, and L. Gorbatikh, "The effect of fibre dispersion on initial failure strain and cluster development in unidirectional carbon/glass hybrid composites," *Compos. Part A Appl. Sci. Manuf.*, 2014.

[59] Y. Swolfs, R. M. McMeeking, V. P. Rajan, F. W. Zok, I. Verpoest, and L. Gorbatikh, "Global load-sharing model for unidirectional hybrid fibre-reinforced composites," *J. Mech. Phys. Solids*, 2015.

[60] Y. Swolfs, L. Gorbatikh, and I. Verpoest, "Stress concentrations in hybrid unidirectional fibre-reinforced composites with random fibre packings," *Compos. Sci. Technol.*, 2013.

[61] J. M. Guerrero, J. A. Mayugo, J. Costa, and A. Turon, "A 3D Progressive Failure Model for predicting pseudo-ductility in hybrid unidirectional composite materials under fibre tensile loading," *Compos. Part A Appl. Sci. Manuf.*, vol. 107, no. February, pp. 579–591, 2018.

[62] Y. Swolfs, I. Verpoest, and L. Gorbatikh, "Maximising the hybrid effect in unidirectional hybrid composites," *Mater. Des.*, 2016.

[63] J. Henry and S. Pimenta, "Modelling hybrid effects on the stiffness of aligned discontinuous composites with hybrid fibre-types," *Compos. Sci. Technol.*, vol. 152, pp. 275–289, 2017.

[64] M. Jalalvand *et al.*, "Energy dissipation during delamination in composite materials – An experimental assessment of the cohesive law and the stress-strain field ahead of a crack tip," *Compos. Sci. Technol.*, 2016.

[65] Y. Swolfs *et al.*, "Tensile behaviour of intralayer hybrid composites of carbon fibre and self-reinforced polypropylene," *Compos. Part A Appl. Sci. Manuf.*, 2014.

[66] Y. Swolfs *et al.*, "The importance of bonding in intralayer carbon fibre/self-reinforced polypropylene hybrid composites," *Compos. Part A Appl. Sci. Manuf.*, 2015.

[67] S. A. Tabatabaei, Y. Swolfs, H. Wu, and S. V. Lomov, "Full-field strain measurements and meso-FE modelling of hybrid carbon/self-reinforced polypropylene," *Compos. Struct.*, 2015.

[68] Y. Swolfs, Y. Meerten, P. Hine, I. Ward, I. Verpoest, and L. Gorbatikh, "Introducing ductility in hybrid carbon fibre/self-reinforced composites through control of the damage mechanisms," *Compos. Struct.*, 2015.

[69] M. Selezneva *et al.*, "Formability study of hybrid carbon fibre/self-reinforced polypropylene composites," in *AIP Conference Proceedings*, 2018.

[70] G. Czél, M. Jalalvand, and M. R. Wisnom, "Demonstration of pseudo-ductility in unidirectional hybrid composites made of discontinuous carbon/epoxy and continuous glass/epoxy plies," *Compos. Part A Appl. Sci. Manuf.*, vol. 72, pp. 75–84, 2015.

[71] J. Tang *et al.*, "EXPLORING DISCONTINUITIES AND HYBRIDIZATION TO DESIGN GRADUAL FAILURE IN UNIDIRECTIONAL CARBON FIBER/SELF-REINFORCED

POLYPROPYLENE COMPOSITES," in *21st International Conference on Composite Materials*, 2017.

[72] J. Tang *et al.*, "Discontinuities as a way to influence the failure mechanisms and tensile performance of hybrid carbon fiber/self-reinforced polypropylene composites," *Compos. Part A Appl. Sci. Manuf.*, 2018.

[73] M. Selezneva *et al.*, "The brittle-to-ductile transition in tensile and impact behavior of hybrid carbon fibre/self-reinforced polypropylene composites," *Compos. Part A Appl. Sci. Manuf.*, 2018.

[74] H. Yu, K. D. Potter, and M. R. Wisnom, "A novel manufacturing method for aligned discontinuous fibre composites (High Performance-Discontinuous Fibre method)," *Compos. Part A Appl. Sci. Manuf.*, 2014.

[75] H. Yu *et al.*, "Aligned Short Fibre Composites With Nonlinear Behaviour," in *ICCM 20*, 2015.

[76] H. Yu, M. L. Longana, M. Jalalvand, M. R. Wisnom, and K. D. Potter, "Pseudo-ductility in intermingled carbon/glass hybrid composites with highly aligned discontinuous fibres," *Compos. Part A Appl. Sci. Manuf.*, 2015.

[77] M. L. Longana, H. Yu, I. Hamerton, and K. D. Potter, "Development and application of a quality control and property assurance methodology for reclaimed carbon fibers based on the HiPerDiF (High Performance Discontinuous Fibre) method and interlaminated hybrid specimens," *Adv. Manuf. Polym. Compos. Sci.*, vol. 4, no. 2, pp. 48–55, 2018.

[78] H. N. Yu, M. L. Longana, M. Jalalvand, M. R. Wisnom, and K. D. Potter, "Hierarchical pseudo-ductile hybrid composites combining continuous and highly aligned discontinuous fibres," *Compos. Part A Appl. Sci. Manuf.*, 2018.

[79] M. L. Longana, N. Ong, H. N. Yu, and K. D. Potter, "Multiple closed loop recycling of carbon fibre composites with the HiPerDiF (High Performance Discontinuous Fibre) method," *Compos. Struct.*, 2016.

[80] M. L. Longana, H. N. Yu, M. Jalavand, M. R. Wisnom, and K. D. Potter, "Aligned discontinuous intermingled reclaimed/virgin carbon fibre composites for high performance and pseudo-ductile behaviour in interlaminated carbon-glass hybrids," *Compos. Sci. Technol.*, vol. 143, pp. 13–21, 2017.

[81] J. Finley, H. Yu, M. L. Longana, S. Pimenta, M. S. P. Shaffer, and K. D. Potter, "Exploring the pseudo-ductility of aligned hybrid discontinuous composites using controlled fibre-type arrangements," *Compos. Part A Appl. Sci. Manuf.*, vol. 107, pp. 592–606, 2017.

[82] M. L. Longana, H. Yu, M. Jalalvand, and K. D. Potter, "The High Performance Discontinuous Fibre (HiPerDiF) technology for consistent quality control of reclaimed carbon fibres," in *ECCM 2016 - Proceeding of the 17th European Conference on Composite Materials*, 2016.

[83] J. Henry and S. Pimenta, "Modelling hybrid effects on the stiffness of aligned discontinuous composites with hybrid fibre-types," *Compos. Sci. Technol.*, 2017.

[84] J. Henry and S. Pimenta, "Semi-analytical simulation of aligned discontinuous composites," *Compos. Sci. Technol.*, 2017.

[85] J. Henry and S. Pimenta, "Virtual testing framework for hybrid aligned discontinuous composites," *Compos. Sci. Technol.*, 2018.

[86] H. P. Ductile and C. Technology, "HiPerDuCT," no. June, 2017.

[87] J. Henry and S. Pimenta, "Increasing damage tolerance in composites using hierarchical brick-and-mortar microstructures," *J. Mech. Phys. Solids*, vol. 118, pp. 322–340, 2018.

[88] S. Pimenta and P. Robinson, "An analytical shear-lag model for composites with 'brick-and-mortar' architecture considering non-linear matrix response and failure," *Compos. Sci. Technol.*, vol. 104, pp. 111–124, 2014.

[89] G. Czél, S. Pimenta, M. R. Wisnom, and P. Robinson, "Demonstration of pseudo-ductility in unidirectional discontinuous carbon fibre/epoxy prepreg composites," *Compos. Sci. Technol.*, 2015.

[90] T.-W. Chou and K. Takahashi, "Non-linear elastic behaviour of flexible fibre composites," *Composites*, 1987.

[91] S. Del Rosso, L. Iannucci, and P. T. Curtis, "Experimental investigation of the mechanical properties of dry microbraids and microbraid reinforced polymer composites," *Compos. Struct.*, 2015.

[92] D. Goyal and J. D. Whitcomb, "Effect of fiber properties on plastic behavior of 2 × 2 biaxial braided composites," *Compos. Sci. Technol.*, 2008.

[93] D. Goyal, J. D. Whitcomb, and X. Tang, "Validation of full 3D and equivalent tape laminate modeling of plasticity induced non-linearity in 2 × 2 braided composites," *Compos. Part A Appl. Sci. Manuf.*, 2008.

[94] T. Wehrkamp-Richter, R. Hinterhölzl, and S. T. Pinho, "Damage and failure of triaxial braided composites under multi-axial stress states," *Compos. Sci. Technol.*, 2017.

[95] T. Wehrkamp-Richter, N. V. De Carvalho, and S. T. Pinho, "A meso-scale simulation framework for predicting the mechanical response of triaxial braided composites," *Compos. Part A Appl. Sci. Manuf.*, vol. 107, no. August, pp. 489–506, 2018.

[96] J. D. Fuller and M. R. Wisnom, "Ductility and pseudo-ductility of thin ply angle-ply CFRP laminates under quasi-static cyclic loading," *Compos. Part A Appl. Sci. Manuf.*, 2018.

[97] F. De Luca, R. Menzel, J. J. Blaker, J. Birkbeck, A. Bismarck, and M. S. P. Shaffer, "Nacre-nanomimetics: Strong, Stiff, and Plastic," *ACS Appl. Mater. Interfaces*, 2015.

[98] F. De Luca *et al.*, "Increasing carbon fiber composite strength with a nanostructured 'brick-and-mortar' interphase," *Mater. Horizons*, vol. 5, no. 4, pp. 668–674, 2018.

[99] F. De Luca, "Fibre-Reinforced Composites with Nacre-Inspired Interphase: A Route Towards High Performance Toughened Hierarchical Composites," Imperial College London, 2016.

[100] G. Grail, S. Pimenta, S. T. Pinho, and P. Robinson, "Exploring the potential of interleaving to delay catastrophic failure in unidirectional composites under tensile loading," *Compos. Sci. Technol.*, vol. 106, pp. 100–109, 2015.

[101] D. B. Anthony, O. R. B. Nogales, M. S. P. Shaffer, A. Bismarck, and S. Pimenta, "Crack Arrest in Finger Jointed Thermoplastic Pes Interleaved Cfrc," *21st Int. Conf. Compos. Mater.*, no. August, pp. 20–25, 2017.

[102] S. Pimenta, "Pseudo-Ductile Failure Mechanism Introduced Into Finger Jointed Thermoplastic Pes Interleaved Cfrc," no. June, pp. 24–28, 2018.

[103] O. Bacarreza *et al.*, "Exploring the Use of Friction To Introduce Ductility," no. August, pp. 20–25, 2017.

[104] J. G. Williams, "On the calculation of energy release rates for cracked laminates," *Int. J. Fract.*, 1988.

[105] ASTM INTERNATIONAL, "ASTM D3039/D3039M: Standard test method for tensile properties of polymer matrix composite materials," *Annu. B. ASTM Stand.*, 2014.

[106] Torayca, "T800S Data Sheet," 2015.

[107] Hexcel ®, "M21 Curing Data Sheet."

[108] G. Czél, M. Jalalvand, and M. R. Wisnom, "Development of pseudo-ductile hybrid composites with discontinuous carbon- and continuous glass prepregs," *16th Eur. Conf. Compos. Mater.*, 2014.

[109] "How Does Laser Cutting Work?" [Online]. Available: http://www.esabna.com/us/en/education/blog/how-does-laser-cutting-work.cfm. [Accessed: 06-Jan-2019].

[110] G. Bullegas, S. T. Pinho, and S. Pimenta, "Engineering the translaminar fracture behaviour of thin-ply composites," *Compos. Sci. Technol.*, 2016.

[111] E. S. Greenhalgh, *Failure analysis and fractography of polymer composites*. 2009.

[112] C. T. Methods, F. O. R. The, M. T. H. E. Engineering, P. Of, and F. Reinforced, "Crag te-st methods for the measurementof the engineering properties of fibre reinforced plastics," *Methods*, 1988.

[113] L. J. Hart-Smith, "Expanding the capabilities of the Ten-Percent Rule for predicting the strength of fibre-polymer composites," in *Failure Criteria in Fibre-Reinforced-Polymer Composites*, 2004.

Appendix 1

Comparison of the analytical tensile response of the specimen free and gauge lengths

This section compares the tensile performance of the free and gauge lengths predicted by the refined analytical model for the UD 6-ply specimens containing a single, three and multiple cuts (at 10 mm intervals) in the two central plies. Figure A-1 shows the schematic distribution of the cuts in the free and gauge lengths of the 6-ply specimens containing a single, three and 10 mm apart periodic cuts in the two central plies (i.e. configurations (3), (4) and (5)). The highlighted 9 mm long regions near the two ends of each configuration denote the video extensometer neglected regions during the tests.

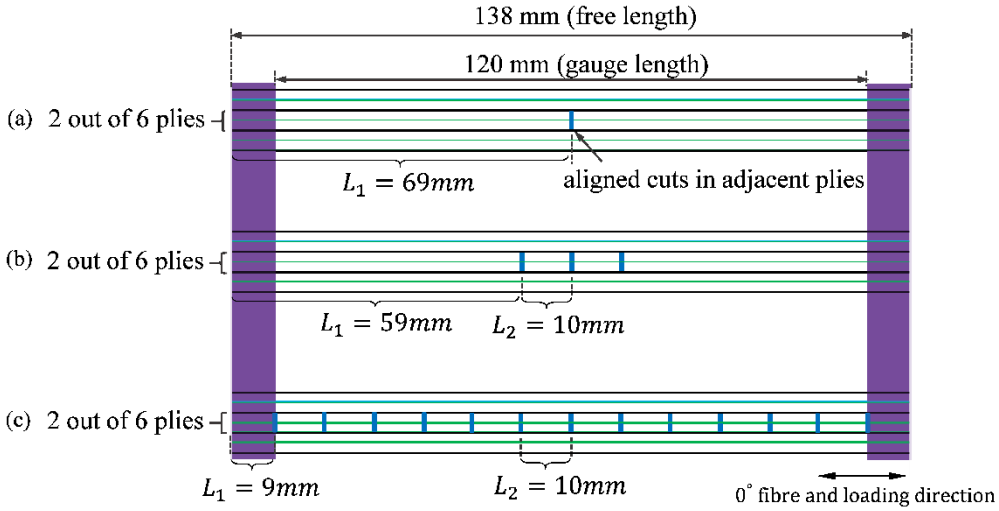


Figure A-1. Schematic side views of the UD 6-ply configurations (with a free length of 138 mm) containing (a) a single (configuration (3)), (b) three (configuration (4)) and (c) periodic cuts at 10mm intervals (configuration (5)) in the two middle plies, respectively.

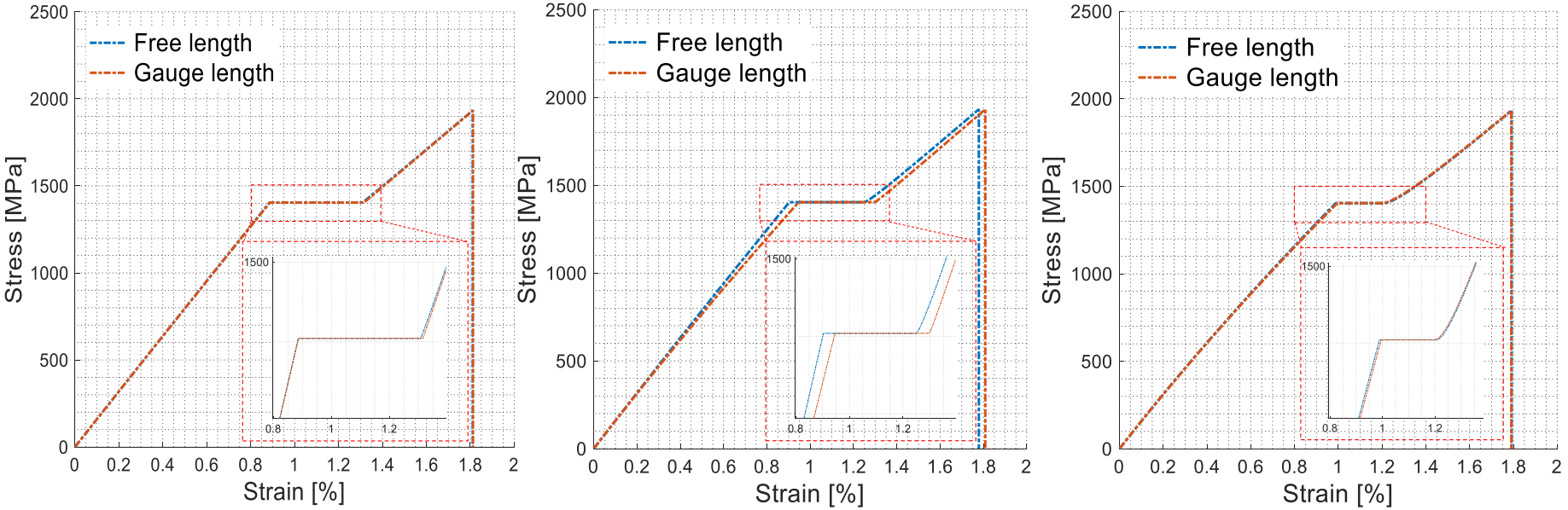
The refined analytical model presented in Section 3.5 for platelets of a specific length is also applicable for UD laminates made of platelets of different lengths. The average tensile strain of the 138 mm free length is taken as the overall extension of all platelets, divided by 138 mm. The average tensile strain of the gauge length is taken as the sum of extension of the platelets in the 120 mm long gauge length region (as shown in Figure A-1), which was monitored by the Imetrum video extensometer, divided by 120 mm. Note that no cut was introduced at the two ends of the free length (during the manufacture process). It means there is no stress transfer zone initiated at the two positions.

For configuration (3), two half-long stress transfer zones are initiated from the middle cut and propagate towards the two ends of the free length. It must be noted that, the evolution of these half-long stress transfer zones in the entire 138 mm free length is considered during the overall loading process, for the predicted tensile response of the free length. However, for the tensile response of the 120 mm gauge length, there is a period that close to the end of plateau stage, the half-long stress transfer zones move out from the 120 mm region to the highlighted 9 mm long regions (see Figure A-1). From this period, the video extensometer begins to neglect the evolution of the two stress transfer zones that migrated into the 9 mm regions, and instead only measures the strain evolution of the inner 120 mm region. (This period can be attempted basing on Figure 3.20.) Thereby, during this period, for a specific remote tensile stress level, the 120 mm gauge length records a lower average tensile strain than that of the 138 mm free length.

Configuration (4) can be regarded as consisting two 59 mm long platelets (each contains one half-long stress transfer zone) and two 10 mm long platelets (each contains two half-long stress transfer zones) in the free length. The way to calculate the strains of the 120 mm long gauge length and the 138 mm long free length is the same as that for the configuration (3).

In terms of configuration (5), there are exactly twelve 10 mm long platelets in the 120 mm gauge length, thereby the overall gauge length stress-strain behaviour is equivalent to that of a single 10 mm long platelet containing two half-long stress transfer zones. While for the free length, the average strain is taken as the overall extension of the twelve 10 mm platelets (all containing two half-long stress transfer zones) and the extension of two 9 mm stress transfer zones (with each containing a half-long stress transfer zone), divided by 138 mm.

The predicted tensile responses of the free and the gauge lengths of configurations (3), (4) and (5) are shown in Figure A- 2 (a), (b) and (c), respectively. The transition stage between the plateau and final strain-hardening stages in the stress-strain curves for each configuration, shown in Figure A- 2 (a) to (c), are enlarged to clearly show the difference. Figure A- 2 (a) and (c) show there is no significant difference in the tensile responses for configurations (3) and (5), containing uniform platelet length. More obvious difference is observed from configuration (4) (see Figure A- 2 (b)), containing three cuts.



(a) (b) (c)

Figure A- 2. Analytical tensile stress-strain response of the free and gauge lengths of UD 6-ply configurations containing (a) a single, (b) three and (c)10 mm apart periodic continuous cuts in the two central plies.

Appendix 2

Laser milling machine

A schematic of the laser machine is shown in Figure A- 3. An example set of parameters employed on the CNC Oxford® A series/Compact laser micromachining machine, to mill a 184 μm thick prepreg, without accumulating excessive heat, is shown in Table A- 1.

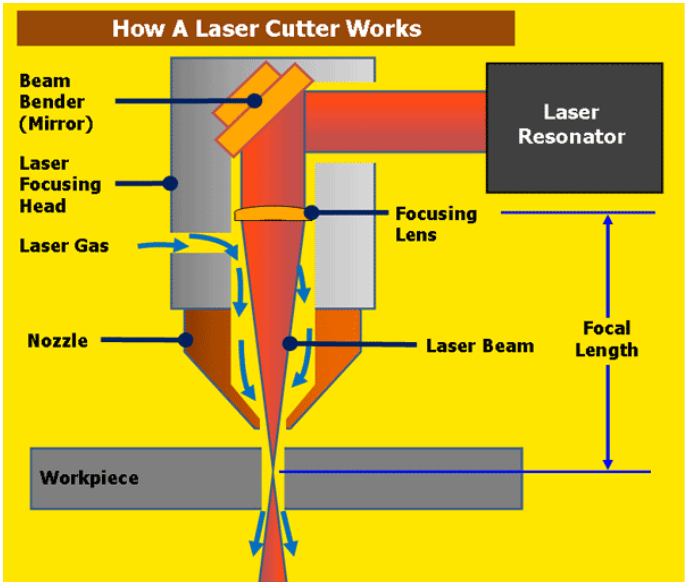


Figure A- 3. Schematic working principle of the laser milling machine. Copied from [109].

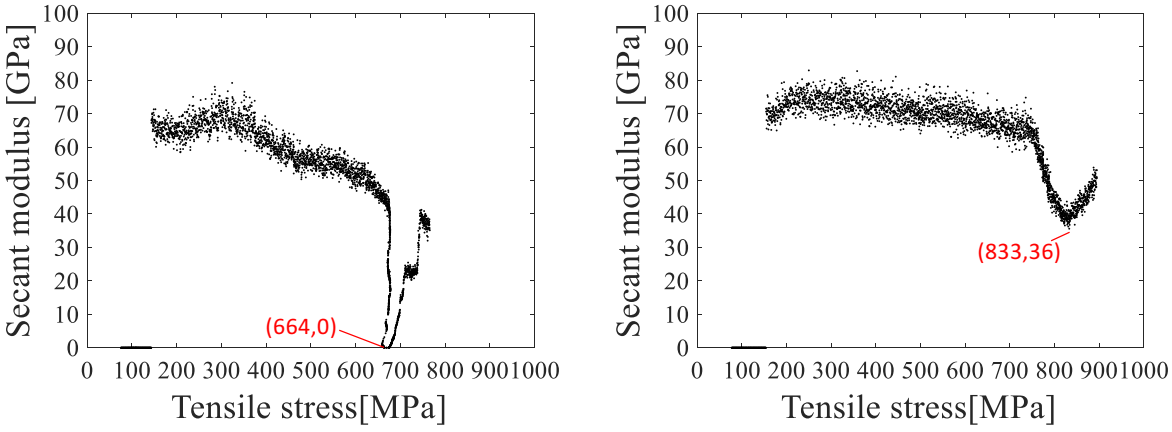
Table A- 1. Summary of laser milling parameters for perforating a 184 µm thick prepreg.

Laser machine setup	
Laser current (A)	3.87
Focal length [mm] (see Figure A- 3)	73.145
Laser milling parameters	
Laser beam pulse frequency [kHz]	30
Percentage of full laser power [%]	23
Cutting speed [mm/s]	100
Pulse repetition rate per feature	110

Appendix 3

Pseudo-yield stress identification technique for the pseudo-ductile multi-directional configurations

The pseudo-yield stresses of the pseudo-ductile multi-directional configurations were derived from the tensile secant modulus relative to the tensile stress diagrams. The pointwise secant moduli for the entire loading process were calculated with a constant strain interval of 1840 $\mu\varepsilon$. This strain interval gives relatively low fluctuation in the tensile secant modulus-tensile stress plots, as shown in Figure A-4. Two example plots of a pseudo-ductile specimen containing cuts with the layup of [90°/0°/+45°/-45°/0°_{c}]s and a '5P-5S' pattern perforated specimen with the layup of [90°/+45°/-45°/0°/0°_{p}]s (investigated in Chapter 6) are shown in Figure A-4. For the cut-ply configuration, the pseudo-yield stress, σ_{ycM}, is determined from the first point, associated with zero secant modulus in the secant modulus-tensile stress diagram, as shown in Figure A-4 (a). The pseudo-yield stress is 664 MPa, for the cut-ply specimen shown in Figure A-4 (a). The pseudo-yield stress, σ_{ypM}, for the perforated-ply specimen was determined from the point with the lowest secant modulus, as shown in Figure A-4 (b). Thereby, the pseudo-yield stress for this perforated-ply specimen is 833 MPa. The associated pointwise secant modulus measured from this point is 36 GPa.



(a) (b)

Figure A-4 Tensile secant modulus-tensile stress curves of the multi-directional pseudo-ductile (a) cut-ply and (b) perforated-ply specimens.